Tuning Roseolumiflavin Properties by Multicomponent Crystallization: Structural, Energetic, and Photophysical Perspective

Inaugural-Dissertation

zur Erlangung des Doktorgrades

Dr. rer. nat.

der Mathematisch-Naturwissenschaftlichen Fakultät

der Heinrich-Heine-Universität Düsseldorf

vorgelegt von

Takin Haj Hassani Sohi

aus Herdecke

Düsseldorf, Januar 2026

aus dem Institut für Anorganische Chemie und Strukturchemie I

der Heinrich-Heine-Universität Düsseldorf

Gedruckt mit der Genehmigung der

Mathematisch-Naturwissenschaftlichen Fakultät der

Heinrich-Heine-Universität Düsseldorf

Berichterstatter:

1. Prof. Dr. Christoph Janiak

2. Prof. Dr. Christian Ganter

Tag der mündlichen Prüfung: 10.03.2026

Eidesstattliche Erklärung

Ich versichere an Eides Statt, dass die Dissertation von mir selbständig und ohne unzulässige fremde Hilfe unter Beachtung der „Grundsätze zur Sicherung guter wissenschaftlicher Praxis an der Heinrich-Heine-Universität Düsseldorf“ erstellt worden ist. Zur Generierung von Ideen, Ergebnissen oder Interpretationen in dieser Arbeit wurde keine generative KI verwendet. Generative KI (ChatGPT-5.2) kam lediglich in begrenztem Umfang zur sprachlichen Überarbeitung zum Einsatz. Die aus fremden Quellen direkt oder indirekt übernommenen Gedanken sind als solche kenntlich gemacht. Die Arbeit wurde bisher weder im Inland noch im Ausland in gleicher oder ähnlicher Form einer anderen Prüfungsbehörde vorgelegt. Es wurden keine früheren erfolglosen Promotionsversuche unternommen.

_____ _____

Ort, Datum Unterschrift

Danksagungen

In diesem Abschnitt gedenke ich meinen Dank an die vielen Weggefährten über meine Studien- und Promotionsphase auszudrücken.

Allen voran möchte ich meiner Betreuerin und Mentorin Frau Dr. Vera Vasylyeva-Shor danken. Trotz meines „Quereinstieges“, von der Bachelorarbeit in der theoretischen Chemie zur Ambition eine Masterarbeit in den Materialwissenschaften zu schreiben, schenkte sie mir ihr Vertrauen. Doch dabei sollte es nicht bleiben, jenes Vertrauen folgte bis hin zur Betreuung über meine gesamte Promotionszeit hinaus. Vera, Ich bin froh durch meine Forschungsarbeit einen Beitrag zu deiner hoffentlich immer weiterwachsenden Arbeitsgruppe geleistet zu haben und dazu über diese Zeit viel gelernt zu haben über Projektentwicklung und -Management. Mir wurde ausreichend Raum gegeben, eigene Ideen voranzutreiben. Gleichzeitig hast du bei Unklarheiten oder Problemen jederzeit unterstützt mit hilfreichen und kreativen Lösungen und stets offener Ansprechbarkeit.

Selbstverständlich gilt mein Dank ebenso Herrn Prof. Dr. Christoph Janiak zur Aufnahme an seinem Lehrstuhl, Bereitstellung von Laboren und Geräten und der Ermöglichung der Teilnahme an weiteren interessanten Projekten, die zu vielen Koautorschaften und der Ansammlung von wertvoller Praxiserfahrung führten. In diesem Kontext sei auch Herrn Prof. Dr. Mohammed Enamullah zu danken, mit dessen Projekte ein Großteil der Koautorschaften realisiert wurde.

Herrn Prof. Dr. Christian Ganter danke ich für seine Bereitschaft, das Zweitgutachten für diese Dissertation zu übernehmen.

Herrn Prof. Dr. Constantin Czekelius gilt mein Dank nicht nur für die Synthese und Bereitstellung von Forschungsobjekten, allen voran verschiedener Flavin- und Acridonderivate, sondern auch, dass mir die Möglichkeit gegeben wurde mich jederzeit bei Fragen an ihn oder seine Mitarbeiter wenden zu können.

Herrn PD Dr. Oliver Weingart danke ich für seine ständige Unterstützung und Hilfsbereitschaft gerade im Hinblick auf die Bedienung von Software. Danke Oliver, deiner Hilfe wegen habe ich mir bestimmt einiges an Grübeln gespart.

Herrn Dr. Gündoğ Yücesan danke ich für die Möglichkeit mich an seinem Projekt beteiligen zu dürfen die schließlich zu einer Publikation führte, für seine wertvollen Beiträge und Hilfestellungen und die ebenso offene und immer freundliche Kommunikation. Ich wünsche alles Gute und viel Erfolg im Aufbau der eigenen Arbeitsgruppe!

Herrn Jun.-Prof. Dr. Markus Suta danke ich ebenso für wichtige Beiträge zu meinen Projekten und seiner Bereitschaft, mir bei Fragen und Unklarheiten wertvolle Hilfestellung zu leisten.

Herr Dr. István Boldog hat ebenfalls einen besonderen Dank verdient. Zunächst in Bezug auf meine Dissertation danke ich dir für dein wertvolles Feedback welches immensen Einfluss auf mein kritisches Denken nahm und mir ermöglichte, die Dinge aus neuen Perspektiven zu betrachten. Darüber hinaus möchte ich auch die persönliche Komponente hervorheben: die unzähligen Gespräche über allerlei Themen, die ich mit dir führen durfte. Es war mir stets eine Freude und hat oftmals zur Bewältigung des Alltagsstresses geholfen.

Den technischen Mitarbeitern gilt natürlich mein Dank für die Bereitschaft bei Fragen aller Art.

Mir ist es ebenso wichtig meinem ehemaligen Betreuer der Bachelorarbeit Herrn Dr. Adrian Heil sowie Frau Prof. Dr. Christel Marian den Dank auszusprechen, die mir einen wichtigen ersten Schritt in die wissenschaftliche Arbeit aufgezeigt und mich damit entscheidend geprägt haben.

Meinen fünf Bachelorstudenten Felix Maaß, Lea Pongratz, René Müller, Martin Polko und Clara Reipen, die ich betreuen durfte, danke ich für ihre Beiträge zur Forschung, ihren Einsatz und letztendlich für die angenehme Zeit im Büro, Labor oder gelegentlich sogar außerhalb der Uni! Es war mir eine Freude Projekte für euch zu entwickeln, mit euch gemeinsam voranzukommen und miteinander Lösungen finden zu können. Euch wünsche ich weiterhin alles Gute für eure Zukunft!

Meinen ehemaligen und aktuellen Arbeitsgruppenkollegen Dr. Daniel Komisarek, Tobias Heinen, Philipp Seiffert und Sarah Merzenich danke ich für die großartige Zeit zusammen und die stete gegenseitige Hilfsbereitschaft. Mit euch wurde diese Zeit zu einer bereichernden Erfahrung! Nicht zu kurz kommen sollten selbstverständlich meine (weiteren, ehemaligen) Bürokollegen. Unter diesen zähle ich noch Dr. Soheil Abdpour, Dr. Abdulrahman Mohabbat und Varvara Ryabuhina. Da Sven Hößel und David Geller auch oft genug dabei waren, seien sie direkt dazu genannt! Vielen Dank für die angenehme Zeit und euch viel Erfolg für die Zukunft!

Allen weiteren Arbeitskreiskollegen, die ich über die Jahre kennenlernen durfte, gilt mein Dank für die schöne Zeit zusammen!

Zum Abschluss sei einzelnen Personen gedankt, die mir stets über die Jahre meinen Rücken gedeckt haben. So meiner Schwester Tanin, die zum jetzigen Zeitpunkt ebenfalls an ihrer Dissertation arbeitet und der ich alles Gute und viel Erfolg wünsche. Auch meiner Freundin Maria möchte ich meinen Dank aussprechen, mir stets beiseite gesessen und, gerade in der kritischen Endphase meiner Dissertation, mir immer wieder Mut zugesprochen zu haben. Meinen Eltern Nasrin und Khosrow danke ich mit Nachdruck, mir diesen akademischen Weg überhaupt erst ermöglicht und geebnet zu haben und widme Ihnen diese Arbeit.

Table of Contents

I. Publication List

First-Author Publications[1]

Co-crystallization of organic chromophore roseolumiflavin and effect on its optical characteristics

T. Haj Hassani Sohi, F. Maaß, C. Czekelius, M. Suta and V. Vasylyeva

CrystEngComm, **2022**, *24*, 7315–7325.

A Comparison Study of Roseolumiflavin Solvates: Structural and Energetic Perspective on Their Stability

T. Haj Hassani Sohi, F. Maaß, C. Czekelius and V. Vasylyeva

Crystals, **2023**, *13*, 1512.

Polyphosphonate covalent organic frameworks

K. Xu*, R. Oestreich*, T. Haj Hassani Sohi*, M. Lounasvuori, J. G. A. Ruthes, Y. Zorlu, J. Michalski, P. Seiffert, T. Strothmann, P. Tholen, A. Ozgur Yazaydin, M. Suta, V. Presser, T. Petit, C. Janiak, J. Beckmann, J. Schmedt auf der Günne and G. Yücesan

* These authors contributed equally.

Nat Commun, **2024**, *15*, 7862.

Tuning Molecular Assembly and Optical Properties via Cocrystallization: A Case Study of Roseolumiflavin in Binary and Ternary Multicomponent Systems

T. Haj Hassani Sohi, L. Pongratz, F. Maaß, S. Merzenich, L. Samperisi, C. Czekelius and V. Vasylyeva

Cryst. Growth Des. **2025**, *25*, 24, 10482–10496

---

[1] Note: All titles are reproduced verbatim from the original publications.

Co-Author Publications

Co-crystals of zwitterionic GABA API's pregabalin and phenibut: properties and application

D. Komisarek, T. Haj Hassani Sohi and V. Vasylyeva

CrystEngComm, **2022**, *24*, 8390–8398.

Polymorphism and Multi-Component Crystal Formation of GABA and Gabapentin

D. Komisarek, F. Demirbas, T. Haj Hassani Sohi, K. Merz, C. Schauerte and V. Vasylyeva

Pharmaceutics, **2023**, *15*.

Indole Diketopiperazine Alkaloids from the Marine Sediment-Derived Fungus Aspergillus chevalieri against Pancreatic Ductal Adenocarcinoma

D. H. El-Kashef, D. D. Obidake, K. Schiedlauske, A. Deipenbrock, S. Scharf, H. Wang, D. Naumann, D. Friedrich, S. Miljanovic, T. Haj Hassani Sohi, C. Janiak, K. Pfeffer and N. Teusch

Marine drugs, **2023**, *22*.

Experimental and computational studies on pseudotetrahedral nickel(ii)-(S or R)-dihalogen-salicylaldiminates with Δ- or Λ-chirality induction at-metal

A. Saadati, H. Amiri Rudbari, M. Aryaeifar, O. Blacque, I. Correia, M. K. Islam, D. Woschko, T. Haj Hassani Sohi, C. Janiak and M. Enamullah

CrystEngComm, **2023**, *25*, 365–377.

Hydrogen-Bonded Ladder Motifs in Naphthalene Dicarboxamides: Influence of Linear vs. Angular Amide Orientation

A. Mohabbat, I. Boldog, T. Haj Hassani Sohi, N. Reistel, P. Seiffert and C. Janiak

Crystals, **2025**, *15*, 406.

Syntheses and X-ray structures of enantiopure Schiff bases (R or S)-2-(((E)-1-(Ar)ethylimino)ethyl)phenol, copper(II) complex and (R or S)-(Ar)ethyl-ammonium sulphate/acetate

M. Enamullah, I. Haque, A. K. Resma, T. Aziz, T. Haj Hassani Sohi, D. Woschko and C. Janiak

Inorganica Chimica Acta, **2025**, *583*, 122657.

Square planar vs. pyramidal copper(ii)-complexes with benzylal vs. naphthylal-based Schiff bases

M. Enamullah, I. Haque, A. K. Resma, G. Abdullah, M. N. Uddin, T. Haj Hassani Sohi, D. Woschko, P. Ferber and C. Janiak

RSC advances, **2025**, *15*, 18358–18371.

Ferromagnetically coupled tetranuclear Ni(ii)-2-oxy-aceto- or benzo-phenonate complexes

I. Haque, M. Enamullah, N. T. Jhumur, B. K. Sidhu, D. E. Herbert, T. Haj Hassani Sohi, L. Havlíček, I. Nemec and C. Janiak

RSC advances, **2025**, *15*, 4250–4261.

Dinuclear vs. mononuclear copper(ii) complexes with nitrophenylimino-benzylal- vs. -naphthylal-based Schiff base ligands

M. Enamullah, I. Haque, G. Abdullah, F. H. Sourav, N. T. Jhumur, M. K. Islam, T. Haj Hassani Sohi, P. Ferber and C. Janiak

New J. Chem., **2025**, *49*, 17106–17123.

Targeted Fluorescence Enhancement of Acridones by Hydrogen Bonding in Solution and Solid State

M. Jantz, D. Klaverkamp, B. Bendel, T. Haj Hassani Sohi, M. Polko, L. Bunnemann, T. Böhmer, M. Putscher, C. Marian, C. Czekelius, V. Vasylyeva, M. Suta, P. Gilch

J. Mater. Chem. C, **2025**, *in revision.*

II. Short Summary

This work constitutes the first systematic investigation of roseolumiflavin, a flavin derivative that emits in the red range, within the framework of a crystal engineering approach. This organic chromophore was chosen as a model flavin to develop multicomponent crystal structures in order to target the modification of solid-state emission behavior. The imide group served as a functional recognition site to form controlled supramolecular synthons based on hydrogen bonds (HB) and halogen bonds (XB).

Binary co-crystals, solvates and hydrates were obtained. In addition, a systematic series of binary co-crystals as well as partially protonated ternary co-crystals with *N*-heterocycles and acids as the second or third component, respectively, was investigated in more detail. One photophysical trend observed in the co-crystal systems is the consistent blue shift in fluorescence compared to pure roseolumiflavin, with the shift increasing with the extent of the reorganization of the packing pattern, even further enhanced in the case of the proton transfer-stabilized ternary systems.

Solvates and hydrates also had a physicochemical effect on thermal stability, supporting the influence of the crystal engineering approach on material properties. Topological analyses allow quantification of selected interaction contributions and the qualitative assessment of dispersive contributions. HB at the imide group of flavins act as a structural guide. Stacking contacts further provide important stability contributions to packing formation.

A concurrent objective was to determine the extent to which these systems can be obtained on the basis of mechanochemical synthesis processes, as this would also allow a more sustainable approach to be pursued. In fact, a large majority of the systems could be formed using a low-solvent liquid-assisted grinding (LAG) method.

In summary, an overarching design principle can be derived from the results: Targeted modification of the solid-state emission of roseolumiflavin can be achieved via the imide group with defined HB and XB supramolecular synthons, which reorganize or replace the stacking pattern in a controlled manner. The resulting change in local interaction hierarchy significantly determines the stability and the degree to which the optical behavior can be influenced.

III. Kurzzusammenfassung

Diese Arbeit dient der ersten systematischen Untersuchung von Roseolumiflavin, einem im roten Bereich emittierenden Flavinderivat, im Rahmen eines Crystal Engineering Ansatzes. Dieses organische Chromophor wurde als Modell-Flavin genutzt, um Multikomponenten-Kristallsysteme zu entwickeln mit der Absicht, das Festkörper-Emissionsverhalten gezielt zu modifizieren. Als funktionelle Anknüpfstelle diente die Imidgruppe, damit kontrollierte supramolekulare Synthone auf Basis von Wasserstoffbrücken (HB) und Halogenbindungen (XB) gebildet werden.

Es wurden binäre Ko-Kristalle, sowie Solvate und ein Hydrat erhalten. Zudem wurde eine systematische Serie binärer, inklusive ternärer Ko-Kristalle mit anteiligem Protonenübertrag, mit *N*-Heterozyklen und Säuren als zweite bzw. dritte Komponente näher untersucht. Ein beobachteter photophysikalischer Trend der Ko-Kristallsysteme ist die konsistent blauverschobene Fluoreszenz gegenüber reinem Roseolumiflavin. Dabei nimmt die Verschiebung mit dem Ausmaß der Reorganisation des Packungsmusters zu und kann in protontransfer-stabilisierten ternären System weiter verstärkt werden. Auch konnte durch Solvate und einem Hydrat ein physikochemischer Einfluss auf thermische Stabilität beobachtet werden, welches den Einfluss des Crystal Engineering Ansatzes auf Materialeigenschaften untermauert. Topologische Analysen ermöglichen die Quantifizierung ausgewählter Wechselwirkungsbeiträge sowie die qualitative Erfassung dispersiver Beiträge. HB an der Imidgruppe des Flavins wirken strukturleitend und motivbildend. Stapelkontakte liefern wichtige Stabilitätsbeiträge zur Bildung der Packungen. Ein paralleles Ziel war es zu ermitteln, inwiefern diese Systeme auf Basis von mechanochemischen Syntheseprozessen erhalten werden können, da hierdurch auch ein übergeordneter nachhaltiger Ansatz verfolgt werden konnte. Tatsächlich konnte eine große Mehrheit der Systeme durch die lösungsmittelarme, flüssigkeitsunterstützte Vermahlung (*liquid-assisted grinding*, LAG) gebildet werden.

Zusammengefasst lässt sich aus den Ergebnissen ein übergreifendes Designprinzip ableiten: Gezielte Modifizierung der Festkörper-Emission von Roseolumiflavin gelingt über die Imidgruppe mit definierten, supramolekularen HB und XB Synthonen, welche das Stapelmuster kontrolliert reorganisieren oder ersetzen. Die daraus resultierende Veränderung der lokalen Wechselwirkungshierarchie bestimmt maßgeblich die Stabilität und inwieweit das optische Verhalten beeinflusst werden kann.

IV. List of Abbreviations

BSM	Basic Structural Motif
COF	Covalent Organic Framework
CSD	Cambridge Structural Database
CSP	Crystal Structure Prediction
DAD	Donor-Acceptor-Donor
DSC	Differential Scanning Calorimetry
FTIR	Fourier-Transform Infrared Spectroscopy
FWHM	Full Width at Half Maximum
HB	Hydrogen Bond
HOMO	Highest Occupied Molecular Orbital
IC	Internal Conversion
ISC	Intersystem Crossing
IUPAC	International Union of Pure and Applied Chemistry
IVR	Intramolecular Vibrational Relaxation
LAG	Liquid-Assisted Grinding
LUMO	Lowest Unoccupied Molecular Orbital
MDPI	Molecular Diversity Preservation International
NCI	Non-Covalent Interaction
NMA	*N*-methyl-acridone
NMR	Nuclear Magnetic Resonance Spectroscopy
OLED	Organic Light-Emitting Diode
PXRD	Powder X-ray Diffraction
QTAIM	Quantum Theory of Atoms in Molecules
SCat	Schreiner's Catalyst
SCXRD	Single-Crystal X-ray Diffraction
TADF	Thermally Activated Delayed Fluorescence
TGA	Thermogravimetric Analysis
TGA-MS	Thermogravimetric Analysis coupled with Mass Spectrometry
XB	Halogen Bond
XPS	X-ray Photoelectron Spectroscopy

1. Introduction

1.1. The Concept of Crystal Engineering

The rise of supramolecular chemistry in the late twentieth century fundamentally reshaped the way chemists approached molecular organization. The “chemistry beyond the molecule”, as J.-M. Lehn defined it[1], placed non-covalent interactions at the center of molecular recognition and self-assembly. Analogous to E. Fischer’s lock-and-key concept from 1894[2], molecules identify partners through a host-guest model based on both energetic and geometrical complementarity[3,4]. The pioneering works of J.-M. Lehn, D. J. Cram and C. J. Pedersen were awarded the 1987 Nobel Prize in Chemistry, highlighting the significance of supramolecular chemistry as a novel emerging discipline.

The development of supramolecular chemistry of molecular systems stimulated the emergence of crystal engineering, a counterpart focusing on solid-state periodic structures. Crystal engineering, which lies at the core of the work presented in this thesis, constitutes a comparatively young branch within the wider framework of chemical history. First introduced in 1955 by R. Pepinsky at the American Physical Society meeting held in Mexico City[5], the term rose to wider attention in the 1970s. The coinage was further consolidated by contributions of G. M. J. Schmidt, whose work on studies on the topochemical photodimerization of cinnamic acid derivatives established the principle that molecular reactivity in the solid state is governed by crystal packing[6,7], and by J. M. Thomas, who reflected on Schmidt’s findings from the perspective of crystal engineering and explicitly introduced examples in the mid-1970s[8,9]. Over the upcoming decades, the mere concept emerged into an established discipline. Bridging organic chemistry, solid-state chemistry and materials science, this emerging discipline is best conceived as an interplay between crystallography and chemistry, as articulated by G. R. Desiraju[10]. Indeed it was Desiraju who, particularly from the 1980s to 1990s, significantly elaborated on its conceptual foundations and the role and versatility of the hydrogen bond[11–20], with today´s understanding of crystal engineering still rooted in his 1989 definition as “*the understanding of intermolecular interactions in the context of crystal packing and the utilization of such understanding in the design of new solids with desired physical and chemical properties*”[18]. Hence, under this premise, understanding intermolecular interactions is not merely informative

but constitutive for what crystal engineering can achieve. The subsequent years witnessed important conceptual and methodological advances. During the 1990s, hydrogen bond motifs were systematically categorized, supported by the development of the graph-set notation by M. C. Etter and J. Bernstein[21] and Desiraju's concept of the supramolecular synthon in 1995[16], which provided a unifying framework for rational crystal design. The following decade expanded towards the exploration of alternative non-covalent interactions such as π···π stacking[22], C—H···π stacking[23–27] and notably halogen bonds. The latter, through the pioneering contributions of P. Metrangolo and G. Resnati[28–33], established itself as an interaction comparable in its utility as a supramolecular design tool to hydrogen bonds and significantly broadened the scope of supramolecular design strategies. At the same time, the crystallographic field underwent major developments especially aided by data-driven analyses and theoretical calculations which transformed a largely experimental science into a computationally assisted discipline. Part of these advancements is the implementation of the Cambridge Structural Database (CSD) in 1965, which has since evolved into the central repository for all published organic and metal-organic small-molecule crystal structures[34].

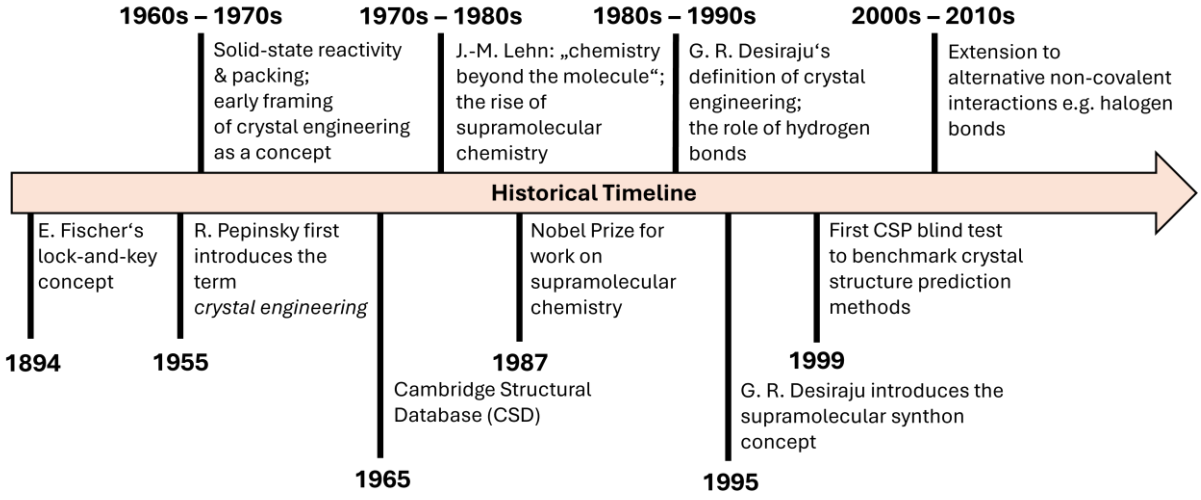

Figure 1 Historical and conceptual milestones shaping the field of crystal engineering.

The continuous curation has established the CSD as a foundational resource for data-based crystallography. In parallel, approaches toward crystal structure prediction (CSP) marked a conceptual leap, moving beyond the question "what is the structure?" towards "what could the structure be?". Among the extensive research conducted in this area (which will not be discussed here in detail as it lies beyond the scope of this

thesis) blind test projects were initiated and hosted by the Cambridge Crystallographic Data Centre since 1999, aiming to evaluate, assess and build upon the status quo of organic crystal structure prediction software and methodologies[35–41]. The rapid progress of artificial intelligence (AI)-based tools may foster the next generation of AI-assisted CSP approaches, lowering computational demands and substantially improving predictive reliability[42–46].

Despite these methodological and computational advances, the predictability of crystal formation remains inherently limited. As Desiraju noted[47], crystal engineering still retains a partly empirical character because molecular self-assembly in the solid state involves a fine interplay of thermodynamic and kinetic factors that cannot yet be fully controlled. Moreover, polymorphism, solvent effects and subtle conformational flexibility frequently determine crystallization outcomes in ways that remain difficult to anticipate[46,48–54]. It is therefore the author's intention to clarify the limitations and contextual boundaries that define this very field. When *engineering* of a crystal is asserted, a rational design approach is the typical assumption. However, such design is naturally constrained by the aforementioned inherent unpredictability of the crystallization process, where direct control remains elusive. D.-K. Bučar in his 2017 perspective article highlighted several challenges of crystal structure design observed in his research group, underscoring the limited predictability of design strategies and, in conclusion, calling for closer interplay between experimentalist and theoretical chemists to overcome these obstacles[55]. To illustrate this further, one study conducted in our research group in 2022 mapped the multicomponent crystallization of racemic baclofen and phenibut with tartaric and malic acid across both solution and mechanochemical routes. The essential conclusion was that hydrate intermediates are pervasive and often outcompete anhydrous targets; phase purity is frequently compromised; and mechanochemistry can selectively produce anhydrous forms. Yet, reproducibility can be challenging, depending on the respective systems[56]. These examples nonetheless are not intended to diminish the scientific value of crystal engineering but rather to demonstrate a critical awareness of the empirical framework with which such studies are carried out. D. Braga, for instance, shares Desiraju's holistic view of this discipline as a rational approach towards functional solid-state materials, describing it as a continuum from analysis to design, albeit without deterministic guarantees. But this is to be understood optimistically, as Braga argues:

“This lack of predictability, instead of weakening the motivation of the crystal makers, has strengthened the need for further experimentation and research”[57]. For the record, Bučar likewise emphasized that the challenging instances he presented were not intended to discourage but rather to raise awareness of potential unexpected outcomes amid numerous successful cases[55]. To conclude this section, it may be emphasized that crystal engineering, though still rooted in empirical observation, is steadily advancing toward more rational and model-guided design, a transition that reflects not only methodological progress but also the maturation of the discipline itself.

1.2. Intermolecular Interactions

A crystal engineer is, unsurprisingly, concerned with crystals. But what does a crystal as a pinnacle of interest actually mean? Is it a *final product*, thus, the outcome of a design process, the material manifestation of a supramolecular intent? Or is it a *model system* through which supramolecular design principles can be evaluated? Does it represent a *tool* through which the crystal engineer can observe, quantify, and ultimately understand intermolecular interactions? Or can it, in some way, even be understood as a medium by which molecules express their preferred modes of association? All those deeper senses are thus valid, and crystals are not merely products but complex symbols of the *language* of molecular self-assembly.

The discussion of the complexity of contexts, associated with crystals in crystal engineering is beyond the scope of this introduction. However, even a naïve approach of direct analysis of characteristic structural patterns is of undeniable value for the experimentalist. What should still be stressed is that a crystal ultimately represents the result of the interplay between all underlying intra- and intermolecular interactions operating within a given system. Viewed from a supramolecular chemistry perspective, the study of the latter is crucial to expand our understanding of a given system, find patterns, motifs or supramolecular synthons to utilize as a tool for rational design. The following section provides a concise overview of the most prominent intermolecular interactions that underpin pattern recognition and guide crystal structure analysis.

1.2.1. The Hydrogen Bond

Among the various non-covalent forces that govern molecular association, the hydrogen bond remains the most comprehensively studied and arguably the most influential in dictating molecular crystal structures. Historically, its recognition dates

back to the early 20th century with pioneering works of W. M. Latimer and W. H. Rodebush in 1920, who, following G. N. Lewis' newly proposed theory of the shared electron pair[58], described the hydrogen atom as capable of being electrostatically attracted by two electronegative centers simultaneously[59]. They suggested that a hydrogen nucleus could be "held between two octets", thereby forming a weak but distinct bridge between molecules. This conceptualization laid the foundation for L. Pauling's later formal definition in *The Nature of the Chemical Bond* in 1939[60] and ultimately established the hydrogen bond as a fundamental organizing principle in both molecular chemistry and crystallography. Spectroscopic and crystallographic studies throughout the mid-20th century refined its description[61–66]. Desiraju emphasized its role as a predictable and designable supramolecular interaction, thereby transforming the hydrogen bond from a structural phenomenon into a design-oriented tool of crystal engineering.

The 2011 International Union of Pure and Applied Chemistry (IUPAC) recommended consensus definition describes the hydrogen bond (HB) as an attractive interaction that forms between a hydrogen atom from one molecular fragment with another fragment, either within the same molecule or between molecules, where evidence of bond formation is observable[67]. A simple depiction is X—H···Y—Z to represent the HB via three dots between the interacting molecular fragments. That said, the interaction itself is not to be understood as a single, uniform physical mechanism. Instead, a hydrogen bond represents a compilation of energetic contributions of electrostatic, polarization, charge-transfer and dispersive character[68–70]. This directly accounts for the wide energetic span observed for the HB, typically ranging from values between <1 kJ/mol up to 40 kJ/mol, which prompted Desiraju and Steiner to classify these in weak, strong and very strong categories[19]. In rare occasions, substantially stronger hydrogen bonds can be detected, such as in the case of HF_2^-, which was measured at 161.5 kJ/mol, or related systems, where interaction energies may far exceed those of conventional HBs[71,72]. These examples, however, represent exceptions and fall well outside the range relevant to most molecular crystals. From a crystal engineering perspective, the directionality of HB plays a particularly important role. HB impose spatial constraints that propagate beyond the local interaction into higher-order organization: Dimers assemble into one-dimensional linear chains, chains into two-dimensional ribbons or networks and ultimately into three-dimensional packing architectures (see Figure 2). In

other words, HB provide a robust structural scaffold for hierarchical assembly in the solid state[21,73–75]. These interactions are not merely described geometrically but also analyzed using topological tools. In particular, R. F. W. Bader's Quantum Theory of Atoms in Molecules (QTAIM)[76,77] is often employed to identify the topology of the electron density associated with bonding interactions. In the case of HB, the obtained electron density parameters can be related to hydrogen bond energies[78], providing a versatile tool to characterize and quantify interaction modes. Ultimately, recurrent HB motifs are recognized as supramolecular synthons, i.e. an abstraction of a self-assembly pathway, which could be used for the "design" of new structures with a reasonably high level of realization, in contrast to variable motifs based on less directional interactions such as generic dispersive contacts[16,47,79]. The aforementioned concept of the supramolecular synthon falls under this category. Arguably one of the most consequential conceptual innovations in the 1990s, the supramolecular synthon framework enabled a shift from purely descriptive crystallography to a more predictive paradigm[16].

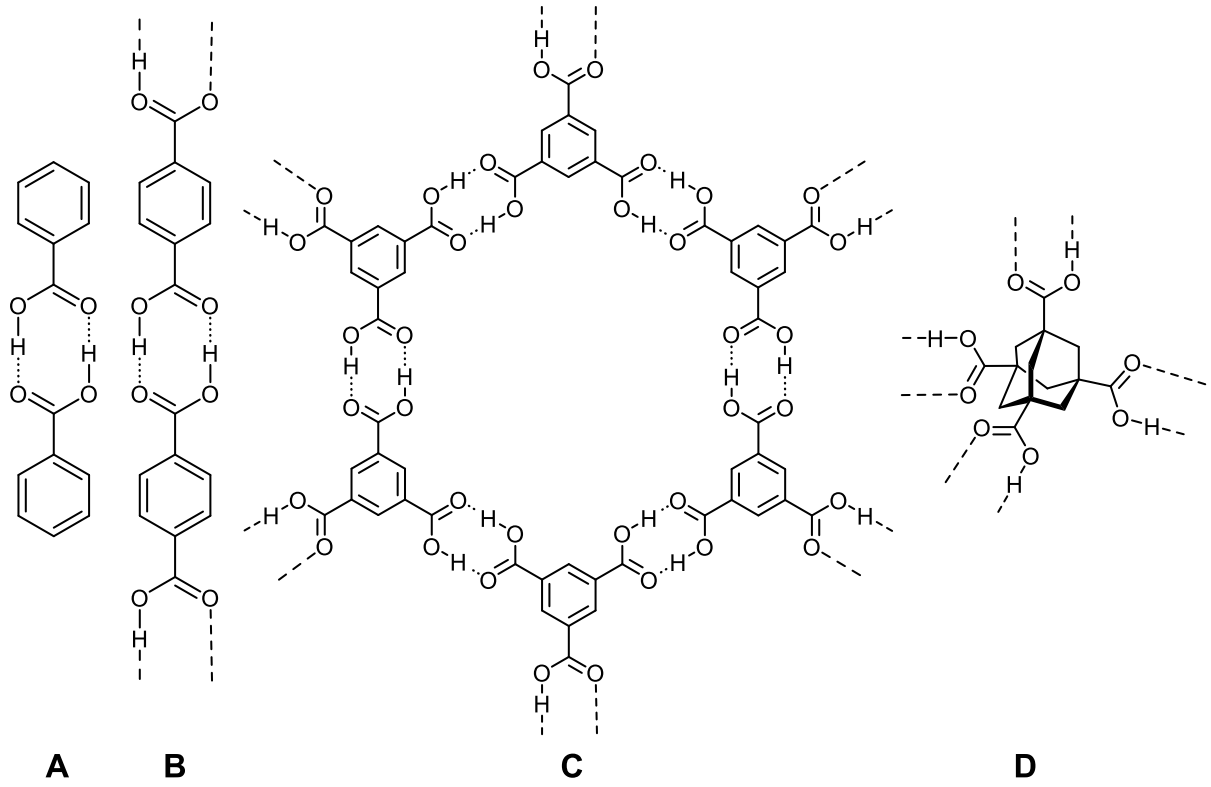

Figure 2 Structural illustration of the 0-dimensional benzoic acid motif **A**, the 1-dimensional terephthalic acid motif **B**, the 2-dimensional trimesic acid motif **C** and the 3-dimensional adamantane-1,3,5,7-tetracarboxylic acid motif **D**.

1.2.2. The Halogen Bond

Having outlined the conceptual and design relevance of HB, it is now necessary to consider halogen bonds (XB) as the second major directional interaction class that, particularly since the early 2000s, has attained a high level of design relevance within supramolecular chemistry. Pioneering works, especially considering the stress on the relevance for modern supramolecular chemistry, are to be contributed to Metrangolo, Resnati and colleagues, who aided in recognition and standardization of the term *halogen bond*[29–31]. First reports of halogen-involved interactions with electron donors date back to 1863[80], with H. Bent[81] and O. Hassel[82] discussing characteristics of related interactions and hydrogen bonds in the late 60s and early 70s, respectively, though the explicit conceptualization of these contacts as a distinct and designable supramolecular interaction class emerged only much later[83]. This culminated in the IUPAC definition of the halogen bond in 2013 as an attractive interaction between the region of positive electrostatic potential on a halogen atom and an electron donor site[84]. The high polarizability of the heavier halogens (particularly Br and I) enables the formation of short-contacts with electron-rich species, whereas this effect is considerably reduced for Cl and essentially negligible for F. Consequently, a positively polarized site forms along the bond axis, located along the prolongation of the covalently bonded halogen atom. T. Clark, J.S. Murray, P. Politzer and colleagues extensively discussed this positive electrostatic region and introduced the term *σ-hole*[83,85–88]. The combination of high polarizability and the alignment along the elongated covalent C—X bond axis results in pronounced directionality, typically displaying nearly linear X···Y geometries with bond angles approaching 180°, often exceeding the geometric precision of HB[28,89–92]. Furthermore, selective perfluorination of XB donors enhances the σ-hole by withdrawing electron density from the halogen atom, thereby strengthening its ability to interact with electron-rich acceptors[29,85,93–95]. The selectivity of the halogen atom, influencing both size and strength, makes this kind of interaction highly tunable. The interaction strength can range from 10 to 200 kJ/mol[28], albeit typical XB would fall in the lower end of this, usually ranging 5 to 30 kJ/mol[96,97]. Figure 3 displays a schematic representation of the halogen bond and some typically observed trends.

Compatibility with HB has been a topic of concern when both possible interacting partners are present. Undoubtedly, the similarity between both bonds can in certain

cases lead to competition and selectivity between HB and XB[98–105], several cases show interplay of both interactions to occur side by side or with the same backbone leading to both coexistence and cooperativity, at times even with synergistic effects[106–112]. A. R. Voth *et al*. highlighted that halogen bonding can either directly compete with hydrogen bonding or both interactions coexist at a shared acceptor[113,114] while C. C. Robertson *et al*. point out the role of the solvent that aids in control of the intermolecular interactions[115]. Overall, the possible synergism of HB and XB provides a powerful extension of the supramolecular design toolkit.

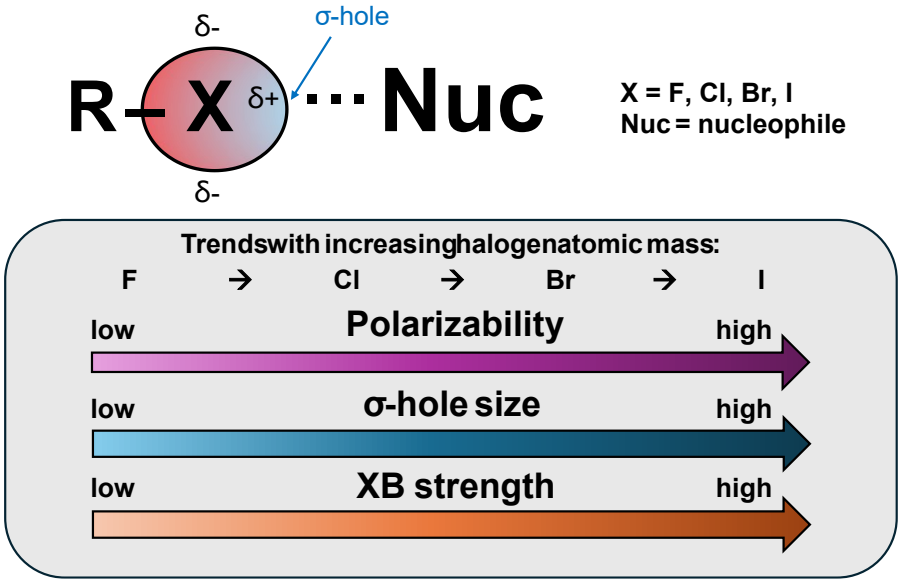

Figure 3 Schematic representation of halogen bond between a R—X fragment and a nucleophile Nuc. Charge distribution around the halogen atom X result in formation of a positive region (σ-hole) along the R—X axis. Trends observed across the halogen series are an increase in polarizability, σ-hole size as well as the strength of the halogen bond donor.

1.2.3. Stacking Interactions and Other Dispersive Forces

While the HB and XB represent the most directional and designable types of intermolecular interactions, they rarely act in isolation. Weaker, yet pervasive dispersive forces frequently contribute to molecular organization, either emerging as stabilizing interactions in the final solid-state structure or subtly influencing the assembly pathway leading to it. These non-directional but omnipresent forces encompass a variety of close-contact interactions, prominently van der Waals interactions. In the sense adopted by Desiraju within crystal engineering, the term encompasses all stabilizing or destabilizing forces that arise from London dispersion and are not attributable to hydrogen bonds or other anisotropic forces[116]. Although individually weak, their ubiquity and cumulative nature essentially render them

significant contributors to both crystal stability and packing preferences[17,116–119]. To qualitatively visualize such weak contacts, non-covalent interaction (NCI) plots provide utility. Based on the electron density as well as the reduced density gradient, NCI plots reveal regions of strong and weak attractive or repulsive interactions. Via them, the contribution of dispersive contacts can be detected, assessed and qualitatively compared[120].

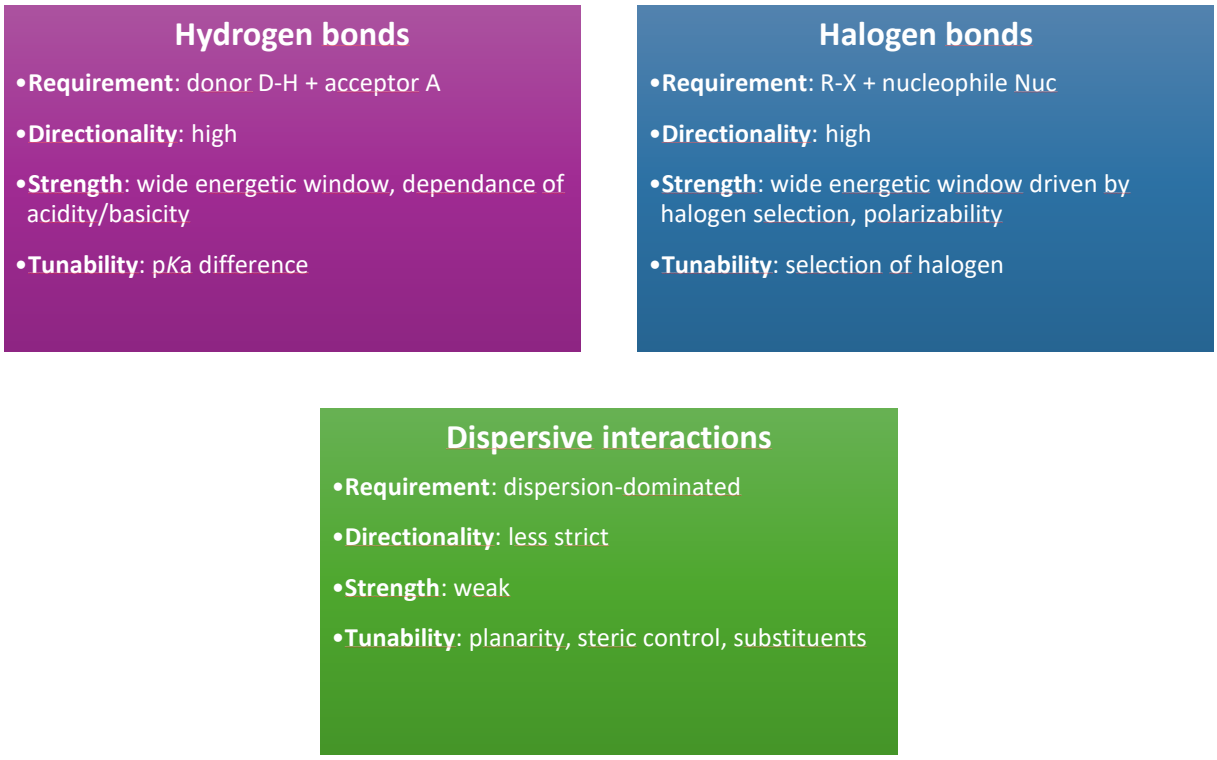

Figure 4 Comparison of key characteristics of hydrogen bonds, halogen bonds and dispersive interactions.

Within this wider dispersive landscape, stacking interactions between aromatic π-systems represent a distinct influential subclass, typically referred to as π···π interactions. In the context of crystal engineering, stacking interactions fulfil a dual role. On the one hand, controlled stacking can be employed as a *design tool*. Predictable motifs allow the crystal engineer to direct molecular assembly and deliberately influence the resulting crystalline architecture. On the other hand, specific stacking arrangements can represent a *design objective* in their own right. Several classes of functional materials derive their properties from a desired stacking geometry, in many cases specific π···π interactions, making the intentional construction of targeted stacking patterns a central goal. Section 1.4. will address these in more detail.

Particularly the π···π interaction was conceptually modelled by C. A. Hunter and J. K. M. Sanders in 1990. Their model assumes that π···π stacking is governed by quadrupole-based electrostatic interactions between aromatic rings to rationalize preferred stacking geometries. Each ring possesses a negative π-electron density above and below the plane and a positive region around the C—H areas[121]. Statistical analyses (on the basis of metal complexes) by C. Janiak establish that nearly all experimentally observed π···π interactions adopt parallel-displaced or slipped geometries rather than perfect face-to-face arrangements[22,121]. Figure 5 illustrates some common, observable stacking geometries. Notably, π···π interactions have long been the subject of debate as their physical origin is often contested. At the core of the debate lies the question of how their physical origin should be interpreted and whether common conceptual pictures misrepresent the underlying forces[122–126]. The C—H···π interaction, as an illustrative case, exemplifies this uncertainty, as it is variably classified as a weak hydrogen bond or as a π-type interaction depending on the system and criteria applied[25,27,127,128]. The classical Hunter-Sanders model provides an important electrostatic framework, although E. Wheeler in 2025 reassessed that some of its popular interpretations are oversimplified. He furthermore demonstrated, that the original Hunter-Sanders potential can still reproduce qualitatively correct trends for certain geometries, yet modern computational analyses show that dispersion-driven and short-range contacts between substituents and π surfaces constitute the primary determinants of π···π stabilization[129].

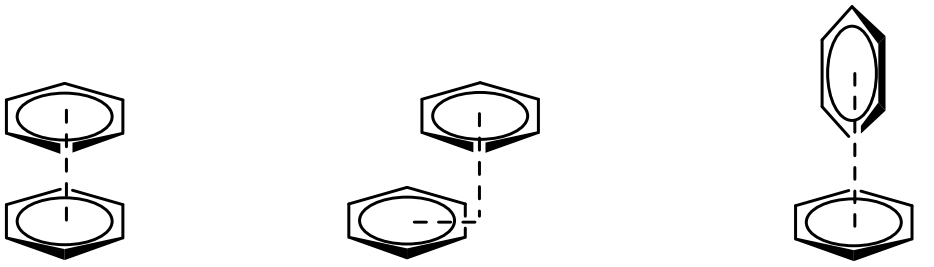

Figure 5 Common stacking motifs: cofacial, parallel-displaced and edge-to-face arrangement.

Dispersive interactions therefore complement directional interactions such as HB and XB and frequently determine the overall packing arrangement. This becomes particularly evident in the solid state, where subtle variations in the underlying

geometry can reorganize the supramolecular architecture and potentially shape structural and functional characteristics.

1.3. Multicomponent Crystals: Co-Crystals and Beyond

In the field of materials science, many opportunities to design tailor-made materials exist, and multicomponent crystals are a prime example. Composed of different molecular components held together by non-covalent forces, novel systems arise consequently with modified or tuned physicochemical features, dependent on the nature of the components, the design target as well as the rational design approach. For example, semiconductor properties can be tuned by donor-acceptor co-crystallization, as shown for the 1:1 co-crystal of 1,5-dihydroxynaphthalene and 7,7′,8,8′-tetracyanoquinodimethane through pairing of π-stacking donor and acceptor. Here, A. Mandal *et al*. observed the resulting co-crystal yield a narrow bandgap of around 1 eV and a low LUMO energy level (-3.8 eV), associated with improved air stability[130]. Another recent example of X. Fan and co-workers reports that four organic charge-transfer co-crystals of *p*-fluoranil deliver improved specific capacity and cycling stability as organic Li-ion battery electrodes relative to the individual components[131]. As a further illustration, the anti-inflammatory drug Diclofenac was 1:1 co-crystallized with picolinamide, leading to improved tabletability and enhanced solubility, as described in a recent study of C. Wu *et al*. in 2025[132]. In fact, a wide range of properties are tunable through multicomponent crystal formation, including mechanical properties[133–138], pharmaceutical performance[139–147], dissolution behavior[140,148–153], photophysical responses or optical characteristics[154–159], among others.

One prominent class of these crystalline materials, foremost for a crystal engineer, is the co-crystal. Although it is common to begin with a straightforward definition, no single, universally applicable definition of a co-crystal exists (while there exists a proposed solution, to which will be referred later in this paragraph). This lack of uniformity stems from the inherently gradual boundaries between the various classes of multicomponent solids, among which co-crystals appear alongside salts, solvates and hydrates. These categories share numerous structural and conceptual features, yet their terminology often implies sharp distinctions that, in practice, are difficult to draw. The question of how co-crystals should be classified has therefore been the subject of debate[160–164]. A detailed recitation of this debate lies beyond the scope of

this work; Still, a brief overview is necessary to clarify the position adopted here and to make explicit the assumptions under which this thesis intends to operate: After the first wave of the flourishing period of crystal engineering, the term *co-crystal* (or *cocrystal*, though we will proceed to use the former) simultaneously gained popularity as a designation for crystalline solids composed of two or more components. Early reflections of Desiraju in 2003, followed by J. D. Dunitz in the same year, initiated a discussion on how clear of a distinction can be made between a co-crystal and other multicomponent crystalline systems and what the prefix “co-” really implies[160,163]? A. D. Bond in 2007 argued that it is essentially synonymous with the older term *multi-component molecular crystals* and that conciseness and convenience were major reasons for the widespread adoption of the new term[161]. A multi-authored 2012 perspective article at last offered a quasi-consensus definition to define co-crystals as following: “*co-crystals are solids that are crystalline single phase materials composed of two or more different molecular and/or ionic compounds generally in a stoichiometric ratio*”[165]. This definition is what the author of this dissertation understands best to operate with, as it establishes a clear and practical framework. That said, what remains unresolved is to what extent solvates or hydrates represent subclasses of co-crystals or whether they should be regarded as distinct categories. In the interest of conceptual clarity, the stance taken here is to treat solvates and hydrates as separate classes in order to avoid ambiguity for the reader. Ultimately, it is less important which definition is considered correct than that a mutual understanding is established regarding the terminology used[164,166]. In the following, there shall be outlined briefly what is structurally understood by the terms *co-crystal*, *solvate* and *hydrate*:

Co-crystals consist of a target molecule and at least one additional component (commonly referred to as a *co-former*) which remains chemically intact within the lattice and does not undergo complete proton transfer, in contrast to salts. The components assemble through supramolecular synthons consisting of non-covalent interactions. These interactions shape the structural identity of a co-crystal and lay the basis for rational design, as the deliberate choice of a co-former allows systematic modification of both the packing arrangement and the resulting functional properties. In a recent 2024 study, A. Mondal *et al*. reported the impact through reduction of the initial 3D hydrogen-bonding network to 2D via co-crystallization of isoniazid with 3,4-dimethylbenzoic acid. By this, a significant decrease in stiffness of the compound was

achieved[167]. In contrast, solvates contain incorporated solvent molecules (with water-containing species specifically classified as hydrates) that originate from the crystallization medium and become part of the lattice. These species are not selected as deliberate co-formers, often stabilizing voids between the primary molecular components. Their presence can arise from coordination, hydrogen bonding, or general inclusion through dispersive contacts. The strict defining feature is that the solvent acts as a *lattice guest* rather than a designed structural partner. In practice, however, they often engage in directional interactions[168–172].

Multicomponent crystalline materials can additionally be classified by the number and nature of their components. Binary systems comprise two components and form the most common case. Ternary systems (and so on) extend this principle by incorporating additional components, thereby increasing the structural complexity but following the same general logic of supramolecular assembly. A further point of classification, though conceptually less clear-cut, concerns the protonation state of the components. Following the 2012 consensus definition, both neutral and ionic species may participate in co-crystal formation, provided that they coexist within a single crystalline phase without full proton transfer between the main molecular components. However, when the dominant mode of association is governed by complete proton transfer, the resulting solid is more appropriately described as a salt. Multicomponent crystals can thus be placed between two extremes, from fully neutral co-crystals on the one end and fully ionic salts on the other. A common approach is the use of the ΔpK_a between the components to indicate whether a system is more likely to form a salt or a neutral co-crystal[153,173,174]. Yet, as shown in S. L. Childs *et al.*'s work, ΔpK_a alone cannot fully predict the outcome, since many systems near the threshold display partial proton transfer and fall within the *salt/co-crystal continuum*[173]. Moreover, consistent terminology for such systems is lacking, in some cases generalized as mere co-crystals, mixed ionized phases or ionic co-crystals[175–177], to name a few.

Taken together, these considerations provide the conceptual framework within which multicomponent crystals are discussed in this thesis. In the following, particular emphasis will be placed on their use as a means to modulate photophysical properties.

1.4. State of the Art: Tuning Luminescent Photophysical Response

At first glance, the concept appears straightforward: physicochemical properties of materials can, in principle, be modulated merely by changing the molecular surroundings without changing the covalent building block. Within such context, the ability to deliberately modify photophysical behavior of organic chromophores in the solid state is central to a wide range of functional materials. Tuning optical features and control over excitation processes underpin recent developments of, for example, organic light-emitting diodes (OLEDs)[178–183], luminescent sensors[184–187] as well as magnetic[188] or mechanochromic[189,190] materials. To achieve predictable changes in absorption and/or emission behavior, quantum yields, luminescence lifetimes or charge transfer processes is therefore a key objective in materials chemistry. B. Li *et al*. in 2024 demonstrate that even variation of the stoichiometric ratio of the donor-acceptor co-components in pyrene-macrocycle and 1,2,4,5-tetracyanobenzene co-crystals results in distinct, tunable solid-state emission from yellow to red color, linking charge-transfer transition state formation to the different ratios[191].

The broad literature on electronic processes in organic and molecular crystals emphasizes that excitation processes in aggregated environments of molecules show distinctively different spectral response compared to an isolated molecule. The fundamentals lie in the ability of condensed phase materials to transport excitation energy ubiquitously and in that environment initiate energy transfer processes, such as luminescence, charge-transfer and photochemical reactions[192–195]. A principal early illustration of such collective solid-state behavior is the Davydov splitting, where intermolecular excitonic coupling causes the separation of degenerate electronic transitions[196]. In the following, the focus is set on π-conjugated organic chromophores, for which the dominant electronic transitions are of π→π* (and occasionally n→π*) character. While the general concepts of exciton formation and environment-dependent tuning of excited states can, in principle, be extended to other types of chromophores, the vast majority of examples are rooted in such π-systems and likewise the discussed compounds with which this thesis is concerned.

Restricting this brief summary of the excitation process to the most common cases of photophysically initiated activities, excitation upon absorption of a photon can be viewed as the transportation of an electron from the electronic ground state S_0 to an

arbitrary higher singlet excited state S_n (n≥1). This would in the following populate excited states, which in turn through relaxation processes follow a hierarchy of pathways. The fast intramolecular vibrational relaxation (IVR) redistributes and/or relaxes vibrational energy from excited modes to other vibrational modes. Internal conversion (IC) relaxes the excess energy from different electronic states, funneling the population into the lowest excited singlet state S_1. These processes are radiation-less. Slower subsequent radiative and competing non-radiative mechanisms ultimately return the molecule to its ground state[192,197,198]. Following Kasha's rule[199], the emission process originates from the lowest electronically excited state. In a spin-allowed singlet-singlet radiative decay $S_1 \rightarrow S_0$, typically exhibiting lifetimes in the nanosecond range, the process is referred to as fluorescence. Population of triplet states is enabled by intersystem crossing (ISC) and after subsequent IVR and IC processes ultimately to the T_1 state, non-radiative $T_1 \rightarrow S_0$ decay is possible. The corresponding radiative decay is called phosphorescence. The term describes a spin-forbidden triplet-singlet $T_1 \rightarrow S_0$ transition, characterized by much longer lifetimes spanning milliseconds to seconds[197,198]. The Jabłoński diagram serves as a convenient tool to illustrate these mechanisms (see Figure 6).

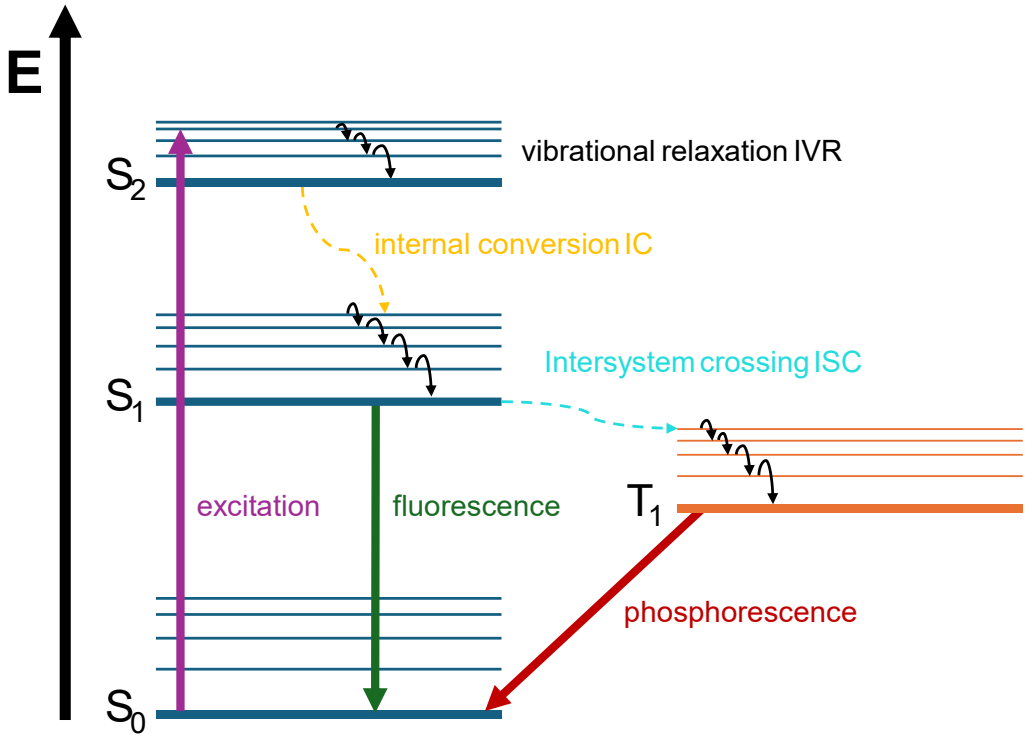

Figure 6 Simplified Jabłoński diagram illustrating excitation, radiative decay (fluorescence and phosphorescence) and the key non-radiative pathways (IVR, IC, ISC).

Once the same chromophores are packed into a crystal lattice, their excited states can no longer be regarded as strictly localized on a single molecule. The crystalline state can have significant influence on the luminescence[200–202], in cases even displaying enhanced emission of a compound in solid-state compared to its emissive capacity in solution[203]. Depending on the molecular packing arrangement or within charge-transfer or intermolecular interaction motifs, the photophysical response can significantly differ[204]. D. Barman *et al*., for example, achieved color-tunability primarily through packing-driven structural transformations, where adjusting acceptor strength induces hybrid stacking modes and yields color-specific polymorphs including, in one case, triplet-harvesting thermally activated delayed fluorescence (TADF)[157]. One and the same chromophore may display markedly different absorption and emission energies, quantum yields and excited-state lifetimes in different crystalline environments, even though its underlying electronic structure would remain essentially unchanged[202,205–207]. In this context, co-crystals offer a particularly attractive way to modulate the photophysical response of an organic chromophore without altering its covalent structure. Here, compared to purely single-component crystals, the co-crystal approach adds a modular aspect. A careful selection of co-formers can thus support adjustment efforts of the photophysical properties. N. Xue *et al*. in 2024 report full-color-tunable TADF by host-guest co-crystals of calix[3]acridan. Besides enhanced quantum yield, the authors stress especially how intentional modulation of the co-formers' electron-withdrawing ability results in fine-tunable emission color response from blue to red[208]. Early supramolecular and co-crystal-based work to demonstrate the modulation of solid-state luminescence emerged in the early 2010s. For example, A. Hori and co-workers in 2008 showed the linkage of two bipyridine derivatives via co-crystallization yields a red-shifted emission band[209], while S. P. Anthony *et al*. in 2009 showed that hydrogen-bonded multicomponent crystals of a triphenylamine-based acid with different amines exhibit blue shifted emission bands in the solid state, enabling reversible switching and tuning of the luminescence by simple supramolecular chemistry[210]. D. Yan *et al.* in 2011 reported the controlled modification of one- and two-photon luminescence of stilbene-type compounds via a co-crystallization approach[211], which in turn was highlighted by J. D. Wuest as a new paradigm to "tune up" light emission in molecular solids[212].

The work on this field has rapidly grown into a general design concept that seeks to systematically exploit the environmental responsiveness of organic chromophores in the solid state. A series of reviews has since highlighted how systematic co-crystallization efforts and related multicomponent crystal engineering strategies have enabled fine controlled tuning of solid-state photophysics. Given the breadth of the field, this section can only highlight selected developments. Several recent reviews provide comprehensive coverage and will be highlighted in the following. M. Singh *et al*. for example summarize recent approaches towards rational design of organic co-crystals with room temperature phosphorescence and report on the structure-property relationship[213]. Complementary perspectives come from reviews on charge-transfer co-crystals by X. Zhang *et al*.[214], the stimuli-responsive behavior of this subclass of organic co-crystals is further reviewed on by L. Sun *et al*.[215]; P.Yu *et al*. provide an overview of diverse aspects, strategies and advancements of crystal engineering approaches on organic optoelectronic materials[154]. A conceptual overview is offered by J. Gierschner *et al*. where the fundamental intra- and intermolecular factors governing luminescence in crystalline organic materials are briefly outlined[216]. D. Yan and co-workers, over the past decade, have published a series of reviews that emphasized the potential to modulate photophysical properties lying within molecular crystalline materials, including co-crystals[155,217–221]. The reader is therefore referred to these comprehensive accounts for an in-depth overview of design strategies, structure-property relationships and the various potential application scenarios.

What this ultimately underscores is that changes in the supramolecular arrangement, rather than modifications to the chromophore itself, can render new photophysical responses accessible, and co-crystals can be a valid tool for this purpose.

1.5. Flavins

Flavins constitute an isoalloxazine core structure, typically yellow-colored, formally corresponding to a 7,8-dimethylbenzo[*g*]pteridine-2,4(3*H*,10*H*)-dione parent structure[222]. See Figure 7 for a structural representation. They feature a chemical versatility which can be attributed to the ability of the isoalloxazine parent to form numerous redox states, each of which featuring different photophysical properties[223–225]. Besides their important roles in biological or metabolic processes, especially when exerting the role as enzyme cofactors in flavoproteins[223,226–229], flavins exhibit

photochemical activity, both in solution environment and in solid state[228]. Flavin derivatives, most notably riboflavin, display the capability as photosensitizers and photocatalysts[222,228,230–232], which makes them an attractive design element for light-responsive platforms[233–236]. In their oxidized form, flavins display absorption bands in solvent environment in visible regions with maxima around 370 nm to 450 nm and in near-UV regions around 220 nm to 270 nm[224]. Flavins typically display fluorescence. Their absorption and emission behavior in solution environment has been investigated in depth (primarily on a theoretical level) including different protonation and redox states[237–249]. The photophysics in the visible region of the oxidized form derive from π-π* transitions of the isoalloxazine core[223,225,247]. It was shown that the choice of the solvent impacts fluorescence quantum yields as well as intensity and shifts of absorption and emission bands, dependent on polarity and proticity[222,247,250–252].

This environmental sensitivity is not only limited to the dissolved species. Flavins can exhibit luminescence in solid state. However, research on this aspect of this compound is scarce. Noteworthy is the work of M. Sikorski's research group on the elucidation of the photophysics of a selection of flavins and flavin-like compounds, where solid state fluorescence spectra are reported next to mostly solution-based investigations. In all cases the crystalline phase measurements displayed red-shifted emission bands compared to those obtained from solution[246,248,253,254]. This can be a consequence of the rigid, defined framework determined by the crystal lattice in contrast to largely monomeric species in solution. That in turn raises the question to what extent intermolecular interactions and packing motifs govern the solid-state photophysics of flavins.

In flavoproteins, the isoalloxazine ring of the flavin is embedded in a network of specific non-covalent interactions[255] which suggests its suitability as a modular element in supramolecular chemistry considerations. Since the isoalloxazine core in the flavin is *per definitionem* 7,8-dimethyl-substituted and the N(10) position is likewise typically functionalized, the N(3) position, surrounded by two electronegative carbonyl sites together constructing the imide functional group, remains the primarily attractive electron affine site[225]. From a supramolecular design perspective, this specific site promises utility. K. Nishimoto *et al*. calculated possible hydrogen bond energies at the hetero atoms in lumiflavin to assess their effect on electron acceptability, reporting the order N(3)H>N(5)>O(12)>N(1)>O(14)[256]. V. M. Rotello *et al*., in an attempt to mimic

complex flavoenzyme interaction patterns, demonstrated that a three-point donor-acceptor-donor (DAD) HB motif between flavin and model receptors sufficed to induce shifts of electron reduction potential, attributed to stabilization of the semiquinone radical[224,257,258]. In fact, a small number of flavin-based multicomponent crystal structures exist like co-crystals[259–262] or solvates[263] and salts[264–268], although the majority of these reports is dated to the 1970s and no dedicated focus was set to elucidate the solid-state structure-property relationships.

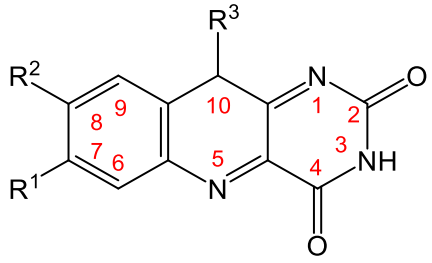

Isoalloxazine: $R^1 = R^2 = R^3 = H$
Flavin group: $R^1 = R^2 = CH_3$
Lumiflavin: $R^1 = R^2 = R^3 = CH_3$
Roseoflavin: $R^1 = CH_3$, $R^2 = N(CH_3)_2$, R^3 = 2,3,4,5-tetrahydroxypentyl
Roseolumiflavin: $R^1 = CH_3$, $R^2 = N(CH_3)_2$, $R^3 = CH_3$

Figure 7 Structure of the isoalloxazine ring system with corresponding atom numbering. Shown are substituent combinations R^1-R^3 for isoalloxazine, the general flavin core and flavin derivatives lumiflavin, roseoflavin and roseolumiflavin.

8-(dimethylamino)-7,10-dimethylbenzo[*g*]pteridine-2,4(3*H*,10*H*)-dione, in the following referred to as roseolumiflavin, is a red-colored flavin derivative. Like its structural parent roseoflavin, it possesses a dimethylamino substituent on C(8) position. Roseoflavin in solution, unlike typically yellow-colored flavins like riboflavin, displays in visible range an absorption maximum around 500 nm[269,270], thereby absorbing tapredominantly in green-blue region. In contrast to roseoflavin, the N(10) position is merely substituted by a methyl group in roseolumiflavin, which facilitates a less sterically restrictive framework, offering increased freedom for targeted structural modification on a supramolecular basis. Prior to the works presented in this thesis, roseolumiflavin was only addressed on a theoretical level by B. Karasulu and W. Thiel, who investigated photophysical properties in vacuum, water and benzene, highlighting the role of the molecular environment in shaping its excited-state landscape[271]. No experimental data or solid-state structural information was available, representing a knowledge gap which the present thesis aims to address.

1.6. Crystallization and the Mechanochemical Approach

A myriad of crystallization techniques exist to obtain the respective solid-state materials. A common saying suggests that crystallization is more art than science, reflecting its strongly empirical and experience-driven character[272,273]. This thesis is concerned with two particular approaches, namely common solvent evaporation methods from solution and mechanochemical synthesis by grinding. In the first case, the compounds are dissolved in a given stoichiometric ratio in a suitable solvent or solvent mixture, and the solvent is set to evaporate. This leads to gradual supersaturation along with the evaporation process and co-crystals can grow as a result. By this, serving as a simple and efficient method, co-crystals can be generated or initial co-crystal screening studies executed[274,275]. One advantage is that by this method single-crystal growth suitable for X-ray diffraction (single-crystal X-ray diffraction, SCXRD) can be achieved directly out of solution, as the crystallographer can control the rate of the evaporation. Slow evaporation is often desired. However, it needs thus to be taken into consideration that the crystallization step can take time[143].

In contrast, mechanochemical crystallization relies on the application of mechanical force, such as grinding or milling, to provoke molecular recognition and synthesis directly in the solid-state. This procedure can be conducted by neat (dry) grinding or accompanied by mere catalytic amounts of liquid (liquid-assisted grinding, LAG). From a crystal engineering aspect, this does not only encompass covalent reactions but also the reorganization of molecular packings and co-crystal formation[276].

No single mechanism for mechanochemical co-crystallization is fully established. Several authors however suggest that it is rather to be understood as a combination of occurring phenomena. In an early review paper of T. Friščić and W. Jones in 2009 they concluded that co-crystal formation under neat grinding may involve concurrent mechanisms like molecular diffusion, eutectic formation or amorphous-phase mediation. The LAG approach likewise could not be fully understood, the liquid may act as a physical lubricant and diffusion medium or provide the basis for templating effects[276]. One initially discussed “hot-spot-theory“, which suggested mechanochemical reactivity to be explained by high temperature spots of over 1000 degrees to emerge during the operation has been criticized[277–279] and rather replaced by later mechanistic interpretations. A. A. L. Michalchuk classified mechanochemical

reactions into three types depending on the primary role of mechanical energy, be it (Type 1) mixing-dominated processes including frictional heating, (Type 2) processes where mechanical energy modifies the stability of the reactants or (Type 3) processes in which it directly excites the system and triggers the reaction. In any case, most real such transformations involve a combination of these mechanisms[280].

Compared to solution-based routes, mechanochemical co-crystallization offers some practical advantages. Reactions can be run under solvent-free or near solvent-free conditions, which can drastically reduce waste and aligns well with green chemistry principles[281–283]. Also, the solid-state approach can overcome problems of solvent choice, especially for poorly soluble systems. Moreover, mechanochemical reactions can follow different pathways, leading to new results[281]. In practice, the outcome can be highly sensitive to parameters such as the mill type, filling degree, ball material or size, and this can both complicate initial studies as well as possible scale-up approaches[284]. On the other hand, this allows flexibility and tuneability of the synthesis parameters.

2. Motivation

In recent years, society has increasingly turned its attention toward sustainable approaches for both novel as well as established subjects. This development is not only addressed at a sociocultural and political level, but it also requires a reconsideration of long-standing design principles. Among the numerous areas affected is the field of materials science. Many technologies operate in close contact with solid-state materials, be it in displays, laser technologies, electronic devices, sensing or related applications. In this context, the pursuit to identify alternative, more environmentally friendly components is an often-considered approach. Alternatively, if resource substitution is not feasible, it is the methodology that may evolve.

As outlined in Section 1.4, the solid-state photophysics of organic chromophores is highly sensitive to their molecular environment. This offers an attractive opportunity to tailor photophysical response through crystal engineering strategies. A variety of π-conjugated systems have been explored over recent years and naturally the outcome of such research depends on the underlying selected compounds. Flavins constitute a versatile molecular building block platform: The isoalloxazine parent structure can be modified with a broad range of functional groups, engendering a large number of derivatives. By this, systematic variation of steric and electronic parameters is achievable while maintaining comparability with the chromophore core. Flavin chromophores are excellent candidates for sustainable metal-free organic solid-sate materials due to their versatility and synthetic accessibility. Exploiting their utility in the context of crystal engineering strategies opens up potential future applications and lays the groundwork for controlled modification of this compound class on a supramolecular level. Despite extensive investigation on their photophysical behavior primarily in solution, flavins have remained surprisingly underexplored in the solid state. Moreover, no prior systematic assessment of the supramolecular multicomponent flavin-based systems regarding fine-tuning of solid-state photophysics is reported, yet the molecular crystalline solids of this class of chromophores exhibit significant potential in this context. Roseolumiflavin, an isoalloxazine derivative and a known red-light emitter, was selected as a promising model system to develop this field. The choice of this particular compound was motivated by several key features that are favorable for a crystal engineering approach:

1. **Solubility**: To initiate supramolecular assembly, it is crucial for the compound to inhibit sufficient solubility, optimally in a wide variety of solvents. This further enables controlled crystal growth and simplifies the initial screening process both to determine crystallization conditions and to decide suitable co-formers. Roseolumiflavin is soluble in a range of polar aprotic and protic solvents and thus allows fine adjustment of crystallization conditions.
2. **Small molecule**: The compact yet modifiable molecule with a limited amount of supramolecular binding sites is advantageous for co-crystallization, allowing facile incorporation and rationalization of the intermolecular interactions (note, that particularly small, synthetically accessible, luminescent organic platforms are relatively scarce). The small size allows better structure-properties relationship analysis to derive correlations. Small residues attached to the isoalloxazine core of roseolumiflavin place it in this category and make it a suitable model compound.
3. **Suitable recognition sites**: A set of suitable supramolecular functionalities known to form predictable supramolecular synthons allows to expect successful crystallization as well as the rationalization of the ensued structure. Roseolumiflavin offers a primary imide-based recognition site and secondary, partially shielded HB sites, with additional potential XB acceptor functionality. Thereby, the competition between interactions is limited, rather a hierarchic synergy is expected.

The focus is set on the utilization of the flavin's imide group as solution-based investigations imply this route to be the most promising, see Section 1.5. Beyond the primary recognition site, the ultimately achieved crystal structure environment of the multicomponent systems will be governed by a subtle interplay of multiple weak, non-covalent interactions. Secondary contacts, such as π···π stacking, additional HB and XB or dispersion-driven interactions can likewise determine relative orientation of the molecular units within the crystal lattice. The different realized supramolecular structures define certain differences in evolution of the excited states, bridging supramolecular structure specifics and solid-state photophysics. Thus, the multicomponent strategy used in this work additionally aims at exploring their influence on structure and properties. The question herein is not only whether a fine-tuning of photophysical properties can be achieved but also to what extent one can predict the outcome. Finally, particular focus is placed on exploring mechanochemical routes to crystallization of such systems, adding a sustainability-oriented dimension to this work.

3. Objectives of the Thesis

The present thesis aims to establish roseolumiflavin as a model flavin chromophore for multicomponent crystal engineering and to derive generalizable design principles when solid-state optical response is sought to be tuned through a supramolecular approach.

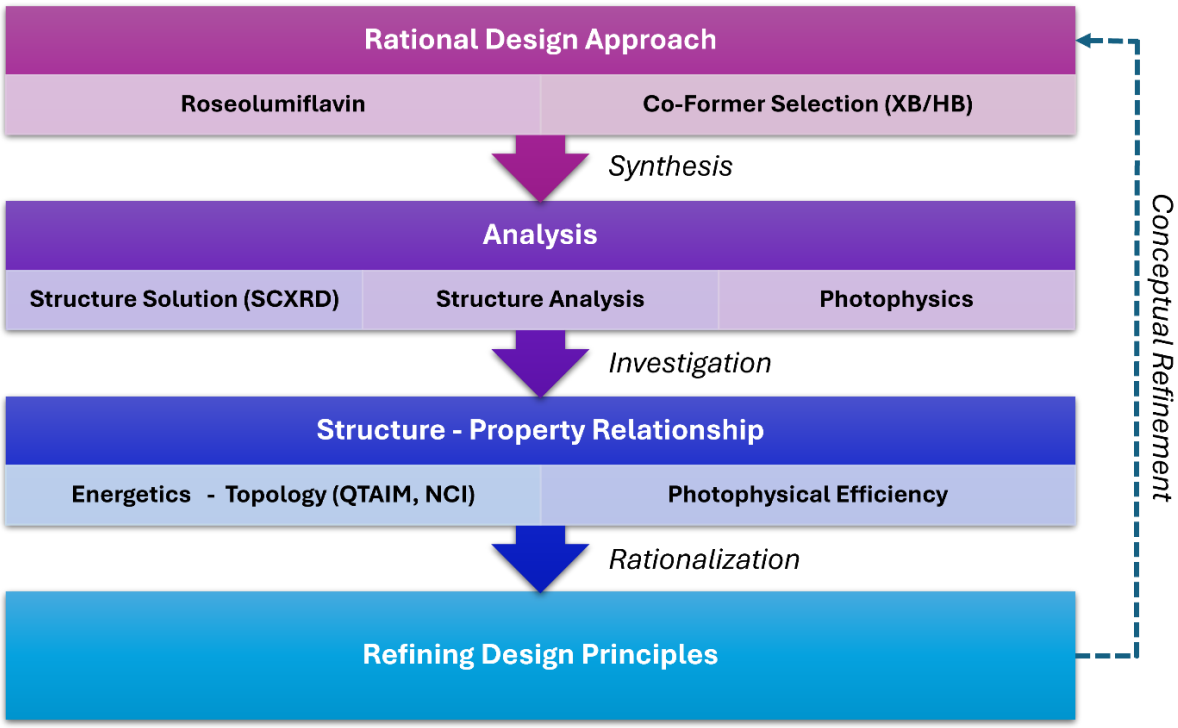

Figure 8 Conceptual workflow of the thesis objectives, linking crystal structures with photophysical, energetics and topology analyses towards the derivation of a design principle for roseolumiflavin-based multicomponent systems.

Specifically, the objectives are to:

i. Identify robust pathways to utilize the flavin's imide group to develop multicomponent supramolecular solids and test the possibility of actualization of different supramolecular synthons (involving HB and XB).
ii. Structurally determine and compare the resulting packing motifs.
iii. Correlate structural differences with solid-state photophysical properties.
iv. Rationalize packing preferences and interaction hierarchies using energetical approach and topological analyses.
v. Establish mechanochemical routes as a sustainable synthetic approach for the selective crystallization of multicomponent systems.

This dissertation consists of three published works, which tackle the goals in different ways reporting roseolumiflavin-based multicomponent crystalline systems.

4. Published Work

The following sections 4.1. to 4.3. cover the results of the dissertation which have been published in international journals. Each section will introduce the publications with a brief summary of its content and key results. The contributing authors are listed and this author's contributions to the projects are listed separately. Figures, schemes and tables will follow a numeration individual to the respective publication and independent to this thesis. The same applies to the references. The corresponding supporting information is likewise included.

The publications are presented in chronological order. All titles are reproduced verbatim from the original publications. Permissions were obtained where required.

4.1. Co-Crystallization of Organic Chromophore Roseolumiflavin and Effect on its Optical Characteristics

Takin Haj Hassani Sohi, Felix Maaß, Constantin Czekelius, Markus Suta, Vera Vasylyeva

DOI: 10.1039/D2CE00589A

CrystEngComm, **2022**, *24*, 7315-7325

Three co-crystals of roseolumiflavin, each connected by different supramolecular synthons at the imide group recognition site, were presented in a first-time systematic study investigating the suitability of a flavin to co-crystallize and the impact on structure and property. For this, acetylene-dicarboxylic acid, 1,4-diiodotetrafluorobenzene and 2,4-diamino-pyrimidine were chosen as small, model co-formers to provide a carboxylic group for acid-amide heterodimer formation, a halogen bond donor to investigate accessibility beyond classical hydrogen bonds and a three-point recognition DAD source. All co-crystals showed blue-shifted fluorescence in red range compared to the near-infrared-emitting roseolumiflavin. It was shown that the degree of close packing between the flavin molecules in the crystal lattice can influence the magnitude of the emission-band shift.

Contributions of the author:

- Conceptualization based on literature research together with Vera Vasylyeva.
- Experimental work, investigation and validation of results, including synthesis of powder samples and single crystals together with Felix Maaß. This includes consistent approaches to optimizing synthesis conditions during the project.
- Measurement and evaluation of emission and excitation spectra in solvent environment, SCXRD, FTIR and DSC.
- Evaluation of TGA measurements.
- Measurement and evaluation of PXRD together with Felix Maaß.
- Measurement and evaluation of solid-state emission spectra, excitation spectra and luminescence lifetimes together with Markus Suta and Felix Maaß.
- Visualization of all figures, tables and data.
- Manuscript writing, literature research and preparation of supporting material.
- Review and editing of manuscript together with Vera Vasylyeva and Constantin Czekelius.
- Revision process together with Vera Vasylyeva, Constantin Czekelius and Markus Suta.

CrystEngComm

ROYAL SOCIETY OF CHEMISTRY

PAPER

View Article Online
View Journal | View Issue

Cite this: *CrystEngComm*, 2022, **24**, 7315

Co-crystallization of organic chromophore roseolumiflavin and effect on its optical characteristics†

Takin Haj Hassani Sohi, [a] Felix Maass, [a] Constantin Czekelius, [b] Markus Suta [c] and Vera Vasylyeva *[a]

Received 28th April 2022,
Accepted 30th July 2022

DOI: 10.1039/d2ce00589a

rsc.li/crystengcomm

A structural study on the solid, microcrystalline chromophore roseolumiflavin was carried out. Based on rational design considerations three binary co-crystals were prepared with a primary focus set on utilizing the imide functional group. Therefore, robust supramolecular synthons, including a carboxylic acid–amide dimer, halogen bonding, as well as a hydrogen-bonded three-point binding motif, were successfully incorporated into the multicomponent systems. All the co-crystals showed a blue-shifted fluorescence in the red range compared to the near-infrared-emitting solid roseolumiflavin. Solvatochromic studies finally elucidated that the degree of close packing between the flavin molecules within the crystal structures was decisive for the emission colour. These results render new possibilities to investigate flavins in the aspect of crystal engineering to tune optical properties of organic chromophores in the solid state.

Introduction

Chirality, catalytic activity, drug-efficacy, charge-transfer processes, thermal behaviour, and mechanical or optical properties[1,2] are some of the possible fields where the application of the crystal engineering concept is manifold. One topic of interest in this area is the modification of organic solid-state chromophores. The applicability of such solids in diverse fields, such as organic or polymeric light-emitting diodes (OLEDs/PLEDs),[3,4] solid-state lasers,[5,6] or fluorescent chemosensors,[7] is attracting great interest in a broad range of research. Moreover, tunability, flexibility, and low-cost characterization add to the great advantages for the potential usability of organic chromophores.[8] The tuneable character has already led to various studies in recent years in the aspect of crystal engineering, focussing on co-crystallization strategies to effectively modulate optical properties.[9–14] Flavins, as a subset of organic solid-state chromophores, belong to the class of isoalloxazines and are especially interesting for biological processes, adapting the role of coenzymes or photoreceptors.[15,16] With a diversity of spectral properties, flavins may act as natural reporters to monitor processes *in vivo*.[17] Here, their selective autofluorescence activity can be utilized to apply these organic compounds as biomarkers in metabolic processes.[18] A comprehensive study in 2004 by Sikorska *et al.* reported strongly red-shifted fluorescence emission spectra in solution for isoalloxazines compared to alloxazines and their constitutional isomers.[19] Isoalloxazines have also exhibited longer decay times and more intense fluorescence.[19–21] Overall, these properties are strongly correlated with the number and position of the substituents. Thus, a common route to affect the luminescence properties of organic chromophores, particularly flavins, is based on derivatisation, with various functional groups affecting the polarity or rigidity of the system.[22] Hereby, in some cases, the fluorescence activity might be hindered. Quenching processes can have several causes, including excited-state reactions, molecular rearrangements, energy transfer, ground-state complex formation, and collisional or configurational crossover-based quenching.[23] In the solid state, organic molecules might exhibit self-quenching processes that result from aggregation and consequent efficient non-radiative relaxation[23] or from close packing in the crystal structures forming strong π···π contacts or hydrogen bonds, which in turn may cause severe fluorescence quenching.[24–26] To

[a] *Laboratory for Molecular Crystal Engineering, Department of Inorganic Chemistry and Structural Chemistry I, Heinrich-Heine-University Duesseldorf, Universitaetstr. 1, 40225 Duesseldorf, Germany. E-mail: vera.vasylyeva-shor@hhu.de*
[b] *Laboratory for Asymmetric Synthesis and Catalysis, Department of Organic Chemistry and Macromolecular Chemistry, Heinrich-Heine-University Duesseldorf, Universitaetstr. 1, 40225 Duesseldorf, Germany*
[c] *Laboratory for Inorganic Photoactive Materials, Department of Inorganic Chemistry and Structural Chemistry II, Heinrich-Heine-University Duesseldorf, Universitaetstr. 1, 40225 Duesseldorf, Germany*

† Electronic supplementary information (ESI) available: CIFs, preparation of **R**, IR, ^{1}H-NMR, ^{13}C-NMR and HRMS spectra, solid-state time-resolved luminescence data, solid-state emission and excitation spectra, solution emission and absorption spectra, thermal (DSC and TG) data. CCDC 2168404–2168407. For ESI and crystallographic data in CIF or other electronic format see DOI: https://doi.org/10.1039/d2ce00589a

overcome this problem, we suggest an alternative strategy to tune the luminescence of flavins upon co-crystallization. It should be noted that experimental studies on flavin derivatives in the solid state are conspicuously scarce. A Cambridge Structural Database survey[27] only indicated a scant amount of available structural investigations of flavins. However, the crystal structures of several simple flavin derivatives[28–30] have been reported along with some solvates[31] and salts.[32–34] Also several co-crystals,[35–38] referred to as molecular complexes, were structurally characterised, with all of them exhibiting strong hydrogen-bonded interaction patterns. The majority of these investigations were carried out in the 1970s. However, no investigations on the structure–property relations for the reported structures have thus far been performed.

The present work is concerned with a structural characterization of 8-(dimethylamino)-7,10-dimethylbenzo[*g*]pteridine-2,4(3*H*,10*H*)-dione, also known as roseolumiflavin (**R**), and the synthesis of its multicomponent crystals (Chart 1). A notable focus was further set on an investigation of the luminescence. Until now, **R** has only been a topic of discussion on a theoretical level by Karasulu and Thiel in 2014, in which the photophysical properties of **R** in different environments were investigated.[39] Experimental data are yet to be published and no structural investigations have been carried out until now. An insight into the molecular self-assembly in the solid state, however, opens a great prospective towards better understanding and controlling the optical properties of flavins.

In this study, we wanted to verify if the implementation of a second entity into the crystal lattice would disturb an anticipated aggregation of **R** and even lead to an enhancement of the luminescence. In addition, it was of interest to clarify which kind of intermolecular interactions and supramolecular synthons were accessible for the co-crystal formation and how they affect the luminescent character of **R**. For this purpose, three co-formers were chosen based on rational design considerations to result in binary co-crystalline phases with **R**.

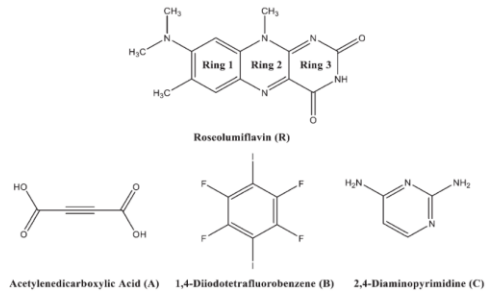

Chart 1 Chemical structures of **R** and the co-formers **A**–**C**; aromatic rings of **R** denote **Rings 1**–**3**.

Hereby, emphasis was placed on utilizing the imide group, which offers donor as well as acceptor functionalities to allow different kinds of intermolecular interactions and to allow it to undergo one-, two-, and three-point recognition patterns during the self-assembly. The high acidity on the N–H centre was assumed to favour hydrogen-bond interactions. *Via* a retrosynthetic approach, both –N–H and –O–H based supramolecular synthons are commonly represented in the literature, promising sufficient adaptability.[40,41] Acetylenedicarboxylic acid (**A**) with its two carboxylic sides is a promising candidate to undergo an acid–amide heterodimer formation, which has been shown to be more favourable over amide–amide or acid–acid homodimers.[42] Another hydrogen-bonded motif, the DAD (donor–acceptor–donor) three-point recognition pattern, was expected to result in a co-crystallisation with 2,4-diamino-pyrimidine (**C**). Further, the nucleophilic character of unsaturated heteroatoms in **R** suggested an affinity towards halogen bonding. Accordingly, a model halogen bond co-former 1,4-diiodotetrafluorobenzene (**B**) was introduced as a possible building block for the one-point molecular recognition. Moreover, the aromatic rings in **B** and **C** could exhibit an additional effect on the overall crystal packing involving π-interactions.

Here, we present a structural characterization of **R** along with a successful synthesis and crystal structure analysis of three new roseolumiflavin co-crystals **R**:**A**, **R**:**B**, and **R**:**C**. A careful crystal packing analysis was performed, which presented various effects of different types of intermolecular interactions on the overall topology. Spectroscopic analyses of all the obtained structures uncovered possibilities to modify the luminescent properties of the organic chromophore *via* co-crystallization. Based on the results, the main purpose of our research was to obtain a better understanding about a potential targeted tuning of the optical properties of roseolumiflavin in the solid state.

Experimental section

Synthesis

Roseolumiflavin (R). **R** was synthesized following a modified procedure by Kasai, Miura, and Matsui.[43] The detailed synthesis conditions are presented in the ESI.† Red rectangular-shaped single crystals of **R** were obtained *via* slow evaporation from its methanol solution at room temperature over several days. IR: 3380, 3250, 3129, 3063, 2984, 2799, 1690, 1633 cm^{-1}. ^{1}H-NMR: 2.45 (s), 3.06 (s), 3.95 (s), 6.88 (s), 7.80 (s), 11.10 (s) ppm. PXRD (characteristic Bragg reflections): 8.64°, 10.11°, 12.48°, 14.09°, 17.32°, 25.85° 2θ.

Roseolumiflavin–acetylenedicarboxylic acid (1:1) co-crystal (R:A). **A** is highly hygroscopic and tends to form a monohydrate, which does not participate in a co-crystallization, according to Tantardini *et al.*[44] Thus, to synthesize the **R**:**A** co-crystal, an excess amount of **A** was used. **A** and **R** were mixed in a 2:1 molar ratio in a micro-centrifuge tube with 15 µL acetonitrile and six milling balls. The sample was ground for 25 min at 15 Hz frequency in a

Retsch MM 400 ball mill. Clear bright red needle-shaped single crystals were obtained *via* seeding in acetonitrile and by slow evaporation of the solvent for 2 weeks at room temperature. IR: 3506, 3440, 3255, 1695, 1684, 1632 cm^{-1}. PXRD (characteristic Bragg reflections): 6.29°, 11.59°, 13.55°, 25.22°, 25.97°, 27.78° 2θ.

Roseolumiflavin–1,4-diiodotetrafluorobenzene (2 : 3) co-crystal (R : B). **R : B** was prepared in a 1 : 1 molar ratio of **R** and **B** in a micro-centrifuge tube with 20 μL methanol and eight milling balls. The sample was ground for 25 min at 15 Hz frequency. Red block-shaped single crystals were obtained *via* seeding in methanol and by a slow solvent evaporation for 1 week at room temperature. All attempts to achieve a 1 : 1 co-crystal by variation of the crystallization parameters and/or molar ratio of the starting materials resulted in the same **R : B** (2 : 3) phase. IR: 3359, 3237, 3126, 2986, 2806, 1683, 1623 cm^{-1}. PXRD (characteristic Bragg reflections): 12.93°, 16.63°, 16.94°, 24.28°, 24.96°, 26.65°, 26.94° 2θ.

Roseolumiflavin–2,4-diaminopyrimidine (1 : 1) co-crystal (R : C). **R** and **C** were dissolved in methanol in a 1 : 1 molar ratio and crystallized after slow evaporation of the solvent at room temperature to give orange-red needle-shaped crystals of **R : C**. IR: 3372, 3322, 3192, 3114, 2978, 2804, 1688, 1652 cm^{-1}. PXRD (characteristic Bragg reflections): 6.14°, 11.47°, 12.64°, 24.84°, 27.15° 2θ.

Thermogravimetric analysis

A Netzsch TG 209 was operated in the range between 30 °C and 600 °C with a 10 °C min^{-1} heating rate under a nitrogen atmosphere. No melting point could be obtained because **R** decomposed before melting.

Infrared spectroscopy

The FT/IR spectra were measured on a Bruker Tensor 37 with an ATR-unit at room temperature (25 °C).

UV-vis and luminescence spectroscopy

Absorption spectra in solution were measured in a UV-vis SPECORD S600 system at room temperature (25 °C). The emission spectra in solution were measured by a HORIBA FluoroMax 4 system at room temperature (25 °C). Qualitative measurements were performed upon excitation with a UV lamp emitting at 366 nm. The photoluminescence excitation spectra were acquired on an Edinburgh Instruments FLS980 spectrometer with a 450 W continuous Xe arc lamp, double grating monochromators for both excitation and emission compartments, and a Hamamatsu R928P thermoelectrically cooled photomultiplier tube for detection. Photoluminescence emission spectra were acquired on an Edinburgh FLS1000 spectrometer with similar features and upon excitation with a VPL-420 laser in continuous wave mode. All excitation spectra were corrected for the lamp intensity and grating efficiency, while emission spectra were corrected for the grating efficiency and sensitivity of the photomultiplier. Time-resolved luminescence measurements were performed using pulsed EPL diode lasers from Edinburgh Instruments with adjustable repetition rates and temporal pulse widths of around 75 ps.

X-Ray diffraction

Powder X-ray diffraction (PXRD) analyses were performed by a Rigaku Miniflex diffractometer in $\theta/2\theta$ geometry at ambient temperature using Cu-Kα radiation (λ = 1.54 182 Å). Single-crystal X-ray diffraction (SCXRD) measurements were carried out on a Bruker APEX Duo diffractometer with a CCD detector, micro-focus X-ray tube, and Mo-Kα radiation (λ = 0.71073 Å) at 140(2) K for **R** and a Rigaku XtaLAB Synergy-S diffraction system with a HiPyx 6000 photon detector, and micro-focus X-ray tube with Cu-Kα radiation (λ = 154 182 Å) measured at 100(2) K for the co-crystals. Cell refinement, data collection, and data reduction on the Rigaku Synergy-S system were performed with CrysAlisPro.[45] On the Bruker APEX Duo, data collection and cell refinement were achieved with APEX2 (ref. 46) and data reduction was performed *via* SAINT.[47] Structure solution was performed by SHELXT 2014/5 (ref. 48) for **R** and **R : B** and SHELXT 2018/2 (ref. 48) for **R : A** and **R : C**. **R : B** was refined with SHELXL-2014/7,[48] **R** was refined with SHELXL-2017/1.[49] **R : B** and **R : C** were refined with SHELXL-2018/3.[49] The co-crystals were additionally refined with the Olex2 software package.[50] All the non-hydrogen atoms were refined with anisotropic displacement parameters. All the hydrogen atoms were experimentally refined. **R : A** and **R : C** crystallized as very thin plates/needles and exhibited an extremely poor diffracting ability, which was reflected in the data quality and quality values. Numerous attempts to obtain larger single crystals failed. The crystallographic data are summarized in Table 1.

Software

Crystal structure figures were prepared by Mercury 2020.2.0.[51] Verbose crystal structure information, including Z′, was obtained *via* PLATON for the Windows Taskbar (Version 1.19).[52] All the spectra were plotted with OriginPro 2019.[53]

Results and discussion

Characterization of R

R crystallizes in the monoclinic space group $P2_1/n$ (no. 14). The asymmetric unit contains one molecule of **R**, four of which shape the unit cell. The crystal structure is based on dimeric supramolecular assemblies connected *via* N–H···O interactions (N2–H···O2: 2.813(2) Å; note: all distances were measured between donor and acceptor molecules unless noted otherwise). Both moieties are twisted with an angle of 8.65° and build up along the crystallographic *a* axis (Fig. 1).

Short hydrogen bonds (C14–H···C3: 2.87(4) Å, C13–H···O1: 2.62(3) Å, C13–H···C2: 2.79(3) Å) along the *b* axis allow for the dimer motifs to form chain-like networks with strong

Table 1 Crystallographic data for **R**, **R**:**A**, **R**:**B**, and **R**:**C**

Name	**R**	**R**:**A** (1:1)	**R**:**B** (2:3)	**R**:**C** (1:1)
Empirical formula	$C_{14}H_{15}N_5O_2$	$C_{14}H_{15}N_5O_2$, $C_4H_2O_4$	$C_{14}H_{15}N_5O_2$, 1.5($C_6F_4I_2$)	$C_{14}H_{15}N_5O_2$, $C_4H_6N_4$
Formula weight [g mol^{-1}]	285.31	354.35	888.10	395.44
Temperature [K]	140(2)	100(10)	100(2)	100.01(13)
Space group (no.)	$P2_1/c$ (14)	*Pbca* (61)	$P\bar{1}$ (2)	$P\bar{1}$ (2)
Crystal system	Monoclinic	Orthorhombic	Triclinic	Triclinic
a [Å]	12.7469(10)	6.9603(4)	7.7683(3)	8.0245(5)
b [Å]	7.0326(8)	18.1475(7)	12.2451(5)	8.4915(5)
c [Å]	14.3336(13)	28.0356(12)	14.6375(5)	14.9566(7)
α [°]	90	90	108.280(4)	87.548(5)
β [°]	99.135(5)	90	91.090(3)	74.813(5)
γ [°]	90	90	96.577(4)	65.130(6)
Volume [Å^3]	1268.6(2)	3541.2(3)	1311.17(9)	889.69(10)
Z/*Z*′	4/1	8/1	2/1	2/1
ρ_{calc} [g cm^{-3}]	1.494	1.498	2.249	1.476
μ [mm^{-1}]	0.105	0.976	28.774	0.854
T_{min}/T_{max}	0.6559/0.7455	0.844/1.000	0.327/0.597	0.698/1.000
F(000)	600	1664	834	416
Crystal size [mm^3]	0.05 × 0.10 × 0.15	0.02 × 0.02 × 0.18	0.02 × 0.05 × 0.05	0.03 × 0.03 × 0.06
θ range [°]	1.987/24.998	3.1490/69.2990	3.185/78.301	3.071/78.995
Completeness [%]	99.6	99.5	99.7	99.7
Recorded reflections	8604	14 153	15 384	12 348
Indep. reflections	2224	3325	5298	3599
Goodness-of-fit F^2	1.007	0.996	1.112	1.006
X-ray source (wavelength [Å])	MoKα (*λ* = 0.71073 Å)	CuKα (*λ* = 1.54184 Å)	CuKα (*λ* = 1.54184 Å)	CuKα (*λ* = 1.54184 Å)
R_1 [$I > 2\sigma(I)$]/wR_2 [all reflns.]	0.0493, 0.1399	0.0617, 0.1645	0.0342, 0.0941	0.0557, 0.1678

displaced stacking interactions where **Ring 2** is stacked above the **Ring 1** (centroid$_{\text{Ring 2}}$···centroid$_{\text{Ring 1}}$: 3.576(4) Å and 3.6280(13) Å), expanding along the *a* axis. Each unit is further supported on either side *via* short hydrogen bonds (C11–H···O1: 3.147(2) Å, C13–H···O1: 3.177(2) Å, C6–H···O1: 2.66(2) Å, C12–H···O2: 2.51(3) Å) building up in a spiral form along the *b* axis, which results from the tilted nature of each stacked dimeric motif alternating along the crystallographic *c* axis. This allows the amide groups to be in a position in close proximity to the methyl groups, ultimately spanning the crystal packing. Additionally, ^{1}H-NMR analysis was performed for confirmation of the purity and for characterization of the compound (for details see the ESI†). The corresponding IR spectrum in Fig. 2 illustrates strong peaks at 1690 and 1633 cm^{-1}, which were assigned to amide C═O stretching modes, while two bands at 3380 and 3250 cm^{-1} originated from the mono-substituted amide N–H stretching mode. The band at 3129 cm^{-1} may have resulted

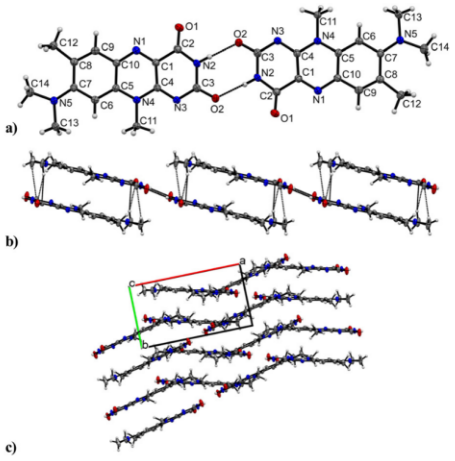

Fig. 1 Crystal packing and intermolecular interactions of **R**. a) Head-to-head dimer motif formed by amide–amide synthon. Labels for H-atoms are omitted for clarity. View along the crystallographic *b* axis. b) π···π interactions stabilize the stacking patterns along the *a* axis. View along the *c* axis. c) Alternating **R** stacks along the *c* axis with each stack tilted at a 26.64° angle. View along the *c* axis.

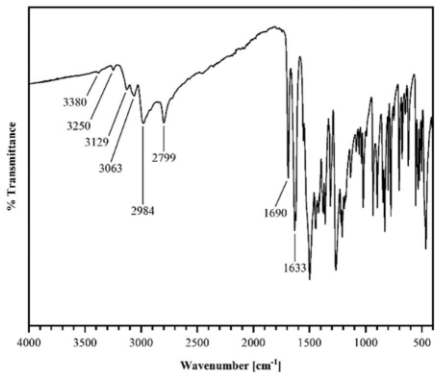

Fig. 2 Infrared spectrum (ATR) of **R** recorded from 400 to 4000 cm^{-1}.

from combination vibrations ν(C═O) + δ(N–H). The vibrational band at 2799 cm^{-1} likely originated from the NC–H stretching mode, while the band at 2984 cm^{-1} could be assigned to C–H stretching vibrations. In addition, bands of aryl C–H vibrations (3063 cm^{-1}) were present.

PXRD analysis

Powder diffraction patterns of the samples **R:A**, **R:B**, and **R:C** synthesized *via* liquid-assisted grinding are depicted in Fig. 3 and distinctly different in comparison to pure **R**, which suggested the formation of new crystal phases. The overall purity of all the co-crystals was in good agreement with the available single-crystal data simulations (Fig. S7–S9 in the ESI†).

SC-XRD analysis of the co-crystals

R:A crystallizes in the orthorhombic space group *Pbca* (no. 61) with one of each of the **R** and **A** molecules setting up the asymmetric unit (Fig. 4). The dicarboxylic functionality of the co-former potentially allows the formation of two hydrogen-bonded interactions with **R** mediated by two carboxylic groups. Indeed, we observed both ends took part in the intermolecular assembly however, each side was connected uniquely. A classic linear assembly between the carboxylic group and the **R** amide group supplanted the favoured dimeric amide–amide formation (donor–acceptor distances N2–H···O3: 2.922(3) Å, O4–H···O2: 2.538(3) Å).

Intermolecular O6–H···O2 interactions (2.616(3) Å) between the second carboxylic group and another unit of **R** ultimately allowed the formation of hydrogen-bonded zig-zag chains to propagate along the crystallographic *b* axis.

The zig-zag chains further intertwine to increase the close-packing efficiency in the crystal structure. This is also due to the carboxylic groups of the **A** units being twisted at an angle of 46.09° between the planes through each carboxylic group. Along the *a* axis, the flavin molecules interact *via* slightly

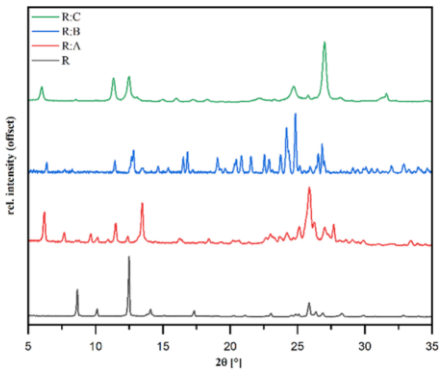

Fig. 3 Powder X-ray diffraction patterns (Cu Kα) of **R** and the co-crystals **R:A**, **R:B** and **R:C**.

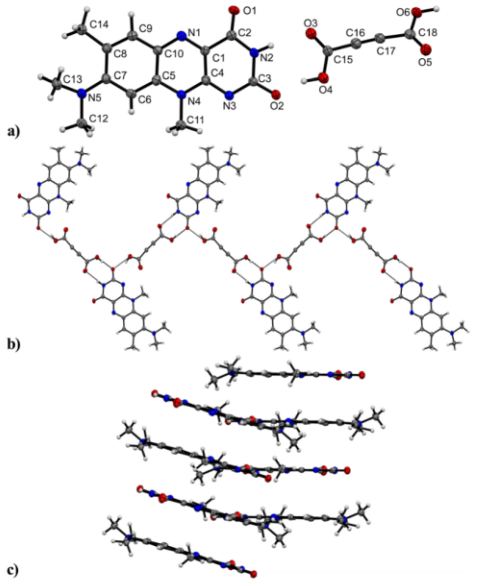

Fig. 4 Crystal structure of **R:A**. a) Asymmetric unit of **R:A**. Labels for H-atoms are omitted for clarity. View along the crystallographic *a* axis. b) Zig-zag chains formed by O–H···O and N–H···O interactions between **A** and **R** along the *b* axis. View along the *a* axis. c) Tilted π···π stacks of **R** molecules. **A** removed for clarity. View along the *b* axis.

disordered π···π stacks ($centroid_{Ring\ 3}$···$centroid_{Ring\ 1}$: 3.5297(12) Å and 3.5090(12) Å, $centroid_{Ring\ 2}$···$centroid_{Ring\ 2}$: 3.5312(15) Å and 3.5087(13) Å), each flavin molecule being inversely oriented to the stacking partner. The stacks are tilted by 17.53° relative to the neighbouring stacks.

R in combination with a model halogen bond donor 1,4-diiodotetrafluorobenzene resulted in a formation of the **R:B** (2:3) co-crystal with one molecule of **R** and 1.5 co-former molecules, assigned as **B1** and **B2** in Fig. 5 in the asymmetric unit cell. The compound crystallizes in the triclinic space group $P\bar{1}$ (no. 2) and contains the familiar amide–amide synthon, which leads to a dimer formation (N1–H···O2: 2.834(6) Å) similar to that in pure roseolumiflavin. Here, moderate π···π stacking interactions were observed again between two flavin molecules with inverse directionality which, mediated by the dimeric motifs, propagate along the *b* axis ($centroid_{out,Ring\ 2}$···$centroid_{out,Ring\ 1}$: 3.684(3) Å, $centroid_{Ring\ 2}$···$centroid_{Ring\ 2}$: 3.727(3) Å). The stacks are displaced along the *c* axis surrounded by **B** molecules offering halogen bonds to build up linear chains.

Through the conjugation of the iodine substituents to the carbonyl groups, the stacked entities are stabilized on either side (I1···O1: 2.800(3) Å, I2···O2: 2.899(3) Å) establishing halogen-bonded chains between the co-former and flavin molecules along the *c* axis. Additional halogen bonds are generated by the symmetry inequivalent second **B** entity

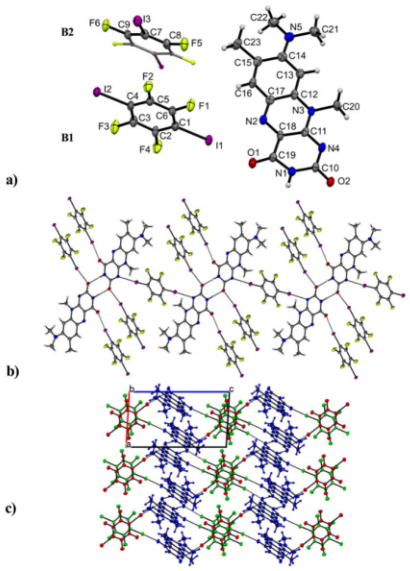

Fig. 5 Intermolecular interactions and crystal packing of **R**:**B**. a) Asymmetric unit of **R**:**B**. The symmetry inequivalent co-formers are labelled as **B1** and **B2**. Symmetry equivalent part of **B2** molecule is shown as capped sticks. Labels for H-atoms are omitted for clarity. View perpendicular to the *bc* plane b) I···N and I···O interactions connect dimeric motifs to build up 2D networks in the crystal packing. View along the *a* axis. c) Symmetry inequivalent stacked co-formers (**B1**: green, **B2**: red) propagate along the *b* axis, I···O and I···N interactions stabilize **R** stacks. View along the *b* axis.

positioned above and below the flavin dimers with slight displacement when connecting with the N4 ring atom (I3···N4: 3.163(4) Å) and thus building up a complex 2D network. Slightly distorted stacks of the symmetry inequivalent co-former entities propagate along the *b* axis with a repetition pattern of two consecutive units of **B1** and one unit of **B2**.

The third and final successfully obtained co-crystal **R**:**C** crystallizes in a triclinic $P\bar{1}$ (no. 2) space group with the asymmetric unit containing one of both a **R** and **C** molecule, respectively (Fig. 6). The **C** and **R** molecules are connected *via* a three-point recognition pattern between the imide group and the amine groups along the crystallographic *c* axis (N9–H···O1: 2909(3) Å; N2–H···N6: 2937(3) Å and N8–H···O2: 2938(3) Å). A similar interaction pattern was found by Scarbrough *et al.* in 1977 between lumiflavin and 2,6-diamino-9-ethylpurine.[35] Two additional hydrogen bonds connect two co-formers (N8–H···N7: 2977(3) Å) to build tetrameric units, which propagate along the *b* axis mediated by strong N–H···N (N9–H···N3: 3190(3) Å) and N–H···O (N9–H···O2: 3097(3) Å) hydrogen bonds as well as C–H···O interactions (C17–H···O2: 3381(3) Å) between **C** and **R** entities.

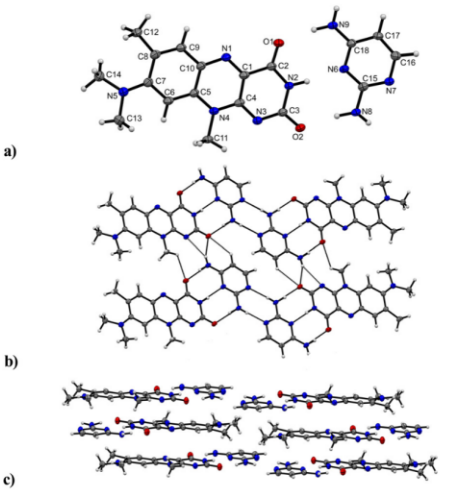

Fig. 6 Intermolecular interactions and crystal packing of **R**:**C** a) asymmetric unit of **R**:**C**. Labels for H-atoms are omitted for clarity. View perpendicular to the *bc* plane. b) Tetrameric motifs connected by hydrogen bonds propagate along the *b* axis mediated by the **C** unit. View along the *a* axis. c) π···π contacts between **C** and **R**. View along the *b* axis.

Further, weak hydrogen bonds C–H···O (C11–H···O1: 3085(3) Å) between adjacent **R** molecules are present as well. The resulting layers are parallel to the *bc* plane. π···π stacks between co-facially adjacent flavin molecules govern an expansion along the *a* axis, where the tetrameric subunits alternate with an inverse orientation of the flavin units on each layer. 2,4-Diaminopyrimidine and flavin molecules arranged in slipped stack formations are additionally stabilized by π···π interactions.

To conclude, **R**:**A** with its edge-to-face arrangement displays a crystal packing driven by the formation of the carboxylic acid–amide dimer, which replaces the amide–amide dimeric supramolecular synthon observed in **R**. In contrast, in **R**:**B** the mentioned amide–amide dimer of **R** molecules is present; however, the dimers are connected with I···O halogen bonds over **B** molecules to give chains of alternating co-former and flavin molecules. Additionally, two flavin molecules are further stabilized by an extra **B** molecule connected *via* short N···I contacts. The **R**:**C** co-crystal contains π···π contacts between the co-former molecules and **R**. These stacked arrangements are further connected by hydrogen-mediated donor–acceptor–donor three-point bonding motifs *via* N–H···O and N–H···N interactions between **C** and **R** entities. The dimeric flavin motifs connected *via* amide–amide synthons only remained in the **R**:**B** co-crystal. These were responsible for the shortest-range interactions in the pure form **R**. The hydrogen-bonded D···A distances in the **R**:**B** crystal structure were in a similar range compared to pure **R**, while in both other co-crystal structures

the distances were significantly larger. Here, it is noteworthy that a mere focus on the N–H···O interaction would only describe one part of the imide group interaction. Since the dimeric **R** motifs are detached, we also consider the C=O group separately. In the case of **R:A**, significantly stronger hydrogen bond interactions were observed, mediated by two separate **A** entities towards the flavin C=O group at a 105.76° angle between both interactions. The O6–H···O2 (1.68(5) Å) as well as O4–H···O2 (1.53(5) Å) hydrogen bond distances were significantly shorter than the N–H···O interactions (Table 2).

The dimeric motif was replaced by a three-point recognition pattern provided by the co-former component in **R:C** where the overall D···A distances were slightly longer; however, the H···O1 and H···O2 distances were slightly shorter than the equivalent H···A interactions in pure **R**, which can be considered as a driving factor for the substitution of the dimer motif. Lastly, π···π stacking interactions were shown to be affected as a result of the co-crystal formations (Table 3). The aromatic rings of **R** are referred to as noted in Chart 1.

Thermal analysis

Thermal stability was investigated by means of thermogravimetric analysis. The thermograms for **R** and its co-crystals are depicted in Fig. S13–S15 in the ESI.† While a decomposition point for pure **R** was observed at 350 °C, the corresponding thermograms for the co-crystals displayed additional plateaus under 350 °C, indicating the decomposition of the co-crystals with the plateaus assigned to the respective components.

The thermogram for **R:A** displayed two processes with the decomposition of **A** located at $T_{\mathbf{R:A},1}$ = 130 °C causing a mass loss of 28% and the decomposition point of **R** is shifted to $T_{\mathbf{R:A},2}$ = 343 °C with a mass loss of 47%. The thermogram for **R:B** exhibited two distinct endothermic processes starting at $T_{\mathbf{R:B},1}$ = 117 °C and $T_{\mathbf{R:B},2}$ = 348 °C, which could be clearly assigned to the respective components of the co-crystal. $T_{\mathbf{R:B},1}$ = 117 °C likely originated from C–I bond breaking processes, resulting in a mass decrease of 68%. $T_{\mathbf{R:B},2}$ = 348 °C represents the decomposition point of **R**, with a 24% mass loss. The thermogram for **R:C** contained two processes, the first of which at $T_{\mathbf{R:C},1}$ = 244 °C could be attributed to the decomposition process of the co-former component **C** with a mass loss of 23%. The second point originated from the decomposition process of **R** starting at $T_{\mathbf{R:C},2}$ = 322 °C with a mass loss of 37%. With regard to the thermal stability of **R**, we hence observed a roughly similar decomposition point in **R:B** compared to pure **R**, whereas the thermal stability was decreased significantly by −28 °C in **R:C** and −7 °C in **R:A**.

Table 2 N–H···O distances of R and multicomponent crystals

Structure	D–H···A	D–H [Å]	H···A [Å]	D···A [Å]
R	N2–H1···O2	0.84(2)	1.98(2)	2.813(2)
R:A	N2–H2···O3	0.88(4)	2.05(4)	2.922(3)
R:B	N1–H1···O2	0.96(5)	1.88(5)	2.834(6)
R:C	N9–H9A···O1	0.98(3)	1.94(3)	2.909(3)
	N2–H2···N6	0.94(4)	2.00(4)	2.937(3)
	N8–H8A···O2	0.99(3)	1.96(3)	2.938(3)

Table 3 π···π stacking distances in R and multicomponent crystals

Structure	π···π	π···π [Å]
R	**Ring 2–Ring 3**^{i}	3.576(4) & 3.6280(13)
R:A	**Ring 2–Ring 2**^{i}	3.5312(15)
	Ring 2–Ring 2^{ii}	3.5087(13)
	Ring 1–Ring 3^{i}	3.5297(12)
	Ring 1–Ring 3^{ii}	3.5090(12)
R:B	**Ring 2–Ring 2**^{iii}	3.727(3)
	Ring 1–Ring 3^{iii}	3.684(3)
R:C	**Ring 1–Ring 3**^{i}	3.3948(15)
	Ring 2–Ring 2^{i}	3.3869(15)
	Ring 2–Ring 3^{iii}	4.1262(16)
	Ring 3–Ring 3^{iii}	3.9787(15)
	Ring 1–C^{iii}	3.5814(15)

^{i} 1 − x, 1 − y, 1 − z; ^{ii} −x, 1 − y, 1 − z; ^{iii} 2 − x, 1 − y, 1 − z.

Optical properties

The co-crystallization exerted an effect on the luminescence properties of roseolumiflavin in the solid state. Fig. 7 presents the powdered, microcrystalline compounds prepared under daylight and excited with a conventional UV lamp at λ_{exc} = 366 nm. While **R** only showed weak visible luminescence (but near-infrared luminescence as will be discussed below), the co-crystals showed a comparably more intense orange-red luminescence. When observing the single and multicomponent crystals under daylight the latter exhibit modified colours compared to **R**.

The luminescence emission spectra confirmed a generally blue-shifted luminescence in the co-crystals compared to solid **R**. The selected excitation wavelength was based on the employed continuous-wave laser, which allowed recording the emission spectra with a higher signal-to-noise ratio. While **R** emitted light in the near-infrared area (λ_{em}^{max} = 733 nm), the co-crystals **R:A**, **R:B**, and **R:C** showed blue-shifted emission bands with maxima at λ_{em}^{max} = 638 nm for **R:A**, λ_{em}^{max}

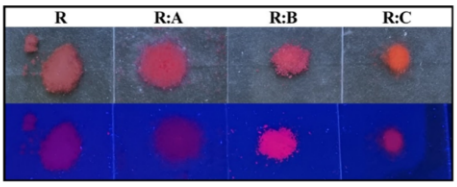

Fig. 7 R, R:A, R:B, and R:C under daylight (top) and excited at λ_{exc} = 366 nm (bottom).

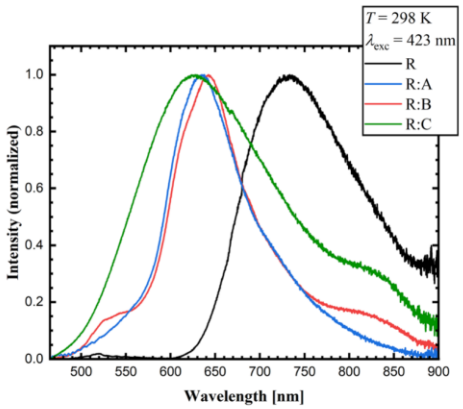

Fig. 8 Experimental emission solid-state spectra of **R**, **R:A**, **R:B**, and **R:C** (λ_{exc} = 423 nm) at room temperature.

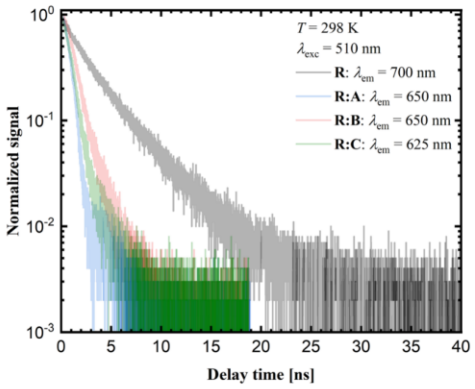

Fig. 9 Experimental solid-state decay curves of **R**, **R:A**, **R:B**, and **R:C**, acquired at room temperature.

= 643 nm for **R:B**, and λ_{em}^{max} = 628 nm for **R:C** with red emission (Fig. 8) at room temperature. These results indicate that the co-crystallization and the consequent inhibition of certain interaction modes in the pure solid **R** could also be noted in the luminescence properties. The emission spectra and excitation spectra of the respective co-formers are available in the ESI.† All the data on the optical properties are summarized in Table 4.

Time-resolved luminescence measurements in the solid state provide additional insights into the photophysical properties of the respective samples. The corresponding decay curves are shown in Fig. 9. The luminescence decay times for the co-crystals **R:A** and **R:C** are close to 1 ns, while for **R:B** a value of 1.42 ns was measured. Yet, the average decay time for pure **R** is around 3 ns. According to the luminescence decay data and the small Stokes shift upon comparison of the emission spectra with the corresponding excitation spectra (see ESI,† Fig. S26–32), the emission of **R** and the co-crystals **R:A**–**R:C** could be assigned to fluorescence. The red-shifted luminescence in the case of pure **R** was related to the stacking of molecular units within the crystalline phase and is typically assigned to aggregate-based emission. Usually, this is accompanied by severe quenching based on the higher probability of non-radiative relaxation for lower energetic transitions. On the other hand, if radiative decay remains the dominant mechanism, the respective decay rate should decrease with the decreasing emission energy due to the lower photon density of states at higher energies.

The observed trend in the time-resolved luminescence data indicates that aggregation-induced quenching was clearly of minor relevance, suggesting that the quantum yield of solid **R** at room temperature cannot be too small.

In order to verify whether the correlation between the aggregation of molecules in the solid and a red-shifted luminescence is given, the absorption and emission spectra of **R** in dilute solutions were also measured. Since **R** generally exhibits a very poor solubility in a number of solvents and the respective co-crystals are not soluble in apolar solvents, the optical properties were investigated in chloroform, acetonitrile, and methanol. Indeed, the emission bands of **R** in solution were even additionally blue-shifted towards the green range, clearly suggesting a trend of the degree of supramolecular bonding within the crystalline solid with the red-shift in the luminescence of **R**. Variations in the solvent polarity did, however, only slightly affect the luminescence, excluding a significant charge-transfer-type nature of the radiatively emitting state (Fig. S20–S22 in the ESI†).

Table 4 Photophysical data for **R** and its co-crystals in the solid state and solvent environment: Solid-state luminescence lifetimes τ, excitation $\lambda_{exc,ss}^{max}$ and emission $\lambda_{em,ss}^{max}$ maxima in the solid state, absorption $\lambda_{abs,solv}^{max}$ and emission $\lambda_{em,solv}^{max}$ maxima in chloroform ($CHCl_3$), acetonitrile (ACN), and methanol (MeOH)

	Solid state			Solution					
				$\lambda_{abs,solv}^{max}$ [nm]			$\lambda_{em,solv}^{max}$ [nm]		
	τ [ns]	$\lambda_{exc,ss}^{max}$ [nm]	$\lambda_{em,ss}^{max}$ [nm]	$CHCl_3$	ACN	MeOH	$CHCl_3$	ACN	MeOH
R	2.85	633	733	487	488	491	533	512	542
R:A	0.99	592, 350	638	483	486	491	524	519	542
R:B	1.42	520, 402	643	490	486	490	546	527	546
R:C	0.98	565, 339	628	486	485	485	536	540	552

The absorption maxima are all in the range of 483–496 nm depending on the system and solvent, which indicated that also the excited state cannot involve a significant charge-transfer-type nature.

No clear fluorescence dependence from the polarity could be observed either. Within the co-crystals, incremental shifts were observed from **R:A** over **R:B** to **R:C** in methanol and acetonitrile. This trend was, however, not consistent for chloroform. Here, **R:C** exhibited the strongest Stokes shift of 56 nm (2093 cm^{-1}). In general, the relatively small Stokes shifts in all systems suggest an excitation from the ground state into the locally exited (LE) state, with no significant relaxation indicating a limited degree of reorganization in the excited state. This is in good agreement with the theoretical calculations reported previously.[39] The charge-transfer processes described by Thiel *et al.*, however, would imply a remarkable reorganization of the charge density and cause a large Stokes shift as well as a rearrangement of the molecular geometry, which was neither observed in solution nor in the solid state.

Based on the experimental results, we propose a mechanism by which the emission bands of **R** and co-crystals correlate with the degree of the crystal packing alteration. In the pure solid roseolumiflavin, the hydrogen-bonded amide–amide dimeric motifs and π···π stacking allow close-packing, which results in strongly red-shifted emission bands based on an aggregation-induced emission. In the solvent environment, this aggregation is inhibited. In solution, both pure **R** and the dissolved co-crystallized compounds showed luminescence with similar wavelengths strongly blue-shifted from the solid **R**. Upon co-crystallization and the introduction of each respective co-former into the crystal lattice, the stacking between different flavin molecules was gradually disturbed but not completely inhibited. Common for all the co-crystals hereby is the partial disruption of the dimeric synthon compared to **R**. Whereas in **R:A** and **R:C**, the amide–amide dimers were resolved and replaced by two- and three-point binding motifs with the co-agents, **R:B** showed just the formation of an additional halogen bond. The last, however, seemed to influence the strength of the hydrogen bonds in the amide–amide dimer. Further, rearranged stacking motifs were noticed in all the multicomponent crystal structures, which resulted in stacking arrangements closer to cofacial patterns, while the pure **R** crystal structure showed merely π···π stacks between **Ring 2** and **Ring 3**. In **R:A** and **R:B** nevertheless, the π-stacks stayed intact, resulting in emission band shifts in similar ranges, with **R:B** showing a smaller shift in accordance with the slightest interference in the interacting modes. **R:C**, on the other hand, partly modified the π-stacks by incorporating **C** units in the interaction pattern. Here, the offset π···π interactions between flavin and 2,4-diaminopyrimidine entities led to significantly shortened flavin–flavin stacks. Thus, the crystal packing of **R** experienced the strongest distortion in **R:C**, yielding the largest blue-shift of all the solid, co-crystalline systems. In solution, the distortion and inhibition of stacking interaction was then extreme, leading to the strongest blue-shift to green luminescence compared to the solid compounds.

Thus, upon comparison with the solvent-based luminescence measurements, we arrived at the conclusion that it is not the nature of the co-former or particular intermolecular interaction itself that leads to changes in the luminescence of the co-crystals compared to the pure solid roseolumiflavin, but rather their effect on the crystal packing; in particular, the distortion of the flavin–flavin hydrogen-bonded motifs and π···π stacking caused by the intermolecular interactions involved. The new environments provided by the respective interaction partners caused a disruption of the close packing of **R** molecules that was translated in their spectroscopic properties in a classic sense of a structure–property relationship.

Conclusions

In this work, we presented the structural analysis of roseolumiflavin (**R**). X-ray analyses on the obtained single crystals helped identify the strong hydrogen-bonded amide–amide synthons in **R** as well as π···π stacking interactions as the driving factors for the molecular self-assembly processes and allowing the construction of the crystal packing. Based on the rational design with specifically selected co-formers, three new co-crystals were synthesized driven by hydrogen and halogen bond interactions. Impressively, the co-crystals showed different interaction patterns (carboxylic acid–amide synthon, three-point binding motifs, halogen bonding) which promises great accessibility for **R** in the aspect of crystal engineering and may serve as grounds for further research in this area on flavins in general. It was shown that the structural versatility also influences the photophysical properties. While the solid **R** showed near-infrared luminescence, the new co-crystals **R:A**, **R:B**, and **R:C** showed blue-shifted emission in the orange-red range. In solution, the dissolved molecules showed green fluorescence. This implies an aggregation-induced red-shift of the luminescence, which, however, could not be severely quenched given the observed elongation of the decay rates with decreasing emission energy. The negligible degree of solvatochromism in both the luminescence and absorption spectra indicated that both the excited and ground state were rather molecularly localized states without a significant degree of charge transfer and formation of a strong electric dipole moment, in agreement with previous theoretical predictions. Overall, our findings indicate a way of tailoring the optical properties of flavins with the aid of crystal engineering.

Conflicts of interest

There are no conflicts to declare.

Acknowledgements

Roseolumiflavin synthesis and SC-XRD analyses were funded by the Deutsche Forschungsgemeinschaft (DFG, German Research Foundation) – 396890929/GRK 2482 and 440366605. We thank the CeMSA@HHU (Center for Molecular and Structural Analytics @ Heinrich Heine University) for recording the NMR- and MS-spectroscopic data. We further thank Tobias Heinen for valuable discussions and the research group of Prof. Peter Gilch for the possibility to measure the emission spectra in solution. The authors are grateful to Prof. Matthias Karg (HHU Düsseldorf) for the access to the FLS980 spectrometer and to PD Klaus Schaper and Prof. Thomas Müller (HHU Düsseldorf) for the possibility to use the pulsed EPL-375, EPL-450, and EPL-510 laser diodes from Edinburgh Instruments for the time-resolved luminescence measurements of the solid compounds.

Notes and references

1 G. R. Desiraju, Chemistry beyond the molecule, *Nature*, 2001, **412**, 397–400.
2 D. Braga, F. Grepioni, L. Maini and M. Polito, in *Molecular Networks. Structure and Bonding*, ed. M. W. Hosseini and D. Braga, Springer-Verlag, Berlin, Heidelberg, 2009, pp. 25–50.
3 C. W. Tang and S. A. VanSlyke, Organic electroluminescent diodes, *Appl. Phys. Lett.*, 1987, **51**, 913–915.
4 R. H. Friend, R. W. Gymer, A. B. Holmes, J. H. Burroughes, R. N. Marks, C. Taliani, D. D. C. Bradley, D. A. D. Santos, J. L. Brédas, M. Lögdlund and W. R. Salaneck, Electroluminescence in conjugated polymers, *Nature*, 1999, **397**, 121–128.
5 A. J. C. Kuehne and M. C. Gather, Organic Lasers: Recent Developments on Materials, Device Geometries, and Fabrication Techniques, *Chem. Rev.*, 2016, **116**, 12823–12864.
6 J. Gierschner, S. Varghese and S. Y. Park, Organic Single Crystal Lasers: A Materials View, *Adv. Opt. Mater.*, 2016, **4**, 348–364.
7 J. Wu, W. Liu, J. Ge, H. Zhang and P. Wang, New sensing mechanisms for design of fluorescent chemosensors emerging in recent years, *Chem. Soc. Rev.*, 2011, **40**, 3483–3495.
8 M. K. Bera, P. Pal and S. Malik, Solid-state emissive organic chromophores: design, strategy and building blocks, *J. Mater. Chem. C*, 2020, **8**, 788–802.
9 D. Yan, A. Delori, G. O. Lloyd, T. Friščić, G. M. Day, W. Jones, J. Lu, M. Wei, D. G. Evans and X. Duan, A cocrystal strategy to tune the luminescent properties of stilbene-type organic solid-state materials, *Angew. Chem., Int. Ed.*, 2011, **50**, 12483–12486.
10 S. Li, Y. Lin and D. Yan, Two-component molecular cocrystals of 9-acetylanthracene with highly tunable one-/two-photon fluorescence and aggregation induced emission, *J. Mater. Chem. C*, 2016, **4**, 2527–2534.
11 Y. Liu, Q. Zeng, B. Zou, Y. Liu, B. Xu and W. Tian, Piezochromic Luminescence of Donor-Acceptor Cocrystals: Distinct Responses to Anisotropic Grinding and Isotropic Compression, *Angew. Chem.*, 2018, **130**, 15896–15900.
12 Y. Liu, A. Li, S. Xu, W. Xu, Y. Liu, W. Tian and B. Xu, Reversible Luminescent Switching in an Organic Cocrystal: Multi-Stimuli-Induced Crystal-to-Crystal Phase Transformation, *Angew. Chem., Int. Ed.*, 2020, **59**(35), 15098–15103.
13 J. Vainauskas, F. Topić, O. S. Bushuyev, C. J. Barrett and T. Friščić, Halogen bonding to the azulene π-system: cocrystal design of pleochroism, *Chem. Commun.*, 2020, **56**, 15145–15148.
14 T. Feiler, B. Bhattacharya, A. A. L. Michalchuk, V. Schröder, E. List-Kratochvil and F. Emmerling, Mechanochemical Syntheses of Isostructural Luminescent Cocrystals of 9-Anthracenecarboxylic Acid with two Dipyridines Coformers, *Crystals*, 2020, **10**, 889.
15 S. O. Mansoorabadi, C. J. Thibodeaux and H. Liu, The diverse roles of flavin coenzymes–nature's most versatile thespians, *J. Org. Chem.*, 2007, **72**, 6329–6342.
16 H. Grajek, Review - Flavins as photoreceptors of blue light and their spectroscopic properties, *Curr. Top. Biophys.*, 2011, **34**, 53–65.
17 V. Massey, The Chemical and Biological Versatility of Riboflavin, *Biochem. Soc. Trans.*, 2000, **28**, 283–296.
18 J. Galbán, I. Sanz-Vicente, J. Navarro and S. de Marcos, The intrinsic fluorescence of FAD and its application in analytical chemistry: a review, *Methods Appl. Fluoresc.*, 2016, **4**, 42005.
19 E. Sikorska, I. V. Khmelinskii, D. R. Worrall, J. Koput and M. Sikorski, Spectroscopy and photophysics of iso- and alloxazines: experimental and theoretical study, *J. Fluoresc.*, 2004, **14**, 57–64.
20 M. Sikorski, E. Sikorska, F. Wilkinson and R. P. Steer, Studies of the photophysics and spectroscopy of alloxazine and related compounds in solution and in the solid state, *Can. J. Chem.*, 1999, **77**, 472–480.
21 S. Salzmann and C. M. Marian, The photophysics of alloxazine: a quantum chemical investigation in vacuum and solution, *Photochem. Photobiol. Sci.*, 2009, **8**, 1655–1666.
22 A. Reiffers, C. Torres Ziegenbein, A. Engelhardt, R. Kühnemuth, P. Gilch and C. Czekelius, Impact of Mono-Fluorination on the Photophysics of the Flavin Chromophore, *Photochem. Photobiol.*, 2018, **94**, 667–676.
23 *Principles of fluorescence spectroscopy (3rd ed)*, ed. J. R. Lakowicz, Springer, New York, Berlin, 3rd edn, 2006.
24 E. Horiguchi, S. Matsumoto, K. Funabiki and M. Matsui, Optical Properties of Novel 2,3-Dicyano-5-methyl-6 H -1,4-diazepine Dyes in the Solid State, *Bull. Chem. Soc. Jpn.*, 2005, **78**, 1167–1173.
25 C.-L. Chiang, M.-F. Wu, D.-C. Dai, Y.-S. Wen, J.-K. Wang and C.-T. Chen, Red-Emitting Fluorenes as Efficient Emitting Hosts for Non-Doped, Organic Red-Light-Emitting Diodes, *Adv. Funct. Mater.*, 2005, **15**, 231–238.
26 Y. Ooyama, T. Nakamura and K. Yoshida, Heterocyclic quinol-type fluorophores. Synthesis of novel imidazoanthraquinol derivatives and their photophysical

properties in benzene and in the crystalline state, *New J. Chem.*, 2005, **29**, 447.

27 I. J. Bruno, J. C. Cole, P. R. Edgington, M. Kessler, C. F. Macrae, P. McCabe, J. Pearson and R. Taylor, *New software for searching the Cambridge Structural Database and visualizing crystal structures (CCDC, ConQuest Version 2020.3.0)*, 2002, 58, 389–397.

28 M. Á. Farrán, R. M. Claramunt, C. López, E. Pinilla, M. R. Torres and J. Elguero, Structural characterization of alloxazine and substituted isoalloxazines: NMR and X-ray crystallography, *ARKIVOC*, 2006, **2007**(4), 20–38.

29 M. Wang and C. J. Fritchie, Geometry of the unperturbed flavin nucleus. The crystal structure of 10-methylisoalloxazine, *Acta Crystallogr., Sect. B: Struct. Crystallogr. Cryst. Chem.*, 1973, **29**, 2040–2045.

30 R. Miura, K. Matsui, K. Hirotsu, A. Shimada, M. Takatsu and S. Otani, X-Ray crystallographic determination of a derivative of a new flavin compound, roseoflavin, *J. Chem. Soc., Chem. Commun.*, 1973, 703.

31 S. T. Caldwell, L. J. Farrugia, S. G. Hewage, N. Kryvokhyzha, V. M. Rotello and G. Cooke, Model systems for flavoenzyme activity: an investigation of the role functionality attached to the C(7) position of the flavin unit has on redox and molecular recognition properties, *Chem. Commun.*, 2009, 1350–1352.

32 R. B. Bates, T. C. Sneath and D. N. Stephens, Crystal structure of 10-methylisoalloxazinium bromide dihydrate, *J. Org. Chem.*, 1970, **35**, 1625–1627.

33 J. S. Sherfinski, A. J. deArmendi and C. J. Fritchie Junior, *American Crystallographic Association Abstracts, Papers (Summer)*, 1974, vol. 238.

34 C. J. Fritchie Jr., G. D. Sproul and T. D. Wade, *Acta Crystallogr., Sect. A: Cryst. Phys., Diffr., Theor. Gen. Crystallogr.*, 1972, **28**, S48.

35 F. E. Scarbrough, H.-S. Shieh and D. Voet, The X-ray crystal structure of the molecular complex bis(lumiflavin–2,6-diamino-9-ethylpurine)–ethanol–water, *Acta Crystallogr., Sect. B: Struct. Crystallogr. Cryst. Chem.*, 1977, **33**, 2512–2523.

36 B. L. Trus, J. L. Wells, R. M. Johnston, C. J. Fritchie Jr. and R. E. Marsh, *American Crystallographic Association Abstracts, Papers (Winter)*, 1970, vol. 36.

37 M. C. Kuo, J. B. R. Dunn and C. J. Fritchie, The crystal structure of a flavin molecular complex: 10-propylisoalloxazine–bis(naphthalene-2,3-diol), *Acta Crystallogr., Sect. B: Struct. Crystallogr. Cryst. Chem.*, 1974, **30**, 1766–1771.

38 D. Voet and A. Rich, The crystal and molecular structure of an intermolecular complex between riboflavin and an adenosine derivative, *Proc. Natl. Acad. Sci. U. S. A.*, 1971, **68**, 1151–1156.

39 B. Karasulu and W. Thiel, Photoinduced intramolecular charge transfer in an electronically modified flavin derivative: roseoflavin, *J. Phys. Chem. B*, 2015, **119**, 928–943.

40 A. Nangia and G. R. Desiraju, Supramolecular Synthons and Pattern Recognition, Design of Organic Solids, *Top. Curr. Chem.*, 1998, **198**, 57–95.

41 G. R. Desiraju, J. J. Vittal and A. Ramanan, *Crystal engineering, A textbook*, World Scientific, Singapore, 2011.

42 S. Saha and G. R. Desiraju, Acid···Amide Supramolecular Synthon in Cocrystals: From Spectroscopic Detection to Property Engineering, *J. Am. Chem. Soc.*, 2018, **140**, 6361–6373.

43 S. Kasai, R. Miura and K. Matsui, Chemical Structure and Some Properties of Roseoflavin, *Bull. Chem. Soc. Jpn.*, 1975, **48**, 2877–2880.

44 C. Tantardini, S. G. Arkhipov, K. A. Cherkashina, A. S. Kil'met'ev and E. V. Boldyreva, Crystal structure of a 2:1 co-crystal of meloxicam with acetyl-endi-carb-oxy-lic acid, *Acta Crystallogr., Sect. E: Crystallogr. Commun.*, 2016, **72**, 1856–1859.

45 *CrysAlisPRO*, Oxford Diffraction/Agilent Technologies UK Ltd, Yarnton, England.

46 *APEX2*, Bruker AX Inc., Madison, 2012.

47 *SAINT*, Bruker Analytical X-Ray Systems, Madison, 2018.

48 G. M. Sheldrick, SHELXT - integrated space-group and crystal-structure determination, *Acta Crystallogr., Sect. A: Found. Adv.*, 2015, **71**, 3–8.

49 J. Lübben, C. M. Wandtke, C. B. Hübschle, M. Ruf, G. M. Sheldrick and B. Dittrich, Aspherical scattering factors for SHELXL - model, implementation and application, *Acta Crystallogr., Sect. A: Found. Adv.*, 2019, **75**, 50–62.

50 O. V. Dolomanov, L. J. Bourhis, R. J. Gildea, J. A. K. Howard and H. Puschmann, OLEX2: a complete structure solution, refinement and analysis program, *J. Appl. Crystallogr.*, 2009, **42**, 339–341.

51 C. F. Macrae, I. Sovago, S. J. Cottrell, P. T. A. Galek, P. McCabe, E. Pidcock, M. Platings, G. P. Shields, J. S. Stevens, M. Towler and P. A. Wood, Mercury 4.0: from visualization to analysis, design and prediction, *J. Appl. Crystallogr.*, 2020, **53**, 226–235.

52 A. L. Spek, Structure validation in chemical crystallography, *Acta Crystallogr., Sect. D: Biol. Crystallogr.*, 2009, **65**, 148–155.

53 *OriginPro*, OriginLab Corporation, Northampton, MA, USA, 2019.

Electronic Supplementary Material (ESI) for CrystEngComm.

Co-crystallization of organic chromophore roseolumiflavin and effect on its optical characteristics

Takin Haj Hassani Sohi, Felix Maass, Constantin Czekelius, Markus Suta and Vera Vasylyeva

Electronic Supplementary Information

Table of contents

1. Synthesis of **R**

All reagents were used in reagent grade without further purification. The solvents were purchased in reagent grade or purified by conventional methods. For reactions requiring an inert atmosphere the glassware was dried in a compartment dryer at 120 °C and standard Schlenk techniques were used to work under a dry nitrogen atmosphere. Reactions were monitored by thin-layer chromatography using aluminium foil-backed silica gel from Macherey-Nagel (ALUGRAM® Xtra SIL G/ UV254) with fluorescence indicator. To concentrate solutions under reduced pressure rotary evaporators (Heidolph Instruments) in combination with membrane pumps by VACUUBRAND were used. For purifications by column chromatography silica gel 60 from Macherey-Nagel (Kieselgel 60 M, 0.04-0.063 mm) was used.

^{1}H- and ^{13}C-NMR-spectra were measured at room temperature using a Bruker Avance III – 300 (300 MHz). The chemical shifts were standardized with traces of chloroform ($\delta(CDCl_3)$ = 7.26 ppm) or dimethylsulfoxide (δ(DMSO-d_6) = 2.50 ppm) in ^{1}H-spectra and with the signal of deuterated chloroform ($\delta(CDCl_3)$ = 77.0 ppm), dimethylsulfoxide (δ(DMSO-d_6) = 39.52 ppm) or formic acid ($\delta(HCO_2H)$ = 166.3 ppm)[1] in ^{13}C-spectra. The coupling constants *J* are given in Hertz (Hz) and the chemical shifts δ in ppm.

IR spectra were recorded using a Bruker Tensor FT/IR 37 spectrometer with ATR-unit or a Jasco FT/IR-6200 spectrometer as KBr pellet. High resolution mass spectra (ESI-HRMS) were measured with a *Bruker Daltonics* UHR-QTOF maXis 4G. For melting point determination, a Büchi Melting Point B-540 apparatus was used. DSC measurements were performed with a Linkam DSC600 at 5°C/min heating rate.

N^1,N^3,N^3,4-Tetramethylbenzene-1,3-diamine

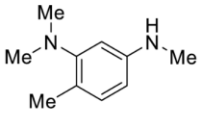

A modified procedure by Brown and Rizzo was followed[2]. In a 250 mL flask N^1,N^1,6-trimethylbenzene-1,3-diamine (5.00 g, 30.1 mM) was dissolved in dichloromethane (150 mL) and triethylamine (4.57 g, 6.29 mL, 45.1 mM) as well as trifluoroacetic anhydride (7.58 g, 5.02 mL, 36.1 mM) added at 0 °C. After stirring for 15 min, water (50 mL) was added and the organic layer separated. After drying over sodium sulfate, the solvent was evaporated.

The residue was dissolved in toluene (60 mL) and benzyltriethylammonium chloride (6.86 g, 30.1 mM) and dimethyl sulfate (4.74 g, 3.57 mL, 37.6 mM) added at 0 °C. Sodium hydroxide solution (50%, 30 mL) was added and stirring continued for 4 h. The reaction was quenched by addition of conc. ammonia (5 mL) and water (100 mL). The aqueous layer was extracted with toluene (3 x 100 mL), the combined organic layers dried over sodium sulfate and the solvent evaporated. Flash column chromatography (silica gel, hexane/ethyl acetate 6:1) gave the product as an orange oil (2.16 g, 12.0 mM, 40%).

^{1}H NMR (300 MHz, $CDCl_3$): δ [ppm] = 6.99 (dd, *J* = 8.0, 0.8 Hz, 1H, C(5)*H*), 6.34 (d, *J* = 2.4 Hz, 1H, C(2)*H*), 6.27 (dd, *J* = 8.0, 2.4 Hz, 1H, C(6)*H*), 3.56 (s, 1H, N*H*), 2.83 (s, 3H, NH*Me*), 2.69 (s, 6H, N*Me*$_2$), 2.23 (s, 3H, Ar-*Me*). **^{13}C NMR** (75 MHz, $CDCl_3$): δ [ppm] = 153.57, 148.40, 131.79, 120.79, 106.61, 103.62, 44.24, 31.23, 17.66. **IR** (thin film): ν [cm^{-1}] = 3406, 2397, 2822, 2781, 1614, 1515, 1327, 1252, 1146, 1106, 796. **HRMS** (ESI): calc'd. for $C_{10}H_{17}N_2$ $[M+H]^+$, 165.1386; found: 165.1388.

8-(Dimethylamino)-7,10-dimethylbenzo[g]pteridine-2,4(3H,10H)-dione; Roseolumiflavin

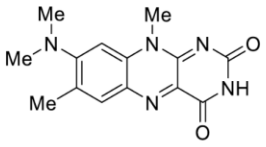

A modified procedure by Kasai, Miura and Matsui was followed[3]. In a 100 mL flask, *N*^{1},*N*^{3},*N*^{3},4-tetramethylbenzene-1,3-diamine (2.16 g, 12.0 mM) was dissolved in methanol (50 mL) and violuric acid added (2.77 g, 15.8 mM). The mixture was heated to reflux for 2.5 h. After cooling to rt, the brick-red precipitate was filtered off and washed with ice-cold methanol. Repeated recrystallization from acetic acid/methanol gave roseolumiflavin (1.62 g, 5.68 mM, 47%).

Mp/DSC: no melting until 330 °C, decomposition at ca. 350 °C. **^{1}H NMR** (600 MHz, DMSO-d_6): δ [ppm] = 11.10 (s), 7.80 (s), 6.88 (s), 3.95 (s), 3.06 (s), 2.45 (s). **^{13}C NMR** (75 MHz, HCO_2H/10% D_2O): δ [ppm] = 161.21, 160.83, 151.21, 143.93, 138.07, 136.19, 135.62, 135.43, 122.34, 99.25, 44.76, 35.37, 22.06. **IR** (ATR): ν [cm^{-1}] = 3380, 3250, 3129, 3063, 2984, 2799, 1690, 1633. **IR** (KBr): ν [cm^{-1}] = 3570, 3517, 2835, 1719, 1700, 1620, 1548, 1522, 1382, 1272, 1096, 941. **HRMS** (ESI): calc'd. for $C_{14}H_{16}N_5O_2$ $[M+H]^+$**,** 286.1299; found: 286.1304.

2. Characterization of **R**

The ^{1}H-NMR (600 MHz) shows weak signals yet significant ones are visible to confirm the presence of respective functional groups. For the magnetically equivalent methyl groups 6 and 7 at the dimethylamine substituent, we locate a singlet at 3.06 ppm (normalized integral: 6.00). Both other methyl substituents on the rings can be detected at 2.45 ppm (3.03) and 3.95 ppm (2.94). We further detect the labile amine group hydrogen 1 at 11.10 ppm (0.94) and both aryl hydrogen signals 2 and 3 at 6.88 ppm (1.02) and 7.80 (1.01), see Figure S1.

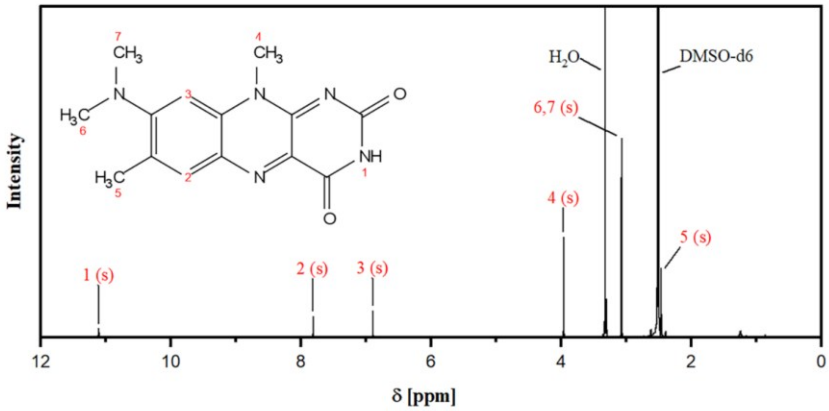

Figure S1: ^{1}H-NMR (600 MHz) of **R** in DMSO-d_6

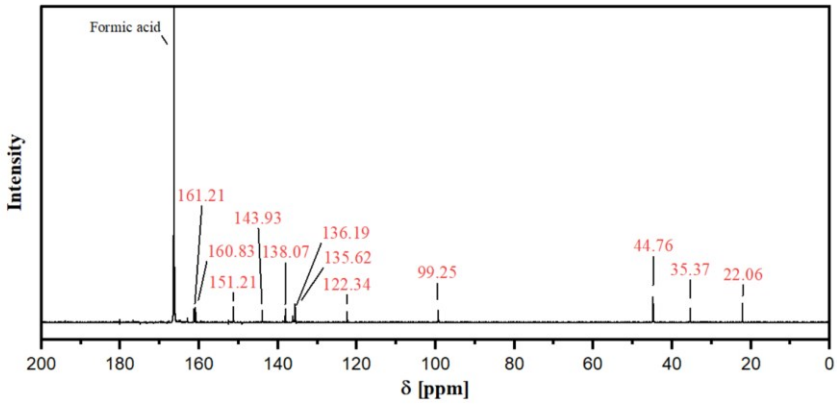

Figure S2: ^{13}C-NMR (75 MHz) of **R** in HCO_2H/10% D_2O

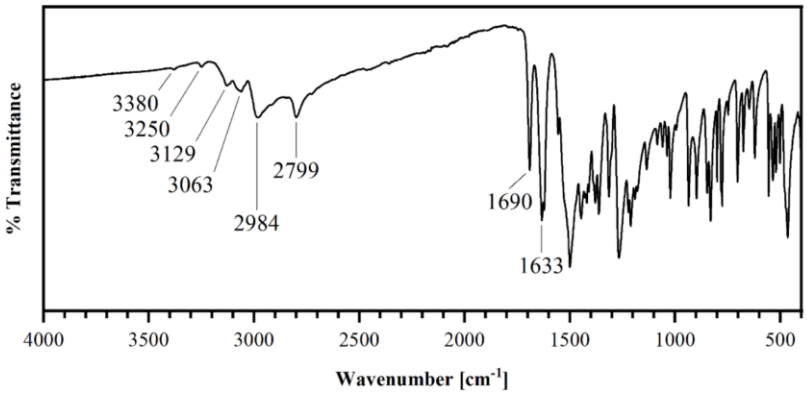

Figure S3: Infrared spectrum (ATR) of **R** recorded from 400 cm-1 to 4000 cm-1

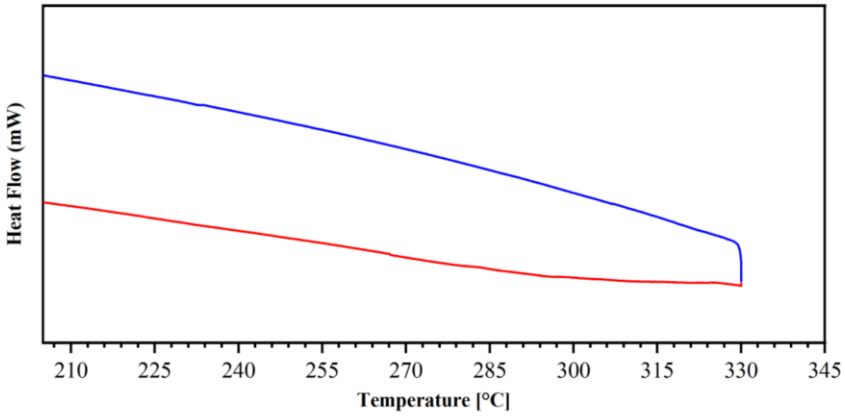

Figure S4: DSC of **R** recorded up to 330°C at 5°C/min heating rate. (red – heating, blue – cooling). No melting or crystallization is detected.

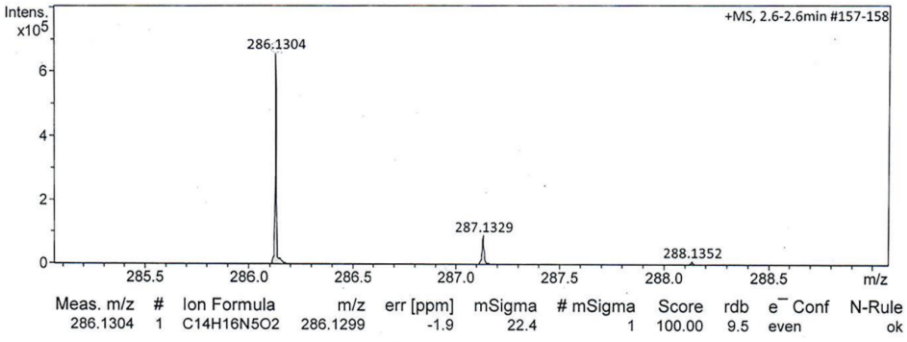

Figure S5: (ESI)-HRMS spectrum of **R**.

5

3. Powder diffraction patterns of **R** and co-crystals

Purity and crystallinity of **R** are confirmed via PXRD analysis displayed in Figure S6 where one can identify characteristic peaks at 8.64°, 10.11°, 12.48°, 14.09°, 17.32° and 25.85° 2θ. The simulated peak at 26.3° is assigned to the signal at 25.85° since the pattern is slightly shifted in the range between 25° to 35° 2θ. The remaining peaks match well with simulated data.

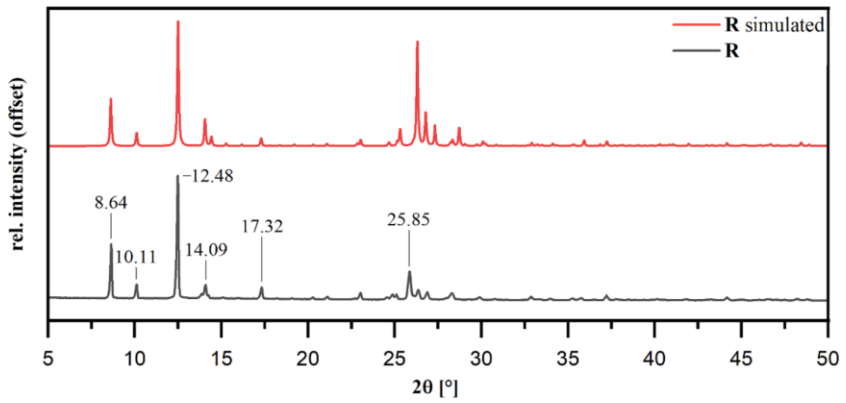

Figure S6: Experimental and simulated from single crystal data PXRD patterns of **R** (Cu Kα radiation)

The powder patterns of **R:A** (Figure S7) are in good agreement with the simulated single crystal patterns and fair crystallinity and purity can be confirmed. We identify significant peaks at 6.29°, 11.59°, 13.55°, 25.22°, 25.97° and 27.78° 2θ. Figure S7 illustrates the powder patterns of the experimental and simulated data. The highest signals are slightly shifted by 0.1° to 0.4° 2 θ, however, intensities and positions match well overall. Since merely the peak at 7.75 °2θ stands out and does not fit either compound (Figure S10) we assume it emerged from impurities.

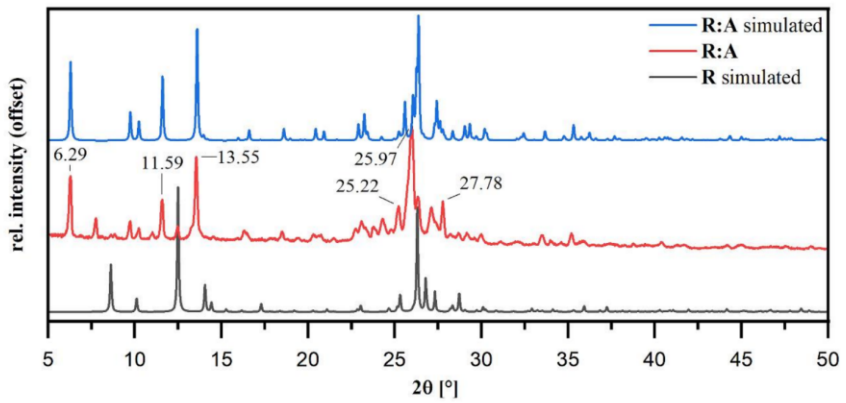

Figure S7: Experimental patterns of **R:A** and **R** and simulated from single crystal powder pattern of **R:A** (Cu Kα radiation)

6

The diffraction patterns of both single crystal and experimental powder sample of **R:B** match well, suggest good crystallinity and do not indicate any phase impurity. Most significant peaks are detected at 12.93°, 16.63°, 16.94°, 24.28°, 24.96°, 26.65° and 26.94° 2θ, see Figure S8.

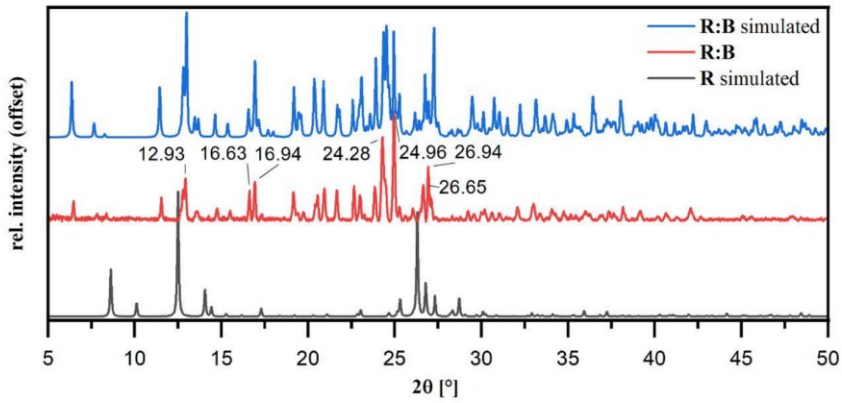

Figure S8: Experimental patterns of **R:B** and **R** and simulated from single crystal powder pattern of **R:B** (Cu Kα radiation)

The significant reflexes of **R:C** are found at 6.14°; 11.47°; 12.64°; 24.84° and 27.15° 2θ (Figure S9). The shift of the reflections at higher angles could be caused either by the sample preparation or by differences in measurement temperatures (SCXRD at 100 K and PXRD at approx. 298 K).

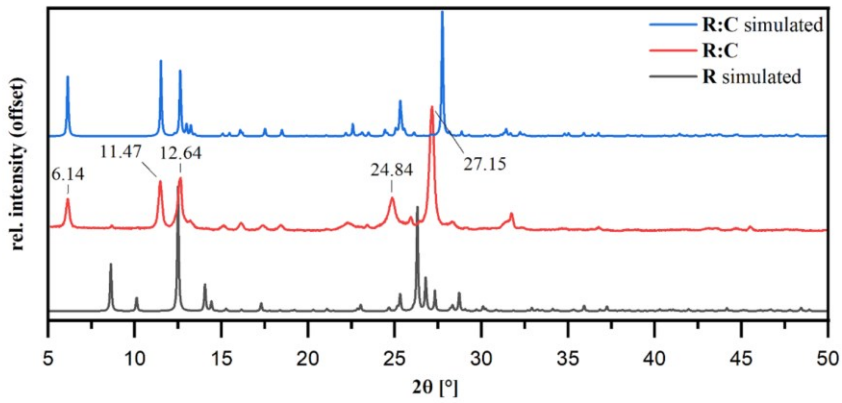

Figure S9: Experimental powder patterns of **R:C** and **R** and simulated from single crystal pattern of **R:C** (Cu Kα radiation)

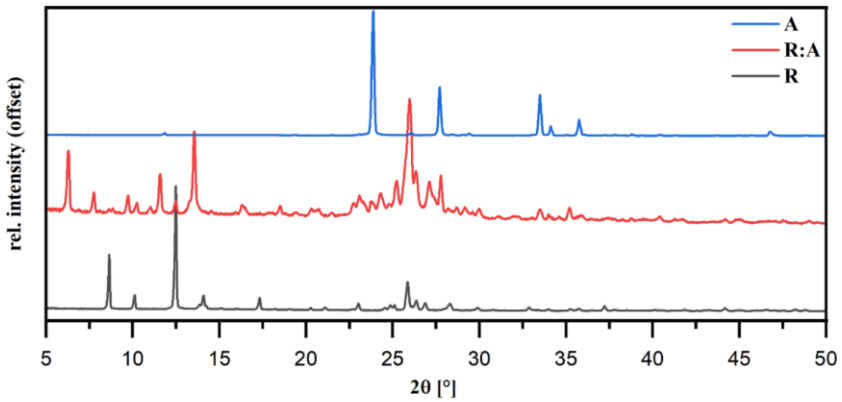

Figure S10: Experimental powder pattern of **R:A** compared to experimental patterns of **R** and **A** (Cu Kα radiation)

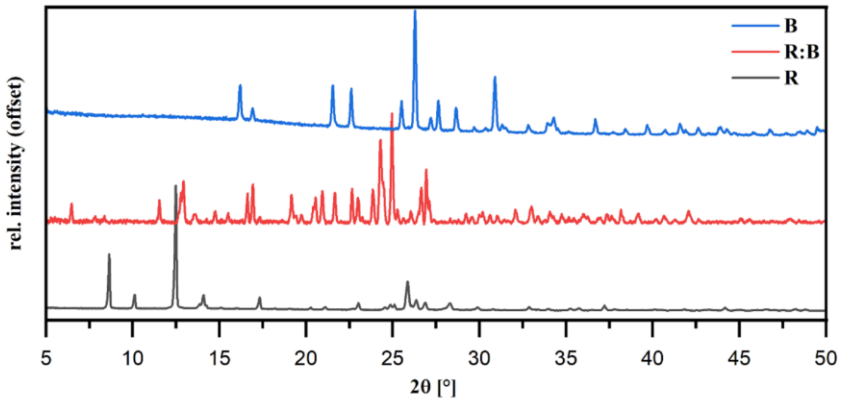

Figure S11: Experimental powder pattern of **R:B** compared to experimental patterns of **R** and **B** (Cu Kα radiation)

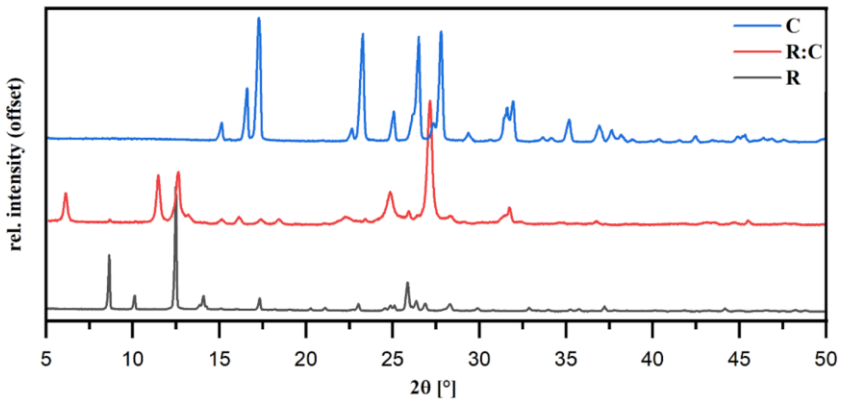

Figure S12: Experimental powder pattern of **R:C** compared to experimental patterns of **R** and **C** (Cu Kα radiation)

4. Thermograms of **R** and co-crystals

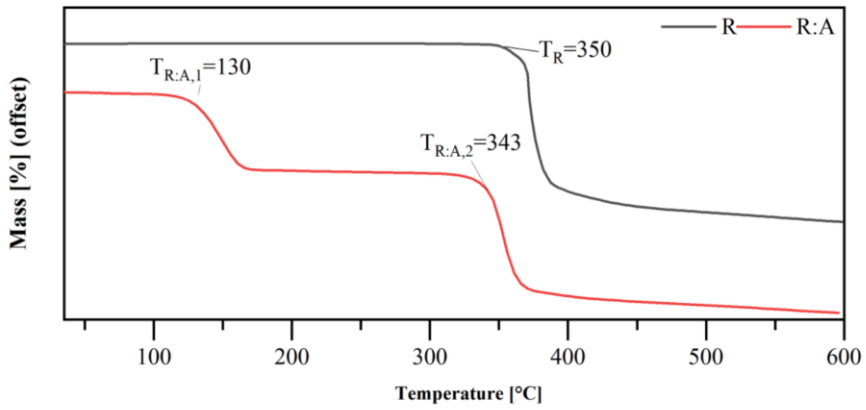

Figure S13: Thermograms of **R:A** and **R** measured between 30-600 °C, nitrogen purge gas, heating rate 10 °C/min.

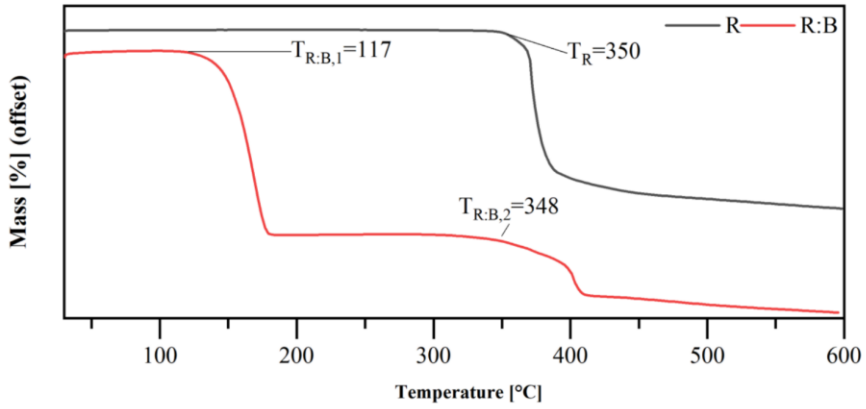

Figure S14: Thermograms of **R:B** and **R** measured between 30-600 °C, nitrogen purge gas, heating rate 10 °C/min.

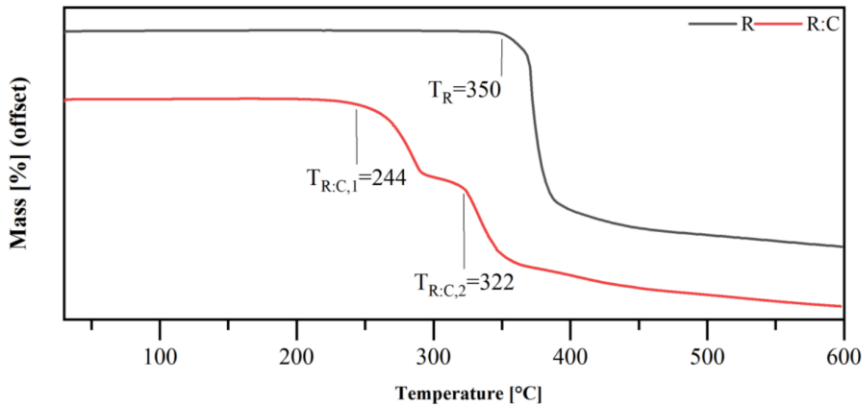

Figure S15: Thermograms of **R:C** and **R** measured between 30-600 °C, nitrogen purge gas, heating rate 10 °C/min.

10

5. IR-spectra of co-crystals

The infrared spectrum of **R:A** (Figure S16) contains two broad bands in the range between 3600 cm^{-1} to 3300 cm^{-1} as well as 3300 cm^{-1} to 2600 cm^{-1} which overlap most of the characteristic bands of **R**. This observation is a good indication for the presence of $O-H$ bonds, which occur ubiquitously in the crystal structure. We further notice blue-shifted $C=O$ bands at 1694 cm^{-1} by +4 cm^{-1}, indicating a shortening of the $C=O$ bond, which may be the effect of the newly built hydrogen bonds with adjacent co-former molecules that leads to the reorganization of the interaction strength and causes a significant shift of the vibrational band. A comparison with the **A** component indicates significant broadening of the $O-H$ band in the co-crystal compared to pure **R**, yet the occurrence of two bands at 3505 cm^{-1} and 3439 cm^{-1} suggests that the extent of overall hydrogen bonding decreased, so these bands are originally likely overlapped in pure **A** which due to the presence of two carboxylic functional groups assumably contains extensive amounts of hydrogen bonding interactions.

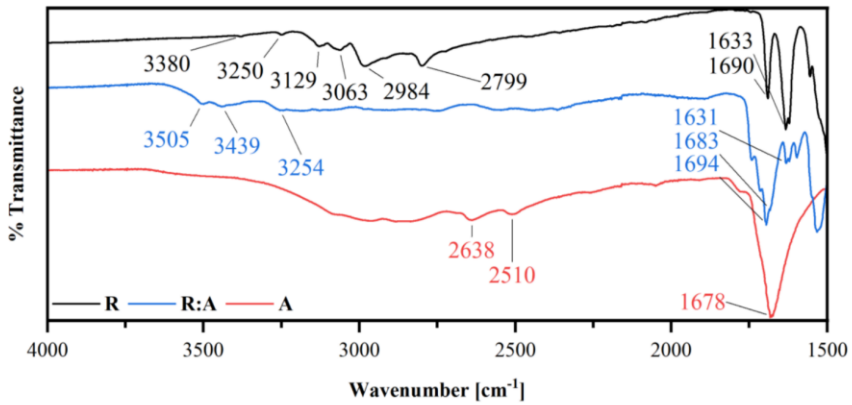

Figure S16: Comparison of IR spectra of **R:A** with **R** and **A**. The fingerprint area (wavenumbers <1500 cm^{-1}) is cut out for clarity. Characteristic bands are highlighted.

Infrared data of **R:B** (Figure S17) shows significant red-shifts for the amide $N-H$ stretching bands at 3359 cm^{-1} and 3237 cm^{-1} with -13 cm^{-1} to -21 cm^{-1} compared to the **R** spectrum. Further, the $C=O$ vibrational bands are also red-shifted to 1683 cm^{-1} and 1623 cm^{-1}. The significant prolongation of the $C=O$ and $N-H$ bonds likely arise from both halogen bonds and hydrogen bonds connecting to the same donor atoms, so that the halogen bonds weaken the hydrogen bond interaction strength. A similar effect was reported by Vasylyeva et al. where N-methylacetamid was co-crystallized with several XB donors including **B** and both XB and HB connected to the same $C=O$ functional group, causing red-shifted $C=O$ stretching bands[4].

A comparison with the co-former spectrum in fingerprint area is shown Figure S19. The C – I asymmetrical stretch at 762 cm^{-1} signifies a blue-shift by +4 cm^{-1} and the C – F stretch at 941 cm^{-1} is slightly blue-shifted by +2 cm^{-1}. The C – C stretching vibrational band at 1455 cm^{-1} is slightly red-shifted with -3 cm^{-1} compared to the free co-former indicating increased electron density in the fluorophenyl rest.

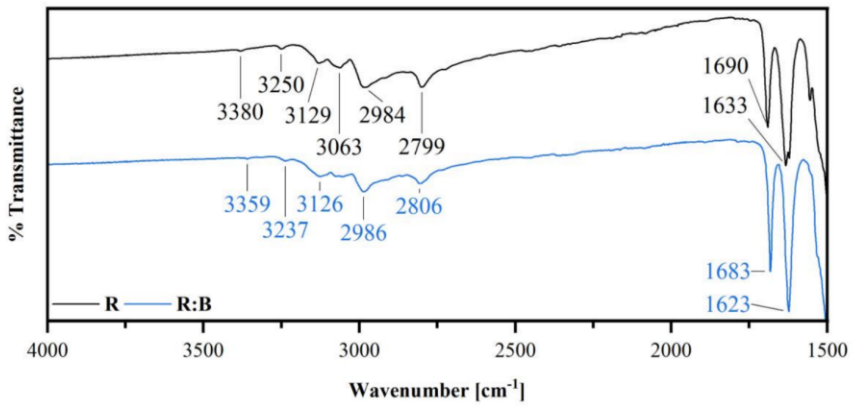

Figure S17: Comparison of IR spectra of **R:B** with **R**. The fingerprint area (wavenumbers <1500 cm^{-1}) is cut out for clarity. Characteristic bands are highlighted.

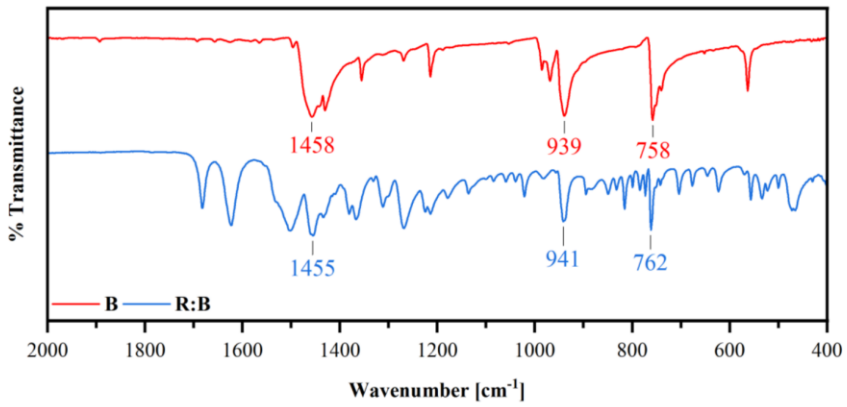

Figure S18: Comparison of IR spectra of **R:B** with **B**. Wavenumbers >2000 cm^{-1} are cut out for clarity. Characteristic bands are highlighted.

The IR spectrum of **R:C** displays a broad, red-shifted band at the 3400 cm^{-1} to 3300 cm^{-1} region which represents the symmetric and asymmetric N – H valence vibrations of the respective compounds. The red-shift is a result of longer N – H bonds in the co-crystal due to the formation of HB between the amino groups of **C** and the imide group of **R** or between the

co-formers. The band representing the C = O vibration at 1688 cm^{-1} is red-shifted by -2 cm^{-1} compared to **R** indicating a slight increase in the bond length.

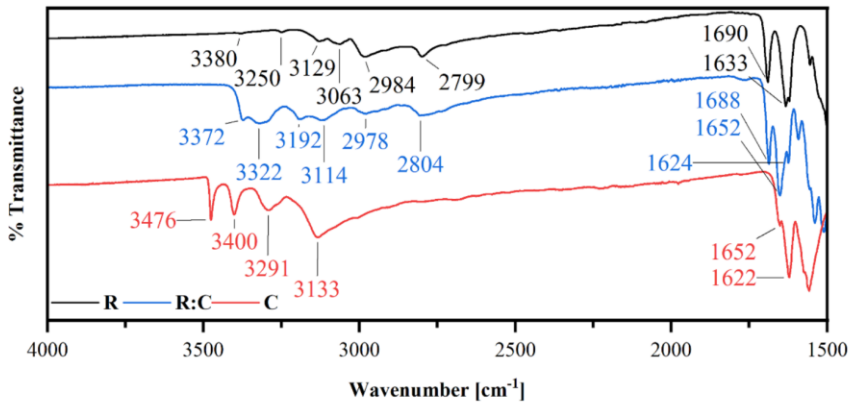

Figure S19: Comparison of IR spectra of **R:C** with **R** and **C**. The fingerprint area (wavenumbers <1500 cm^{-1}) is cut out for clarity. Characteristic bands are highlighted.

6. Lifetimes, excitation and emission spectra of **R**, co-crystals and co-formers

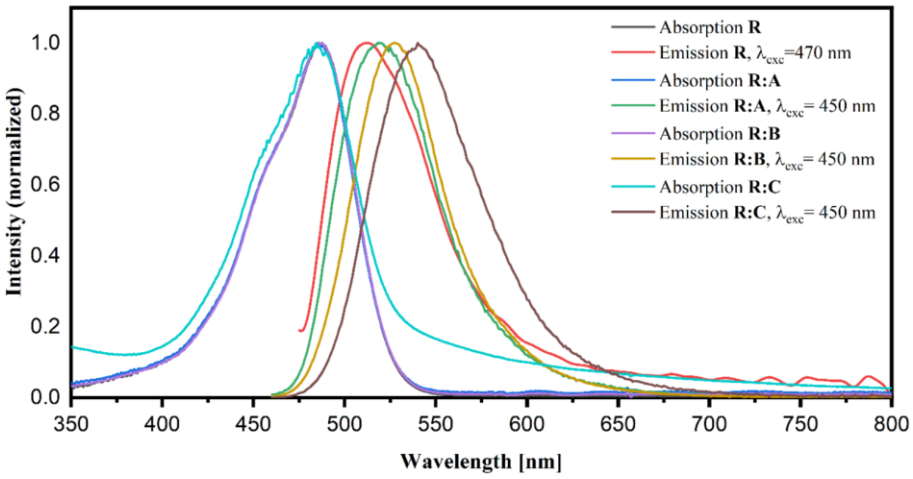

Figure S20: Normalized absorption and emission spectra of **R**, **R:A**, **R:B** and **R:C** in acetonitrile at room temperature

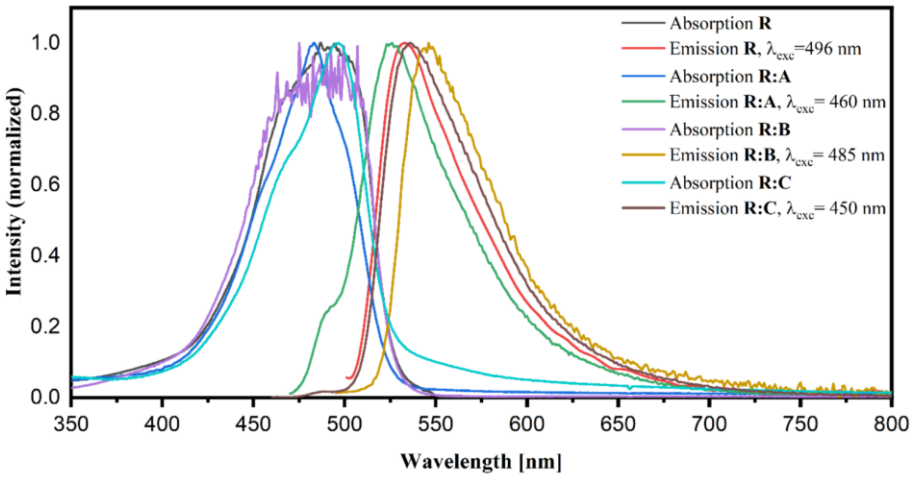

Figure S21: Normalized absorption and emission spectra of **R**, **R:A**, **R:B** and **R:C** in chloroform at room temperature

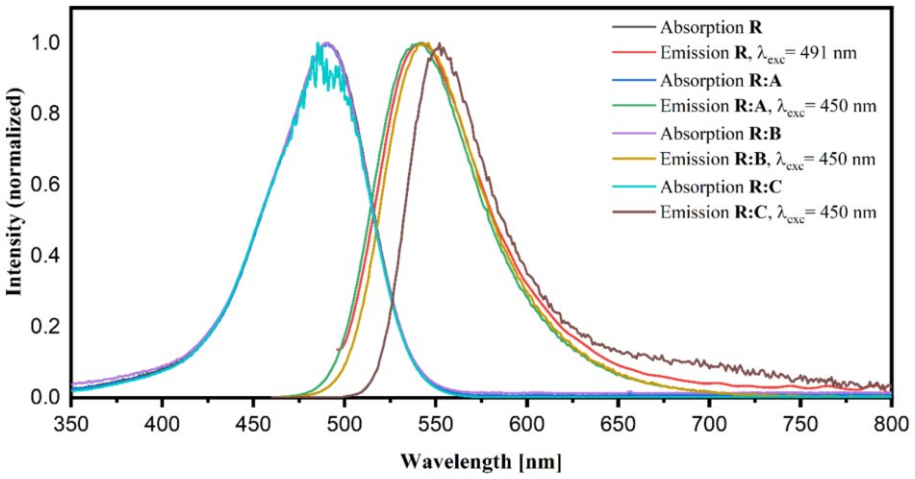

Figure S22: Normalized absorption and emission spectra of **R**, **R:A**, **R:B** and **R:C** in methanol at room temperature

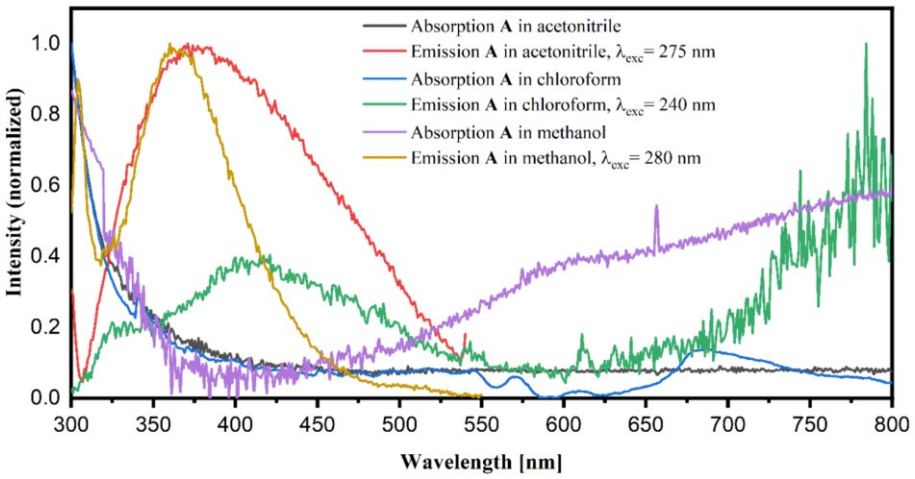

Figure S23: Normalized absorption and emission spectra of **A** in acetonitrile, chloroform and methanol at room temperature

15

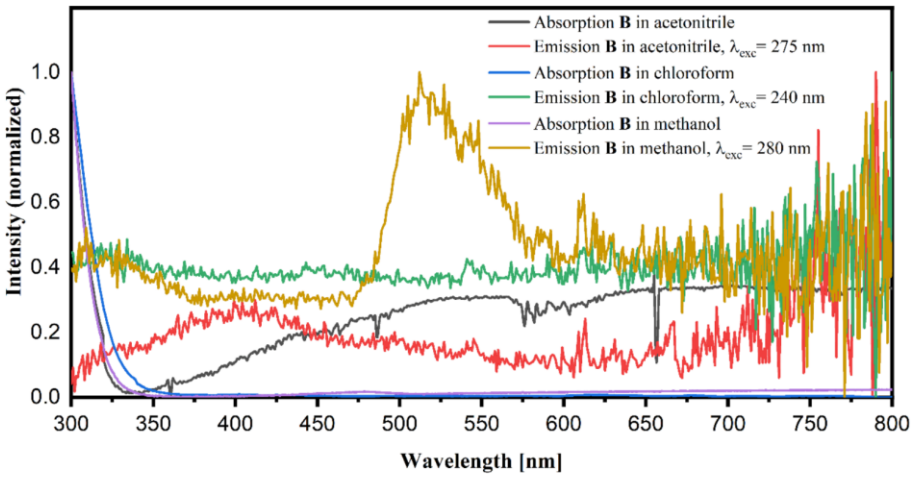

Figure S24: Normalized absorption and emission spectra of **B** in acetonitrile, chloroform and methanol at room temperature

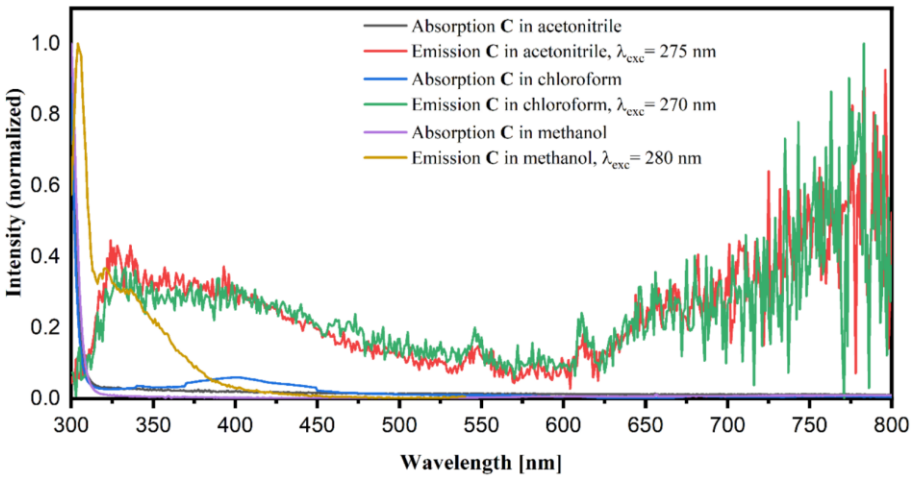

Figure S25: Normalized absorption and emission spectra of **C** in acetonitrile, chloroform and methanol at room temperature

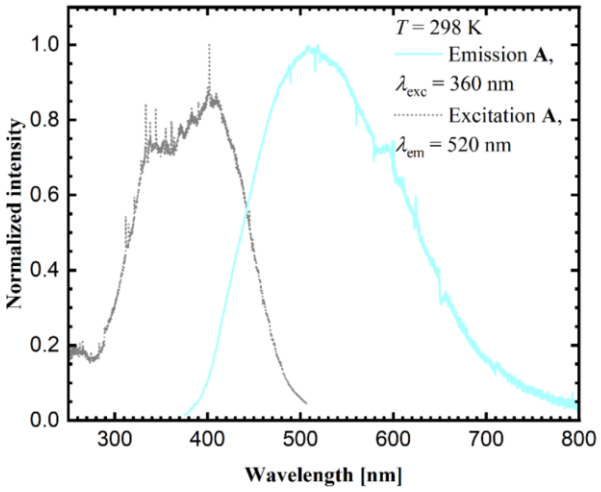

Figure S26: Normalized solid-state excitation and emission spectra of **A** at room temperature

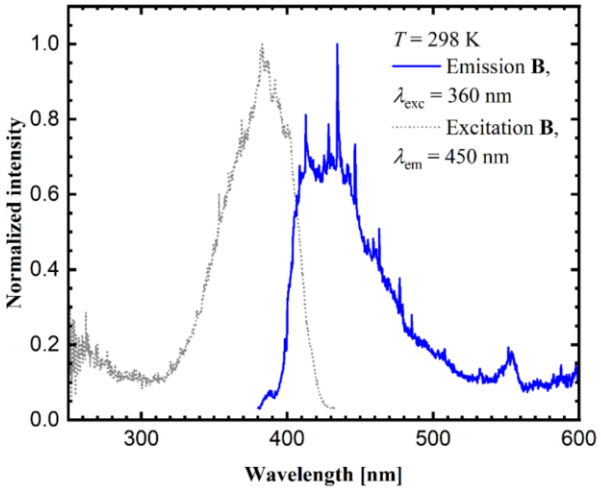

Figure S27: Normalized solid-state excitation and emission spectra of **B** at room temperature

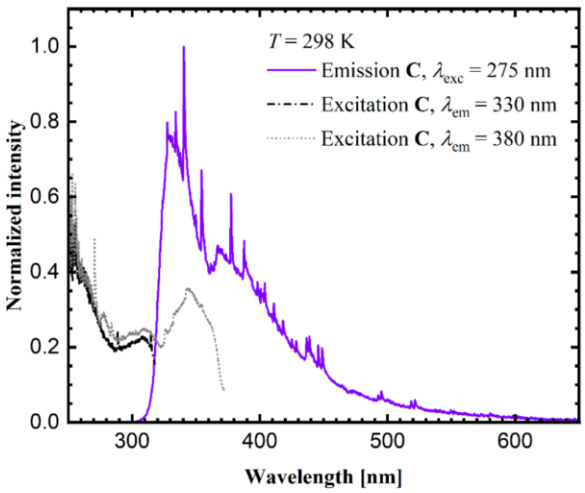

Figure S28: Normalized solid-state excitation and emission spectra of **C** at room temperature

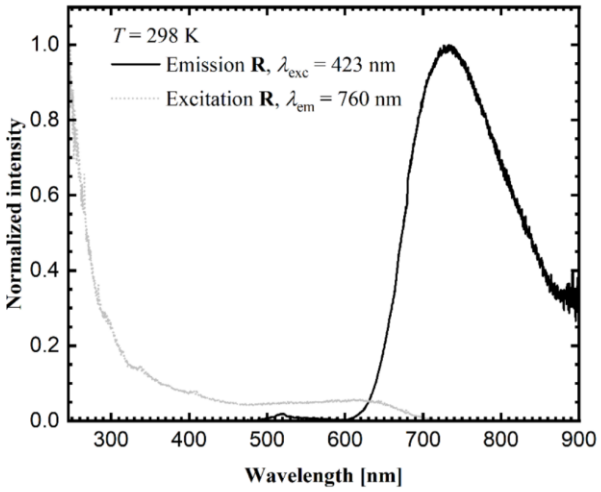

Figure S29: Normalized solid-state excitation and emission spectra of **R** at room temperature

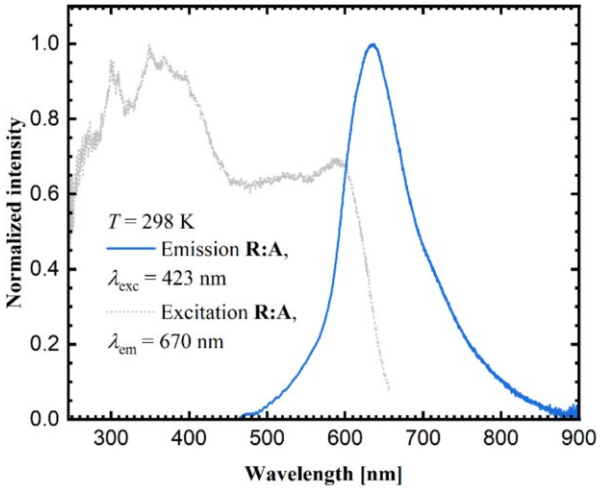

Figure S30: Normalized solid-state excitation and emission spectra of **R:A** at room temperature

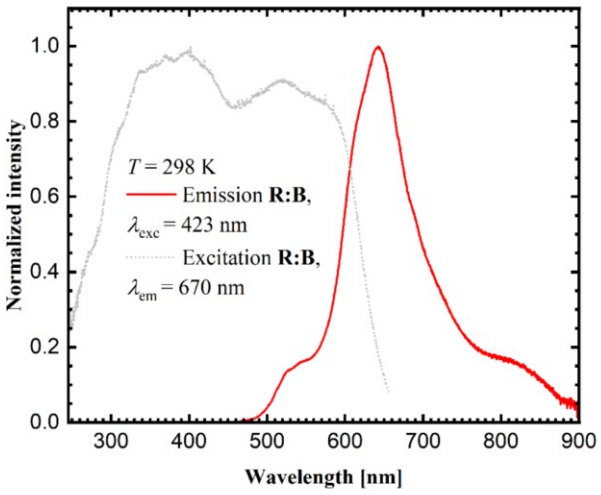

Figure S31: Normalized solid-state excitation and emission spectra of **R:B** at room temperature

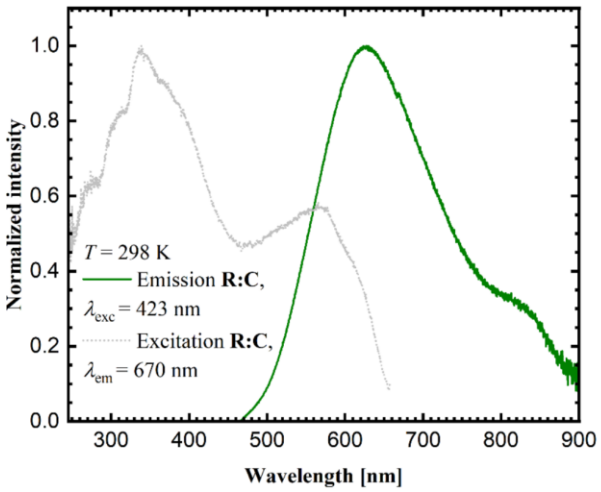

Figure S32: Normalized solid-state excitation and emission spectra of **R:C** at room temperature

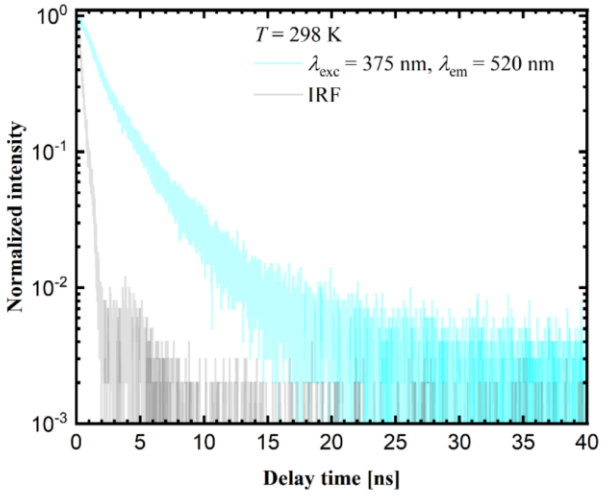

Figure S33: Normalized solid-state luminescence decay curves of **A** with instrument response function (IRF), acquired at room temperature

20

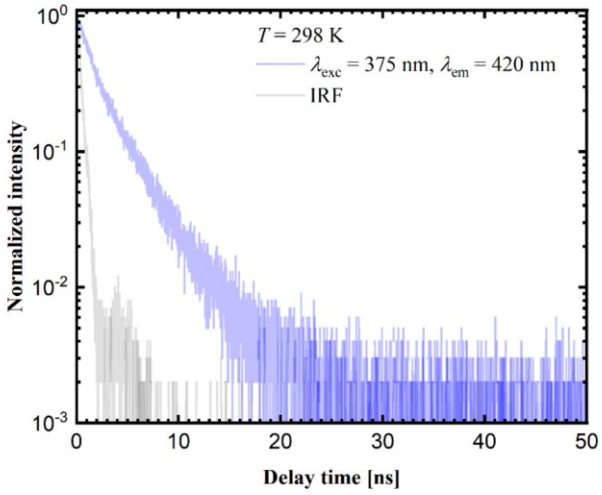

Figure S34: Normalized solid-state luminescence decay curves of **C** with instrument response function (IRF), acquired at room temperature

No luminescence decay curves for co-former **B** could be measured as the required excitation wavelength is below 375 nm and no pulsed EPL laser diode sources with UV wavelengths were available for respective time-resolved measurements at our institute.

7. References

1 N. Chen and J. Xu, HCOOH, an Inexpensive, Convenient, and Practical 13C NMR Solvent for Strong Polar Amino Acids and their Derivatives, *LOC*, 2009, **6**, 349–353.

2 S. A. Brown and C. J. Rizzo, A “One-Pot” Phase Transfer Alkylation/Hydrolysis of o -Nitrotrifluoroacetanilides. A Convenient Route to N -ALKYL o -Phenylenediamines, *Synthetic Communications*, 1996, **26**, 4065–4080.

3 S. Kasai, R. Miura and K. Matsui, Chemical Structure and Some Properties of Roseoflavin, *BCSJ*, 1975, **48**, 2877–2880.

4 V. Vasylyeva, S. K. Nayak, G. Terraneo, G. Cavallo, P. Metrangolo and G. Resnati, Orthogonal halogen and hydrogen bonds involving a peptide bond model, *CrystEngComm*, 2014, **16**, 8102–8105.

4.2. A Comparison Study of Roseolumiflavin Solvates: Structural and Energetic Perspective on Their Stability

Takin Haj Hassani Sohi, Felix Maaß, Constantin Czekelius, Vera Vasylyeva

DOI: 10.3390/cryst13101512

Crystals, **2023**, *13(10)*, 1512

In this study, a set of solvates and hydrates was reported and structurally characterized. Phase stability was investigated via lattice energy calculations and showed an energetic benefit for all the systems. Via *Crystal Explorer*, total interaction energy calculations were conducted and identified cofacial stacks to have significant impact on crystal lattice stability. QTAIM analysis evaluated single intermolecular interactions within the investigated fragments. The study further showed that thermal stability is tuned by solvent inclusion.

Contributions of the author:

- Conceptualization based on literature research together with Vera Vasylyeva.
- Experimental work, investigation and validation of results, including synthesis of powder samples and single crystals together with Felix Maaß. This includes consistent approaches to optimizing synthesis conditions during the project.
- Measurement of SCXRD and FTIR; measurement of PXRD together with Felix Maaß. Evaluation of the data and results.
- Evaluation of TGA measurements.
- Generation of *Gaussian* input files, calculations of lattice energies via *Quantum Espresso*, QTAIM and *Crystal Explorer* calculations. Evaluation of the results.
- Visualization of all figures, tables and data.
- Manuscript writing, literature research and preparation of supporting material.
- Review and editing of manuscript together with Vera Vasylyeva.
- Revision process together with Vera Vasylyeva.

crystals

MDPI

Article

A Comparison Study of Roseolumiflavin Solvates: Structural and Energetic Perspective on Their Stability

Takin Haj Hassani Sohi [1], Felix Maass [1], Constantin Czekelius [2] and Vera Vasylyeva [1,*]

[1] Laboratory for Molecular Crystal Engineering, Institute of Inorganic Chemistry and Structural Chemistry I, Heinrich-Heine-University Duesseldorf, Universitaetstr. 1, 40225 Duesseldorf, Germany
[2] Laboratory for Asymmetric Synthesis and Catalysis, Department of Organic Chemistry and Macromolecular Chemistry, Heinrich-Heine-University Duesseldorf, Universitaetstr. 1, 40225 Duesseldorf, Germany
* Correspondence: vera.vasylyeva-shor@hhu.de

Abstract: Roseolumiflavin is a deep red microcrystalline derivative of isoalloxazine that exhibits a weak photophysical activity in the solid state. In aqueous as well as in acidic solution of formic or acetic acid, respectively, it tends to form solvates. Herein, we present a set of binary and ternary roseolumiflavin solvates including one hydrate and a solvate hydrate. The impact of the solvent on solvate formation along with an in-depth structural analysis was investigated. Calculations of the lattice energies provide insight into the phase stability of the evaluated systems showing an energetic benefit for all solvates with values up to −395.82 kJ/mol. The total interaction energies between molecules calculated via Crystal Explorer further identified cofacial π···π stacks to be the most strongly bonding fragments in the crystal lattices for all systems except the formic acid solvate, followed by remarkably weaker hydrogen-bonded arrangements. The energetic contributions of single intermolecular interactions within the fragments are evaluated by an atoms-in-molecules approach. It is shown that physicochemical properties, such as thermal stability, can be tuned depending on the incorporated solvent molecules despite a high decomposition temperature of the chromophore.

Keywords: solvate formation; chromophore; phase stability; lattice energy; interaction energy; stacking; hydrogen bonds; thermal stability

check for updates

Citation: Haj Hassani Sohi, T.; Maass, F.; Czekelius, C.; Vasylyeva, V. A Comparison Study of Roseolumiflavin Solvates: Structural and Energetic Perspective on Their Stability. *Crystals* **2023**, *13*, 1512. https://doi.org/10.3390/cryst13101512

Academic Editors: Wenjin Li and Muhammad Junaid

Received: 29 September 2023
Revised: 13 October 2023
Accepted: 16 October 2023
Published: 18 October 2023

1. Introduction

8-(Dimethylamino)-7,10-dimethylbenzo[*g*]pteridine-2,4(3*H*,10*H*)-dione, also known as roseolumiflavin (**R**), is an organic chromophore emitting deep red-light which is derived from the class of flavin compounds. Prior research on **R** has shown its capability to co-crystalize with a set of miscellaneous coformers, providing either hydrogen-bonded or halogen-bonded interaction motifs, which led to altered photophysical properties [1]. These findings display the versatility of such compounds with regard to its propensity to build up novel structures. Therefore, different rational design strategies could be adopted on solid state organic chromophores to enhance their applicability in a wide range of fields [2,3]. The aforementioned crystal engineering approach can be stressed out even further when solvate systems are considered. Solvates are solid phases of a compound that form in the respective environment, typically in solution or by exposition to solvent vapor, where solvent components are incorporated into the crystal lattice by weak interactions [4,5]. If the solvent is water, these systems are referred to as hydrates. Just like their co-crystalline counterparts, these multicomponent systems can alter physicochemical properties of their respective host molecule as well such as melting point, solubility, mechanical properties, stability, or processability, amongst others [5,6]. Setting a clear cut between terminologies for crystalline phases has been a topic of discussion. Reminiscent of the scientific debate regarding the justification of the term pseudopolymorphism [7–10], for example, we may also point to a recent proposal of Grothe et al. in 2016 to employ a set of seven classifications

to differentiate between salts, co-crystals, and solvates to avoid ambiguity [11]. In the following, *solvates* and *hydrates* are merely used as a general term for a multicomponent system of **R** including either solvent molecules or, in the case of hydrates, water molecules. Knowledge about the occurrence and the circumstances resulting in solvate formation is of industrial importance, especially for pharmaceuticals and dyes, considering the effect that solvent inclusion solely based on intermolecular interactions can have on the compound properties in the crystalline state [4,12]. Granted, weak intermolecular interactions, the most prominent being the hydrogen bond, induce molecular recognition and provide stability for the crystalline state of organic compounds [13,14]. For example, the hydrate of the pharmaceutical drug phenibut, although thermodynamically not preferred, may form as a metastable intermediate in the transformation of phenibut and its salt phase, which is solely stabilized by weak intermolecular hydrogen bonds [15]. Likewise, in the case of the drug 5-fluorouracil, Heinen et al. faced challenges when producing solvent-free co-crystals due to the propensity of the corresponding hydrate to form highly stabilized hydrogen-bonded networks [16]. These examples show how solvates can compete with and hinder the desired outcome, e.g., co-crystal formation, generally in an unpredictable and uncontrolled manner. Indeed, solvates often appear as unwanted by-products during crystallizations or in synthesis processes. Thus, not much attention is paid to extensive investigations of the driving factors for the solvate formation. However, a combination of the solvates' crystal structure interpretation and topological analysis of the involved intermolecular interactions on the one hand, alongside the evaluation of energetic contributions for their formation on the other hand, can provide important information, which can help to improve the prediction and to gain control over the desired phase crystallisation. With this work, we aim to encourage researchers not to disregard investigations of solvate and hydrate solid-state systems, as this set of multicomponent crystals in many cases contains useful information to add to a better understanding of properties, favoured mechanisms, and structural characteristics of its underlying component.

Herein, we report the discovery and structural characterisation of two new binary and one ternary solvates of **R** (Scheme 1) along with its hydrate: roseolumiflavin:formic acid solvate (1:1, **R:HCOOH**), roseolumiflavin:acetic acid solvate (1:1, **R:AcOH**), roseolumiflavin:water:acetic acid solvate hydrate (1:1:1, **R:H_2O:AcOH**), and roseolumiflavin:trihydrate (1:3, **R:3H_2O**).

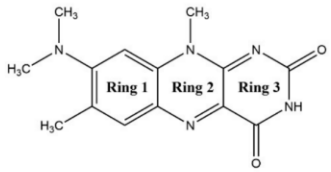

Scheme 1. Roseolumiflavin (**R**).

Intermolecular interactions present in the obtained crystal lattice of **R** and its multicomponent systems are further investigated in terms of their energetic impact on the phase formation, since this biologically relevant organic chromophore is still scarcely examined, especially on a molecular level. Besides our initial experimental article [1], to the best of our knowledge, only one publication exists investigating the photophysical activity of **R** in different virtual environments based on theoretical models [17]. In that regard, it is of importance to gain an in-depth understanding of the intricate interaction patterns in the crystal structures that ultimately construct the solid phases. Previous research indicated the strength of the hydrogen-bonded dimeric motif in the crystal structure of pure **R**, which has been a primary target of a co-crystallization strategy to functionalize [1]. This is also in agreement with prior publications of related flavin co-crystals [18–21], which determine hydrogen-bonded interactions to be the driving force for structural arrangement. Based on

the crystalline structure of **R**, we proceed to scrutinize the strongest interactions present in the crystalline phase via both the atoms-in-molecules (AIM) method implemented in the MultiWFN package [22] and the model interaction energies approach [23] provided by CrystalExplorer21 [24]. These results are compared to those of the herein reported crystal structures of the roseolumiflavin solvates to gain better insight in the crucial determining factors for the assembly of multicomponent systems of the flavin.

2. Materials and Methods

2.1. Synthesis

1:1 Roseolumiflavin:formic acid solvate (**R:HCOOH**): Red needles of **R:HCOOH** were obtained from a solution of 3 mg of **R** in 1 mL formic acid and slow evaporation of the solvent at ambient temperature. **R:HCOOH** could be reproduced confidently via a solvent evaporation method. Bragg reflections [°2θ]: 6.4, 10.32, 14.7, 25.12, 27.0; IR [cm^{-1}]: 3341, 3159, 3015, 2800, 1694, 1668, 1643; TGA [°C] (mass loss [%]): 119 (5), 371 (58).

1:1 Roseolumiflavin:acetic acid solvate (**R:AcOH**): Clear, red rectangular-shaped plates of **R:AcOH** were obtained from a solution of 3 mg of **R** in 2 mL acetic acid and slow evaporation of the solvent at ambient temperature. Reproduction of the structure was possible in arbitrary amounts of solvent via a solvent evaporation method. Bragg reflections [°2θ]: 6.44, 11.93, 14.4, 15.3; IR [cm^{-1}]: 3428, 3280, 3207, 3065, 3040, 2811, 1688, 1644; TGA [°C] (mass loss [%]): 103 (16), 353 (52).

1:3 Roseolumiflavin:trihydrate (**R:3H_2O**): Thin, light-red needles of **R:3H_2O** were obtained from dissolution of 1 mg of **R** in 1 mL water and slow evaporation of the solvent. The hydrate precipitates immediately after **R** comes into contact with the solvent at ambient temperature. **R:3H_2O** could be reproduced confidently via a solvent evaporation method. Bragg reflections [°2θ]: 7.26, 9.62, 10.94, 13.11, 15.97, 18.94, 30.22, 31.45, 33.36, 35.24, 41.42, 44.79; IR [cm^{-1}]: 3379, 3249, 3131, 3070, 2995, 2804, 1695, 1637; TGA [°C] (mass loss [%]): 48 (15), 288 (51).

1:1:1 Roseolumiflavin:water:acetic acid solvate hydrate (**R:H_2O:AcOH**): Red, block-shaped crystals of **R:H_2O:AcOH** were noticed as a side product in vessels of **R:AcOH** samples due to their distinct morphology and were picked for X-ray measurements. Numerous further attempts for a targeted reproduction of the structure under variation of conditions such as solvent amount, additives, and temperature have failed; incremental addition of water resulted in precipitation of the hydrate. Thus, besides the theoretical calculations based on the crystal structure obtained from single crystal X-ray measurements, no further experimental analyses could be carried out for this particular compound.

2.2. X-ray Measurements

A Rigaku Miniflex diffractometer (Rigaku, Tokyo, Japan) was used for powder X-ray diffraction (PXRD) measurements in θ/2θ geometry at ambient temperature (20 °C) using Cu-Kα radiation (λ = 1.54182 Å). Single-crystal X-ray diffraction (SCXRD) measurements were carried out on a Bruker APEX Duo diffractometer (Bruker, Billerica, MA, USA) with a CCD detector, micro-focus X-ray tube, and Mo-Kα radiation (λ = 0.71073 Å) at 140(2) K for R:AcOH, **R:3H_2O** and R:AcOH:H_2O and a Rigaku XtaLAB Synergy-S diffraction system (Rigaku, Tokyo, Japan) with a HiPyx 6000 photon detector, and micro-focus X-ray tube with Cu-Kα radiation (λ = 1.54182 Å) measured at 100(2) K for **R:HCOOH**. Cell refinement, data collection, and data reduction on the Rigaku Synergy-S system were performed with CrysAlisPro [25]. On the Bruker APEX Duo, data collection and cell refinement were achieved with APEX2 [26] and data reduction was performed via SAINT [27]. Structure solution was conducted by SHELXT 2014/5 [28] for R:AcOH, **R:3H_2O,** and R:AcOH:H_2O and SHELXT 2018/2 [28] for R:HCOOH. R:AcOH:H_2O was refined with SHELXL-2014/7 [28], R:AcOH and **R:3H_2O** were refined with SHELXL-2017/1 [29] and **R:HCOOH** was refined with SHELXL-2018/3 [29]. **R:HCOOH** was refined with the Olex2 software package (OlexSys Ltd., Durham, England, v.1.5) [30]. All non-hydrogen atoms were refined with anisotropic displacement parameters. All hydrogen atoms were ex-

perimentally refined. All structures are deposited in the CCDC with following numbers: 2294770-2294773.

2.3. Thermogravimetric Analysis (TGA)

TGA measurements were performed on a Netzsch TG 209 (NETZSCH, Selb, Germany) in the range between 30 °C and 600 °C with a 10 °C min^{-1} heating rate under a nitrogen atmosphere. In total, 5 mg of each compound was analysed.

2.4. FTIR Measurements

The FTIR spectra were recorded on a Bruker Tensor 37 (Bruker, Billerica, MA, USA) with an ATR-unit at ambient temperature (25 °C) in the range between 4000 cm^{-1} and 400 cm^{-1}.

2.5. Chemicals

Roseolumiflavin was synthesized as reported previously [1]. Formic acid (≥98%) and acetic acid (≥99.8%) were purchased from Sigma-Aldrich (Sigma-Aldrich, St. Louis, MO, USA) and used without further purification. Deionized water was used for the hydrate crystallisation.

2.6. Software

The software package MultiWFN [22] was used for AIM calculations based on .wfn files of molecular geometries based on crystal structure data. The .wfn files were generated by a density function theory (DFT) method using Gaussian16 [31] at a B3LYP/6-31G** level of theory for comparability with calculated model interaction energies [23] derived from CrystalExplorer21 [24], which are parametrized for the same combination of functional and basis set. Quantum Espresso (QE) PWSCF (Quantum ESPRESSO Foundation, Cambridge, UK, v. 6.6) was utilized for calculations of lattice energies with the atomic pseudopotentials originating from the QE pslibrary, following the approach described by Komisarek et al. in 2022 [32], with the exception that initial geometry optimization was done via the "relax" command. Hydrogen bond interaction energies based on bond critical points were predicted via the model proposed by Emamian et al. in 2019 [33]. Mercury 2022.3.0 [34] was used for structural figure preparation, and verbose crystal structure information was derived from PLATON for Windows Taskbar (A.L.Spek, Utrecht University, Utrecht, The Netherlands, Version 1.19) calculations [35].

3. Results

3.1. Single Crystal X-ray Diffraction (SCXRD)

Four new solvate structures, including a hydrate, were yielded from single crystal X-ray measurements. In the following section, a structural analysis of each structure is provided. Table 1 displays the overview of the important crystallographic data for **R:HCOOH**, **R:AcOH**, **R:3H$_2$O**, and **R:AcOH:H$_2$O**. In all the presented structures, no (de)protonation is observed, verified additionally by IR-analysis (see Figure S1 in ESI).

The formic acid solvate **R:HCOOH** (1:1) crystallizes in the monoclinic space group $P2_1$. The asymmetric unit contains two units of each molecule (Z = 4, Z′ = 2). Each **R** molecule is connected to an adjacent formic acid molecule via hydrogen-bonded (HB) interactions (graph set notation *D* [36] O3-H3···O1: 2.577(5) Å and O7-H7A···O5: 2.598(6) Å). Amide-amide homodimeric interactions ($R_2^2(8)$, N2-H2···O6: 2.828(6) Å and N7-H7···O2: 2.768(6) Å) between the imide groups of each two neighbouring **R** units propagate along the crystallographic b-axis, constructing tetrameric motifs of two **R** and two acid molecules, see Figure 1a. The same amide-amide dimer is present in the single-component **R** structure, as described previously [1]. Along the c-axis, these tetrameric motifs organize themselves in a herringbone arrangement mode. The **R** molecules are further arranged along the a-axis in a cofacial π···π stacking orientation ($centroid_{out}$···$centroid_{out}$: 3.796(3) Å, $centroid_{middle}$···$centroid_{middle}$: 3.796(3) Å) parallel towards each other, see Figure 1b.

Table 1. Crystallographic data of **R:HCOOH**, **R:AcOH**, **R:3H$_2$O** and **R:AcOH:H$_2$O**.

Name	R:HCOOH	R:AcOH	R:3H$_2$O	R:AcOH:H$_2$O
Empirical formula	$C_{14}H_{15}N_5O_2$, CO_2H_2	$C_{14}H_{15}N_5O_2$, $C_2H_4O_2$	$C_{14}H_{15}N_5O_2$, 3(H_2O)	$C_{14}H_{15}N_5O_2$, $C_2H_4O_2$, H_2O
Molecular weight [g/mol]	331.33	345.36	339.36	363.38
Temperature [K]	100(10)	140(2)	140(2)	140(2)
Space group	$P2_1$	$P\bar{1}$	$P\bar{1}$	$P2_1/c$
Crystal system	monoclinic	triclinic	triclinic	monoclinic
a [Å]	3.79570(10)	7.8393(7)	6.852(6)	7.1439(9)
b [Å]	20.0858(5)	8.2797(7)	9.281(8)	15.574(2)
c [Å]	18.9737(6)	14.0559(12)	12.685(11)	15.2510(19)
α [°]	90	73.647(5)	79.26(3)	90
β [°]	93.755(3)	77.917(5)	74.75(3)	1689.5(4)
γ [°]	90	67.478(5)	87.10(3)	90
Volume [Å^3]	1443.44(7)	803.34(13)	764.6(11)	1689.5(4)
Z/Z′	4/2	2/1	2/1	4/1
ρ_{calc} [g/cm^3]	1.525	1.428	1.474	1.429
μ [1/mm]	0.953	0.106	0.114	0.108
T_{min}/T_{max}	0.698/1.000	0.959/0.993	0.945/0.989	0.979/0.996
F(000)	696	364	360	768
Crystal size [mm^3]	0.01 × 0.02 × 0.18	0.07 × 0.08 × 0.40	0.10 × 0.10 × 0.50	0.04 × 0.10 × 0.20
θ range[°]	3.1690/76.7990	1.520/26.000	1.691/24.996	1.873/25.990
Completeness [%]	99.0	99.2	99.4	99.8
Recorded reflections	4600	9851	10180	12686
Independent reflections	4165	3139	2667	3310
Goodness-of-fit F^2	1.057	1.047	1.026	1.037
X-ray source	CuKα (λ = 1.54184 Å)	MoKα (λ = 0.71073 Å)	MoKα (λ = 0.71073 Å)	MoKα (λ = 0.71073 Å)
R_1/wR_2	0.0527/0.1474	0.0534/0.1584	0.0796/0.2499	0.0432/0.1205

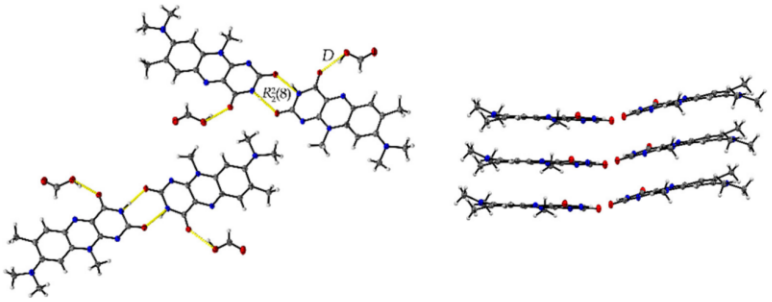

(**a**) (**b**)

Figure 1. (**a**) Herringbone arrangement of tetrameric substructures along the c-axis in **R:HCOOH**. View along the a-axis. (**b**) Propagation of π···π interacting flavin stacks along the a-axis. View along the c-axis.

The **R:AcOH** (1:1) solvates crystallize in the triclinic $P\bar{1}$ space group with one acetic acid molecule and one **R** molecule in an asymmetric unit cell (Z = 2, Z′ = 1). Along the crystallographic a-axis, two **R** molecules align via strong inversely oriented cofacial π···π stacks ($centroid_{out}$···$centroid_{out}$: 3.5008(14) Å, $centroid_{middle}$···$centroid_{middle}$: 3.4567(13) Å). The stacks build up brick layer structures in the crystal packing connected by offset π···π interactions (C2···C10 3.323(4) Å, see Figure 2b).

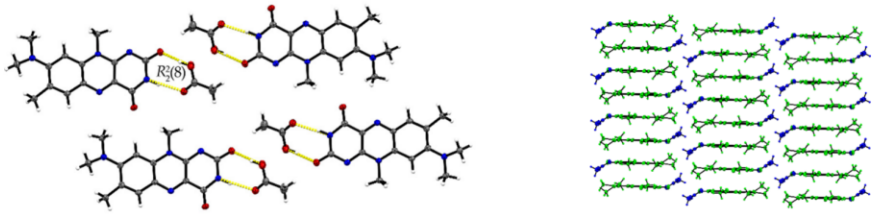

(**a**) (**b**)

Figure 2. (**a**) Hydrogen-bonded acid-amide dimers of **R** and acetic acid in **R:AcOH**. View along the crystallographic b-axis. (**b**) Stacking motifs formed along the a-axis. Coloured by symmetry equivalent entities (**R**: green, acetic acid: blue). View perpendicular to bc-plane.

Opposite to the **R** and **R:HCOOH** structures, the amide-amide homodimers in **R:AcOH** are replaced by an acid-amide heterodimeric motif. An acetic acid molecule interacts with the flavin's imide group ($R_2^2(8)$, O3–H···O2: 2.596(2) Å, N2–H···O3: 2.879(2) Å). Adjacent acetic acid molecules support the dimeric synthons via short C16–H···O2 contacts (3.420(3) Å) to give tetrameric units. Further, tetramers are connected via multiple **R** molecules stabilizing the pattern by C–H···O interactions of average 3.2–3.5 Å, in particular facilitated by the convenient orientation of the **R** methyl substituents to form narrow hydrogen-bonded layers along the ab-plane (Figure 2a).

Single crystals of **R:3H$_2$O** (1:3) are of a remarkably thin, fine needle-like shape in bright red colour, which tend to agglomerate immediately. The needles are sized between 0.01 mm and 0.05 mm in width and up to 0.5 mm in length. The resolved structure belongs to the triclinic $P\overline{1}$ space group with one **R** and three water molecules in an asymmetric unit cell ($Z = 2$, $Z' = 1$). **R** molecules align via π···π interactions along the crystallographic a-axis and construct slip-stacked interaction geometries ($centroid_{out}$···$centroid_{out}$: 3.678(4) Å and 3.597(4) Å, $centroid_{middle}$···$centroid_{middle}$: 3.697(4) Å and 3.678(4) Å). These stacking motifs are separated along the c-axis by water molecules that replace the typical amide-amide synthon and instead provide several O–H···O and N–H···O interactions between the flavin stacks (N2–H···O5: 2.774(5) Å, N3–H···O4: 2.981(5) Å, O1–H···O5: 2.752(4) Å, O1–H···O4: 2.759(4) Å) as well as O–H···O interactions to neighbouring water molecules (O3–H5···O4: 2.833(5) Å, O3–H4···O4: 2.887(4) Å, O3–H···O5: 2.805(5) Å). This results in a much more complex crystal architecture when compared to all other reported structures, which consist of alternating **R** stacks and hydrogen-bonded sequences of water molecules (Figure 3b), propagating along the b-axis. Among the complexity of the present HB interactions, we can identify three main ring-motives, each built up by four molecules. Hereby, two similar tetrameric subsequences of the type $[R_4^4(12)]$, constructed of two **R** and two water molecules each, form a zig-zag chain $C_4^3(10)[[R_4^4(12)]_{O5}, [R_4^4(12)]_{O4}]$ (Figure 3a). The third ring system $[R_4^4(10)]_{O3}$ encloses one **R** and three water molecules which allows a connection to the next stacked layer. The short contacts between neighbouring **R** molecules provided by the C11-methyl side chain and the amide group (C11–H···O2: 2.66 Å) allow for the expansion of the flavins along the b-axis.

The ternary **R:AcOH:H$_2$O** (1:1:1) solvate hydrate crystallizes in the monoclinic $P2_1/c$ space group and the red block-shaped crystals appear in sizes between 0.04 mm to 0.20 mm. One molecule of each individual component is found in the asymmetric unit ($Z = 4$, $Z' = 1$). Remarkably, similar to **R:AcOH**, an amide-amide dimeric motif typical for flavins is replaced by a supramolecular acid-amide synthon (Figure 4). However, not only does one acetic acid molecule serve as a substitute but is supported by a water molecule to give strongly bound trimeric motifs with donor-acceptor distances O5–H···O4 (2.7077(18) Å) and N3–H···O2 (2.952(2) Å). Such an arrangement enables tilted **R** stacks at 34.93° angle along the b-axis due to the flexible positioning of the small solvate molecules. The slip-stacked π···π connections ($centroid_{out}$···$centroid_{out}$: 3.5732(10) Å, $centroid_{middle}$···$centroid_{middle}$:

3.5545(9) Å) are formed with one flavin molecule oriented inversely to the other one along the a-axis. Each isolated, nearly cofacial stack is alternating with a neighbouring offset stack (C2···N4: 3.429(2) Å and C7···N2: 3.4108(19) Å). The tilted stacks are stabilized by hydrogen-bonded zig-zag chains built up of trimers along the b-axis (graph set notation $C_1^1(8)R_3^3(10)$). Those are mainly induced by water molecules serving as a mediator between the carbonyl groups of two flavin molecules (O5–H···O3: 2.8608(17) Å) and one acetic acid component, itself stabilized by the O1–H···O5 (2.5483(19) Å) interaction.

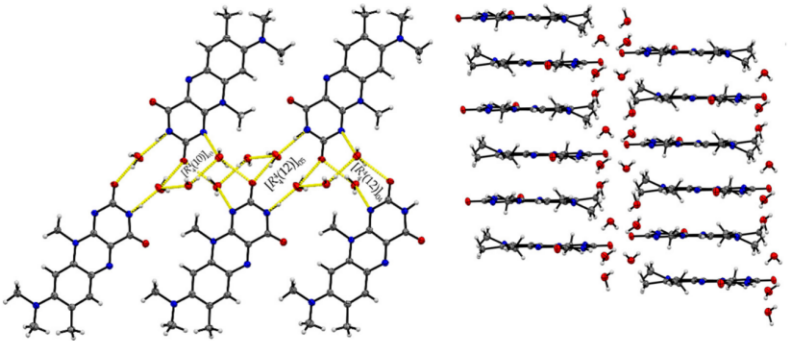

(**a**) (**b**)

Figure 3. (**a**) The imide group in **R:3H$_2$O** interacts with water molecules giving different tetrameric ring motifs; those build up hydrogen-bonded chains (C_4^3 (10)[[R_4^4(12)]$_{O5}$, [R_4^4(12)]$_{O4}$]) along the crystallographic b-axis. View along the a-axis. (**b**) **R** stacks are connected via complex O–H···O interaction patterns involving water entities.

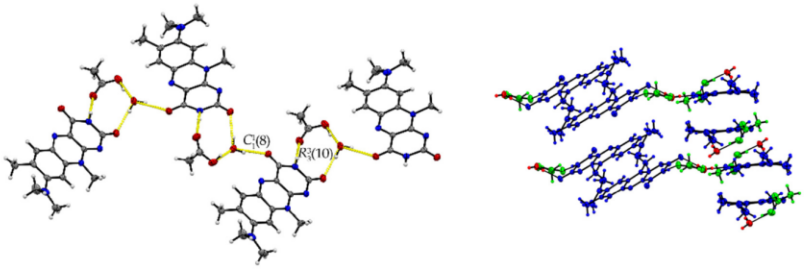

(**a**) (**b**)

Figure 4. (**a**) Hydrogen-bonded chains between solvate O–H groups and **R** amide groups connect trimeric motifs along the b-axis in **R:AcOH:H$_2$O**. View along the a-axis. (**b**) Quasi-cofacial π···π stacks connected by offset stacking interaction alternate along the a-axis. View along the c-axis. Coloured by symmetry inequivalence for clarity (**R**: blue, acetic acid: green, water: red).

3.2. Powder X-ray Diffraction (PXRD)

The synthesized solvates were characterized via powder diffraction pattern analysis. In comparison to pure **R**, clearly distinct new diffraction patterns can be observed, verifying the synthesis of new phases (Figure 5). Experimental powder patterns are reproducible in agreement with the simulated patterns obtained from SCXRD data (see Figures S2–S4 in ESI), which confirms the overall phase purity for **R:3H$_2$O**, **R:HCOOH**, and **R:AcOH**. Hereby, **R:AcOH** shows a strong preferred orientation of the (0 0 1)-plane in the experimental powder pattern. The simulated PXRD was therefore adapted with a March–Dollase factor of 0.6 for a better comparison (Figure S2 in ESI).

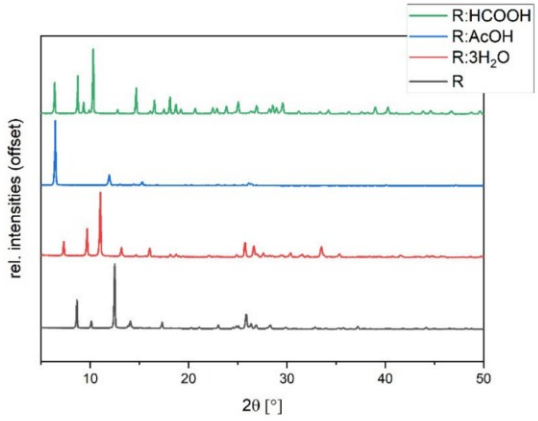

Figure 5. Experimental powder diffraction patterns of **R:AcOH**, **R:3H$_2$O**, **R:HCOOH** in comparison to **R**.

3.3. Thermogravimetric Analysis (TGA)

Thermal stability studies were conducted by thermogravimetric analysis of each compound, including **R**. Pure **R** decomposes in one step at T_R of 350 °C (Figure 6). The thermogram of **R:AcOH** features two mass losses. The first one, with an onset of 103 °C and a mass loss of 16%, is apparently due to the solvent release from the crystal lattice. This equates to 0.93 moles of solvent molecules. The second one at 353 °C is indistinctively attributed to the decomposition point of **R** with a mass loss of 52%. **R:3H$_2$O** also degrades in two steps. The first with an onset at 48 °C indicates an early evaporation of water, causing 15% of a mass decrease (2.82 moles of water molecules). The second step at 288 °C (mass loss of 51%) shows a remarkably strong shift in decomposition temperature of **R** to lower temperatures.

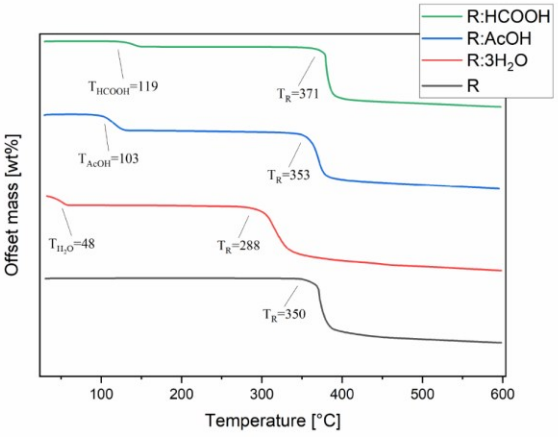

Figure 6. Thermogravimetric analyses of **R**, **R:AcOH**, **R:3H$_2$O** and **R:HCOOH** taken from 30 to 600 °C, under nitrogen atmosphere at 10 K/min heating rate. Extrapolated onset decomposition temperatures are given.

For **R:HCOOH**, the first step at 119 °C with a mass loss of 5% indicates the release of the formic acid. This corresponds to only 0.35 mole of the solvent, which is probably caused by a partial loss of solvent molecules from the crystal lattice prior to the TG analysis during the sample storage. The second step, again representing the start of decomposition of the chromophore, is set at 371 °C with a mass loss of 58%, reaching a significantly higher decomposition point of the chromophore.

3.4. Computational Studies

An evaluation of the phase stability of the new structures is investigated by comparison of lattice energies and topology analyses via the atoms-in-molecules (AIM) approach, as well as intermolecular interaction energies. Based on the method described and validated by Komisarek et al. [32], lattice energies (E_{lat}) for each solvate structure and **R** are calculated. The results demonstrate that the formation of all reported solvate structures is driven by a considerable gain in energy when compared to pure **R** with its E_{lat} of −181.08 kJ/mol (Table 2) This explains why the formation of the solvate phases is preferred in the respective solvent environment. Hereby, **R:HCOOH** shows just a slight energetic benefit with −197.58 kJ/mol. A noteworthy observation is the relative positioning of energies for **R:AcOH:H_2O** with E_{lat} of −352.46 kJ/mol, which is set between both **R:AcOH** and **R:3H_2O**, showing lattice energies of −283.55 kJ/mol and −395.82 kJ/mol, respectively. Since in all our attempts to systematically reproduce said system, the hydrate formation was favoured, these findings indicate that the ternary system is an intermediate product when both solvents are present, thus a targeted crystallization of that intermediary stage is challenging. The formation of **R:3H_2O** is the most beneficial, which goes along with our experimental observation of its immediate precipitation once **R** is treated with water.

Table 2. Overview of the calculated lattice energies (E_{lat}), strongest pairwise interaction energies (E_{tot}) of a central flavin molecule in a 3.8 Å cluster, and estimated binding energies (BE) for HB interactions for **R**, **R:HCOOH, R:AcOH**, **R:AcOH:H_2O**, and **R:3H_2O**.

Structure	Quantum Espresso	Crystal Explorer	AIM	Intermolecular Interaction
	E_{lat} [kJ/mol]	E_{tot} [kJ/mol]	$BE_{estimated}$ [kJ/mol]	
R	−181.06	−113.4	-	cofacial π···π stack
		−127.1	-	cofacial π···π stack
		−43.4	−19.34	N2-H···O2
			−19.34	N2-H···O2
			−5.56	C11-H···O1
		−36.5	−5.11	C13-H···O1
			−2.32	C13-H···N1
			−2.09	C6-H···O1
R:HCOOH	−197.58	−58.5	−31.15	O3-H···O1
			−27.75	O7-H···O5
		−41.6	−25.88	O6···H-N2
			−22.88	N7-H···O2
		−36.5	-	cofacial π···π stack
		−33.2	−8.95	C28-H···O6
			−4.88	C13-H···O5
R:AcOH	−283.55	−110.0	-	cofacial π···π stack
		−70.5	-	offset π···π stack
		−64.9	-	offset π···π stack
		−62.0	−35.95	O2···H-O3
			−21.02	N2-H···O4

Table 2. *Cont.*

Structure	Quantum Espresso	Crystal Explorer	AIM	Intermolecular Interaction
	E_{lat} [kJ/mol]	E_{tot} [kJ/mol]	$BE_{estimated}$ [kJ/mol]	
R:AcOH:H_2O	−352.46	−116.3	-	cofacial π···π stack
		−70.5	-	offset π···π stack
		−34.8	−23.38	O4···H-O5
		−30.8	−3.57	O3···H-C1
R:3H_2O	−395.82	−110.7	-	cofacial π···π stack
		−104.6	-	cofacial π···π stack
		−32.6	−0.92	C6-H···O2
			−2.69	C11-H···O2
		−32.4	−2.60	C13-H···O2
			−18.35	O1···H-O4
		−26.5	−22.94	O1···H-O5
		−25.1	−30.11	N2-H···O5
		−18.0	−10.68	N3···H-O4

To gather a profound understanding of the driving forces that lead to the formation of the respective crystal lattice, the specific molecular surroundings of the chromophore weres investigated for each structure. For this, we utilized the model interaction energies method implemented in CrystalExplorer21 [23]. Here, a 3.8 Å cluster of molecules encompassing one flavin molecule is generated, approximating the first interaction environment of the selected central molecule. The energy of interaction acting upon the central flavin molecule with each of the neighbour molecules within the cluster is calculated via a DFT approach at a B3LYP/6-31G** level of theory. For each two interacting molecules, the total interaction energy E_{tot}, which encloses the sum of electrostatic (E_{ele}), polarization (E_{pol}), dispersion (E_{dis}), and exchange-repulsion (E_{rep}) energies, each multiplied with respective scaling factors, is calculated and can be quantified. This approach provided us a first overall understanding of the most strongly bonded molecular fragments in each crystalline phase, which dominate and drive their architectures. The highest impact within the total interaction energy between the molecules is provided by the intermolecular interactions involved. Following this, we approximate the strongest contributors. For each structure, the four highest calculated total energies of molecular interaction are given in Table 2, along with the assigned contributing intermolecular interactions. A complete table is provided in the ESI (Table S5). For **R:3H_2O**, additional interactions are given, generally of a weaker total energy but of a high binding energy, which will be discussed further.

Evaluation of the pairwise interactions for **R** via CrystalExplorer shows the highest values being supplied by units that provide π···π stacks as well as the aforementioned amide-amide hydrogen-bonded dimer between two flavins. Noteworthy, a flavin moiety adjacent to the dimethylamine residue provides some strong molecular interaction energies in close energetic range as well, which can be found in nearly all structures except **R:HCOOH**, with E_{tot} values around −30 kJ/mol. The highest contribution in **R:AcOH, R:AcOH:H_2O**, and **R:3H_2O** again is given by cofacial π···π stacked units with total interaction energies around −110 kJ/mol. Still, cofacially stacked flavin moieties provide the highest total molecular energetic gain in **R** with up to −127.1 kJ/mol. The contribution energies drop down to −64 kJ/mol the more the stacks are offset in the arrangements present in **R:AcOH, R:AcOH:H_2O**. Solely in **R:AcOH**, a pairwise interaction of a solvate molecule and the flavin's imide group, which corresponds to HB (−62.0 kJ/mol), provides an energetic benefit at a similar range compared to the stacks. Otherwise, all hydrogen-bonded fragments corresponding to amide-amide, acid-amide dimers, or interactions with water molecules in **R**, **R:AcOH, R:AcOH:H_2O**, and **R:3H_2O** exhibit highest E_{tot} values between −30 to −43 kJ/mol, being clearly outnumbered by the π···π stacking. The **R:HCOOH**

structure stands out of all investigated systems with an absolute value of the π···π interactions contributing fragment being significantly lower than in the other structures. Here, the strongest total energy is directly induced by the formic acid unit, which interacts via hydrogen bonds with the flavin.

Finally, based on these initial observations and results, an AIM analysis [37] shall elucidate whether bond critical points (BCPs), in line with the underlying theoretical concept, do exist along the respective pathways, aiding in the identification of the respective interactions. Additionally, by applying a fitted equation provided by Emamian et al. [33] we estimate the binding energies (BE) of the located HBs. In this way, an energetic contribution of the single intermolecular bond can be verified. To the best of our knowledge, no equation for the estimation of π···π interactions is available yet. The AIM analysis confirms bond critical points with stabilizing interaction energies located between the dimeric units of two **R** molecules in the pure flavin structure. The estimated binding energies are summarized in Table 2. These interactions can be identified as moderately strong hydrogen bonds at −19.3 kJ/mol, particularly in relative comparison to the further identified hydrogen-bonding interactions between the dimethylamine residue and the imide group of two adjacent **R** moieties, ranging between −2.3 and −5.1 kJ/mol. The structural positioning of the units allows further C6-H···O1 and C11-H···O1 HBs with similar energetic gain. Comparable stabilizing interactions are observed in **R:AcOH**, with binding energies ranging between −2.4 and −4.2 kJ/mol, which is slightly lower than those in **R**. In **R:AcOH**, the dimeric flavin unit is replaced by hydrogen-bonded motifs with the acid unit. In absolute values, the binding energies are significantly stronger when compared to the hydrogen bonds provided in the amide-amide synthon in the **R** crystal lattice. In **R:AcOH:H_2O**, moderately strong interaction motifs are provided not only by the water molecules but the acetic acid unit as well. The water molecules interact with the imide group over O4···H-O5 (−23.4 kJ/mol) and O3···H-O5 (15.4 kJ/mol) HBs. The acetic acid units provide stabilizing HB via N3-H···O2 at 14.7 kJ/mol and even weak interactions with the solvate methyl group via O3···H-C1 at −3.6 kJ/mol. In **R:3H_2O**, the dimeric motif has also been replaced by water molecules. Comparing the binding energies, we observe interactions around 1.5 times higher than the amide-amide synthon in pure **R**. The strongest interaction is observed between O5···H-N2 at −30.1 kJ/mol, followed by an adjacent water molecule interacting with the carbonyl group via O1···H-O5 with an energetic benefit of −22.94 kJ/mol and further stabilizing interactions with energetic values around −10 kJ/mol. On the other hand, the aforementioned methyl group HB interactions to neighbouring flavin units are weaker ranging from −0.92 to −2.69 kJ/mol. Lastly, in **R:HCOOH** we identified strong HBs between acid units and the flavin with −31.15 (O3-H···O1) and −27.75 kJ/mol (O7-H···O5), while the dimeric hydrogen-bonded flavin units also contribute to the stability with −25.88 and −22.88 kJ/mol, respectively. Moreover, according to our AIM analyses, the structural peculiarity of tilted adjacent flavin molecules with their dimethylamine residue directed towards the nearby carbonyl group provide even further stabilizing effects with −8.95 kJ/mol between C28-H···O6 and −4.88 kJ/mol between C13-H···O5.

4. Discussion

Our findings display the versatility of **R** with respect to solvation, evident not only in the formation of various compounds but also in their altered crystal structure. While an amide-amide synthon between two flavin molecules is present in both **R** and **R:HCOOH**, in the other solvates the solvent molecules replace these hydrogen-bonded interactions with additional stabilizing benefits in their respective crystal lattices. The estimated HBs in total outweigh the already moderate to strong hydrogen bonded amide-amide motif. Considering identified π···π interactions, what stands out is the strength of the fragment contributions being significantly higher in comparison to the HBs, at around −100 to −120 kJ/mol in cofacial systems and around −65 to −70 kJ/mol when offset. The strongest molecular contribution by cofacial stacks is present in the pure **R** structure followed by

R:AcOH:H_2O, **R:AcOH**, and **R:3H_2O**. Noteworthy, the **R:HCOOH** stacks merely provide energetic benefits at −36.6 kJ/mol, which are around one-third of the observed values in the other structures. Comparing the π···π distances with those of pure **R**, we find overall slightly shorter distances between the flavin units in **R:AcOH** and **R:AcOH:H_2O**, similar range distances in **R:3H_2O**, and longest distances in **R:HCOOH**. See Table 3 for the respective values.

Table 3. π···π Distances measured for **R**, **R:AcOH**, **R:3H_2O**, **R:AcOH:H2O** and **R:HCOOH**.

Structure	π···π	π···π [Å]
R	Ring 2–Ring 3 [i]	3.576(4) and 3.6280(13)
R:AcOH	Ring 2–Ring 2 [i] Ring 1–Ring 3 [i]	3.4567(13) 3.5008(14)
R:3H_2O	Ring 2–Ring 2 [ii] Ring 1–Ring 3 [ii]	3.697(4) and 3.678(4) 3.678(4) and 3.597(4)
R:AcOH:H_2O	Ring 2–Ring 2 [iii] Ring 1–Ring 3 [iii]	3.5545(9) 3.5732(10)
R:HCOOH	Ring 1–Ring 1 [iv] Ring 2–Ring 2 [iv] Ring 3–Ring 3 [iv]	3.796(3)

[i] $1-x, 1-y, 1-z$; [ii] $-x, 1-y, -z$; [iii] $-x, 1-y, 1-z$; [iv] $-1+x, y, z$ and $1+x, y, z$.

In the case of **R:HCOOH**, the solvate molecules add to the stability of the dimeric unit by the formation of HB alongside the imide group. Further, graph set notation analyses show that the presence of water molecules results in the formation of hydrogen-bonded chains in both **R:3H_2O** and **R:AcOH:H_2O**, whereas the two other solvates are limited to finite interactions. These added benefits are represented in the calculated lattice energies as well, considering calculated E_{lat} decreases along the row **R** > **R:HCOOH** > **R:AcOH** > **R:AcOH:H_2O** > **R:3H_2O**. This results in the most stable lattice for the **R** trihydrate. The ring distances, however, do not vary by large values; the longest and shortest absolute centroid-centroid distances observed in **R:HCOOH** and **R:3H_2O**, respectively, merely differ by ca. 0.2 Å in comparison to **R**. Assuming the intermolecular interactions to be of significance, this suggests the aforementioned HBs to be the primary determining factor for the lattice energy alteration. The high energetic benefit of the hydrate further confirms the experimental observations, where the slightest presence of water in solvate samples resulted in an exclusively preferred formation of the hydrate. This is due to the contribution of two strong HB between water and flavin molecules. Furthermore, graph set notation analyses display the complexity of the hydrogen-bonded motifs building up HB chains that enclose two hydrogen-bonded rings and further ring-motifs involving water molecules, which contribute to the close interaction of the flavin layers in the crystal structure. Here, AIM calculations show binding energies of up to −30 kJ/mol, being considerably predominant compared to HBs of −19.34 kJ/mol in pure **R**. The second lowest lattice energy is attributed to the ternary **R:AcOH:H_2O** system, which in absolute values is to be set between **R:AcOH** and **R:3H_2O**. Again, this is in agreement with our experimental observations and could offer an explanation for the failed attempts to reproduce the structure. Since the energetic benefit from **R:3H_2O** is significantly higher than in **R:AcOH**, the hydrate formation is thermodynamically preferred. Nonetheless, the ternary system can be an intermediary product in a reorganization process from a first step acetic acid solvate formation towards the building of the hydrate. As a result, the intermediary product is then accessible in randomized occasions, but solely as a side product.

On the other hand, from TG analyses we observed a strongly shifted decomposition point of the chromophore towards lower temperatures in the hydrate at 288 °C when compared to that of **R** at 350 °C. While **R:AcOH** is not significantly altered at this point, **R:HCOOH** shows a significantly higher decomposition temperature for the **R** component at

371 °C. The thermal stability of **R** in the solvate systems with T_R(**R:HCOOH**) > T_R(**R:AcOH**) > T_R(**R:3H$_2$O**) nearly counterpose order derived from E_{lat}. We suggest that the structural alteration in the hydrate may be of such significance that an optimized reorganization of the flavin molecules after solvent vaporization is hindered, resulting in earlier decomposition. In addition, the strongest hydrogen bonds formed between water and flavin molecules are at once missing after the water release. On the other hand, the chromophore may rearrange to an even more stable arrangement when the formic acid components evaporate, resulting in a later decomposition point. This might be due to the initial arrangement of stacked flavin units in the **R:HCOOH** crystal lattice differing significantly from those of the other compounds. From the one side, **R:HCOOH** is the only solvate structure in which the **R**-**R** amide-amide dimer remained intact, and, on the other side, the only one where flavin molecules are not inversely stacked. While this could be the cause of the higher calculated E_{tot} due to a positive electrostatic component (see Table S5 in ESI for the detailed information of the components of E_{tot}), the molecular rearrangement after the thermal activation may cause altered agglomeration of flavin stacks.

5. Conclusions

Within the scope of crystal engineering, challenges arise when solvate systems are considered. Often solvates and hydrates are an unwanted by-product in the experimental setting, yet these multicomponent systems can provide valuable insight into the investigated compounds. Here, we took a deeper look into the structural and energetic environment of three solvates as well as one hydrate of roseolumiflavin. These compounds display interesting features when compared to the flavin, not only from the crystallographic perspective, but based on observations on thermal properties as well. Previous research assumed that the hydrogen-bonded dimeric motif between two adjacent flavin units in roseolumiflavin provides significant benefits in terms of stability, next to the $\pi\cdots\pi$ stacking interactions. While the latter is present in all solvate systems, the former is replaced by hydrogen-bonded motifs with the respective solvent molecules in all but the **R:HCOOH** structure. Energetic calculations of pairwise molecular interactions underline the strength of cofacial $\pi\cdots\pi$ stacking, followed by the offset stacks. Hence, stacking interactions remain the most important driving force in the formation of **R** and its solvate structures. HBs are energetically considerably outnumbered in average by -40 to -70 kJ/mol. However, confirmed by AIM calculations, high binding energies of single hydrogen bonds in combination with the large overall number of such interactions seem to be able to promote the formation of new phases. The significance of energetic benefits is also evident in the calculated lattice energies. While **R:HCOOH** provides a more stable lattice by only ca. -16 kJ/mol when compared to **R**, the lattice energy of **R:3H$_2$O** is more than twice as low as the pure flavin. And yet, the experimental observations show that from a thermal behaviour aspect, the hydrate leads to significantly earlier decomposition of the chromophore, while the presence of the formic acid component delays the decomposition of **R** by around 20 °C. To conclude, calculations on the theoretical level based on single crystal structures along with the careful examination of the interaction modes can provide valuable inputs into the crystal architecture and allows a detailed description of its topologies. A reliable prediction of tuneable physicochemical properties, however, remains challenging not least due to the complexity and versatility of roseolumiflavin systems.

Supplementary Materials: The following supporting information can be downloaded at: https://www.mdpi.com/article/10.3390/cryst13101512/s1, Figure S1: Comparison of IR spectra of **R:HCOOH**, **R:AcOH**, **R:3H$_2$O** with **R**. Characteristic bands are highlighted; Figure S2: Experimental powder pattern of **R:AcOH** compared to simulated patterns of **R:AcOH** and adjusted simulated pattern for consideration of preferred orientation from single crystal data; Figure S3: Experimental powder pattern of **R:3H$_2$O** compared to simulated pattern from single crystal data; Figure S4: Experimental powder pattern of **R:HCOOH** compared to simulated pattern from single crystal data; Figure S5: Asymmetric unit of **R:HCOOH**. View along the crystallographic a-axis; Figure S6: Asymmetric unit of **R:AcOH**. View along the crystallographic a-axis; Figure S7: Asymmetric unit of **R:3H$_2$O**. View

along the crystallographic a-axis; Figure S8: Asymmetric unit of **R:AcOH:H_2O**. View along the crystallographic a-axis; Table S1: Geometries of hydrogen-bonded interactions of **R:AcOH**; Table S2: Geometries of hydrogen-bonded interactions of **R:3H_2O**; Table S3: Geometries of hydrogen-bonded interactions of **R:AcOH:H_2O**. Table S4: Geometries of hydrogen-bonded interactions of **R:HCOOH**; Table S5: Crystal Explorer model interaction energies calculations, overview of strongest molecular interaction energy contributions in 3.8 Å cluster on central flavin unit with verbose parameters.

Author Contributions: Conceptualization, T.H.H.S. and V.V.; methodology, T.H.H.S. and F.M.; software, T.H.H.S.; validation, T.H.H.S., F.M. and V.V.; formal analysis, T.H.H.S. and F.M.; investigation, T.H.H.S. and F.M.; resources, C.C. and V.V.; data curation, V.V.; writing—original draft preparation, T.H.H.S.; writing—review and editing, T.H.H.S. and V.V.; visualization, T.H.H.S.; supervision, V.V.; project administration, V.V.; funding acquisition, V.V. All authors have read and agreed to the published version of the manuscript.

Funding: This research was funded by the Deutsche Forschungsgemeinschaft (DFG, German Research Foundation)—440366605 and 396890929/GRK 2482.

Data Availability Statement: All crystal structures are deposited in the Cambridge Structural Database CSD (CCDC numbers: 2294770-2294773) and can be found at https://www.ccdc.cam.ac.uk/structures.

Acknowledgments: Computational support and infrastructure were provided by the "Centre for Information and Media Technology" (ZIM) at the University of Duesseldorf (Germany).

Conflicts of Interest: The authors declare no conflict of interest. The funders had no role in the design of the study; in the collection, analyses, or interpretation of data; in the writing of the manuscript; or in the decision to publish the results.

References

1. Haj Hassani Sohi, T.; Maass, F.; Czekelius, C.; Suta, M.; Vasylyeva, V. Co-crystallization of organic chromophore roseolumiflavin and effect on its optical characteristics. *CrystEngComm* **2022**, *24*, 7315–7325. [CrossRef]
2. Bera, M.K.; Pal, P.; Malik, S. Solid-state emissive organic chromophores: Design, strategy and building blocks. *J. Mater. Chem. C* **2020**, *8*, 788–802. [CrossRef]
3. Singh, M.; Liu, K.; Qu, S.; Ma, H.; Shi, H.; An, Z.; Huang, W. Recent advances of cocrystals with room temperature phosphorescence. *Adv. Opt. Mater.* **2021**, *9*, 2002197. [CrossRef]
4. Griesser, U.J. The importance of solvates. In *Polymorphism in the Pharmaceutical Industry*; Hilfiker, R., Ed.; Wiley-VCH: Weinheim, Germany, 2006; pp. 211–233. ISBN 9783527311460.
5. Boothroyd, S.; Kerridge, A.; Broo, A.; Buttar, D.; Anwar, J. Why do some molecules form hydrates or solvates? *Cryst. Growth Des.* **2018**, *18*, 1903–1908. [CrossRef]
6. Healy, A.M.; Worku, Z.A.; Kumar, D.; Madi, A.M. Pharmaceutical solvates, hydrates and amorphous forms: A special emphasis on cocrystals. *Adv. Drug Deliv. Rev.* **2017**, *117*, 25–46. [CrossRef]
7. Seddon, K.R. Pseudo polymorph: A polemic. *Cryst. Growth Des.* **2004**, *4*, 1087. [CrossRef]
8. Desiraju, G.R. Counterpoint: What's in a name? *Cryst. Growth Des.* **2004**, *4*, 1089–1090. [CrossRef]
9. Bernstein, J. And another comment on pseudo-polymorphism. *Cryst. Growth Des.* **2005**, *5*, 1661–1662. [CrossRef]
10. Nangia, A. Pseudopolymorph: Retain this widely accepted term. *Cryst. Growth Des.* **2006**, *6*, 2–4. [CrossRef]
11. Grothe, E.; Meekes, H.; Vlieg, E.; Ter Horst, J.H.; de Gelder, R.D. Solvates, salts, and cocrystals: A proposal for a feasible classification system. *Cryst. Growth Des.* **2016**, *16*, 3237–3243. [CrossRef]
12. Desiraju, G.R.; Vittal, J.J.; Ramanan, A. *Crystal Engineering: A Textbook*; World Scientific: Singapore, 2011; ISBN 978-981-4338-75-2.
13. Aakeröy, C.B.; Seddon, K.R. The hydrogen bond and crystal engineering. *Chem. Soc. Rev.* **1993**, *22*, 397–407. [CrossRef]
14. Videnova-Adrabińska, V. The hydrogen bond as a design element in crystal engineering. Two- and three-dimensional building blocks of crystal architecture. *J. Mol. Struct.* **1996**, *374*, 199–222. [CrossRef]
15. Komisarek, D.; Pallaske, M.; Vasylyeva, V. Crystal structure and thermal properties of phenibut, phenibut H2O and phenibut HCl: A case for phase stability based on structural considerations. *Z. Anorg. Allg. Chemie* **2021**, *647*, 984–991. [CrossRef]
16. Heinen, T.; Hoelscher, S.; Vasylyeva, V. Structural study of anhydrous and hydrated 5-fluorouracil co-crystals with nicotinamide and isonicotinamide. *Z. Kristallogr.—Cryst. Mater.* **2022**, *237*, 109–116. [CrossRef]
17. Karasulu, B.; Thiel, W. Photoinduced intramolecular charge transfer in an electronically modified flavin derivative: Roseoflavin. *J. Phys. Chem. B* **2015**, *119*, 928–943. [CrossRef] [PubMed]
18. Scarbrough, F.E.; Shieh, H.-S.; Voet, D. The X-ray crystal structure of the molecular complex bis(lumiflavin–2,6-diamino-9-ethylpurine)–ethanol–water. *Acta Crystallogr. B Struct. Sci.* **1977**, *33*, 2512–2523. [CrossRef]
19. Wells, J.L.; Trus, B.L.; Johnston, R.M.; Marsh, R.E.; Fritchie, C.J. Crystal structure of the yellow molecular complex lumiflavin–bis(naphthalene-2,3-diol). *Acta Crystallogr. B Struct. Sci.* **1974**, *30*, 1127–1134. [CrossRef]

20. Kuo, M.C.; Dunn, J.B.R.; Fritchie, C.J. The crystal structure of a flavin molecular complex: 10-propylisoalloxazine–bis(naphthalene-2,3-diol). *Acta Crystallogr. B Struct. Sci.* **1974**, *30*, 1766–1771. [CrossRef]
21. Voet, D.; Rich, A. The crystal and molecular structure of an intermolecular complex between riboflavin and an adenosine derivative. *Proc. Natl. Acad. Sci. USA* **1971**, *68*, 1151–1156. [CrossRef]
22. Lu, T.; Chen, F. Multiwfn: A multifunctional wavefunction analyzer. *J. Comput. Chem.* **2012**, *33*, 580–592. [CrossRef]
23. Mackenzie, C.F.; Spackman, P.R.; Jayatilaka, D.; Spackman, M.A. CrystalExplorer model energies and energy frameworks: Extension to metal coordination compounds, organic salts, solvates and open-shell systems. *IUCrJ* **2017**, *4*, 575–587. [CrossRef] [PubMed]
24. Spackman, P.R.; Turner, M.J.; McKinnon, J.J.; Wolff, S.K.; Grimwood, D.J.; Jayatilaka, D.; Spackman, M.A. CrystalExplorer: A program for Hirshfeld surface analysis, visualization and quantitative analysis of molecular crystals. *J. Appl. Crystallogr.* **2021**, *54*, 1006–1011. [CrossRef] [PubMed]
25. *CrysAlisPRO*, v171.42; Oxford Diffraction/Agilent Technologies UK Ltd.: Yarnton, UK, 2022.
26. *APEX2*, v2012; Bruker AX Inc.: Madison, WI, USA, 2012.
27. *SAINT*, v2018; Bruker Analytical X-ray Systems: Madison, WI, USA, 2018.
28. Sheldrick, G.M. SHELXT—Integrated space-group and crystal-structure determination. *Acta Crystallogr. A Found. Adv.* **2015**, *71*, 3–8. [CrossRef]
29. Sheldrick, G.M. Crystal structure refinement with SHELXL. *Acta Crystallogr. C Struct. Chem.* **2015**, *71*, 3–8. [CrossRef] [PubMed]
30. Dolomanov, O.V.; Bourhis, L.J.; Gildea, R.J.; Howard, J.A.K.; Puschmann, H. OLEX2: A complete structure solution, refinement and analysis program. *J. Appl. Crystallogr.* **2009**, *42*, 339–341. [CrossRef]
31. Frisch, M.J.; Trucks, G.W.; Schlegel, H.B.; Scuseria, G.E.; Robb, M.A.; Cheeseman, J.R.; Scalmani, G.; Barone, V.; Petersson, G.A.; Nakatsuji, H.; et al. *Gaussian 16, Revision C.01*; Gaussian, Inc.: Wallingford, CT, USA, 2016.
32. Komisarek, D.; Haj Hassani Sohi, T.; Vasylyeva, V. Co-crystals of zwitterionic GABA API's pregabalin and phenibut: Properties and application. *CrystEngComm* **2022**, *24*, 8390–8398. [CrossRef]
33. Emamian, S.; Lu, T.; Kruse, H.; Emamian, H. Exploring nature and predicting strength of hydrogen bonds: A correlation analysis between Atoms-in-Molecules descriptors, binding energies, and energy components of symmetry-adapted perturbation theory. *J. Comput. Chem.* **2019**, *40*, 2868–2881. [CrossRef]
34. Macrae, C.F.; Sovago, I.; Cottrell, S.J.; Galek, P.T.A.; McCabe, P.; Pidcock, E.; Platings, M.; Shields, G.P.; Stevens, J.S.; Towler, M.; et al. Mercury 4.0: From visualization to analysis, design and prediction. *J. Appl. Crystallogr.* **2020**, *53*, 226–235. [CrossRef]
35. Spek, A.L. Structure validation in chemical crystallography. *Acta Crystallogr. D Biol. Crystallogr.* **2009**, *65*, 148–155. [CrossRef]
36. Etter, M.C.; MacDonald, J.C.; Bernstein, J. Graph-set analysis of hydrogen-bond patterns in organic crystals. *Acta Crystallogr. B* **1990**, *46*, 256–262. [CrossRef]
37. Bader, R.; Nguyen-Dang, T.T. *Quantum Theory of Atoms in Molecules–Dalton Revisited*; Elsevier: Amsterdam, The Netherlands, 1981; pp. 63–124. ISBN 9780120348145.

Supplementary Material

A Comparison Study of Roseolumiflavin Solvates: Structural and Energetic Perspective on Their Stability

Takin Haj Hassani Sohi, Felix Maass, Constantin Czekelius, Vera Vasylyeva*

IR analysis

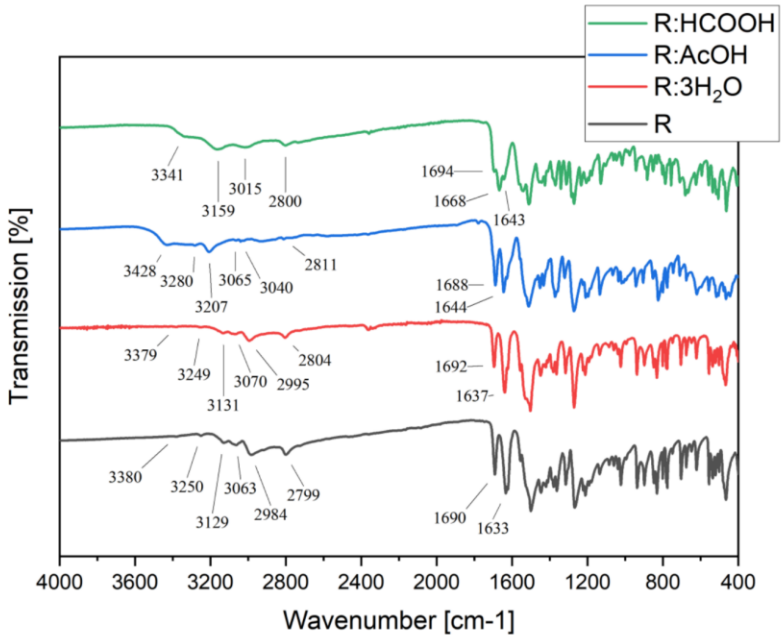

*Figure S1: Comparison of IR spectra of **R:HCOOH**, **R:AcOH**, **R:3H₂O** with **R**. Characteristic bands are highlighted.*

In comparison to **R**, for **R:AcOH** a new broad band at 3428 cm^{-1} appears which likely originates from O−H stretching vibration and overlaps the high N-H stretching band of pure **R** at 3380 cm^{-1}. Likewise, the band at 3207 cm^{-1} may be caused by intermolecular bonded O−H group. The amide C=O vibration at 1644 cm^{-1} is blue-shifted by +11 cm^{-1} while the band at 1689 cm^{-1} remains unmodified. Strong blue-shifts for the C−H vibrations at 2811 cm^{-1} by +12 cm^{-1} and the NC−H vibration at *ca.* 3030 cm^{-1} by *ca.* +36 cm^{-1} evince noticeable effects on the methyl group bonds.

R:3H₂O contains slightly blue-shifted C=O vibrational bands by 4 to 5 cm^{-1}, the N−H stretching bands are unaltered. The NC−H hydrogen stretching band at 2804 cm^{-1} is blue-shifted by +5 cm^{-1}, so are the bands for C−H vibrations at 3070 cm^{-1} by +7 cm^{-1} and 2995 cm^{-1} by +11 cm^{-1}, indicating substantial increase in bond strength in the new packing environment.

The spectrum for **R:HCOOH** displays a broad band at 3341 cm^{-1} representing the O-H vibration band of the solvent molecule. Here, the N-H stretching vibrational mode of the imide group at 3159 cm^{-1} is overlapped by it. The broad band at 3015 cm^{-1} is likely caused by C-H stretching vibrations of the **R** methyl groups, blue-shifted by +26 cm^{-1}. Also, the C=O stretching bands of the imide group at 1694 cm^{-1} and 1643 cm^{-1} are blue-shifted by +5 cm^{-1} and +10 cm^{-1}, respectively. At 1668 cm^{-1} a new band arises, which is to be identified as the C=O stretching mode of the acid unit.

Simulated PXRD patterns

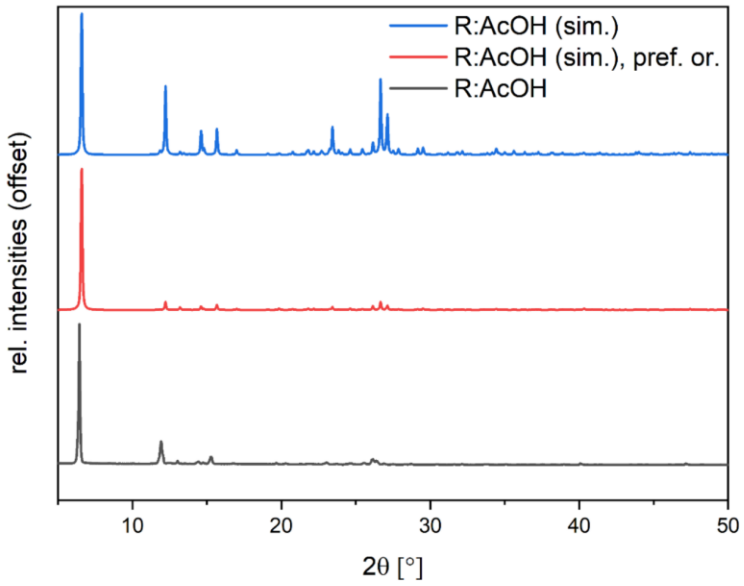

*Figure S2: Experimental powder pattern of **R:AcOH** compared to simulated patterns of **R:AcOH** and adjusted simulated pattern for consideration of preferred orientation from single crystal data.*

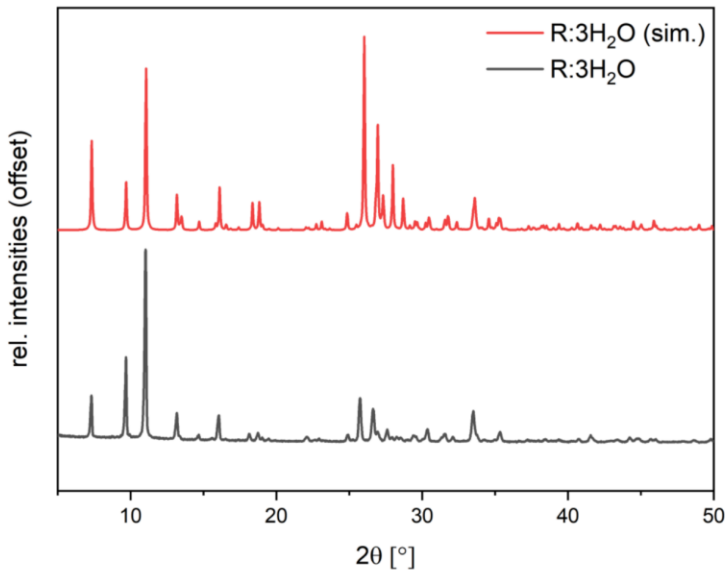

*Figure S3: Experimental powder pattern of **R:3H₂O** compared to simulated pattern from single crystal data.*

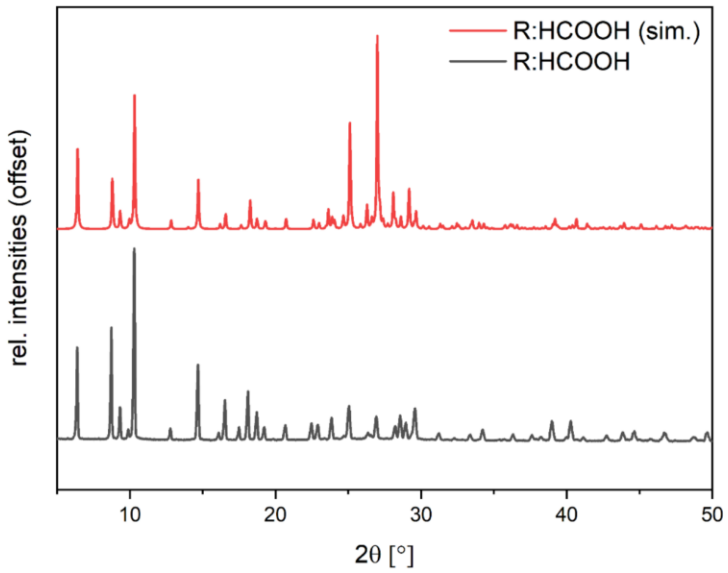

*Figure S4: Experimental powder pattern of **R:HCOOH** compared to simulated pattern from single crystal data.*

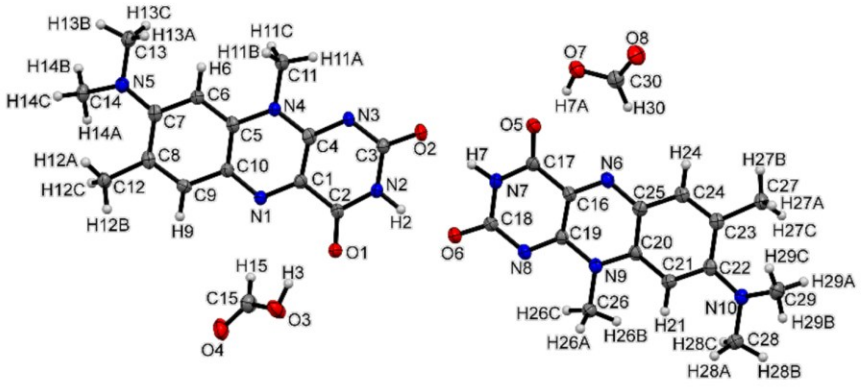

*Figure S5: Asymmetric unit of **R:HCOOH**. View along the crystallographic a-axis.*

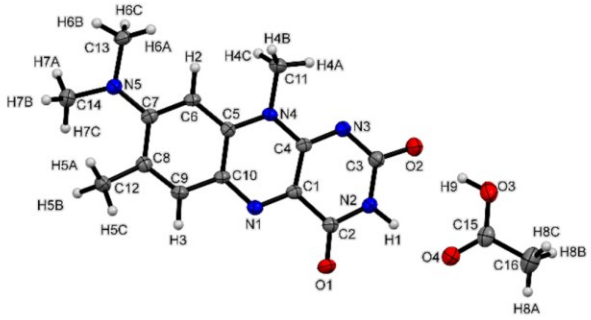

*Figure S6: Asymmetric unit of **R:AcOH**. View along the crystallographic a-axis.*

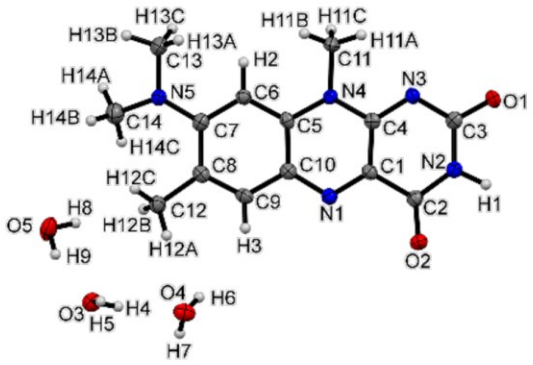

*Figure S7: Asymmetric unit of **R:3H_2O**. View along the crystallographic a-axis.*

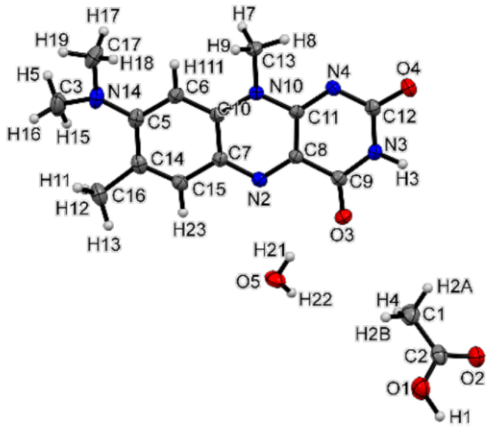

*Figure S8: Asymmetric unit of **R:AcOH:H₂O**. View along the crystallographic a-axis.*

Overview of the hydrogen bonds

D-H···A	D−H [Å]	H···A [Å]	D···A [Å]	D−H···A [°]
N1-H1···O4	0.94(3)	1.95(3)	2.879(2)	170(3)
O3-H9···O2	0.88(4)	1.72(4)	2.596(2)	173(4)
C6-H2···O1	0.95(2)	2.53(2)	3.472(3)	172(2)
(intra) C11-H4A···N3	0.96(2)	2.20(2)	2.725(3)	112.8(18)
C16-H8B···O2	0.95(3)	2.47(3)	3.420(3)	173(3)

*Table S1: Geometries of hydrogen bonded interactions of **R:AcOH**.*

D-H···A	D−H [Å]	H···A [Å]	D···A [Å]	D−H···A [°]	A−H···A [°]	Sum(XY,YZ)
N2-H1···O5	0.99(6)	1.78(6)	2.774(5)	174(6)		
O3-H4···O4	0.83(4)	2.06(4)	2.887(4)	176(4)		
O3-H5···O4	0.93(5)	1.91(5)	2.833(5)	172(4)		
O4-H6···N3	0.77(7)	2.29(7)	2.981(5)	151(7)		
O4-H7···O1	0.79(5)	2.00(5)	2.759(4)	160(5)		
O5-H8···O1	0.89(6)	1.87(6)	2.752(4)	168(5)		
O5-H9···O3	0.89(5)	1.95(5)	2.805(5)	161(4)		
C11-H11A···N3	0.98	2.52	3.429(6)	154		
(intra) C11-H11A···N3	0.98	2.33	2.698(5)	101'	99'	354

*Table S2: Geometries of hydrogen bonded interactions of **R:3H₂O**.*

D-H···A	D−H [Å]	H···A [Å]	D···A [Å]	D−H···A [°]
O1-H1···O5	1.02(3)	1.54(3)	2.5483(19)	170(3)
N3-H3···O2	0.91(2)	2.05(2)	2.952(2)	173.1(15)
O5-H21···O3	0.831(12)	2.066(14)	2.8608(17)	160(2)
O5-H22···O4	0.835(16)	1.881(16)	2.7077(18)	170.5(19)
C13-H7···O4				
(intra) C13-H8···N4	0.98	2.58	3.461(2)	150
C17-H18···O3	0.98	2.26	2.723(2)	108
C15-H23···O1	0.98	2.52	3.386(2)	147
C6-H111···O4	0.949(18)	2.406(18)	3.352(2)	175.4(13)

*Table S3: Geometries of hydrogen bonded interactions of **R:AcOH:H₂O**.*

D-H···A	D−H [Å]	H···A [Å]	D···A [Å]	D−H···A [°]
N2-H2···O6	0.95(8)	1.91(7)	2.828(6)	163(6)
O3-H3···O1	0.89(12)	1.78(12)	2.577(5)	148(9)
N7-H7···O2	0.92(7)	1.86(8)	2.768(6)	175(7)
O7-H7A···O5	0.82	1.8	2.598(6)	165
C11-H11A···N3	0.96	2.25	2.719(7)	109
C26-H26C···N8	0.96	2.32	2.694(7)	102

*Table S4: Geometries of hydrogen bonded interactions of **R:HCOOH**.*

Lattice Energy and AIM calculations

The lattice Energy E_{lat} was calculated following the equation (1)

$$E_{lat} = \frac{E_{iss}}{Z} - \frac{\sum E_{isg,n}}{Z'} \quad (1)$$

where E_{lat} represents the lattice energy, E_{iss} the ideal static solid energy, E_{isg} the ideal static gas energy for each molecule, as well as Z and Z' the respective crystallographic parameters.

The binding energy (BE) in kcal/mol for neutral HBs based on the electron density at the BCPs can be estimated via following equation (2) provided by Emamian et al. [33]

$$BE \approx -223.08 \times \rho(r_{BCP}) + 0.7423 \quad (2)$$

With the electron density ρ in a.u. provided by the MultiWFN program package [22].

Crystal Explorer molecular interaction energies

Structure	Crystal Explorer model interaction energies calculations						
	N	Sym.op.	E_{ele}	E_{pol}	E_{dis}	E_{rep}	E_{tot}
R	2	x+1/2, -y+1/2, z+1/2	-23.7	-12.9	-21.9	25.8	-37.7
	1	-x, -y, -z	-45.6	-10.1	-116.9	71.5	-113.4
	1	-x, -y, -z	-56.1	-11.8	-122.3	76.8	-127.1
	1	-x, -y, -z	-70.8	-20.8	-14	95.5	-43.4
R:AcOH	1	x, y, z	-103.6	-24.4	-13.4	125.1	-62.0
	1	-x, -y, -z	-44.9	-11.7	-108.7	66.0	-110.0
	1	-x, -y, -z	-30.1	-7.6	-56.8	35.6	-64.9
	1	-x, -y, -z	-34.8	-11.8	-59.9	44.1	-70.5
	2	2-x, 1-y, 1-z	-21.6	-12.0	-21.9	26.0	-34.7
R:AcOH:H_2O	1	x, y, z	-41.0	-8.9	-8	35.6	-34.8
	1	1-x, 1-y, 2-z	-26.9	-5.4	-6.1	24.9	-22.4
	1	1-x, 0.5+y, 1.5-z	-48.8	-9.9	-5.4	57.2	-28.3
	1	-x, -y, -z	-27.6	-8.6	-66.4	37.1	-70.5
	1	-x, -y, -z	-53.4	-11.1	-113.6	76.6	-116.3
	2	x, -y+1/2, z+1/2	-20.0	-10.3	-14.0	16.1	-30.9
R:3H_2O	1	-x, -y, -z	-44.8	-9.2	-98.8	57.8	-104.6
	1	-x, -y, -z	-47.5	-9.8	-105.3	62.3	-110.7
	2	x, y, z	-18.3	-9.7	-16.4	13.2	-32.6
	1	x, y, -1+z	-45.2	-10.3	-5.5	44.9	-32.4
	1	x, 1+y, -1+z	-42.0	-9.7	-5.7	51.0	-25.1
	1	1-x, 1-y, -z	-42.1	-8.8	-4.1	45.7	-26.5
	1	1-x, 1-y, -z	-20.0	-8.3	-10.4	29.7	-18.0
R:HCOOH	1	x, y, z	-71.0	-20.7	-14.3	99.2	-41.6
	2	x, y, z	25.5	-9.8	-114.2	70.0	-36.5
	2	-x, y+1/2, -z	-25.8	-10.3	-15.7	24.9	-33.2
	1	x, y, z	-75.3	-19.1	-12.5	74.6	-58.5

Table S5: Crystal Explorer model interaction energies calculations, overview of strongest molecular interaction energy contributions in 3.8 Å cluster on central flavin unit with verbose parameters.

The scale factors used in Crystal Explorer molecular interaction energy calculations for CE-B3LYP (B3LYP/6-31G(d,p) electron densities are: k_{ele}=1.057, k_{pol}=0.74, k_{disp}=0.871 and k_{rep}=0.618.

4.3. Tuning Molecular Assembly and Optical Properties via Cocrystallization: A Case Study of Roseolumiflavin in Binary and Ternary Multicomponent Systems

Takin Haj Hassani Sohi, Lea Pongratz, Felix Maaß, Sarah Merzenich, Laura Samperisi, Constantin Czekelius, Vera Vasylyeva

DOI: 10.1021/acs.cgd.5c01261

Cryst. Growth Des., **2025***, 25*, 24, 10482–10496

In this final study of roseolumiflavin, a set of *N*-heterocyclic co-formers was chosen to explore the incremental influence on photophysical properties as a result of co-crystallization. A series of binary and ternary flavin co-crystals (the latter referred to as molecular ionic co-crystals due to partial proton transfer from an acid molecule to the co-former) are reported and predominantly prepared via eco-friendly LAG method. Single-crystal structures show that the original packing in the flavin is replaced and this molecular rearrangement results in blue-shifted emission relative to the parent flavin, the most pronounced in the ternary systems. Supported by QTAIM and NCI analyses the dominance of strong hydrogen bonds is derived from the crystal structure data which stabilizes the systems and stacking/dispersion interactions both contribute to structural robustness and help rationalize observed trends in photophysical response across the series of multicomponent systems.

Contributions of the author:

- Conceptualization based on literature research and prior investigations together with Vera Vasylyeva.
- Experimental work, investigation and validation of results, including synthesis of powder samples and single crystals together with Lea Pongratz and Felix Maaß. This includes consistent approaches to optimizing synthesis conditions during the project.
- Measurement and evaluation of pK_a values, SCXRD and FTIR.
- Preparation and evaluation of CIE 1931 coordinates.
- Evaluation of TGA measurements and CHNS elemental analyses.
- Measurement and evaluation of PXRD together with Lea Pongratz and Felix Maaß.
- Measurement and evaluation of solid-state emission and excitation spectra including calculation of FWHM and Stokes shifts together with Sarah Merzenich.
- Generation of *Gaussian* input files, calculations of QTAIM, NCI plots and basic structural motifs (BSM). Evaluation of the results.
- Visualization of all figures, tables and data.
- Manuscript writing, literature research and preparation of supporting material.
- Review and editing of manuscript together with Vera Vasylyeva.
- Revision process together with Vera Vasylyeva, Sarah Merzenich and Constantin Czekelius.

CRYSTAL GROWTH & DESIGN

pubs.acs.org/crystal Article

Tuning Molecular Assembly and Optical Properties via Cocrystallization: A Case Study of Roseolumiflavin in Binary and Ternary Multicomponent Systems

Takin Haj Hassani Sohi, Lea Pongratz, Felix Maaß, Sarah Merzenich, Laura Samperisi, Constantin Czekelius, and Vera Vasylyeva*

Cite This: *Cryst. Growth Des.* 2025, 25, 10482−10496 Read Online

ACCESS | Metrics & More | Article Recommendations | Supporting Information

ABSTRACT: Extending our previous work on cocrystallization of roseolumiflavin (**R**), the rational design approach with various *N*-heterocyclic coformers has been explored to systematically tune photophysical properties of the chromophore. A series of binary and, for the first time, ternary flavin cocrystals was systematically synthesized and analyzed with particular focus on the modification of spectroscopic behavior. Structural analyses based on obtained single crystal data reveal distinct molecular packing patterns, with binary cocrystals maintaining either face-to-face or slipped stacking motifs, while ternary systems demonstrate acid-mediated protonation effects and modified π-stacking arrangements. The original hydrogen-bonded **R** dimer is replaced by a donor−acceptor−donor (DAD) motif and, in the case of the ternary systems, further stabilized through hydrogen bonds with acid molecules. The structural modifications directly correlate with the photophysical behavior, as all cocrystals exhibit blue-shifted fluorescence relative to **R**. The most pronounced influence on the spectral behavior occurs in ternary cocrystals with the emission band shifts of up to 158 nm. This work expands on to this date scarcely available knowledge of flavin cocrystallization and highlights the role of hydrogen bonding, stacking interactions and coformer selection in fine-tuning its optical properties.

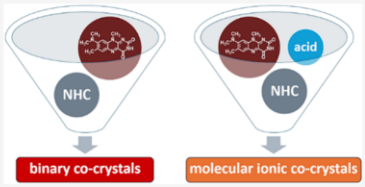

1. INTRODUCTION

Organic cocrystals, in the context of photoactive materials, offer a promising avenue for enhancing targeted properties of a compound. By integrating different molecular components into a single crystalline structure through intermolecular interactions, cocrystals can exhibit a photophysical behavior that surpasses that of individual components while advantageous characteristics in the design process such as low-cost syntheses or highly flexible tunability facilitate reasonable interest in this field.[1−7] Crystal engineering enables the design of novel cocrystals with tailored photophysical properties by utilizing intermolecular interactions, such as $\pi\cdots\pi$ stacking[8] and hydrogen bonding.[9] These various capabilities make cocrystallization an attractive route for improving the performance of photofunctional materials reported in recent studies on organic solid-state luminophores,[10−17] sensors,[18,19] or light-emitting devices such as OLEDs.[20,21] For instance, a recent study by Zhang et al. reported the formation of organic cocrystal alloys based on three light-emitting donor−acceptor systems that enable full-color emission and white light generation through composition-controlled stacking arrangements.[22] These systems also exhibited circularly polarized luminescence, highlighting the relevance of supramolecular control in designing functional optoelectronic materials.

Due to its particular photophysical characteristics and structural versatility—both in its pure form and in relation to its role in the formation of multicomponent crystals like solvates and cocrystals—8-(dimethylamino)-7,10-dimethylbenzo[*g*]pteridine-2,4(3*H*,10*H*)-dione, in the following referred to as roseolumiflavin (**R**), has been the subject of recent scientific research. Thus, this deep red isoalloxazine derivative may be an appealing candidate for studies examining the spectrum of tunability in the context of crystal engineering. Our group has previously examined the potential of roseolumiflavin to cocrystallize with different coformer partners, leading to varying optical properties.[23] Specifically, cocrystals of roseolumiflavin have demonstrated blue-shifted fluorescence emissions in comparison to the near-infrared emission of the pure compound. This hypsochromic shift in fluorescence has been attributed to the different degrees of molecular packing within the crystal structures, which could be strategically manipulated through crystal engineering techniques. Further, in our study in 2023 we analyzed the structural and energetic stability of various solvates which roseolumiflavin is prone to

Received: September 3, 2025
Revised: November 17, 2025
Accepted: November 18, 2025
Published: November 25, 2025

https://doi.org/10.1021/acs.cgd.5c01261
Cryst. Growth Des. 2025, 25, 10482−10496

Scheme 1. Molecular Structures of R, Selected Coformers 2,4-Diaminopyrimidine (1), 2,4-Diamino-1,3,5-triazine (2), 2,4,6-Triaminopyrimidine (3), 2,4,6-Triamino-1,3,5-triazine (4) As Well As Acetic Acid (A) and Formic Acid (F) Acting as Third Components

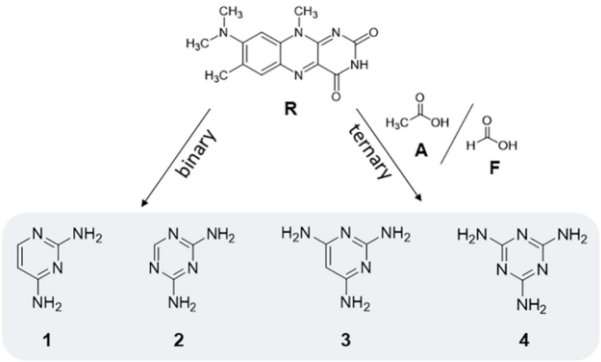

form in crystalline state.[24] Energetic evaluations, e.g., via lattice energy calculations, have indicated that these solvates possess substantial energetic advantages, enhancing their phase stability. These studies are meant to disclose roseolumiflavin's characteristics and behaviors with regards to structural and optical properties. Yet, while previous studies have provided a general overview of roseolumiflavin and its chemical behavior, we aim to take a new approach to selectively achieve color changes through strategic selection of the coformer, which in recent past has been shown to affect optical or photophysical behavior of the respective cocrystal.[10,25−28] Another aspect of today's chemistry, or rather, the general modern society is the challenge of reducing waste and the approach toward sustainable alternatives to conventional methods. Recent advances toward *green chemistry* garnered attention on mechanochemical synthesis.[29−31] Among the available techniques, mechanochemistry offers an efficient, solvent-free and environmentally friendly approach for the preparation of organic materials.[32] In addition, mechanochemical reactions, typically driven by grinding or milling, easily enable the formation of cocrystals under mild conditions, significantly shortened reaction times and reduced waste by waiving the need for bulk solvents.[33−36]

The present work is concerned with an environmentally benign systematic rational design approach to cocrystallize roseolumiflavin with the objective to obtain photoactive solid-state materials with desired emission band properties depending on the selected coformer compound. For this, control over the emission spectra is achieved by careful preselection of respective derivatives of said coformer. Expanding on our previously gathered knowledge and, based on the roseolumiflavin:2,4-diaminopyrimidine cocrystal reported in 2022,[23] a set of amino-substituted simple *N*-heterocycles were selected for further cocrystallization experiments (Scheme 1).

The heterocycle derivatives are selected due to several reasons. On the one hand, increasing the number of N atoms in the ring framework from a pyrimidine- to a triazine-ring leads to a more localized overall electron density inside the ring. This results in tuning of the hydrogen-bond acceptor capacity as well as alteration of potential stacking interactions. On the other hand, the amine substituents on the heterocycles are varied to systematically investigate and optimize the chemical and physical properties of the compounds as well as to promote further intermolecular interaction motifs. Additionally, implementation of organic acids as a third component can enhance an overall electronic density distribution via protonation of the system and thus contribute to structural and/or physicochemical alteration. Two moderately strong proton donors, formic acid (**F**) and acetic acid (**A**), were chosen as simple model compounds. Based on the differences of the pK_a values being in the range 0−3 for all combinations of acids with **R** and coformers, a formation of an intermediate multicomponent system somewhere on a salt/cocrystal continuum[37] might occur. In the case of a proton transfer from the acid to either a coformer or the chromophore molecule, molecular assembly will be additionally stabilized through charge-assisted hydrogen bonds.

To provide further insight into the bonding characteristics, topological analyses of the electron densities based on the crystal structures are carried out within the framework of Bader's quantum theory of atoms in molecules (QTAIM).[38] To qualitatively assess noncovalent interactions (NCI), in this study mainly to identify the stacking modes, respective NCI analyses are conducted with the NCIplot program package.[39] These complementary approaches enable a detailed description of the electron density features and interaction types contributing to crystal stability. Performed multifaceted analysis will add to a deeper understanding of the intermolecular interactions' contribution on structural and photophysical characteristics of the respective cocrystals and allow a control of targeted properties by rational selection of the coformer in future.

2. MATERIALS AND METHODS

2.1. Mechanochemistry. For syntheses, a liquid assisted grinding (LAG) approach, i.e., grinding with a small amount of liquid, was employed, as during initial investigations we found the absence of a liquid did not initiate the cocrystallization process. In fact, all but one system could be synthesized via a mechanochemical approach, with the exception being **R:3:F** which could only be obtained in pure phase via a classic crystallization from a solvent. All obtained products were analyzed via PXRD and IR-Spectroscopy (Tables S1−S19 in SI) to confirm new phase formation and purity.

https://doi.org/10.1021/acs.cgd.5c01261
Cryst. Growth Des. 2025, 25, 10482−10496

2.2. Synthesis of Roseolumiflavin and Multicomponent Systems. Roseolumiflavin was prepared as reported previously.[23] **1** (>98%) was purchased from BLDpharm, **2** (>98%) and **3** (>98%) from TCI, **4** (≥99%) from Acros Organics. **A** (≥99%) and **F** (≥98%) were purchased from Sigma-Aldrich and Methanol (≥99%) from Fisher Scientific. All chemicals were used without further purification.

In contrast to the LAG, single crystal growth under various conditions proved challenging. For most multicomponent systems, crystallization from solution resulted in small, ultrathin platelets of extremely poor diffracting quality. For samples **R:1:A**, **R:1:F** and **R:2:A** no single crystals of suitable quality could be obtained. Attempts to synthesize **R:2:F** and **R:4:F** systems under different mechanochemical and solution-based conditions were unsuccessful, yielding only mixed-phase materials without any evidence of new crystalline phases.

*2.2.1. Roseolumiflavin (**R**) and Roseolumiflavin:2,4-diaminopyrimidine (**R:1**).* **R** and **R:1** were synthesized following the procedure described in our previous work.[23]

*2.2.1.1. **R:1:A**—Roseolumiflavin:2,4-diaminopyrimidine:acetic acid.* In a similar procedure to **R:1**, 15.32 mg (53.7 μmol) **R** and 5.94 mg (53.9 μmol) **1** were mixed in a 1:1 ratio and ground in a ball mill for 25 min at 15 Hz with excess amounts of 50 μL **A** (0.874 mmol). A new phase is given as an orange powder. Single crystals suitable for X-ray analysis could not be obtained. PXRD/°2θ: 8.04, 11.40, 12.39, 16.20, 20.90, 26.30; IR/cm^{-1}: 3159, 3072, 2988, 2803, 1690; TGA/°C: 118, 258, 335; Solid-state spectroscopy: $\lambda_{Em,max}$ = 590 nm, $\lambda_{Ex,max}$ = 545 nm.

*2.2.1.2. **R:1:F**—Roseolumiflavin:2,4-diaminopyrimidine:formic acid.* 17.52 mg (61.4 μmol) **R** and 6.75 mg (61.3 μmol) **1** were combined in a 1:1 molar ratio ground in a ball mill for 25 min at 15 Hz with excess amounts of 50 μL **F** (0.967 mmol) to give orange-reddish powder. No single crystal structure of this system could be obtained. PXRD/°2θ: 11.12, 11.35, 12.17, 13.17 17.20, 22.34, 22.82, 26.60; IR/cm^{-1}: 3316, 3133, 2991, 2806, 1690, 1673, 1625; TGA/°C: 102, 255, 310; Solid-state spectroscopy: $\lambda_{Em,max}$ = 596 nm, $\lambda_{Ex,max}$ = 542 nm.

*2.2.1.3. **R:2**—Roseolumiflavin:2,4-diamino-1,3,5-triazine.* 16.06 mg (56.3 μmol) **R** and 6.25 mg (56.4 μmol) **2** were mixed in a 1:1 molar ratio and ground in a ball mill for 25 min at 15 Hz via LAG with 10 μL methanol. The product then was put into methanol to evaporate over several days. This process yielded light red plate crystals in 1:1 ratio for SCXRD measurements. CCDC No. 2482925. PXRD/°2θ: 6.12, 11.58, 12.44, 25.34, 27.70; IR/cm^{-1}: 3433, 3305, 3123, 2990, 2807, 1686, 1642; Solid-state spectroscopy: $\lambda_{Em,max}$ = 646 nm, $\lambda_{Ex,max}$ = 583 nm

*2.2.1.4. **R:2:A**—Roseolumiflavin:2,4-diamino-1,3,5-triazine:acetic acid.* 18.18 mg (63.8 μmol) **R** and 6.78 mg (61.2 μmol) **2** were mixed in a 1:1 molar ratio and ground in a ball mill for 25 min at 15 Hz with excess amount of 50 μL **A** (0.874 mmol) to result in an orange microcrystalline product. No single crystals could be obtained for SCXRD analysis. PXRD/°2θ: 6.55, 9.13, 13.71, 19.75, 26.48, 27.72; IR/cm^{-1}: 3584, 3434, 3373, 3131, 2975, 2787, 1656, 1631; TGA/°C: 119, 235, 335; Solid-state spectroscopy: $\lambda_{Em,max}$ = 617 nm, $\lambda_{Ex,max}$ = 575 nm.

*2.2.1.5. **R:3**—Roseolumiflavin:2,4,6-triaminopyrimidine.* 4.90 mg (17.2 μmol) **R** and 1.13 mg (9.0 μmol) **3** were combined in a 2:1 ratio in a ball mill for 25 min and 15 Hz via LAG with 10 μL methanol. The product was put in methanol for slow evaporation, producing clear red plate-shaped crystals at room temperature and the single crystal structure yielded a cocrystal in a 2:1 ratio. CCDC No. 2482923. PXRD/°2θ: 6.20, 11.14, 12.34, 13.44, 15.40, 26.72, 27.84.; IR/cm^{-1}: 3335, 3196, 2945, 2744, 1690, 1637; Solid-state spectroscopy: $\lambda_{Em,max}$ = 668 nm, $\lambda_{Ex,max}$ = 622 nm.

*2.2.1.6. **R:3:A**—Roseolumiflavin:2,4,6-triaminopyrimidine:acetic acid.* This ternary system was synthesized by mixing 18.85 mg (66.1 μmol) **R** and 8.21 mg (65.6 μmol) **3** in a 1:1 molar ratio in a ball mill for 25 min and 15 Hz with excess amount of 50 μL **A** (0.874 mmol). Yellow crystalline plates of a 1:1:2 ratio crystal structure were obtained through slow evaporation from methanol at ambient temperature. CCDC No. 2482923. PXRD/°2θ: 11.94, 12.88, 24.14, 26.82, 27.46; IR/cm^{-1}: 3312, 3149, 2996, 2797, 1688, 1662, 1645; Solid-state spectroscopy: $\lambda_{Em,max}$ = 585 nm, $\lambda_{Ex,max}$ = 556 nm.

*2.2.1.7. **R:3:F**—Roseolumiflavin:2,4,6-triaminopyrimidine:formic acid.* 17.23 mg (60.4 μmol) **R** and 7.50 mg (60.0 μmol) **3** in a 1:1 molar ratio were ground in a ball mill for 25 min and 15 Hz with addition of excess amounts of 50 μL **F** (0.967 mmol). A solution of the product was prepared in methanol. Upon slow evaporation, the solution yielded yellow plate-like crystals in 1:1:2 ratio. CCDC No. 2482922. PXRD/°2θ: 11.92, 12.78, 14.16, 24.34, 26.98, 27.38, 28.42; IR/cm^{-1}: 3376, 3166, 3070, 2954, 2924, 2805, 1700, 1663, 1642; Solid-state spectroscopy: $\lambda_{Em,max}$ = 581 nm, $\lambda_{Ex,max}$ = 560 nm.

*2.2.1.8. **R:4**—Roseolumiflavin:2,4,6-triamino-1,3,5-triazine.* 24.14 mg (84.6 μmol) **R** and 5.67 mg (48.8 μmol) **4** were ground in molar 2:1 ratio in a ball mill for 25 min and 15 Hz via LAG with 10 μL methanol. The microcrystalline, light red product was measured via electron diffraction (ED) to gain the respective crystal structure data (2:1). CCDC No. 2482849. PXRD/°2θ: 6.90, 12.50, 13.14, 23.22, 24.98, 26.28; IR/cm^{-1}: 3332, 3196, 1684, 1633; Solid-state spectroscopy: $\lambda_{Em,max}$ = 657 nm, $\lambda_{Ex,max}$ = 582 nm.

*2.2.1.9. **R:4:A**—Roseolumiflavin:2,4,6-triamino-1,3,5-triazine:-acetic acid.* A ternary system of **R**, 1,3,5-triazine-2,4,6-triamine and acetic acid was formed by mixing 19.21 mg (67.3 μmol) **R** and 8.56 mg (67.9 μmol) **4** in a 1:1 molar ratio in a ball mill for two times 25 min at 15 Hz with excess amount of 50 μL **A** (0.874 mmol). The product was put in dimethyl sulfoxide and the solution evaporated slowly at room temperature, yielding orange plate-like crystals of a 1:1:2 **R:4:A** crystal structure. CCDC No. 2482924. PXRD/°2θ: 11.10, 11.66, 13.66, 26.70, 28.14. IR/cm^{-1}: 3471, 3418, 3273, 3132, 2802, 1702, 1662; Solid-state spectroscopy: $\lambda_{Em,max}$ = 575 nm, $\lambda_{Ex,max}$ = 539 nm.

2.3. Solid-State Spectroscopy. Solid-state photoluminescence excitation and emission spectra were acquired on an Edinburgh FS5 spectrometer equipped with a 150 W CW ozone-free xenon arc lamp, a Czerny−Turner monochromator with plane gratings and a thermoelectrically cooled PMT-900 detector operated in single-photon counting mode. To reduce unwanted stray light, optical filters were placed between the sample and the detector. In samples **R:1**, **R:2**, **R:3**, **R:1:F** and **R:3:F**, the low fluorescence intensity made it difficult to fully suppress light originating from higher diffraction orders of the monochromator. These contributions manifest as residual peaks in the emission spectrum, observed at 765 nm. For the excitation spectra and emission spectra of **R:3**, **R:1:A** and **R:3:A**, a FLS1000 photoluminescence spectrometer from Edinburgh Instruments was used. It is equipped with a 450 W Xe arc lamp for excitation, double excitation and emission monochromators in Czerny-Turner configuration and a thermoelectrically cooled (−20 °C) photomultiplier tube PMT-980 (Hamamatsu). The emission spectra were corrected with respect to the grating efficiency and PMT sensitivity, while excitation spectra were additionally corrected with respect to the lamp intensity. It is to be noted that the emission bands of multicomponent systems have been cut off at 800 nm wavelength mark, as due to second order diffraction residual peaks arise in the range of 815 to 850 nm. The full emission band profiles are available in SI (Figure S22). The chromaticity coordinated (x,y) in the CIE 1931 color space were calculated by the OriginLab Chromaticity App implementation[40] based on emission spectra recorded for the crystalline samples.

2.4. Topological Analyses and Bond Strength Evaluation. QTAIM and NCIplot analyses were performed using the MultiWFN software (version 3.8)[41,42] based on electron density data obtained from single-point calculations at the B3LYP/6−31G** level of theory.[43−46] The wave function files were generated via Gaussian 16[47] and topological parameters such as bond critical points (BCPs) or electron density $\rho(r)$ were extracted to assess the nature and strength of hydrogen bonding interactions. The presence of a (3, −1) critical point between donor and acceptor atoms along with its characteristic electron densities, served as indicators for the existence of intermolecular hydrogen bonds. Based on the model proposed by Emamian et al. in 2019[48] the obtained electron densities are converted into binding energies (BE). The reduced density gradient

https://doi.org/10.1021/acs.cgd.5c01261
Cryst. Growth Des. 2025, 25, 10482−10496

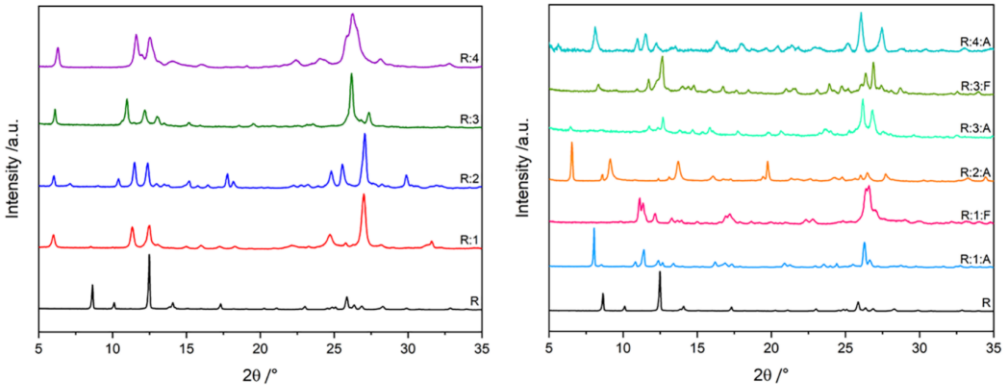

Figure 1. Comparison of powder diffraction (20 °C, 5−35° 2theta) patterns of **R** with all obtained binary (left) and ternary phases (right).

(RDG) was computed and analyzed to obtain insight about noncovalent interactions between stacking motifs. Isosurfaces were generated with an isovalue at a cutoff of 0.6 and visualized using VMD,[49] where weak attractive interactions appeared as green regions between rings. The sign of the second eigenvalue λ_2 of the Hessian matrix of $\rho(r)$ was used to distinguish between attractive and repulsive interactions. Basic structural motifs (BSMs) within the crystal structures were manually identified using Mercury[50] and verified through topological analysis of supramolecular synthons.

2.5. X-ray and Electron-Diffraction. Powder X-ray diffraction (PXRD) measurements were performed on a Rigaku Miniflex diffractometer in $\theta/2\theta$ geometry using Cu−Kα radiation (λ = 1.54182 Å) room temperature, with a step size of 0.0100° and a scanning speed of 5.0°/min. For single-crystal X-ray diffraction (SCXRD) suitable crystals were mounted on cryo-loops and data collected Rigaku XtaLAB Synergy-S diffraction system with a HiPyx 6000 detector and Cu−Kα radiation (λ = 1.54184 Å) at 100.0(2) K for **R:2**, **R:3**, **R:3:A**, **R:3:F** and 293(2) K for **R:4:A**. Data collection, refinement and reduction were processed using CrysAlisPro.[51] Numeric absorption correction is performed using a multifaceted crystal model. The structures were solved via ShelXT[52] and refined using ShelXL[53] in conjunction with the Olex2 software suite.[54] All the non-hydrogen atoms were refined with anisotropic displacement parameters, and the hydrogen atoms were refined experimentally.

For the 3D electron diffraction (3D ED) measurements, **R:4** crystals were deposited on a transmission electron microscopy (TEM) grid. 3D electron diffraction (3D ED) data were collected at room temperature on an ELDICO ED-1 electron diffractometer. The device is equipped with a LaB_6 source operating at an acceleration voltage of 160 kV (λ = 0.02851 Å). For the data collection and initial data assessment, the software Eldix was used. Crystals were located and centered in scanning transmission electron microscopy (STEM) imaging mode using a single diode brightfield detector and 3D ED data were collected in diffraction mode (parallel beam, beam size of approximately 700 nm) with a hybrid-pixel detector (Dectris QUADRO). 3D ED data collection was performed under continuous rotation with an angular step of 1° per frame and an exposure time of 1 s per frame. Data were collected over a large tilt range (−60° to +60°). 3D ED data were recorded with a diffraction resolution of *ca.* 1.1 Å. A total of eight data sets from eight individual crystals were collected. Data processing, evaluation and merging were done using the APEX4 software package.[55] The 3D ED data were indexed, integrated and merged using the APEX4 software package. Unit cell and space group resulted consistent among all the collected data sets. After unit cell determination, the 3D ED data were searched for additional domains and the frames were integrated and corrected for Lorentz effects, scan speed, background and absorption using SAINT[56] and SADABS.[57] Data from two individual crystals diffracting at highest resolution were merged. The resulting completeness of 94.5% allowed successful structure determination and stable refinement. Structure solution from the 3D ED data was carried out using ShelXT[32,33] and structure refinement was carried out using ShelXL integrated in the ShelXle[58] software. In the refinement calculations, atomic scattering factors and wavelength for electrons were used. Least squares refinement was carried out within the kinematical approximation by minimizing the function $\sum w(F_{obs}^2 - F_{calc}^2)^2$ with the ShelXL weighting scheme and using neutral electron scattering factors provided within the ShelXle software. Refinement of non-H atoms was carried out using anisotropic atomic displacement parameters, while H atoms were added subsequently with a riding model. The hydrogen atom at O5 in **R:3:F** and at O6 in **R:4:A** was fixed during refinement. PLATON for Windows was used to extract bonding information from crystal structure data.[59] Absorption corrections (Gaussian or analytical, as implemented in CrysAlisPro) were applied based on crystal morphology, selecting the method yielding optimal refinement results.

2.6. Infrared Spectroscopy. Fourier-transform infrared (FT-IR) spectra were obtained using a Bruker Tensor 37 spectrometer with an ATR unit at room temperature (25 °C), covering functional group identification and analysis of characteristic vibrational modes.

2.7. Thermogravimetric Analysis. Thermogravimetric analysis (TG) was performed for samples **R:1:A**, **R:1:F** and **R:2:A** on a Netzsch TG 209 F3 Tarsus with 10 K/min in a temperature range from 30 °C−600 °C.

2.8. Elemental Analysis. Elemental (CHN) analysis was performed for samples **R:1:A**, **R:1:F** and **R:2:A** with a Vario Micro Cube from Elementar Analysentechnik.

3. RESULTS

3.1. Structural Analysis and the Role of Hydrogen Bonds. One primary goal of our synthesis approach was to focus on sustainability with the intent to reduce solvent waste, avoid complex purification processes and pursue effective and high-yield syntheses. A mechanochemical synthesis thus has been chosen to gather respective multicomponent products, recognizing its potential to provide suitable, crystalline products with minimal environmental footprint.[60] A set of nine new binary and ternary **R** systems were synthesized and **R:1** revisited. All new phases were obtained via liquid-assisted grinding, except **R:3:F** which resulted from slow evaporation out of methanol. For all obtained bulk microcrystalline materials powder X-ray diffraction (PXRD) identified a new

https://doi.org/10.1021/acs.cgd.5c01261
Cryst. Growth Des. 2025, 25, 10482−10496

phase formation different from the starting components. Overviews of the experimental powder patterns of the binary systems and the ternary systems, each in comparison to pure **R**, are provided in Figure 1. Characteristic peaks are listed under each compound in Section 2. Comparisons of experimental data with simulated PXRD patterns obtained from single crystal data confirm the purity of the new systems (SI Figures S11−S19). **R:1:A**, **R:1:F** and **R:2:A** were structurally solely characterized by PXRD as no crystals suitable for a single crystal X-ray analysis could be obtained under various conditions due to weak diffraction capacity. For these products infrared spectroscopy, thermogravimetric analysis and elemental analysis were performed to provide insight into the molecular composition and corroborate the incorporation of the acid into the newly formed phase. The thermograms show a mass loss in three steps corresponding to each three components and thus suggesting formation of the ternary systems (see Figures S33−S35 in SI). This is in good agreement with the elemental analysis data (Table S3). The infrared spectra show changes in the carbonyl stretching region at approximately 1700 cm^{-1} as well as broadened O−H stretching bands at 2500−3300 cm^{-1}, indicating the presence of the acid components. These overlap with the existing imide stretching bands of the flavin, which concurrently appears as a result of the **R**···coformer interaction. Among the observed spectral changes, the COO^- stretching vibrations represent the most reliable indicators of the protonation via the acid component in the crystalline phase, with the asymmetric stretch appearing at 1550−1610 cm^{-1} and the symmetric stretch at 1380−1430 cm^{-1} (see Figures S5−S7 in SI).

A commonly applied guideline to estimate whether the molecular assembly will result in the formation of neutral cocrystals or salt-like species is based on the difference of the components' pK_a values. The resulting ΔpK_a (=pK_a(base) − pK_a(acid)) for the binary systems are ΔpK_a(**R**, **1**) = 0.31−0.17, ΔpK_a(**R**, **2**) = 1.69, ΔpK_a(**R**, **3**) = 0.85−0.73, ΔpK_a(**R**, **4**) = 2.41 based on the pK_a values in water at 20 °C (Table S1 in SI). These fall within the range of the salt/cocrystal continuum wherein a cocrystal or a salt is not indisputably defined. A bigger challenge emerges when multicomponent systems with more than two components are concerned. Here, as per usual procedure, the two components with highest and lowest pK_a values would be examined, being **R** and the respective acids. Yet from the crystal structure data discussed below it is evident that indeed the coformers are protonated. Thus, all possible pairwise ΔpK_a combinations were evaluated. In any case, while the ΔpK_a heuristic (>3 → salt, <0 → cocrystal, 0−3 → "continuum") would suggest predominantly ionic behavior for some pairs, our systems do not uniformly conform to this prediction. Values obtained from pK_a of the coformer and the respective acids range from near 0 (e.g., ΔpK_a(**4**, **A**) = 0.40) up to >3 (e.g., ΔpK_a(**1**, **F**) = 3.49−3.63). We therefore use ΔpK_a as a qualitative guide only; the actual protonation state in the solid is concluded from crystallographic metrics rather than from ΔpK_a alone.

Single crystals suitable for SCXRD analysis were obtained for six following systems: **R:2**, **R:3**, **R:4**, **R:3:A**, **R:3:F** and **R:4:A**. Phases consisting of two components show a neutral cocrystal character and are further referred to as binary cocrystals, similar to **R:1**. In **R:3:A**, **R:3:F** and **R:4:A** an observed proton transfer shifts the obtained multicomponent systems from neutral cocrystals to mixed state phases on the salt/cocrystal continuum.[37] No consistent terminology for multicomponent crystals containing both salt-like and cocrystal-like features has yet been established, often described simply as cocrystals, mixed ionized phases, ionic cocrystals with incorporated inorganic counterion or as being located somewhere on the salt/cocrystal continuum depending on differences of pK_a values.[37,61−63] Since, within this survey, strong multiple hydrogen bonds still remain the main force in the formation of the crystal architecture between neutral and charged parts, we propose to refer to these ternary systems as molecular ionic cocrystals.

All obtained crystal structures display alteration of the initial lattice arrangement of **R**, consistent with previous findings that coformers modify the native molecular packing of **R**, thus, impacting its structural and optical characteristics. The structures can be categorized depending on the occurring hydrogen-bonded motifs.

*3.1.1. Binary **R:1** and **R:2** Cocrystals—Tetrameric Hydrogen-Bonded Motifs.* **R:2** crystallizes in the triclinic space group $P\bar{1}$, with the asymmetric unit consisting of one of each molecular component (Z = 2). The crystal structure is stabilized by the intended and desired DAD hydrogen bonding motif with key interactions involving N−H···N and N−H···O hydrogen bonds as described in our prior study.[23] The therein reported structure was likewise resynthesized and compared in this work, here named **R:1**.

The intermolecular interactions in **R:2** establish a two-dimensional, nearly planar network between four formula units in a -**R**-**2**-**2**-**R**- arrangement along the crystallographic *c*-axis, with two **2** units stabilizing this arrangement via N10−H···N7 (2.962(3) Å) interactions, reinforcing the crystal lattice. The hydrogen-bonding pattern demonstrates the key bonding motif of the cocrystal's donor−acceptor framework. In fact, this very pattern is equivalently observable in **R:1** that analogously crystallizes in $P\bar{1}$ (Figure 2). The respective DAD motif features N10−H···O1 2.879(3) Å and N9−H···O2 2.977(3) Å distances, supported by N3−H···N6 interactions at 2.900(2) Å. Besides the aforementioned hydrogen bonded tetrameric motifs, notable additional propagation alongside the crystallographic *b*-axis is observable in **R:2** via N9−H···O1 contacts between the flavin and **2** component at 2.918(3) Å, facilitating a hydrogen-bonded chain-like network. While similar proximity of the amine group of **1** and the **R** carbonyl group in **R:1** is observable, the N9−H···O1 distance of 3.097(4) Å implies weaker interaction.

*3.1.2. Binary **R:3** and **R:4**—Trimeric Arrangement.* In continuation of the structural analyses, the focus is set on the two further obtained crystal structures, **R:3** and **R:4**. **R:3** crystallizes in the triclinic space group $P\bar{1}$. Again, a three-point recognition pattern involving the imide group and amine groups along the *c*-axis is observed, albeit, with a significantly different packing pattern. Here, each coformer entity undergoes two DAD interactions with flavin components from both sides, essentially resulting in a trimeric motif (Figure 3a). The N8−H···N12 interaction has a donor−acceptor distance of 2.893(7) Å, or 2.908(8) Å for N3−H···N11, respectively, emphasizing its role in that particular molecular alignment. The adjacent amide−amide interactions are quantified by a N14−H···O3 donor−acceptor distance of 2.912(7) Å and a N15−H···O4 distance of 2.994(7) Å, or N14−H···O1 (2.842(8) Å) and N13−H···O2 (2.970(9) Å) for the opposing molecular component. Yet, like **R:2**, hydrogen-bonded N−H···O interactions alongside the crystallographic *b*-axis initiate chain-like network patterns.

https://doi.org/10.1021/acs.cgd.5c01261
Cryst. Growth Des. 2025, 25, 10482−10496

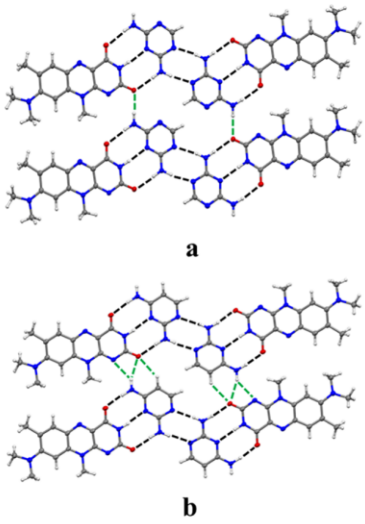

Figure 2. Comparison of **R:2** (**a**) and **R:1** (**b**) with highlighted structure stabilizing intermolecular interactions. Along the crystallographic *b*-axis, the carbonyl group of **R** and the amine of the coformer add to increased robustness of the packing, effectively initiating hydrogen-bonded chains. Viewed from the crystallographic *a*-axis.

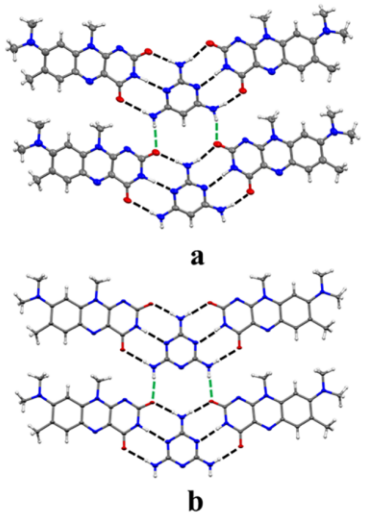

Figure 3. Comparison of **R:3** (**a**) and **R:4** (**b**) displaying the three-point recognition DAD pattern between **R** and coformer with hydrogen bonds shown in black dotted lines. Trimers are formed by two flavin units interacting from either side of the coformer. Trimers are linked via further N−H···O hydrogen bonds, indicated by green dotted line. Viewed along the crystallographic *a*-axis.

The **R:4** crystal structure displays resembling features. Based on ED measurements, structure determination yielded a crystal structure in monoclinic *C*2/*c* symmetry, with one flavin component and half a *N*-heterocycle manifesting the asymmetric unit. The emerging three-point recognition pattern is characterized by donor−acceptor distances at N6−H6A···O1 (2.98(5) Å), N1−H···N8 (2.91(5) Å) and N7−H7A···O2 (2.84 Å), located within the range of strong and directional hydrogen bonds. Additional orthogonal N−H···O hydrogen bonds support the structural stability and likely initiate molecular assemblance (Figure 3b).

*3.1.3. Structural Similarities of Ternary Systems **R:3:A**, **R:3:F** and **R:4:A**.* The ternary cocrystals **R:3:A** and **R:3:F** crystallize in a triclinic lattice, **R:4:A** in a monoclinic crystal lattice. Each system contains two acid molecules per **R**:coformer pair. Within this constellation both acid molecules interact only with the coformer unit. In particular, one acid entity initiates a proton transfer, increasing the electrostatic character of the formed charge-assisted hydrogen bond O4···H−N7^{+}. Figure 4 illustrates on the example of **R:3:A** how each coformer molecule is involved in the hydrogen-bonded DAD motif with a chromophore on the one side and into a DDD···AAA pattern with two acid entities on its protonated side. This pattern is likewise observable in **R:3:F** and **R:4:A**.

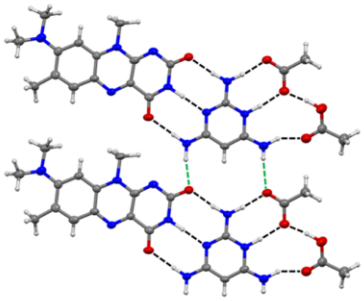

Figure 4. Intermolecular interactions in **R:3:A**. A three-point DAD recognition pattern between **R** and **3** entities. Further DDD···AAA interaction (black dotted lines) between the protonated side of **3** with two **A** molecules build a tetrameric motif including all three components. Tetramers linked via two N−H···O interactions (green dotted lines) propagate to chain arrangements. Viewed along the crystallographic *a*-axis.

The resulting N−H···O and N−H···N bonded donor−acceptor distances between **R** and coformer range between 2.8 and 3.0 Å, suggesting significant interaction strength and stabilizing character. Like the interactions of the DAD motif, the N−H···O bonds between coformer and acid molecules form a DDD···AAA three-point recognition pattern and range between 2.8 and 2.9 Å, which suggests their significant role with regards to stability contributions to the lattice.

3.2. Comparison and Structural Impact of Stacking Interactions. **R** possesses one aromatic ring (in the following referred to as **I**) and two nonaromatic heterocycles (the middle ring **II** and the imide group-containing ring **III**), paving pathways for both localized and delocalized interactions. Thus, our approach is to first identify the stacking interactions in pure **R** and compare similarities and differences in the cocrystal phases. In pure **R**, columnar stacking occurs between rings **I** and **II** at a distance ranging from 3.5 to 3.9 Å, propagating along the crystallographic *b*-axis. Parallel to the *ab*-plane, these

https://doi.org/10.1021/acs.cgd.5c01261
Cryst. Growth Des. 2025, 25, 10482−10496

columns arrange into tilted layers, adopting a tilt at a 26.64° angle in a herringbone-like packing motif. A comprehensive stacking pattern analysis of the obtained cocrystal structures reveals significant modification of the original interaction motif when incorporating the *N*-heterocycles. Yet again, within these modifications some commonalities are apparent. Table 1 shows the corresponding stacking distances measured from centroid distances of the respective rings. In **R:2** a coformer unit initiates slipped-stacked $\pi\cdots\pi$-motifs between ring **I** and the triazine-core of **2** at 3.5749(12) Å. Further, the **R**···**R** stacking pattern is modified as well. At around 3.4 Å, two flavin units form a nearly coplanar stacking of inversely oriented planes with significantly tighter centroid distances. This pattern is likewise present in **R:1** showing insignificant differences in bond lengths.

Table 1. Centroid Stacking Distances Obtained from Crystal Structure Data of R, Its Binary and Ternary Phases, Given in Ascending Order[a]

	interacting rings	$d_{centroids}$ (Å)		interacting rings	$d_{centroids}$ (Å)
R	II···III^{i}	3.5757(13)	**R:3:A**	III···III^{v}	3.358(3)
	II···III^{iv}	3.6280(13)		**3**···I^{i}	3.612(3)
R:1	II···II^{i}	3.3869(15)		III···II^{ix}	3.995(3)
	I···III^{i}	3.3948(15)	**R:3:F**	III···III^{i}	3.363(2)
	III···**1**^{ii}	3.5815(15)		I···**3**^{i}	3.6418(17)
	III···III^{ii}	3.9787(15)		II···III^{ii}	3.8932(16)
R:2	II···II^{i}	3.3842(13)	**R:4:A**	I···**4**^{iv}	3.473(3)
	I···III^{i}	3.3880(14)		**4**···III^{iv}	3.513(3)
	III···**2**^{i}	3.5749(12)		**4**···II^{i}	3.514(3)
R:3	II$_a$···II^{vi}[b]	3.373(3)			
	I$_a$···III^{vi}	3.390(3)			
	I$_a$···III^{vii}	3.461(3)			
	II$_a$···II^{viii}	3.580(3)			
	III$_b$···I^{vi}	3.636(3)			
	II$_b$···II^{vi}	3.662(3)			
	I$_b$···III^{viii}	3.731(3)			
R:4	I···II^{iii}	3.64(7)			

[a]The cut-off is set at <4.0 Å. Rings of **R** are referred to as **I**, **II** and **III** in all systems. [b]Two symmetrically inequivalent **R** units in **R:3** are indexed with a and b; (i) $1-x, 1-y, 1-z$ (ii) $2-x, 1-y, 1-z$ (iii) $3/2-x, 3/2-y, -z$ (iv) $1-x, -y, 1-z$ (v) $-x, -y, 1-z$ (vi) $1-x, 1-y, 2-z$ (vii) $x, y, 1+z$ (viii) $x, y, -1+z$ (ix) $-x, 1-y, 1-z$.

R:3 and **R:4**, on the other hand, in contrast to **R:1** and **R:2**, feature different modifications to the stacking pattern as there is no involvement of the coformer ring. The presence of **3** and **4**, respectively, results in shorter **R**···**R** stacking distances and rearrangement of the interacting rings. In **R:3**, rings **I** and **III′** and both middle rings **II** and **II′** of two molecular units interact in a range of ∼3.4 Å to ∼3.7 Å with slipped stacked arrangement, a motif similar to pure **R**. However, in **R:4** the structural rearrangement displays mere overlap of the benzene and middle ring, resulting in **I**-**II′** interactions. The imide ring system is not involved in any stacking motif in the set cutoff range of 4.0 Å. Noteworthy, while in **R** the stacking interactions form infinite columnar motifs, in **R:4** stacking dimers are laterally separated from each other. For the ternary systems, entirely different patterns arise. The crystal packing is significantly altered and so are the stacking arrangement sequences. The original **R**···**R** stacks are partially disrupted by the incorporated coformers in both **R:3** ternary systems. In **R:3:A** a slipped stacked arrangement of the coformer ring with the **R** benzene ring **I** facilitates $\pi\cdots\pi$ interactions at 3.612(3) Å. Two **R** molecules interact here via cofacial arrangement of rings **III**-**III′** (3.358(3) Å) and **II**-**III′** (3.995(3) Å) which further contributes to the robustness of the crystal architecture. Likewise, **R:3:F** shows identical patterns, merely of differing lengths, with the $\pi\cdots\pi$ interaction between **I** and the coformer ring at 3.6418(17) Å as well as the **III**-**III′** (3.363(2) Å) and

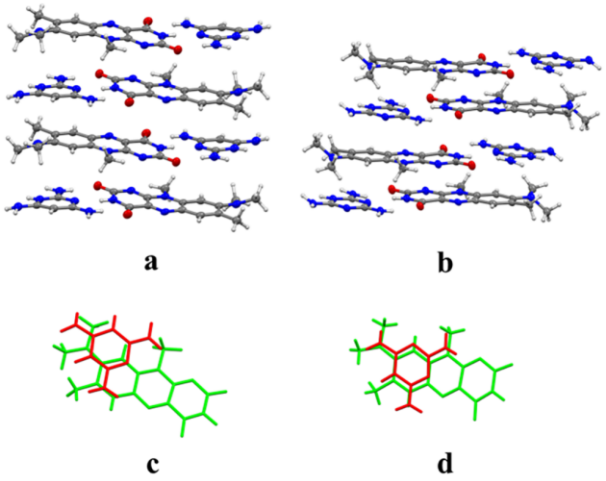

Figure 5. Stacking arrangements in **R:3:A** (a) and **R:4:A** (b). Alternating **R**···coformer layers propagate along the crystallographic *a*-axis, viewed along the *b*-axis. Viewed along the *a*-axis, stronger cofacial arrangement of the flavin aromatic ring and the coformer is evident in the **R:4:A** cocrystal (d) than in the **R:3:A** cocrystal (c). For better clarity in (c, d), the flavin is colored green and the coformer red.

https://doi.org/10.1021/acs.cgd.5c01261
Cryst. Growth Des. 2025, 25, 10482−10496

Table 2. Overview of the Crystal Structures Including Electron Density $\rho(r)$ at Bond Critical Points (BCP), Individual Calculated Binding Energies (BE), Calculated Binding Energies R···X[a] and Binding Energies from BSM Calculations

	electron density $\rho(r)$ at BCP (10^{-2} e/Å^3)		individual calculated BE (kJ/mol)	calculated BE R···X[a] (kJ/mol)	calculated BE BSMs (kJ/mol)
R	N2−H···O2^{i}	2.42	−19.50	−39.00	−39.00
	O2···H−N2^{i}	2.42	−19.50		
R:1	O1···H−N9	2.56	−20.84	−65.40	−165.81
	N2−H···N6	2.78	−22.89		
	O2···H−N8	2.65	−21.67		
R:2	O1···H−N10	2.27	−18.07	−56.48	−150.67
	N3−H···N6	2.76	−22.68		
	O2···H−N9	2.02	−15.73		
R:3	O3$_a$···H−N14	2.72	−22.26	−69.75$_a$−64.56$_b$	−134.31
	N8$_a$−H···N12	2.10	−16.53		
	O4$_a$···H−N15	3.65	−30.96		
	O1$_b$···H−N14	3.58	−30.38		
	N6$_b$−H···N11	1.70	−12.80		
	O2$_b$···H−N13	2.62	−21.38		
R:4	O1···H−N7	2.34	−18.74	−52.68	−105.35
	N1−H···N8	2.48	−20.08		
	O2···H−N6	1.82	−13.85		
R:3:A	O1···H−N9	2.50	−20.29	−83.22	−260.38
	N3−H···N6	3.96	−33.85		
	O2···H−N8	3.44	−29.04		
	O3···H−N9′	2.57	−20.92		
	O4···H−N7$^{+\prime}$	3.85	−57.20		
	O6···H−N10′	3.88	−32.43		
	O4^{-}···H−O5″	7.48	−66.65		
R:3:F	O1···H−N9	2.09	−16.40	−57.45	−225.89
	N3−H···N6	2.51	−20.33		
	O2···H−N8	2.55	−20.71		
	O3···H−N9′	3.49	−29.50		
	O4···H−N7$^{+\prime}$	2.95	−45.48		
	O6···H−N10′	2.41	−19.41		
	O4^{-}···H−O5″	8.27	−74.06		
R:4:A	O1···H−N10	1.77	−13.39	−59.50	−239.53
	N3−H−N6	3.09	−25.73		
	O2···H−N9	2.51	−20.38		
	O5···H−N11′	2.45	−19.79		
	O4···H−N7$^{+\prime}$	3.69	−55.73		
	O3···H−N10′	3.02	−25.10		
	O4^{-}···H−O7″	8.84	−79.41		

[a]X—interacting partner involved in hydrogen bonding; ′—binding energies between acid molecule and coformer; ″—binding energies between two acid molecules in the crystal structure interacting in the BSM model; indices a and b—two symmetrically inequivalent molecules of **R** in **R:3**; (i) 2 − *x*, 1 − *y*, 1 − *z*.

II-III′ (3.8932(16) Å) interactions (see Figure 5 for comparison).

Isolated, these interactions may not seem connected, however, in a -**3**-**R**-**R**- sequence columns of stacking patterns do propagate alongside the crystallographic *a*-axis. In **R:4:A**, the coformer units almost cofacially stack over the aromatic ring **I** of the **R** units initiating strong $\pi\cdots\pi$ stacking interactions at 3.473(3) Å. These stack columns propagate along the crystallographic *a*-axis, solely connected via aromatic ring interactions. Remarkably, no short **R**···**R** interactions are present in this structure.

3.3. QTAIM and NCIplot Analyses. To quantify the strength of intermolecular hydrogen bonding motifs across the investigated crystal structures, a topological analysis of the electron density based on Bader's quantum theory of atoms in molecules (QTAIM) is conducted on the seven available crystal structures **R**, **R:1**, **R:2**, **R:3**, **R:4**, **R:3:A**, **R:3:F** and **R:4:A**. Focus is particularly set on the intermolecular interaction involving the imide group of **R**, where electron density values at the calculated bond critical points (BCPs) are evaluated, further converted into binding energies (BE)[48] (Table 2).

In the crystal structure of pure **R**, no intermolecular DAD motifs are present. Instead, the dimeric motif built of two **R** molecules interacting via amide−amide hydrogen bonding serves as a reference for further comparisons of obtained binding energies of the hydrogen bonds. The N−H···O hydrogen bonds here each are characterized by binding energies of −19.50 kJ/mol, resulting in a total HB stabilization energy of −39.00 kJ/mol within the **R**···**R** dimer. These values correspond to the expected energies of strong hydrogen bonds according to Desiraju and Steiner,[64] based on the proposed classification by Jeffrey.[65] Upon cocrystallization with different *N*-heterocyclic coformers, an increase in hydrogen bonding

https://doi.org/10.1021/acs.cgd.5c01261
Cryst. Growth Des. 2025, 25, 10482−10496

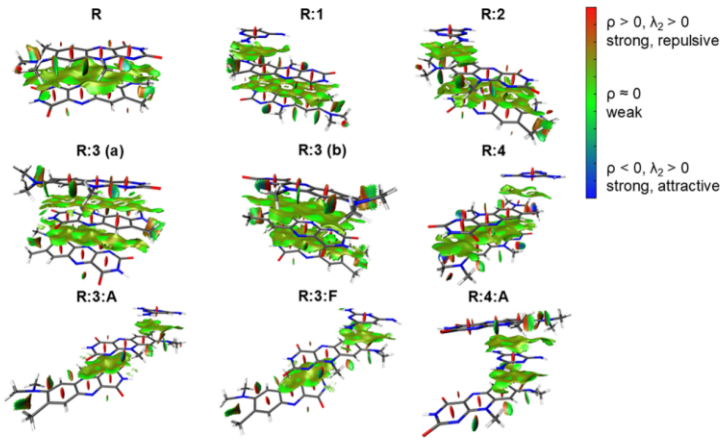

Figure 6. RDG isosurfaces (cutoff = 0.6) of **R** and all cosystems. For **R:3** two models for each symmetrically inequivalent unit a and b are shown. Green areas indicate the location of the stacking interaction between the involved regions.

strength is observed, underlining one driving factor for reassembly. The calculated total binding energies of the resulting DAD motifs are set in a range between −52.68 and −83.22 kJ/mol. To allow a more meaningful comparison of the intermolecular binding strengths across structurally distinct cocrystals, Vasylyeva et al. in 2012 introduced the concept of basic structural motifs (BSMs).[66] In contrast to a simple summation of individual hydrogen bond energies, the BSM approach focuses on the identification of the energetically dominant aggregation units within the crystal lattice—such as dimers, trimers or tetramers—that govern the overall lattice stabilization. Given the considerable variation in hydrogen bonding networks between herein reported binary and ternary cocrystals, BSM-based analysis facilitates a normalization of binding energies across different supramolecular topologies. For instance, the tetrameric assemblies observed in **R:1** and **R:2** exhibit cumulative BSM binding energies of −165.81 and −150.67 kJ/mol, respectively, while the trimeric binary systems **R:3** and **R:4** display somewhat lower BSM binding energies of −134.31 and −105.35 kJ/mol. All selected BSM models are listed in SI (Figure S23).

The most pronounced stabilization is observed in the ternary molecular ionic cocrystals, mainly due to the energetic benefit of the hydrogen bonds between two acid molecules forming the basic structural motif. A substantial contribution is provided by the charge-assisted O−H···O$^-$ and N$^+$−H···O hydrogen bonds ranging from −66.65 to −79.41 kJ/mol and −45.48 to −57.20 kJ/mol, respectively. According to Desiraju and Steiner, the former fall within the range of very strong hydrogen bonds, albeit close to the lower boundary of this classification,[64] while the latter can be considered strong. In these systems, the calculated BSM binding energies exceed −225.89 kJ/mol, reaching up to −260.38 kJ/mol for **R:3:A**. These findings highlight the cooperative strengthening of the hydrogen bonding network, especially upon incorporation of the third component acid molecules. This effect likely originates from spatial complementarity between electrophilic and nucleophilic regions, as shown by Shukla et al., who demonstrated that the formation and stability of supramolecular motifs are driven by directional electrostatic interactions between complementary charge-depleted and charge-concentrated regions.[67]

A qualitative NCIplot analysis helps to classify the nature of the intermolecular interactions between stacking regions of overlapping ring fragments, providing insight into the local electron density topology. Based on sign(λ_2)ρ descriptors, a relative quantitative analysis is performed to reflect the character of the interactions. For this, based on crystal structure data for each structure, stacking patterns surrounding a selected chromophore unit were isolated and an NCI analysis performed. The nature of the noncovalent interactions is illustrated by color-coded isosurfaces based on the sign(λ_2)ρ descriptor. Blue surfaces represent strong attractive interactions, while red regions highlight repulsive interactions resulting from steric hindrance or close-contact repulsion. Weak dispersive interactions are characterized by green isosurface areas and sign(λ_2)ρ values close to zero.[39] In the case of the investigated stacks, the latter is expected. In Figure 6 the visualized isosurfaces (cutoff value = 0.6) verify the presence and position of the NCI surface regions between stacks of **R** and/or coformer units with sign(λ_2)ρ values between −0.01 and 0.01 au. The corresponding reduced density gradients (RDG) scatterplots (see Figures S24−S32 in SI) display distinct spikes in aforementioned sign(λ_2)ρ regions, indicative of weak dispersive interactions.

Pronounced surfaces, not only in the flavin−flavin overlap zone but likewise between the coformer fragment and the flavin, are observable in **R:1** and **R:2**. In contrast, **R:3** and **R:4** exhibit more segmented NCI regions between the coformer and the flavin. This is in accordance with the tilted and shifted molecular arrangement in the crystal structures. Also, in the ternary systems green isosurfaces between the chromophore and the coformer are allocated, especially above and below the benzene ring (ring **I**) of the flavin and the adjacent heterocyclic plane. In contrast to the binary systems, within the **R**···**R** stacks the surfaces do not spread along all three flavin rings and are herewith less pronounced. This reflects a clear displacement of the stacking interaction focus on **R**···coformer arrangements. It

https://doi.org/10.1021/acs.cgd.5c01261
Cryst. Growth Des. 2025, 25, 10482−10496

is to be noted that in the case of **R:3** two independent stacking motifs involving different molecular orientations were analyzed separately, thus resulting in two separate NCI topologies.

3.4. Photophysical Characteristics. Under standard daylight conditions, distinct color differences are observable for each of the ten individual multicomponent compounds compared to pure **R**. In addition to our previously published observations[23] not only the range of colors is expanded from dark red up to bright orange but the systems also expose a degree of selectivity in their solid-state emission characteristics. Ternary systems predominantly emit in the orange-green region, whereas binary systems favor the light red region of the electromagnetic spectrum. Notably, both types of systems exhibit a consistent blue-shift relative to the starting material, highlighting a significant modification in their photophysical properties.

The CIE 1931 coordinates (Table 3) assess the perceived color of the luminescence of all systems, visualized in the CIE diagram (Figure 7). To facilitate comparison across different cocrystals, all experimental emission spectra (Figure 8), which will be discussed below, were normalized to their respective maxima prior to the CIE transformation resulting in a fine, distinct distribution in high wavelength area. The perceived colors of the binary cocrystals are detected in the red area, while the remaining ternary ionic cocrystal phases, with the exception of **R:2:A**, are distributed in the orange color range, **R** serving as a reference middle ground.

Table 3. Emission Maxima ($\lambda_{Em,max}$), Excitation Maxima ($\lambda_{Ex,max}$), Full Width at Half Maximum (FWHM), Stokes Shift and CIE 1931 Coordinates of R and Obtained Cocrystal Phases

	$\lambda_{Em,max}$ (nm)	$\lambda_{Ex,max}$ (nm)	FWHM (Gaussian fit)	Stokes shift (nm)	Stokes shift (cm^{-1})	CIE 1931 coordinates (x, y)
R	733	633	158	100	2155	0.64, 0.35
R:3	668	622	97	46	1107	0.70, 0.30
R:4	657	582	102	75	1961	0.68, 0.31
R:1	652	613	141	39	976	0.65, 0.35
R:2	646	583	80	63	1673	0.68, 0.32
R:2:A	617	575	50	42	1184	0.64, 0.35
R:1:F	596	542	85	54	1570	0.59, 0.41
R:1:A	590	545	89	45	1399	0.58, 0.42
R:3:A	585	556	76	29	892	0.57, 0.45
R:3:F	581	560	81	21	654	0.55, 0.44
R:4:A	575	539	78	36	1162	0.52, 0.48

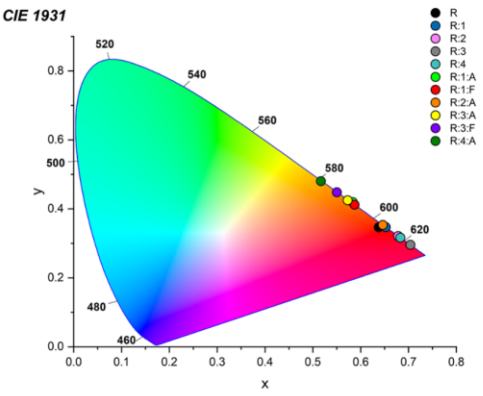

Figure 7. CIE 1931 color diagram including all obtained crystal phases.

The solid-state emission bands of the binary cocrystals (Figure 8) emerge in the range between 668 and 646 nm. **R:2** shows the strongest spectral shift $\lambda_{Em,max}$ = 646 nm relative to pure **R** at 733 nm. As for the ternary systems, the most pronounced emission band shift is assigned to **R:4:A** at $\lambda_{Em,max}$ = 575 nm. In comparison to the emission band of pure **R**, the bands appear narrower as evident from calculations of full width at half-maximum (FWHM) distributions of Gaussian fitted plots listed in Table 3. Moreover, the mixed ionized systems emit even narrower bands than their binary cocrystal analogues. The bandwidth decreases from 158 nm in **R** up to 80 nm in **R:2** and further to 50 nm in **R:2:A**. Among the systems the Stokes shift narrows down in comparison to the 100 nm Stokes shift of pure chromophore **R**. While the binary cocrystals show moderate shift between 39 and 75 nm, the molecular ionic cocrystals display smaller Stokes shifts, with **R:3:F** exhibiting the lowest value of 21 nm.

4. DISCUSSION

4.1. Structural Analysis of Roseolumiflavin Multicomponent Systems. Examination of the crystal structures highlights a clear evolution in molecular packing across the binary and ternary systems. **R:1** and **R:2** adopt face-to-face π-stacking of **R** units with nearly coplanar **R**···coformer arrangements stabilized by tetrameric hydrogen-bonded DAD motifs, whereas **R:3** and **R:4** exhibit tilted and slipped stacking arrangements. A more pronounced alteration in the stacking pattern emerges in the ternary molecular ionic cocrystals **R:3:A**, **R:3:F** and **R:4:A**. Here, the coformers rearrange to form π-stacking interactions with the flavin unit, leading to reorganization of the original stacking arrangement. This incorporation of the coformers into the π-stacking increases structural complexity and likely contributes to stronger modulated optical responses compared to the binary cocrystals. Additionally, a proton transfer from acid molecules to the *N*-heterocyclic coformer further enhance the ring electron density and modify the overall electronic distribution of the respective systems. This is in line with the carried out NCIplot analyses. The isosurfaces generated from the electron density confirm weak dispersive interactions between stacked units, primarily visualized as green, flat-shaped surfaces in the sign(λ_2)ρ range of approximately −0.01 to +0.01 au, indicative of the van der Waals forces. In **R:1** and **R:2** these isosurfaces are continuous and spatially extended between nearly cofacially arranged flavin moieties, which correlate with tighter stacking distances and enhanced overlap. Further, coformer ring fragments also establish interaction with the aromatic ring of **R**. In contrast, in **R:3** and **R:4** due to tilted or slipped geometric arrangement, the NCI isosurfaces between the coformer ring and the flavin units appear less continuous and spatially confined. This reduced surface overlap may contribute to the less pronounced emission shifts observed for these compounds. Notably, in the investigated ternary systems, the dominant NCI surfaces relocate from stacked flavin units to regions between the coformer and the chromophore. Observed realignment of dispersion-dominated interactions visually confirms the disruption of **R**···**R** stacking replaced by

https://doi.org/10.1021/acs.cgd.5c01261
Cryst. Growth Des. 2025, 25, 10482−10496

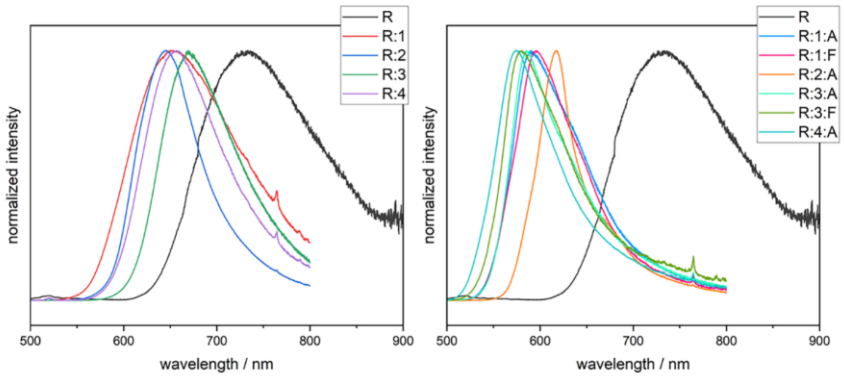

Figure 8. Solid-state emission bands of **R** compared to blue-shifted ternary systems (left) and binary systems (right). All phases were excited at λ_{Ex} = 423 nm, except for **R:1:A** and **R:3:A** (λ_{Ex} = 400 nm). The spikes at 765 nm result from higher diffraction orders of the monochromator.

alternating **R**···coformer stacking motifs. These findings underline how weak noncovalent forces support the new supramolecular arrangement in ternary systems. Complementing these weak dispersive forces, strong hydrogen bonds emerge as the dominant structure-directing interactions within the crystal lattices. This is evident from the calculated binding energies of the crystal structures (see Table 3). Not only is the initial N−H···O interaction in **R** classified as a strong hydrogen bond, but the DAD motif in the cocrystals also contributes substantial stabilization ranging from −52.68 to −83.22 kJ/mol. Moreover, a trend of increased stabilization of the BSMs is observable from binary to ternary systems. The energetic environment as a stabilizing factor of the BSMs exceeds values over −105.35 kJ/mol for **R:4**, up to −165.81 kJ/mol for **R:1** regarding the binary systems. The BSMs of the ternary systems reach values as high as −260.38 kJ/mol in the case of **R:3:A**. The consistently high binding energies across all systems affirm that strong, classical hydrogen bonds are the dominant driving interactions for the multicomponent crystal formation. The ternary structures demonstrate that hydrogen bonding is both energetically significant due to their partial ionized character and also capable of reorganizing entire packing motifs, replacing the prior **R**···**R** interactions and resulting in distinctly altered packing arrangements. The particular arrangement and positioning of the acid molecules in the same layer of the coformer and chromophore interaction pattern in each ternary system grants interactions from the coformer via a quasi-three-point recognition framework. Thereby, the acid molecules substitute the stabilizing role of the coformer or of a flavin's imide group of the binary system counterpart (see **R:1** and **R:2** for the former, **R:3** and **R:4** for the latter). Further, the arrangement of the acids is particularly noteworthy, as the resulting interaction motif closely resembles the three-point recognition pattern, essentially mirroring it on the opposite side of the coformer and thereby enhancing the overall robustness of the system. Evidentially, the incorporation of the acid molecules is crucial for stabilization of the ternary systems, as their presence fundamentally shapes the supramolecular framework. These findings align with the recent survey on flavin-based supramolecular systems by Mouli and Mishra, where intermolecular interactions dictate gel formation and stimuli-responsive behavior.[68] Therein, π-stacking variations and molecular modifications influence material properties, particularly in redox-active environments and the role of hydrogen bonds in stabilizing supramolecular structures is highlighted. Furthermore, reported protonation effects contribute to molecular rearrangement, underscoring the significance of hydrogen-bonding networks in controlling structural and electronic characteristics, similar to our findings on molecular ionic cocrystals.

Despite their differences, all resulting cocrystals exhibit consistent hydrogen-bonded DAD substitution patterns with comparable π-stacking motifs. This suggests that the number of nitrogen atoms in the coformer ring has no significant influence on the crystal packing or supramolecular architecture, underlining the dominant role of the substitution pattern over the heterocycle's electronic structure. The data underline the crucial role of hydrogen bonding not merely as a stabilizing force, but as a determinant of crystal architecture. This agrees with Desiraju and Steiner's characteristics of strong and, especially, very strong hydrogen bonds[64] for charge-assisted ones as present in the **R** crystal systems. To date and to the best of our knowledge unprecedented for flavin-based cocrystals, these structural rearrangements highlight the potential of ternary assembly to tailor emission by direct π-interactions involving the coformer itself.

4.2. Spectroscopic Properties. Spectroscopic analysis indicated substantial shifts in emission wavelengths across the cocrystals, with all systems exhibiting shorter wavelengths compared to pure **R**. The sequence of emission bands from longest to shortest wavelengths follows the order **R**, **R:3**, **R:4**, **R:1**, **R:2**, **R:2:A**, **R:1:F**, **R:1:A**, **R:3:A**, **R:3:F** and **R:4:A**. This progression suggests that cocrystallization with selected coformers and specific stacking motifs directly influence the emission profile, including additional impact when acid molecules are involved. The observed structural motifs correlate with these spectroscopic shifts, especially in the arrangement and degree of stacking modes. Cocrystals such as **R:1** and **R:2**, with face-to-face stacking patterns and nearly planar layers, exhibit shorter wavelength emissions than **R**, suggesting that closer stacking enhances electronic coupling, leading to blue-shifted emissions. Meanwhile, **R:3** and **R:4** with their tilted and slipped stacking patterns show emissions closer to that of **R** which matches the reduced electronic

https://doi.org/10.1021/acs.cgd.5c01261
Cryst. Growth Des. 2025, 25, 10482−10496

overlap observed in these cocrystals. Molčanov and Kojić-Prodić describe similar weak interactions in nonaromatic systems, where multipolar electrostatic forces and dispersion effects dominate.[69] The ternary ionic cocrystals, in particular **R:4:A**, where the chromophore stacking is entirely replaced by **R**···coformer interactions, displays the most pronounced blue-shifts possibly due to the altered stacking arrangement involving closer π-stacking with the coformer. The coformer's direct involvement in stacking interactions appears to strengthen electronic interactions by reducing stacking distances, especially where **R**···**R** stacking is replaced by alternating **R**···coformer layers. This pattern implies that shorter stacking distances and direct coformer involvement are key drivers of further blue-shift. In addition, with increased structural complexity, from the pure compound **R** to the binary systems and the ternary systems, a trend of narrowing emission bands is observed. This supports the notion that modified stacking geometries lead to more suppressed nonradiative decay pathways due to rigid packing.

Yet, it is crucial to acknowledge that direct correlations between structural packing and emission properties are constrained to a subset of the studied ternary systems. Specifically, **R:3:F, R:3:A** and **R:4:A** exhibit the strongest blue-shifts, suggesting a significant impact of their stacking motifs and protonation effects on fluorescence behavior. However, due to the smaller emission shifts in the remaining obtained ternary systems, their contributions to the broader structure−property framework remain unclarified. This inherent limitation in our interpretation is to be noted, as the exact role of molecular packing and acid interactions across all ternary structures cannot be generalized with the same level of confidence. Instead, our conclusions rely on observed trends and approximated correlations rather than definitive cause-effect relationships for all remaining systems.

4.3. Influence of Coformer Selection on Emission Control. The observed variation in emission maxima, bandwidth and Stokes shifts highlights the pivotal role of coformer selection in fine-tuning the optical properties of roseolumiflavin-based cocrystals. Regarding the binary cocrystals, a substantial hypsochromic shift of the emission band maxima is observed for **R:1** ($\Delta\lambda_{Em,max}$ = 81 nm) and **R:2** ($\Delta\lambda_{Em,max}$ = 87 nm) which adopt nearly coplanar face-to-face stacking motifs, enhancing electronic coupling between the stacked chromophores. The pronounced blue-shift in emission maxima reflects a modification of the excited-state energy profile due to tight stacking and the resulting electronic delocalization. Beyond binary systems, ternary systems introduce an additional tuning parameter: protonation-induced charge redistribution within the lattice. The incorporation of proton-donating components such as acetic acid or formic acid leads to partial protonation of the *N*-heterocyclic coformers, thereby modifying their electronic density and interaction profile. This observation cannot be fully rationalized based on ΔpK_a values alone. For the binary systems, the calculated ΔpK_a values (0.17−2.57) fall within the so-called salt/cocrystal continuum. The multiple acid−base pairs coexisting in the ternary systems make the situation even more complex while further the coformers rather than **R** are protonated, despite ΔpK_a considerations suggesting otherwise. Consequently, the systems studied here are best described as mixed ionized phases and for clarification of the partially ionized character, we chose to label them as molecular ionic cocrystals. In these protonated systems, this adjustment is reflected in both the hydrogen-bonding network and stacking arrangements. The coformers both participate directly in stacking interactions with the flavin units and further effectively replace the original **R**···**R** stacking motifs. As a result, the chromophores become separated by alternating coformer layers, enforcing a more defined, periodic stacking pattern. This facilitates more narrowing of the emission bands and smaller Stokes shifts, which point to reduced vibronic coupling, presumably resulting from a more rigid excited-state geometry within the crystal lattice.

Additionally, QTAIM analysis confirms that ternary systems exhibit the strongest binding energies within their basic structural motifs, with up to −260.38 kJ/mol for **R:3:A**. Complementary NCIplot visualizations show dense green isosurfaces between **R** and coformer units, indicative of dispersion-dominated but spatially extensive interactions, indicating a cooperative effect of dominant hydrogen bonding and supportive stacking interaction.

The results discussed point out that a strategic combination of a coformer with a complementary proton-donating component, if needed, allows for tailored optical responses, providing fine control over color purity and emission characteristics. The CIE profiles shown above illustrate how each emission color can be finely adjusted, from deep red to orange. This further demonstrates that photophysical properties such as emission wavelength, bandwidth and Stokes shift can be modulated in a targeted and predictable manner, establishing a versatile design framework adaptable to individual use-case. Within the series investigated, **R:3:A** emerges as the most effective system in terms of color purity, offering both sharp emission and a relatively small Stokes shift of 892 cm^{-1}.

5. CONCLUSION

In this study, we build upon our previous work on cocrystallization of **R** and significantly expand those findings by exploring ternary systems, implementing a new level of complexity in the supramolecular assembly, with the aim to establish the fundamental structure−property relationships. By careful combination of structural studies on micro- and single-crystalline multicomponent systems, topological analysis of the crystal packing, quantification of the involved intermolecular interaction via quantum chemical calculations and NCI analysis followed by steady-state spectroscopy we provide a multifaceted perspective on roseolumiflavin's cocrystallization capability and limitations. Observed structural variations are linked to spectroscopic emission band shifts relative to pure **R**. The novel systems not only exhibit new spectral bands but also reveal a degree of selectivity in their emission characteristics. Here, the emission trends show that the selection of the coformer and particular stacking arrangements are important factors in determining spectral shifts of **R** into orange-green range for ternary and light red region for binary cocrystals.

Moderate organic acid molecules introduced as a third component play an active role in crystal arrangement processes, particularly through protonation and hydrogen bond rearrangements. Ternary systems in this case represent mixed intermediate states, molecular ionic cocrystals, where neutral and charged molecular entities are combined into the crystalline lattice via multiple intermolecular interactions. In all discussed binary and ternary systems, a strong hydrogen bonded three-point recognition DAD pattern is integrated which replaces the original dimeric motif of **R**···**R**. Hydrogen

https://doi.org/10.1021/acs.cgd.5c01261
Cryst. Growth Des. 2025, 25, 10482−10496

bonds clearly dominate structure formation in all reported systems in conjunction with the calculated energy values for BSMs. Binary cocrystals adopt face-to-face or tilted stacking in contrast to the ternary systems which exhibit a gradual transition in stacking behavior. The inclusion of proton-donating components disrupts the original flavin stacking motifs, replacing **R**···**R** interactions with coformer-mediated π-stacking. This in turn leads to reduced electron delocalization between flavin molecules, contributing to the largest spectral shifts observed in this study.

Our findings showcase how cocrystallization fine-tunes the spectral properties of **R** as well as provide a deeper understanding about the effects of subtle variations in stacking and protonation on photophysical behavior. Both binary and ternary cocrystals can be used to systematically fine-tune π-stacking and emission properties in flavin-based systems. Coformer selection is crucial to modulate the impact on stacking modes, allowing targeted adjustment of emission wavelength and band narrowing. Moreover, in the ternary systems, the positioning of the acid molecules appears to replicate aspects of the DAD-type recognition motif observed in the binary systems. Although not forming a true DAD array, the spatial mimicry suggests that embedded acid molecules can play an active role in reinforcing or replacing directional interactions. This finding highlights an underexplored aspect of crystal engineering: the structural involvement of these cocrystallized species in modulating both molecular packing and electronic environments, herein examined for roseolumiflavin-based systems. This may pave the way for advancements in optoelectronics, sensing and material engineering when flavins are the object of interest. This is complemented by sustainability factors being included into synthesis considerations as apart from one all multicomponent systems can be produced via green mechanochemical synthesis. By integrating it into flavin-based cocrystallization, a solvent-free, scalable and environmentally friendly method for tailoring optical materials is established.

■ ASSOCIATED CONTENT

Supporting Information

The Supporting Information is available free of charge at https://pubs.acs.org/doi/10.1021/acs.cgd.5c01261.

> Additional PXRD patterns, crystallographic data tables, pK_a values, IR spectra, full solid-state emission and excitation spectra, thermal data (TGA) and elemental analyses, BSM models, and RDG surfaces (PDF)

Accession Codes

Deposition Numbers 2482849 and 2482922−2482926 contain the supplementary crystallographic data for this paper. These data can be obtained free of charge via the joint Cambridge Crystallographic Data Centre (CCDC) and Fachinformationszentrum Karlsruhe Access Structures service.

■ AUTHOR INFORMATION

Corresponding Author

Vera Vasylyeva − *Molecular Crystal Engineering Laboratory, Institute for Inorganic and Structural Chemistry, Heinrich-Heine University Düsseldorf, 40225 Düsseldorf, Germany;* orcid.org/0000-0001-7734-7406; Email: vera.vasylyeva-shor@hhu.de

Authors

Takin Haj Hassani Sohi − *Molecular Crystal Engineering Laboratory, Institute for Inorganic and Structural Chemistry, Heinrich-Heine University Düsseldorf, 40225 Düsseldorf, Germany;* orcid.org/0000-0001-6902-077X

Lea Pongratz − *Molecular Crystal Engineering Laboratory, Institute for Inorganic and Structural Chemistry, Heinrich-Heine University Düsseldorf, 40225 Düsseldorf, Germany*

Felix Maaß − *Molecular Crystal Engineering Laboratory, Institute for Inorganic and Structural Chemistry, Heinrich-Heine University Düsseldorf, 40225 Düsseldorf, Germany*

Sarah Merzenich − *Molecular Crystal Engineering Laboratory, Institute for Inorganic and Structural Chemistry, Heinrich-Heine University Düsseldorf, 40225 Düsseldorf, Germany*

Laura Samperisi − *ELDICO Scientific, 4123 Allschwil, Switzerland*

Constantin Czekelius − *Laboratory for Asymmetric Synthesis and Catalysis, Institute for Organic Chemistry and Macromolecular Chemistry, Heinrich-Heine University Düsseldorf, 40225 Düsseldorf, Germany;* orcid.org/0000-0002-2814-8686

Complete contact information is available at: https://pubs.acs.org/10.1021/acs.cgd.5c01261

Author Contributions

The manuscript was written through contributions of all authors. All authors have given approval to the final version of the manuscript.

Funding

Roseolumiflavin synthesis and SC-XRD analyses were funded by the Deutsche Forschungsgemeinschaft (DFG, German Research Foundation)—396890929/GRK 2482 and 440366605.

Notes

The authors declare no competing financial interest.

■ ACKNOWLEDGMENTS

We thank Jun.-Prof. Dr. Markus Suta for providing spectroscopic data of two products.

■ ABBREVIATIONS

PXRD, powder X-ray diffraction; SCXRD, single crystal X-ray diffraction; **R**, roseolumiflavin; **1**, 2,4-diaminopyrimidine; **2**, 2,4,6-triaminopyrimidine; **3**, 2,4,6-triaminopyrimidine; **4**, 2,4,6-triamino-1,3,5-triazine; **A**, acetic acid; **F**, formic acid; IR, infrared; QTAIM, quantum theory of atoms in molecules; CIE, Commission internationale de l'éclairage; LAG, liquid-assisted grinding; NCI, noncovalent interactions; DAD, donor−acceptor−donor; TGA, thermogravimetric analysis; BE, binding energy; BSM, basic structural motif

■ REFERENCES

(1) Sun, L.; Yang, F.; Zhang, X.; Hu, W. Stimuli-responsive behaviors of organic charge transfer cocrystals: recent advances and perspectives. *Mater. Chem. Front.* **2020**, *4* (3), 715−728.

(2) Dar, A. A.; Malik, A. A. Photoluminescent organic crystals and co-crystals. *J. Mater. Chem. C* **2024**, *12* (27), 9888−9913.

(3) Yan, D.; Evans, D. G. Molecular crystalline materials with tunable luminescent properties: from polymorphs to multi-component solids. *Mater. Horiz.* **2014**, *1* (1), 46−57.

(4) Jiang, M.; Zhen, C.; Li, S.; Zhang, X.; Hu, W. Organic Cocrystals: Recent Advances and Perspectives for Electronic and Magnetic Applications. *Front. Chem.* **2021**, *9*, No. 764628.
(5) Lu, B.; Fang, X.; Yan, D. Luminescent Polymorphic Co-crystals: A Promising Way to the Diversity of Molecular Assembly, Fluorescence Polarization, and Optical Waveguide. *ACS Appl. Mater. Interfaces* **2020**, *12* (28), 31940−31951.
(6) Wuest, J. D. Molecular solids: Co-crystals give light a tune-up. *Nat. Chem.* **2012**, *4* (2), 74−75.
(7) Barman, D.; Annadhasan, M.; Bidkar, A. P.; Rajamalli, P.; Barman, D.; Ghosh, S. S.; Chandrasekar, R.; Iyer, P. K. Highly efficient color-tunable organic co-crystals unveiling polymorphism, isomerism, delayed fluorescence for optical waveguides and cell-imaging. *Nat. Commun.* **2023**, *14* (1), No. 6648.
(8) Yao, Z.-F.; Wang, J.-Y.; Pei, J. Control of $\pi-\pi$ Stacking via Crystal Engineering in Organic Conjugated Small Molecule Crystals. *Cryst. Growth Des.* **2018**, *18* (1), 7−15.
(9) Desiraju, G. R. Crystal engineering: from molecule to crystal. *J. Am. Chem. Soc.* **2013**, *135* (27), 9952−9967.
(10) Liu, J.-J.; Liu, T.; Xia, S.-B.; He, C.-X.; Cheng, F.-X.; Lin, M.-J.; Huang, C.-C. Cocrystals of naphthalene diimide with naphthalene derivatives: A facile approach to tune the luminescent properties. *Dyes Pigm.* **2018**, *149*, 59−64.
(11) Huang, S.; Xu, J.; Peng, Y.; Guo, M.; Cai, T. Facile Tuning of the Photoluminescence and Dissolution Properties of Phloretin through Cocrystallization. *Cryst. Growth Des.* **2019**, *19* (12), 6837−6844.
(12) Ouyang, J.; Liu, L.; Li, Y.; Chen, M.; Zhou, L.; Liu, Z.; Xu, L.; Shehzad, H. Cocrystals of carbamazepine: Structure, mechanical properties, fluorescence properties, solubility, and dissolution rate. *Particuology* **2024**, *90*, 20−30.
(13) Liu, Y.; Zeng, Q.; Zou, B.; Liu, Y.; Xu, B.; Tian, W. Piezochromic Luminescence of Donor-Acceptor Cocrystals: Distinct Responses to Anisotropic Grinding and Isotropic Compression. *Angew. Chem., Int. Ed.* **2018**, *57* (48), 15670−15674.
(14) Fan, S.; Liu, X.; Yao, S.; Xing, G.; Xu, X.; Shi, G.; Song, Z.; Feng, G. Organic Luminescent Cocrystals Based on Benzotriazole Derivatives: Synthesis, Characterization, Crystal Structure and Fluorescence Behavior. *Chem. - Eur. J.* **2025**, *31* (11), No. e202403889.
(15) Zhang, J.; Chen, J.; Yang, B.; Ma, S.; Yin, L.; Liu, Z.; Xiang, W.; Liu, H.; Zhao, J.; Sheng, P. Energy Level, Crystal Morphology and Fluorescence Emission Tuning in Cocrystals via Molecular-Level Engineering. *Chem. - Eur. J.* **2023**, *29* (10), No. e202202915.
(16) Jiang, Z.; Zhang, Y.; Du, C.; Khan, A.; Usman, R.; Wang, M. Modulation of Solid-State Fluorescence Properties for Anthracene Chalcone Heterocyclic Compounds by Charge-Transfer Cocrystal Self-Assembly: Molecular Stacking Mode and DFT Analysis. *Cryst. Growth Des.* **2024**, *24* (14), 6036−6050.
(17) Zhang, C.; Ning, Z.; Gong, Z.; Zhou, L.; Xu, L.; He, F.; Gao, Z.; Heng, J. Y. Y.; Du, S.; Ouyang, J. Uncovering the Molecular Stacking Patterns and Tuning Fluorescence Properties of Organic Molecular Crystals through Cocrystallization. *Cryst. Growth Des.* **2025**, *25* (8), 2465−2475.
(18) Wu, J.; Liu, W.; Ge, J.; Zhang, H.; Wang, P. New sensing mechanisms for design of fluorescent chemosensors emerging in recent years. *Chem. Soc. Rev.* **2011**, *40* (7), 3483−3495.
(19) Yan, D.; Bučar, D.-K.; Delori, A.; Patel, B.; Lloyd, G. O.; Jones, W.; Duan, X. Ultrasound-assisted construction of halogen-bonded nanosized cocrystals that exhibit thermosensitive luminescence. *Chem. - Eur. J.* **2013**, *19* (25), 8213−8219.
(20) Yang, S.; Li, Y.; Kang, F.; Li, F.; Zhao, S.; Sun, Y.; Zhang, C.; Zhang, Q. Recent Progress in Organic Cocrystal-Based Superlattices and Their Optoelectronic Applications. *Adv. Funct Mater.* **2025**, *35*, No. 2504976, DOI: 10.1002/adfm.202504976.
(21) Park, S. K.; Kim, J. H.; Ohto, T.; Yamada, R.; Jones, A. O. F.; Whang, D. R.; Cho, I.; Oh, S.; Hong, S. H.; Kwon, J. E.; Kim, J. H.; Olivier, Y.; Fischer, R.; Resel, R.; Gierschner, J.; Tada, H.; Park, S. Y. Highly Luminescent 2D-Type Slab Crystals Based on a Molecular Charge-Transfer Complex as Promising Organic Light-Emitting Transistor Materials. *Adv. Mater.* **2017**, *29* (36), No. 1701346, DOI: 10.1002/adma.201701346.
(22) Zhang, J.-X.; Zhao, S.; Jiang, J.-H.; Lv, Z.-J.; Luo, J.; Shi, Y.; Lu, Z.; Wang, X.-D. Organic Cocrystal Alloys: From Three Primary Colors to Continuously Tunable Emission and Applications on Optical Waveguides and Displays. *Small* **2024**, *20* (33), No. e2400313.
(23) Sohi, T. H. H.; Maass, F.; Czekelius, C.; Suta, M.; Vasylyeva, V. Co-crystallization of organic chromophore roseolumiflavin and effect on its optical characteristics. *CrystEngComm* **2022**, *24* (41), 7315−7325.
(24) Sohi, T. H. H.; Maass, F.; Czekelius, C.; Vasylyeva, V. A Comparison Study of Roseolumiflavin Solvates: Structural and Energetic Perspective on Their Stability. *Crystals* **2023**, *13* (10), No. 1512.
(25) Yan, D.; Delori, A.; Lloyd, G. O.; Friščić, T.; Day, G. M.; Jones, W.; Lu, J.; Wei, M.; Evans, D. G.; Duan, X. A cocrystal strategy to tune the luminescent properties of stilbene-type organic solid-state materials. *Angew. Chem., Int. Ed.* **2011**, *50* (52), 12483−12486.
(26) Li, M.; Li, Z.; Zhang, Q.; Peng, B.; Zhu, B.; Wang, J.; Liu, L.; Mei, X. Fine-Tuning the Colors of Natural Pigment Emodin with Superior Stability through Cocrystal Engineering. *Cryst. Growth Des.* **2018**, *18* (10), 6123−6132.
(27) Sun, Y.; Ye, Y.; Qi, L.; Bai, Y.; Hu, X.; Xuanyuan, S.; Xie, C. Tuning Solid-State Emission of 9-Anthraldehyde through Cocrystal Engineering. *Crystals* **2023**, *13* (4), No. 595.
(28) Zhang, X.; Li, Z.; Han, R.; Lin, J.; Li, M.; Zhou, J.; Wu, S.; Gong, J. Modulation of luminescence properties of cocrystals composed of amino substituted dimethyl phthalates and 1,2,4,5-tetracyanobenzene by crystal engineering. *CrystEngComm* **2024**, *26* (22), 2976−2988.
(29) Ardila-Fierro, K. J.; Hernández, J. G. Sustainability Assessment of Mechanochemistry by Using the Twelve Principles of Green Chemistry. *ChemSusChem* **2021**, *14* (10), 2145−2162.
(30) Arfelis, S.; Martín-Perales, A. I.; Nguyen, R.; Pérez, A.; Cherubin, I.; Len, C.; Malpartida, I.; Bala, A.; Fullana-I-Palmer, P. Linking mechanochemistry with the green chemistry principles: Review article. *Heliyon* **2024**, *10* (14), No. e34655.
(31) Fantozzi, N.; Volle, J.-N.; Porcheddu, A.; Virieux, D.; García, F.; Colacino, E. Green metrics in mechanochemistry. *Chem. Soc. Rev.* **2023**, *52* (19), 6680−6714.
(32) Friščić, T.; Mottillo, C.; Titi, H. M. Mechanochemistry for Synthesis. *Angew. Chem.* **2020**, *132* (3), 1030−1041.
(33) Braga, D.; Maini, L.; Grepioni, F. Mechanochemical preparation of co-crystals. *Chem. Soc. Rev.* **2013**, *42* (18), 7638−7648.
(34) Solares-Briones, M.; Coyote-Dotor, G.; Páez-Franco, J. C.; Zermeño-Ortega, M. R.; de la O Contreras, C. M.; Canseco-González, D.; Avila-Sorrosa, A.; Morales-Morales, D.; Germán-Acacio, J. M. Mechanochemistry: A Green Approach in the Preparation of Pharmaceutical Cocrystals. *Pharmaceutics* **2021**, *13* (6), No. 790, DOI: 10.3390/pharmaceutics13060790.
(35) Wenger, L. E.; Hanusa, T. P. Synthesis without solvent: consequences for mechanochemical reactivity. *Chem. Commun.* **2023**, *59* (96), 14210−14222.
(36) Komisarek, D.; Taskiran, E.; Vasylyeva, V. Maleic Acid as a Co-Former for Pharmaceutically Active GABA Derivatives: Mechanochemistry or Solvent Crystallization? *Materials* **2023**, *16* (6), No. 2242, DOI: 10.3390/ma16062242.
(37) Childs, S. L.; Stahly, G. P.; Park, A. The salt-cocrystal continuum: the influence of crystal structure on ionization state. *Mol. Pharmaceutics* **2007**, *4* (3), 323−338.
(38) Bader, R. F. W. *Atoms in Molecules: A Quantum Theory*, The International Series of Monographs on Chemistry; Clarendon Press, 2003; Vol. *22*.
(39) Johnson, E. R.; Keinan, S.; Mori-Sánchez, P.; Contreras-García, J.; Cohen, A. J.; Yang, W. Revealing noncovalent interactions. *J. Am. Chem. Soc.* **2010**, *132* (18), 6498−6506.
(40) OriginLab Corporation. OriginPro.

(41) Lu, T.; Chen, F. Multiwfn: a multifunctional wavefunction analyzer. *J. Comput. Chem.* **2012**, *33* (5), 580−592.
(42) Lu, T. A comprehensive electron wavefunction analysis toolbox for chemists, Multiwfn. *J. Chem. Phys.* **2024**, *161* (8), No. 082503, DOI: 10.1063/5.0216272.
(43) Becke, A. D. Density-functional thermochemistry. III. The role of exact exchange. *J. Chem. Phys.* **1993**, *98* (7), 5648−5652.
(44) Lee, C.; Yang, W.; Parr, R. G. Development of the Colle-Salvetti correlation-energy formula into a functional of the electron density. *Phys. Rev. B* **1988**, *37* (2), 785−789.
(45) Vosko, S. H.; Wilk, L.; Nusair, M. Accurate spin-dependent electron liquid correlation energies for local spin density calculations: a critical analysis. *Can. J. Phys.* **1980**, *58* (8), 1200−1211.
(46) Stephens, P. J.; Devlin, F. J.; Chabalowski, C. F.; Frisch, M. J. Ab Initio Calculation of Vibrational Absorption and Circular Dichroism Spectra Using Density Functional Force Fields. *J. Phys. Chem. A* **1994**, *98* (45), 11623−11627.
(47) Frisch, M. J.; Trucks, G. W.; Schlegel, H. B.; Scuseria, G. E.; Robb, M. A.; Cheeseman, J. R.; Scalmani, G.; Barone, V.; Petersson, G. A.; Nakatsuji, H.; Li, X.; Caricato, M.; Marenich, A. V.; Bloino, J.; Janesko, B. G.; Gomperts, R.; Mennucci, B.; Hratchian, H. P.; Ortiz, J. V.; Izmaylov, A. F.; Sonnenberg, J. L.; Williams-Young, D.; Ding, F.; Lipparini, F.; Egidi, F.; Goings, J.; Peng, B.; Petrone, A.; Henderson, T.; Ranasinghe, D.; Zakrzewski, V. G.; Gao, J.; Rega, N.; Zheng, G.; Liang, W.; Hada, M.; Ehara, M.; Toyota, K.; Fukuda, R.; Hasegawa, J.; Ishida, M.; Nakajima, T.; Honda, Y.; Kitao, O.; Nakai, H.; Vreven, T.; Throssell, K.; Montgomery, J. A., Jr.; Peralta, J. E.; Ogliaro, F.; Bearpark, M. J.; Heyd, J. J.; Brothers, E. N.; Kudin, K. N.; Staroverov, V. N.; Keith, T. A.; Kobayashi, R.; Normand, J.; Raghavachari, K.; Rendell, A. P.; Burant, J. C.; Iyengar, S. S.; Tomasi, J.; Cossi, M.; Millam, J. M.; Klene, M.; Adamo, C.; Cammi, R.; Ochterski, J. W.; Martin, R. L.; Morokuma, K.; Farkas, O.; Foresman, J. B.; Fox, D. J. *Gaussian 16, Revision C.01*, Gaussian, Inc. 2016.
(48) Emamian, S.; Lu, T.; Kruse, H.; Emamian, H. Exploring Nature and Predicting Strength of Hydrogen Bonds: A Correlation Analysis Between Atoms-in-Molecules Descriptors, Binding Energies, and Energy Components of Symmetry-Adapted Perturbation Theory. *J. Comput. Chem.* **2019**, *40* (32), 2868−2881.
(49) Humphrey, W.; Dalke, A.; Schulten, K. VMD: visual molecular dynamics. *J. Mol. Graphics* **1996**, *14* (1), 33−38.
(50) Macrae, C. F.; Sovago, I.; Cottrell, S. J.; Galek, P. T. A.; McCabe, P.; Pidcock, E.; Platings, M.; Shields, G. P.; Stevens, J. S.; Towler, M.; Wood, P. A. Mercury 4.0: from visualization to analysis, design and prediction. *J. Appl. Crystallogr.* **2020**, *53* (Pt 1), 226−235.
(51) Oxford Diffraction /Agilent Technologies UK Ltd.. CrysAlisPRO.
(52) Sheldrick, G. M. SHELXT—integrated space-group and crystal-structure determination. *Acta Crystallogr., Sect. A:Found. Adv.* **2015**, *71* (Pt 1), 3−8.
(53) Sheldrick, G. M. A short history of SHELX. *Acta Crystallogr., Sect. A:Found. Crystallogr.* **2008**, *64* (Pt1), 112−122.
(54) Dolomanov, O. V.; Bourhis, L. J.; Gildea, R. J.; Howard, J. A. K.; Puschmann, H. OLEX2: a complete structure solution, refinement and analysis program. *J. Appl. Crystallogr.* **2009**, *42* (2), 339−341.
(55) Bruker AX Inc.. *Apex Suite of Crystallographic Software, APEX4*, 2022.
(56) Bruker Analytical X-Ray Systems. *SAINT*, 2012.
(57) Bruker AX Inc.. *SADABS*, 2016.
(58) Hübschle, C. B.; Sheldrick, G. M.; Dittrich, B. ShelXle: a Qt graphical user interface for SHELXL. *J. Appl. Crystallogr.* **2011**, *44* (Pt 6), 1281−1284.
(59) Spek, A. L. Single-crystal structure validation with the program PLATON. *J. Appl. Crystallogr.* **2003**, *36* (1), 7−13.
(60) Pagola, S. Outstanding Advantages, Current Drawbacks, and Significant Recent Developments in Mechanochemistry: A Perspective View. *Crystals* **2023**, *13* (1), No. 124.
(61) Losev, E. A.; Boldyreva, E. V. A salt or a co-crystal − when crystallization protocol matters. *CrystEngComm* **2018**, *20* (16), 2299−2305.
(62) Bhogala, B. R.; Basavoju, S.; Nangia, A. Tape and layer structures in cocrystals of some di- and tricarboxylic acids with 4,4′-bipyridines and isonicotinamide. From binary to ternary cocrystals. *CrystEngComm* **2005**, *7* (90), 551−562.
(63) Wang, T.; Stevens, J. S.; Vetter, T.; Whitehead, G. F. S.; Vitorica-Yrezabal, I. J.; Hao, H.; Cruz-Cabeza, A. J. Salts, Cocrystals, and Ionic Cocrystals of a "Simple" Tautomeric Compound. *Cryst. Growth Des.* **2018**, *18* (11), 6973−6983.
(64) Desiraju, G.; Steiner, T. *The Weak Hydrogen Bond: In Structural Chemistry and Biology*, IUCr Monographs on Crystallography; Oxford University Press, 2001; Vol. 9.
(65) Jeffrey, G. A. *An Introduction to Hydrogen Bonding*, Topics in Physical Chemistry; Oxford University Press, 1997.
(66) Vasylyeva, V.; Shishkin, O. V.; Maleev, A. V.; Merz, K. Crystal Structures of Fluorinated Pyridines from Geometrical and Energetic Perspectives. *Cryst. Growth Des.* **2012**, *12* (2), 1032−1039.
(67) Shukla, R.; Aubert, E.; Brezgunova, M.; Lebègue, S.; Fourmigué, M.; Espinosa, E. The origin of synthons and supramolecular motifs: beyond atoms and functional groups. *IUCrJ* **2025**, *12* (Pt 3), 334−357.
(68) Vinod Mouli, M. S. S.; Mishra, A. K. Flavin based supramolecular gel displaying multi-stimuli triggered sol-gel transition. *Org. Biomol. Chem.* **2023**, *21* (27), 5622−5628.
(69) Molčanov, K.; Kojić-Prodić, B. Towards understanding π-stacking interactions between non-aromatic rings. *IUCrJ* **2019**, *6* (Pt 2), 156−166.

Electronic Supplementary Information for "Tuning Molecular Assembly and Optical Properties via Co-Crystallization: a Case Study of Roseolumiflavin in Binary and Ternary Multicomponent Systems"

Takin Haj Hassani Sohi[a], Lea Pongratz[a], Felix Maaß[a], Sarah Merzenich[a], Laura Samperisi[b], Constantin Czekelius[c], Vera Vasylyeva[a*]

a: Molecular Crystal Engineering Laboratory, Institute for Inorganic and Structural Chemistry, Heinrich-Heine University Düsseldorf, Universitätsstrasse 1, 40225 Düsseldorf, Germany

b: ELDICO Scientific, c/o Switzerland Innovation Park Basel Area AG, Hegenheimermattweg 167 A, 4123 Allschwil, Switzerland

c: Laboratory for Asymmetric Synthesis and Catalysis, Institute for Organic Chemistry and Macromolecular Chemistry, Heinrich-Heine University Düsseldorf, Universitätsstrasse 1, 40225 Düsseldorf, Germany

1. pK_a values

Table S1. Acid dissociation constants (pKa) of **R**, co-formers **1**, **3**, **4**, **A**, **F** at 20 °C, of **2** at 25 °C, and calculated ΔpK_a values for selected pairs. Literature values are indicated by superscripts.

	R	**1**	**2**	**3**	**4**	**A**	**F**
pK_a	7.57	7.26[1], 7.4[2]	5.88[3]*	6.72[2], 6.84[1]	5.16[1]	4.76	3.77
		R, **1**	**R**, **2**	**R**, **3**	**R, 4**	**R**, **A**	**R**, **F**
ΔpK_a		0.31 - 0.17	1.69	0.85 - 0.73	2.41	2.81	3.80
		1, **A**	**2**, **A**	**3**, **A**	**4**, **A**		
ΔpK_a		2.50 - 2.64	1.12	1.96 - 2.02	0.40		
		1, **F**	**2**, **F**	**3**, **F**	**4**, **F**		
ΔpK_a		3.49 - 3.63	2.11	2.95 - 3.01	1.39		

* The corresponding K_b was measured at 25 °C as reported in [3].

pK_a of **R** was derived from the experimentally measured pH value and the known concentration c_0 using the equilibrium expression $K_a=[H^+]^2/(c_0 - [H^+])$, with $[H^+]=10^{-pH}$. For a solution containing 2.03 mg of the compound (M_W = 285.31 g·mol^{-1}) in 30 mL of water ($c_0 = 2.37 \cdot 10^{-4}$ M) and a measured pH of 5.60, this yields pK_a=7.57.

2. Infrared Spectroscopy

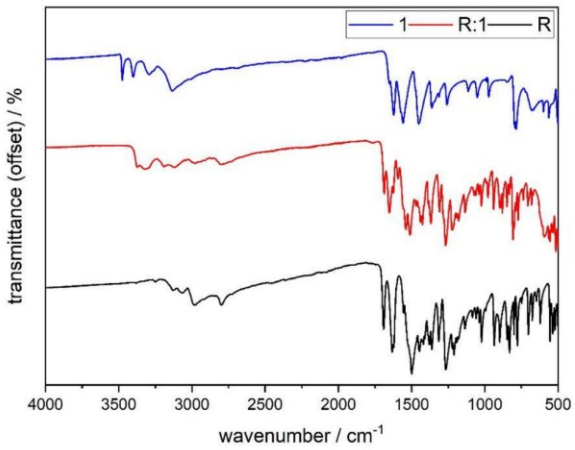

Figure S1. Infrared spectrum (ATR) of **R:1**, recorded from 500 to 4000 cm^{-1}, displayed in comparison to **R** and **1**.

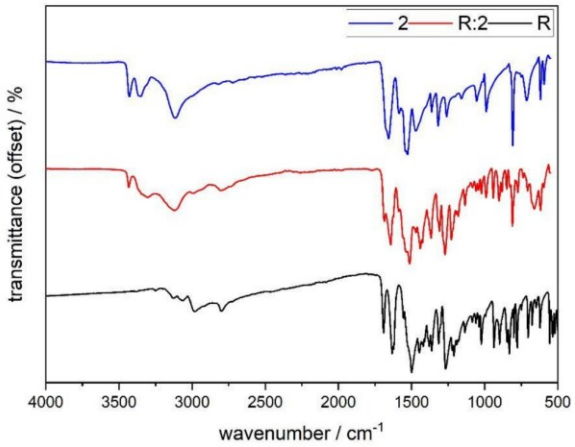

Figure S2. Infrared spectrum (ATR) of **R:2**, recorded from 500 to 4000 cm^{-1}, displayed in comparison to **R** and **2**.

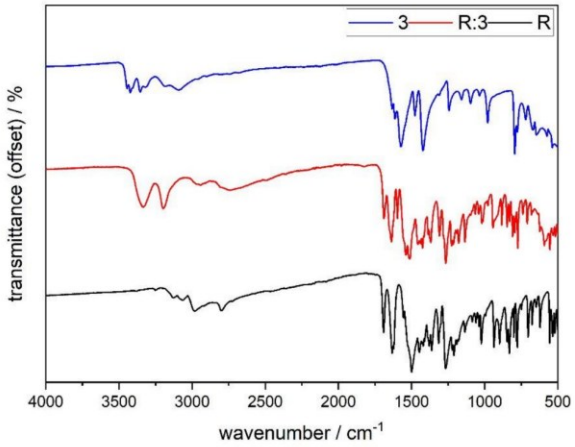

Figure S3. Infrared spectrum (ATR) of **R:3**, recorded from 500 to 4000 cm^{-1}, displayed in comparison to **R** and **3**.

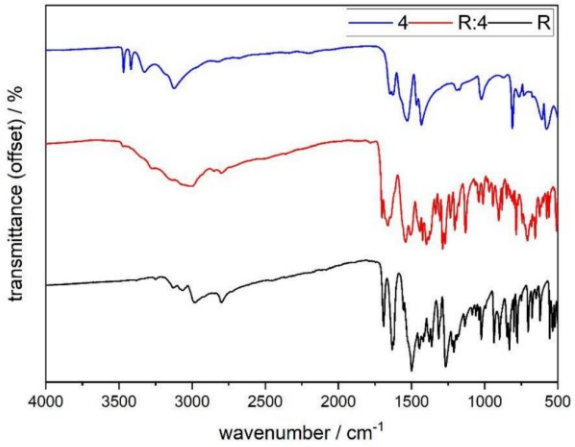

Figure S4. Infrared spectrum (ATR) of **R:4**, recorded from 500 to 4000 cm^{-1}, displayed in comparison to **R** and **4**.

Following **Figures S5–S10** present the IR spectra of the ternary systems containing acetic acid (**A**) and formic acid (**F**), together with the spectra of the pure acids for comparison. The characteristic C=O stretching bands of the acids at ca. 1700 cm^{-1} overlap with those of the flavin and partially with the C=N vibrations of the co-formers, preventing a clear identification of the band shifts. However, changes in the high-wavenumber region indicate the formation of N–H interactions,

while variations in the shape and intensity of the C=O and C–O bands further support the formation of the ternary systems.

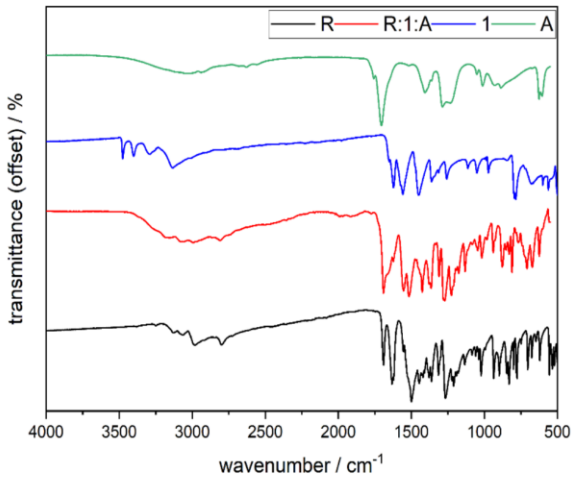

Figure S5. Infrared spectrum (ATR) of **R:1:A**, recorded from 500 to 4000 cm^{-1}, displayed in comparison to **R**, **A** and **1**.

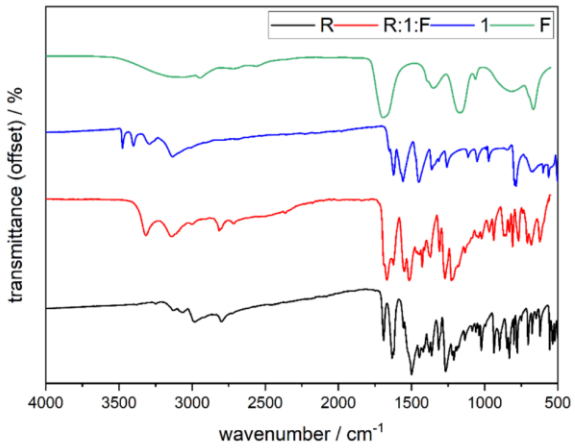

Figure S6. Infrared spectrum (ATR) of **R:1:F**, recorded from 500 to 4000 cm^{-1}, displayed in comparison to **R**, **F** and **1**.

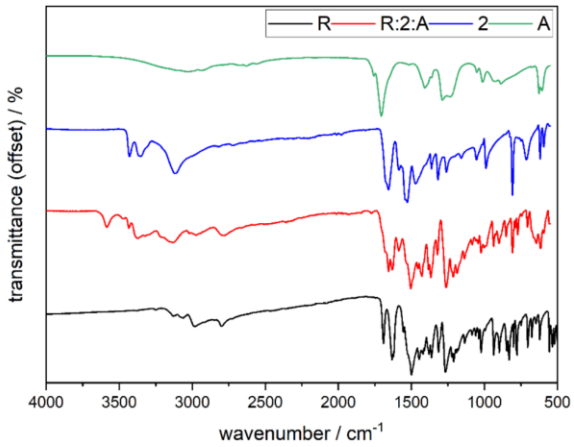

Figure S7. Infrared spectrum (ATR) of **R:2:A**, recorded from 500 to 4000 cm^{-1}, displayed in comparison to **R**, **A** and **2**.

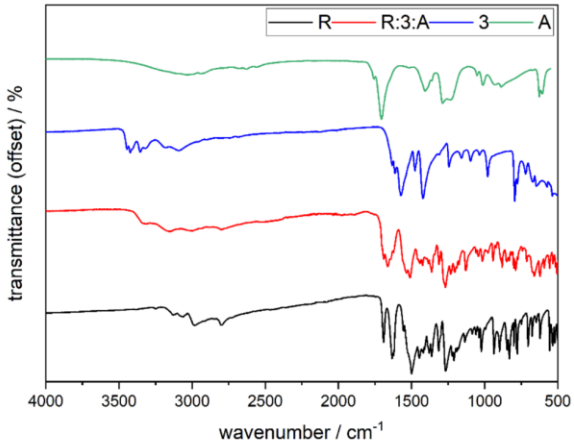

Figure S8. Infrared spectrum (ATR) of **R:3:A**, recorded from 500 to 4000 cm^{-1}, displayed in comparison to **R**, **A** and **3**.

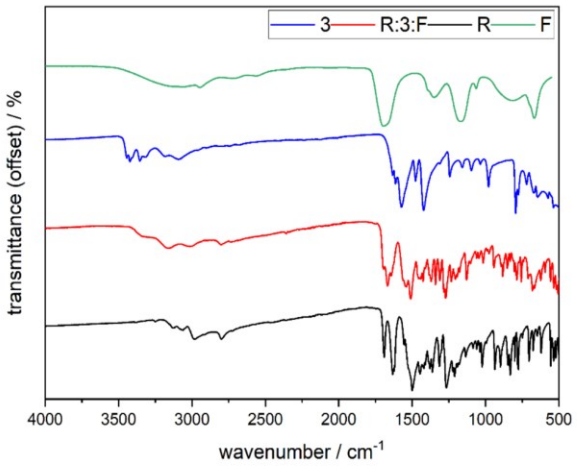

Figure S9. Infrared spectrum (ATR) of **R:3:F**, recorded from 500 to 4000 cm^{-1}, displayed in comparison to **R**, **F** and **3**.

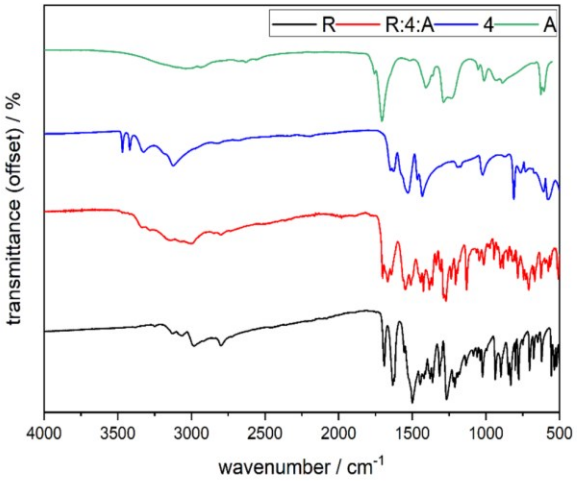

Figure S10. Infrared spectrum (ATR) of **R:4:A**, recorded from 500 to 4000 cm^{-1}, displayed in comparison to **R**, **A** and **4**.

3. Crystallographic Tables & Powder X-Ray Diffraction (PXRD)

Table S2. Crystallographic Tables of **R:4**, **R:2**, **R:3**, **R:3:A**, **R:3:F** and **R:4:A**

Identification code	**R:2**	**R:3**	**R:4***	**R:3:A**	**R:3:F**	**R:4:A**
CCDC deposition No.	2482925	2482923	2482849	2482926	2482922	2482924
Chemical Formula	$C_{14}H_{15}N_5O_2$, $C_3H_5N_5$	$2(C_{14}H_{15}N_5O_2)$, $C_4H_7N_5$	$2(C_{14}H_{15}N_5O_2)$, $C_3H_6N_6$	$C_{14}H_{15}N_5O_2$, $C_4H_8N_5$, $C_2H_4O_2$, $C_2H_3O_2$	$C_{14}H_{15}N_5O_2$, $C_4H_8N_5$, CH_2O_2, CHO_2	$C_{14}H_{15}N_5O_2$, $C_3H_7N_6$, $C_2H_4O_2$, $C_2H_3O_2$
Empirical formula	$C_{17}H_{20}N_{10}O_2$	$C_{32}H_{37}N_{15}O_4$	$C_{31}H_{36}N_{16}O_4$	$C_{22}H_{30}N_{10}O_6$	$C_{20}H_{26}N_{10}O_6$	$C_{21}H_{29}N_{11}O_6$
Formula weight	396.43	695.76	696.76	530.56	502.51	531.55
Temperature/K	100.0(2)	100.00(10)	298(2)	100.00(10)	100.00(10)	293(2)
Crystal system	triclinic	triclinic	monoclinic	triclinic	triclinic	monoclinic
Space group	*P*-1	*P*-1	*C*2/*c*	*P*-1	*P*-1	$P2_1/c$
a/Å	7.9437(3)	8.2060(14)	15.1(3)	7.3834(7)	7.3091(5)	6.9308(4)
b/Å	8.3605(4)	13.780(2)	8.18(15)	8.2310(7)	8.2170(6)	8.1084(5)
c/Å	14.9910(7)	14.556(3)	26.1(5)	22.264(2)	21.0127(14)	43.058(3)
α/°	90.516(4)	78.933(14)	90	92.702(7)	88.024(6)	90
β/°	104.323(4)	83.249(14)	101.14(5)	93.050(8)	89.921(5)	92.344(6)
γ/°	113.173(4)	75.852(14)	90	115.480(9)	64.686(7)	90
Volume/Å^3	880.48(7)	1562.1(5)	3165(101)	1216.0(2)	1140.02(15)	2417.8(3)
Z	2	2	4	2	2	4
ρ_{calc}g/cm^3	1.495	1.479	1.462	1.449	1.464	1.460
μ/mm^{-1}	0.881	0.859	0	0.913	0.942	0.932
F(000)	416	732	560	560	528	1120
Crystal size/mm^3	0.077 × 0.031 × 0.015	0.033× 0.021 × 0.013	-	0.078 × 0.06 × 0.04	0.1 × 0.041 × 0.032	0.147 × 0.046 × 0.041
Radiation	Cu Kα (λ = 1.54184 Å)	Cu Kα (λ = 1.54184 Å)	electrons (λ = 0.02508 Å)	Cu Kα (λ = 1.54184 Å)	Cu Kα (λ = 1.54184 Å)	Cu Kα (λ = 1.54184 Å)
2Θ range for data collection/°	6.128 - 158.748	6.204 -134.154	0.112 - 1.41	7.978 - 144.992	11.922 – 157.624	8.22 - 135.998
Index ranges	-10 ≤ h ≤ 9, -10 ≤ k ≤ 10, -19 ≤ l ≤ 18	-9 ≤ h ≤ 9, -16 ≤ k ≤ 14, -17 ≤ l ≤ 17	-14 ≤ h ≤ 14, -8 ≤ k ≤ 8, -25 ≤ l ≤ 25	-7 ≤ h ≤ 9, -10 ≤ k ≤ 10, -27 ≤ l ≤ 27	-9 ≤ h ≤ 7, -10 ≤ k ≤ 10, -23 ≤ l ≤ 26	-7 ≤ h ≤ 8, -6 ≤ k ≤ 9, -51 ≤ l ≤ 51
Reflections collected	10586	16854	4352	13513	12956	12845
Independent reflections	3499	5463	1484	4614	4506	4354
Data/restraints/parameters	3499/0/342	5463/1/499	1484/264/237	4614/39/454	4506/1/429	4354/1/383
Goodness-of-fit on F^2	1.026	0.969	1.056	0.975	0.978	1.098
Final R indexes [I>=2σ (I)]	R_1 = 0.0477 wR_2 = 0.1127	R_1 = 0.0833, wR_2 = 0.1712	R_1 = 0.2492, wR_2 = 0.5791	R_1 = 0.0685 wR_2 = 0.1354	R_1 = 0.0615 wR_2 = 0.1541	R_1 = 0.0984 wR_2 = 0.2571
Final R indexes [all data]	R_1 = 0.0803 wR_2 = 0.1275	R_1 = 0.2075 wR_2 = 0.2261	R_1 = 0.3372, wR_2 = 0.6544	R_1 = 0.1861 wR_2 = 0.1956	R_1 = 0.1038 wR_2 = 0.1804	R_1 = 0.1324 wR_2 = 0.2759
Largest diff. peak/hole/ e Å^{-3}	0.19/-0.25	0.33/-0.33	0.27/-0.22	0.27/-0.2	0.25/-0.36	0.53/-0.39

* Data from 3D electron diffraction (3D ED) measurements on microcrystalline sample.

The following experimental powder diffraction patterns were recorded at room temperature, whereas the calculated patterns are based on single-crystal data collected at lower temperatures listed in Table S2. The observed shifts in peak positions are attributed to temperature-dependent changes in the lattice parameters.

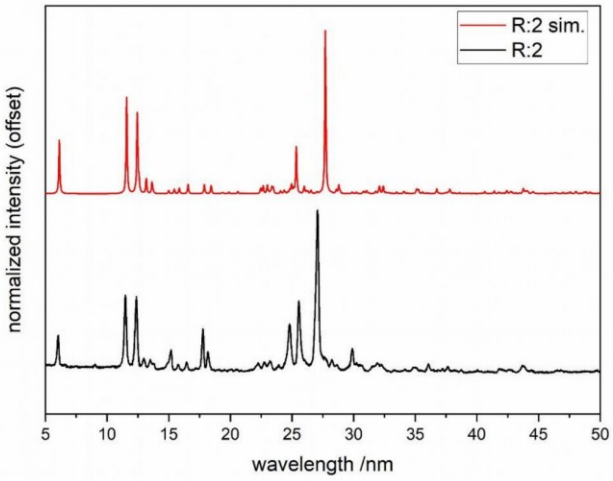

Figure S11. Experimental and simulated from single crystal data PXRD patterns of **R:2** (Cu Kα radiation).

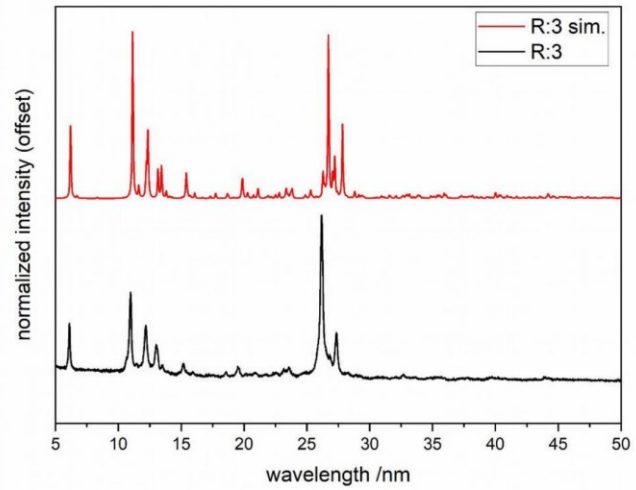

Figure S12. Experimental and simulated from single crystal data PXRD patterns of **R:3** (Cu Kα radiation).

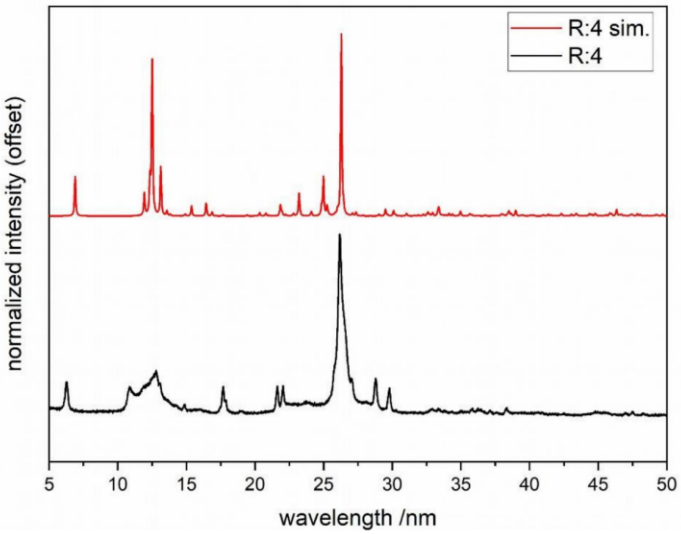

Figure S13. Experimental and simulated from single crystal data PXRD patterns of **R:4** (Cu Kα radiation).

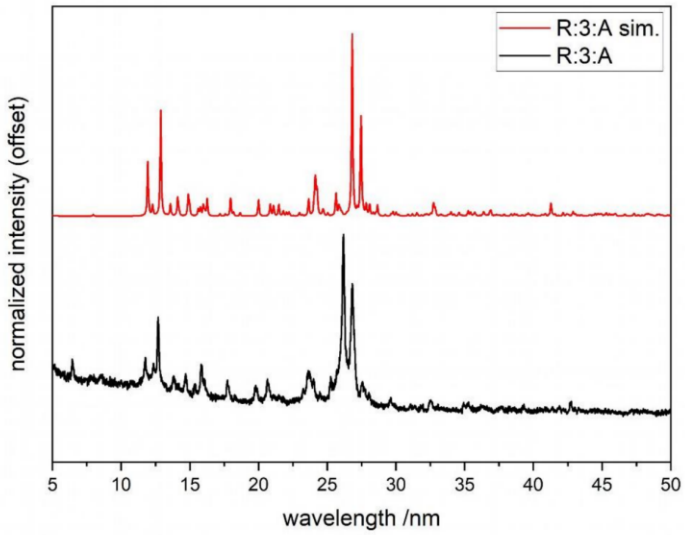

Figure S14. Experimental and simulated from single crystal data PXRD patterns of **R:3:A** (Cu Kα radiation).

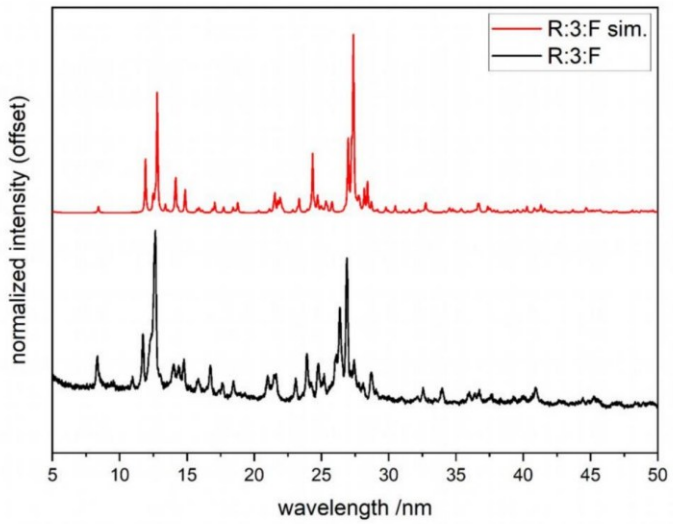

Figure S15. Experimental and simulated from single crystal data PXRD patterns of **R:3:F** (Cu Kα radiation).

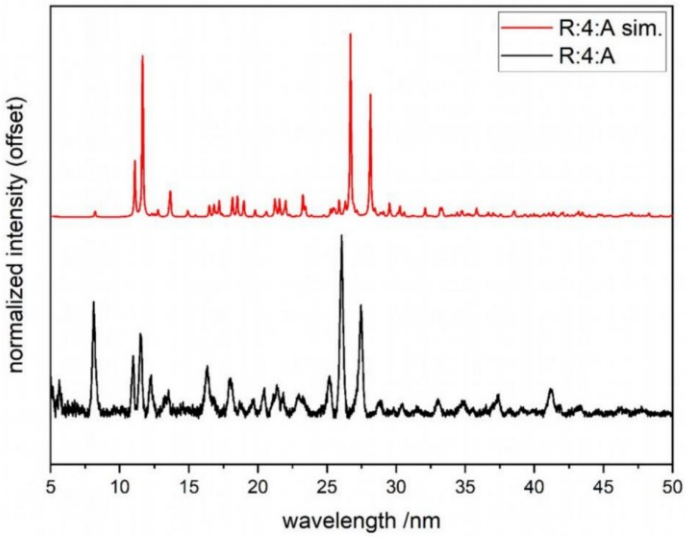

Figure S16. Experimental and simulated from single crystal data PXRD patterns of **R:4:A** (Cu Kα radiation).

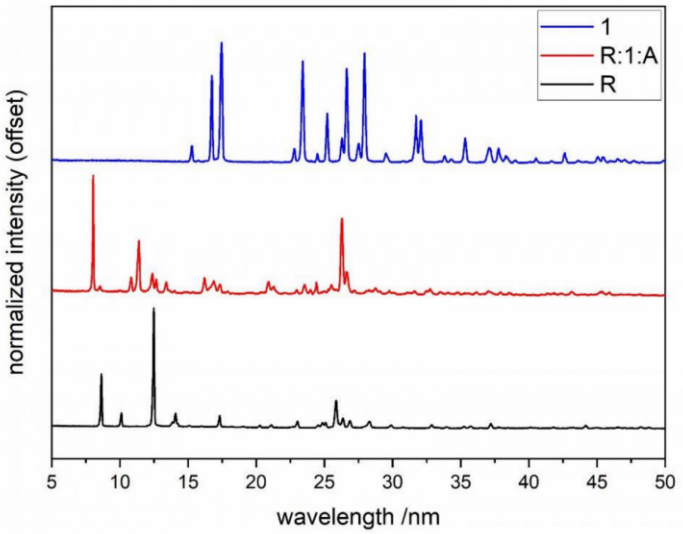

Figure S17. Experimental PXRD patterns of **R:1:A** in comparison to PXRD patterns of **R** and **1** (Cu Kα radiation).

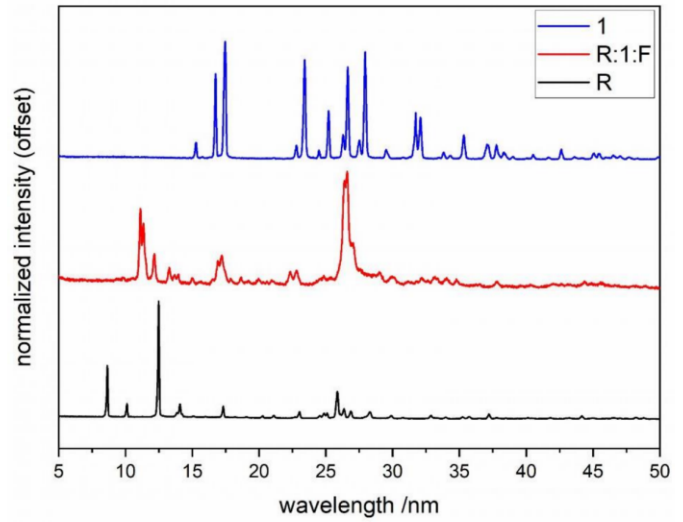

Figure S18. Experimental PXRD patterns of **R:1:F** in comparison to PXRD patterns of **R** and **1** (Cu Kα radiation).

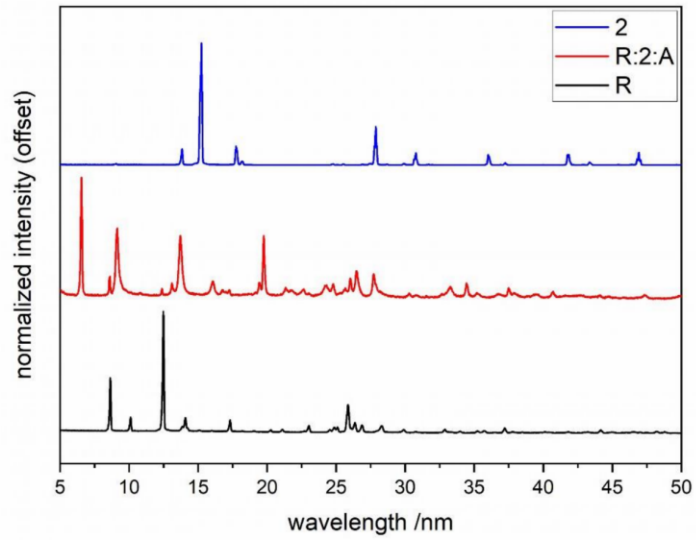

Figure S19. Experimental PXRD patterns of **R:2:A** in comparison to PXRD patterns of **R** and **2** (Cu Kα radiation).

4. Excitation Spectra and Emission Spectra

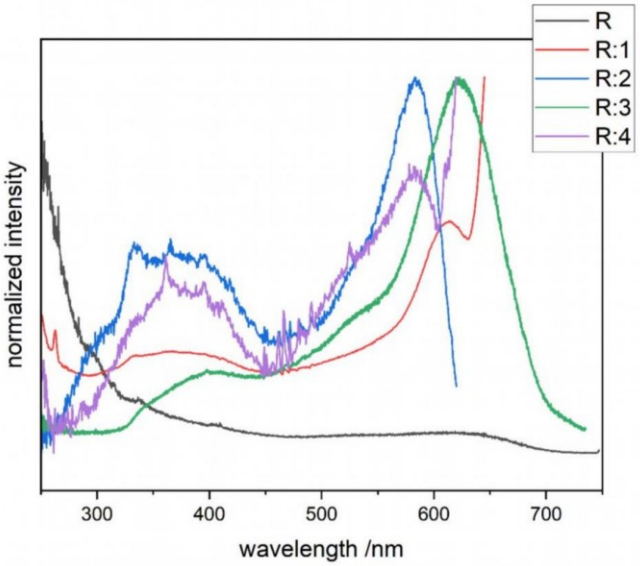

Figure S20. Normalized solid-state excitation spectra of **R** (λ_{em}=700 nm), **R:1** (λ_{em}=670 nm), **R:2** (λ_{em}=650 nm), **R:3** (λ_{em}=750 nm) and **R:4** (λ_{em}=600 nm).

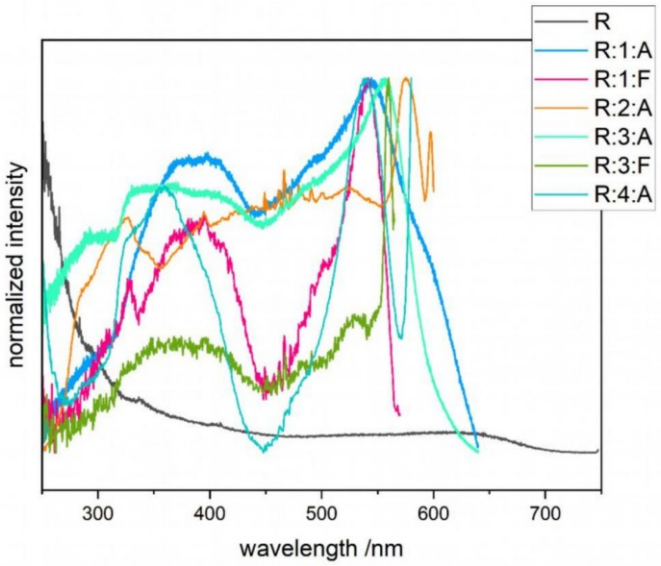

Figure S21. Normalized solid-state excitation spectra of **R** (λ_{em}=700 nm), **R:1:A** (λ_{em}=650 nm), **R:1:F** (λ_{em}=650 nm), **R:2:A** (λ_{em}=640 nm), **R:3:A** (λ_{em}=650 nm), **R:3:F** (λ_{em}=500 nm) and **R:4:A** (λ_{em}=610 nm).

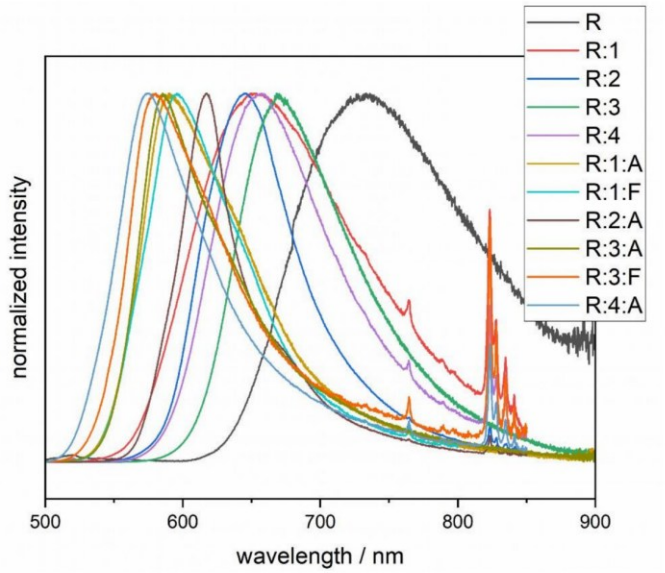

Figure S22. Full solid-state emission spectra of **R** **R:1**, **R:2**, **R:3**, **R:4**, **R:1:A**, **R:1:F**, **R:2:A**, **R:3:A**, **R:3:F** and **R:4:A.** All phases were excited at 423 nm, except for **R:1:A** and **R:3:A** which were excited at 400 nm. Spikes at 765 nm and in the range > 800 nm result from light originating from higher diffraction orders of the monochromator.

5. Basic Structural Motifs

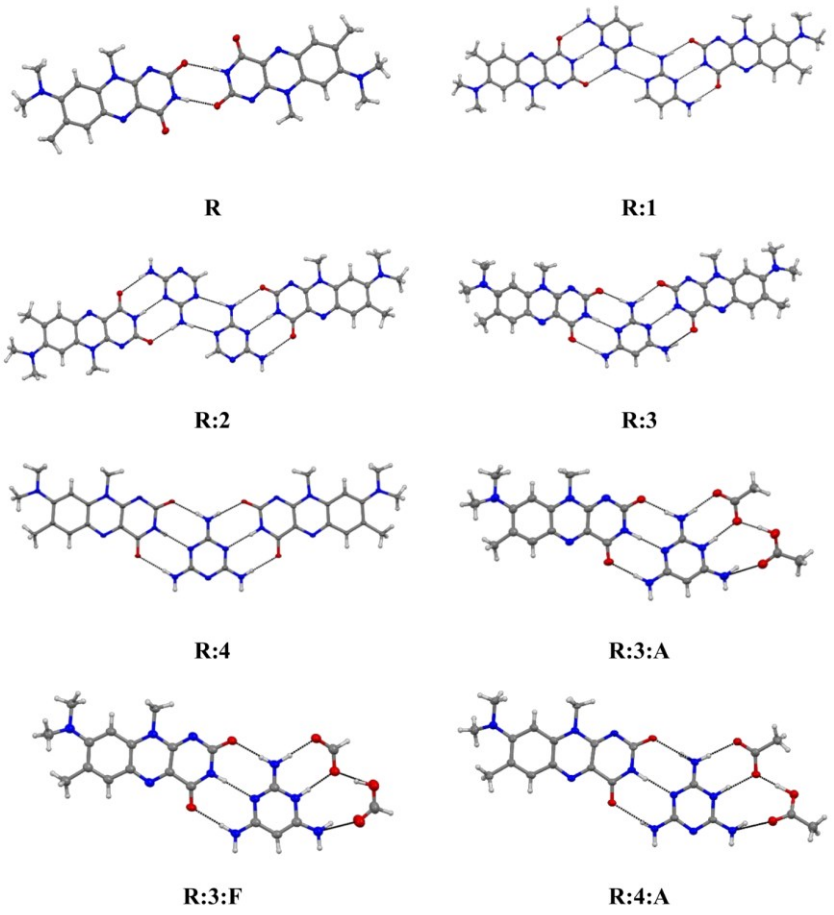

Figure S23. Selected basic structural motifs of crystal structures of **R**, **R:1**, **R:2**, **R:3**, **R:4**, **R:3:A**, **R:3:F**, **R:4:A**.

6. NCI Scatterplots

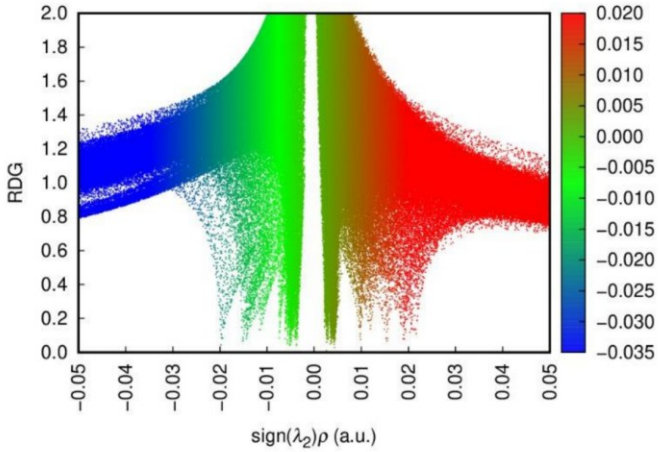

Figure S24. RDG Scatterplot of **R**.

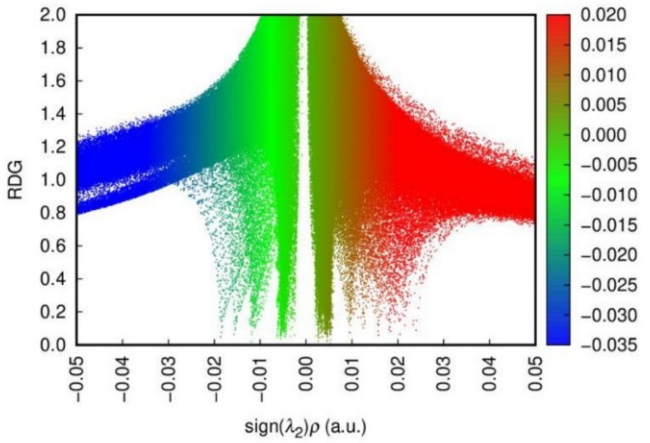

Figure S25. RDG Scatterplot of **R:1**.

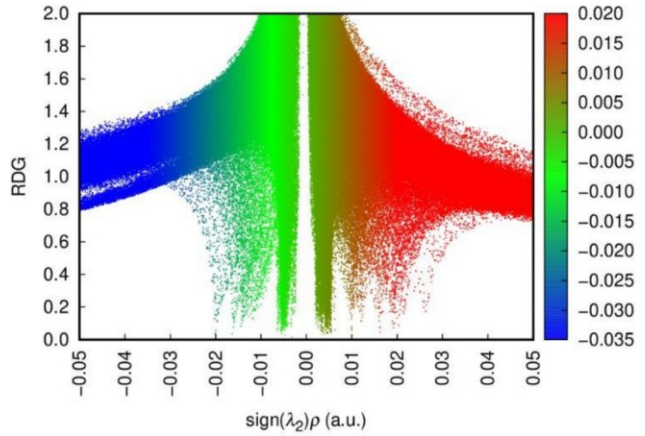

Figure S26. RDG Scatterplot of **R:2**.

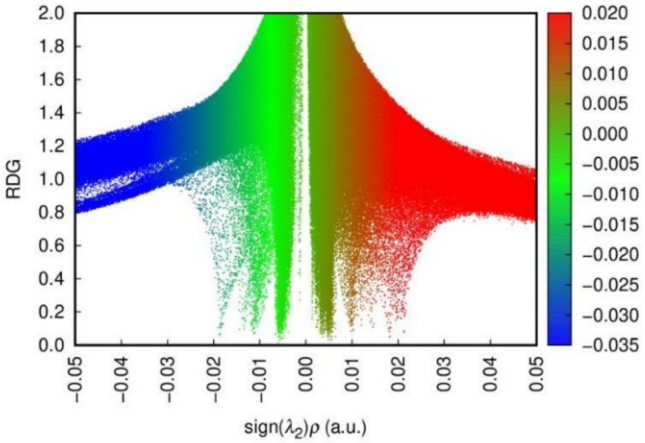

Figure S27. RDG Scatterplot of **R:3** (a).

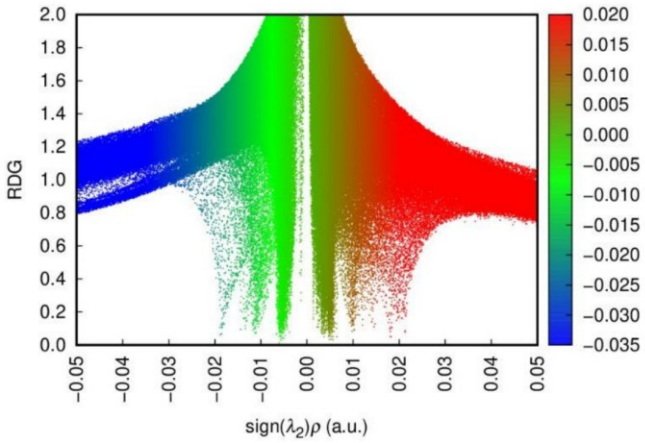

Figure S28. RDG Scatterplot of **R:3** (b).

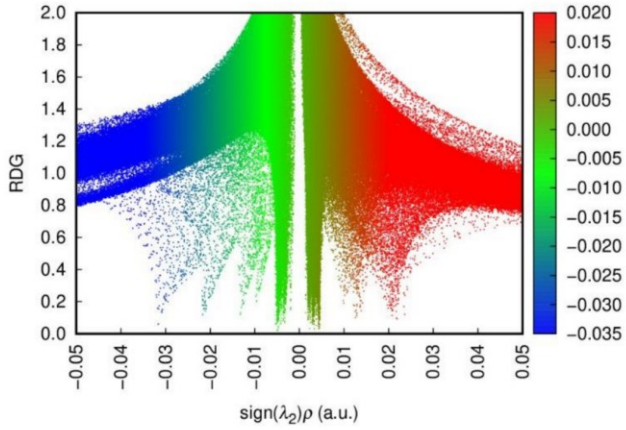

Figure S29. RDG Scatterplot of **R:4**.

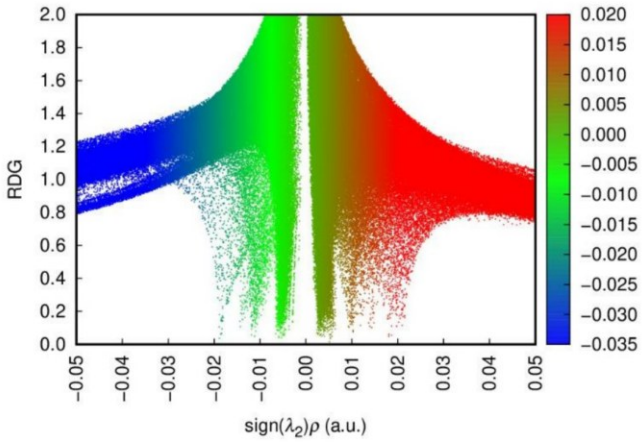

Figure S30. RDG Scatterplot of **R:3:A**.

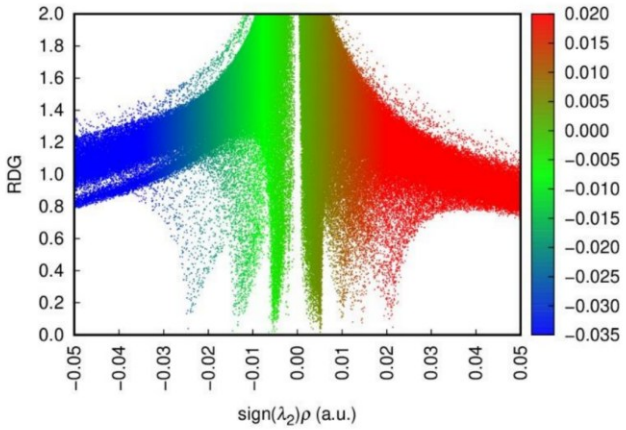

Figure S31. RDG Scatterplot of **R:3:F**.

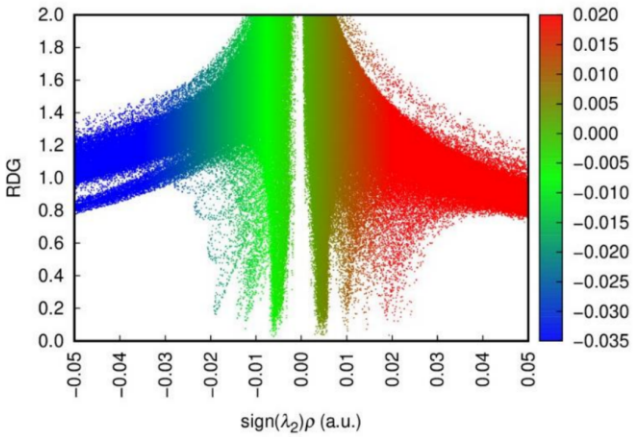

Figure S32. RDG Scatterplot of **R:4:A**.

7. Thermograms of **R:1:A**, **R:1:F** and **R:2:A**

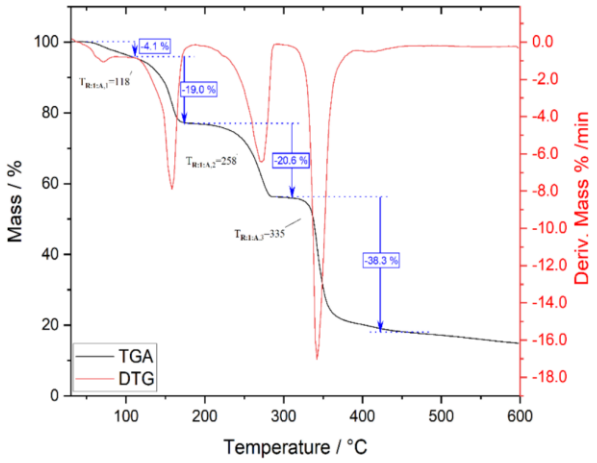

Figure S33. Thermogram of **R:1:A** including DTG curve measured between 30-600 °C, nitrogen purge gas, heating rate 10 °C/min.

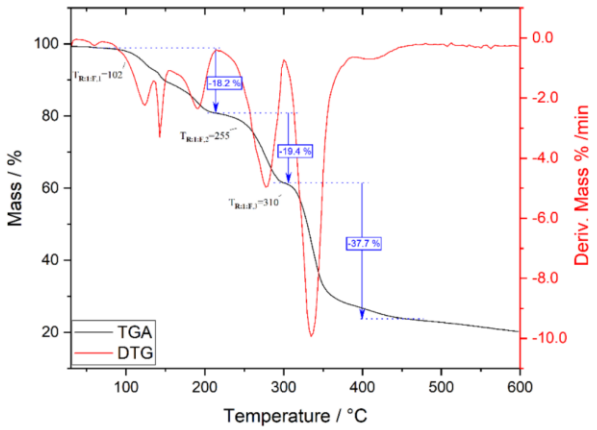

Figure S34. Thermogram of **R:1:F** including DTG curve measured between 30-600 °C, nitrogen purge gas, heating rate 10 °C/min.

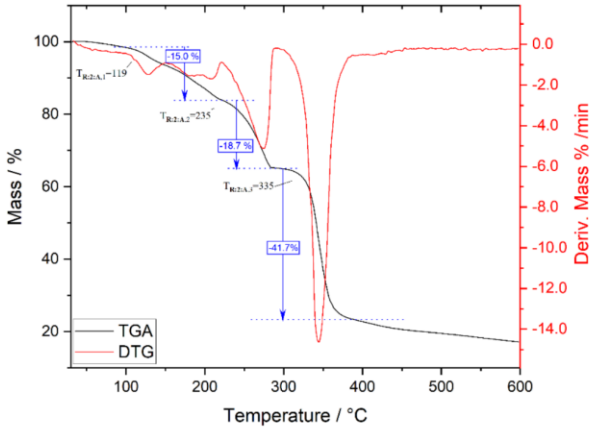

Figure S35. Thermogram of **R:2:A** including DTG curve measured between 30-600 °C, nitrogen purge gas, heating rate 10 °C/min.

Aside from an initial 4% mass decrease attributed to moisture loss in the **R:1:A** sample, each thermogram exhibits three main decomposition steps. The first step corresponds to the loss of the acid component in a sequential manner, which might indicate the stepwise release of the differently incorporated acid molecules. The onset temperatures for these steps of each compound are $T_{\mathbf{R:1:A},1}$=118°C, $T_{\mathbf{R:1:F},1}$=102°C and $T_{\mathbf{R:2:A},1}$=119°C. The decomposition of the *N*-heterocyclic component is represented by the second step at onset temperatures of $T_{\mathbf{R:1:A},2}$=258°C, $T_{\mathbf{R:1:F},2}$=255°C and $T_{\mathbf{R:2:A},2}$=235°C. Finally, the flavin initiates decomposition at onset temperatures $T_{\mathbf{R:1:A},3}$=335°C, $T_{\mathbf{R:1:F},3}$=310°C and $T_{\mathbf{R:2:A},3}$=335°C. Due to nitrogen purge gas environment, no full decomposition is ensured and the remaining residual mass is thus to be expected as a result.

8. Elemental (CHN) Analyses of **R:1:A**, **R:1:F** and **R:2:A**

Table S3. Elemental analysis (calculated, experimental, and difference values in %) for the phases **R:1:A**, **R:1:F** and **R:2:A**; calculated values based on a 1:1:2 composition.

	R:1:A (1:1:2)			**R:1:F** (1:1:2)			**R:2:A** (1:1:2)		
	calc. /%	exp. /%	Δ. /%	calc. /%	exp. /%	Δ. /%	calc. /%	exp. /%	Δ. /%
C	51.25	50.55	0.7	49.27	48.48	0.79	48.82	49.04	0.22
H	5.62	5.51	0.11	5.12	5.06	0.06	5.42	5.26	0.16
N	24.44	23.63	0.81	25.84	25.67	0.17	27.1	28.44	1.34

REFERENCES

(1) Albert, A.; Goldacre, R.; Phillips, J. 455. The strength of heterocyclic bases. *J. Chem. Soc.* **1948**, 2240.

(2) Roth, B.; Strelitz, J. Z. Protonation of 2,4-diaminopyrimidines. II. Dissociation constants of 6-amino derivatives and anion effects in moderately strong acid. *J. Org. Chem.* **1970**, *35* (8), 2696–2702.

(3) Dudley, J. R. Cyanuric Chloride Derivatives. IX. Dissociation Constants of Substituted Melamines and Related Triazines. *J. Am. Chem. Soc.* **1951**, *73* (7), 3007–3008.

5. Conclusion

This dissertation is concerned with the main objective of establishing roseolumiflavin as a model flavin chromophore for multicomponent crystal engineering attempts. Along these lines, it aims to derive generalizable design principles for tuning solid-state optical response of flavins via supramolecular assembly. Three published works tackle these goals. The thesis objectives (see Chapter 3) were approached systematically.

First, the imide group of roseolumiflavin proved to be a reliable and accessible source for controlled, rational design. Binary co-crystals constructed via different supramolecular synthons illustrated the versatility of this flavin with respect to different interaction patterns, validating its suitability as a crystal engineering platform. Novel multicomponent structures could be obtained using both HB- and XB-donating co-formers. These results provided the foundation for a subsequent study with a selection of *N*-heterocyclic derivatives to systematically probe how targeted co-former variation influences structure-property relationships.

Second, the resulting packing motif analyses, primarily addressed in the first and third study, support the hypothesis that the central structure-property relationship regarding emission tuning via supramolecular assembly is governed strongly by the perturbation of flavin-flavin packing. After successful supramolecular assembly and structural characterization, spectroscopic measurements consistently show that co-crystals exhibit blue-shifted fluorescence in comparison to the pure flavin and the magnitude of the shift is determined by the extent to which both hydrogen bonding and stacking flavin···flavin packing motifs are reorganized or even replaced. This is particularly evident through the involvement of π-stacking co-formers. The observed optical modulation can be attributed primarily to the co-former-induced rearrangement of the packing environment rather than to its structural identity. The second study complements these findings by identifying π···π stacking as a stabilizing contributor in most phases. Solvate and hydrate formations expanded the accessible multicomponent structures beyond co-crystals, demonstrating additional adaptability of the flavin. Based on lattice energy calculations from obtained single-crystal structure data a consistent energetic benefit of solvent inclusion could be identified. Moreover, their inclusion demonstrates that physicochemical behavior such as thermal stability is likewise tunable. In the third study, the expanded series of co-formers, focusing on a

set of *N*-heterocycle derivatives, redefined the attainable window of emission behavior and highlighted the role of charge-assisted interactions. Different derivatives emit within a defined wavelength range, showing that deliberate co-former selection and modification influence the luminescence response translated through effects on emission bandwidth narrowing or Stokes shift variations, for example. Acid inclusion, initiating proton transfer between acid and co-former, extended emission shifts up to 158 nm relative to roseolumiflavin.

Third, topological analyses such as QTAIM and NCI plots based on obtained single-crystal structure data rationalize the occurrence of specific packing motifs. NCI surface visualizations for the ternary systems in the final study underline stacking-related interaction regions and their shift from flavin···flavin to flavin···co-former contacts from binary to ternary systems. Complementary, QTAIM quantifies the HB strengths, including the desired imide group recognition site. This illustrates the relative stabilization of the supramolecular motif. Basic structural motif analysis reveals a clear stabilization trend from binary to ternary systems, with binding energies reaching -165.81 kJ/mol in observed binary systems, up to -260.38 kJ/mol in ternary systems. Together, these approaches show that motif selection is governed by the connectivity between co-former and flavin at the imide group recognition site providing energetic benefit, while packing is driven by stacking and dispersive force, adding robustness.

Finally, mechanochemistry was demonstrated as a viable, sustainable synthesis strategy for the multicomponent phases. The vast majority of the obtained novel crystalline phases could be produced or reproduced by LAG methods, reducing reliance on bulk solvents and providing a basis for more sustainable future studies.

Taken together, this thesis provides a basis to derive a design principle to construct multicomponent systems of roseolumiflavin: Targeted modification of solid-state emission can be tuned in a broad color range. By co-former-induced modification of the native flavin···flavin stacking motif rather than by interaction type alone. Co-formers with suitable ring systems can intervene in the stacking or packing environment, allowing the adjustment of emission band shifts and further fine-tuning through derivatization. Additional acid incorporation extends the luminescence response range, as shown via proton transfer and the resulting changes in packing arrangement. This demonstrates a rational approach to form emission bands within a desired range.

6. Additional Publications

In this chapter all further publications will be listed and briefly presented with contributions of the author.

The first publication presented, titled "*Polyphosphonate covalent organic frameworks*", will include a list of this author's contributions and a short summary as this author shares first authorship; thus, it will be presented more verbosely. Furthermore, the following publication, titled "*Targeted Fluorescence Enhancement of Acridones by Hydrogen Bonding in Solution and Solid State*", will be highlighted similarly, as parts of the project and related contributions originated from the bachelor's thesis of Martin Polko, conceptualized and supervised by this author.

All following publications are listed in chronological order and include a list of this author's contributions as a co-author.

The co-authorship primarily includes single-crystal preparation and selection, followed by SCXRD measurements, data preparation for publication, preparation of crystallographic tables, structure solution and evaluation of the results. Further contributions include lattice energy calculations, QTAIM and NCI plot calculations including validation and evaluation of the results and the preparation of figures and plots.

All titles are reproduced verbatim from the original publications.

Polyphosphonate covalent organic frameworks

K. Xu*, R. Oestreich*, T. Haj Hassani Sohi*, M. Lounasvuori, J. G. A. Ruthes, Y. Zorlu, J. Michalski, P. Seiffert, T. Strothmann, P. Tholen, A. Ozgur Yazaydin, M. Suta, V. Presser, T. Petit, C. Janiak, J. Beckmann, J. Schmedt auf der Günne and G. Yücesan

* These authors contributed equally.

Nat Commun, **2024**, *15*, 7862.

A novel class of polyphosphonate covalent organic frameworks (COFs) constructed via P-O-P linkages are reported. Prepared via a reagent-free, one-step thermal condensation, the structure is investigated in different thermal and chemical environments. The P-O-P formation and the transition to partially amorphous microporous states are investigated by 31P solid-state NMR, FTIR, XPS and TGA-MS. The polyphosphonate COF exhibits good stability in water and water vapor and electrochemical stability in 0.5 M Na_2SO_4. Effective CO_2 capturing is facilitated due to narrow pores of the COF.

Contributions of the author:

- Performance of temperature-variable PXRD measurements.
- Testing of chemical stability.
- Writing of paragraph in manuscript about the temperature-variable PXRD measurements including chemical stability in differing environments.

Targeted Fluorescence Enhancement of Acridones by Hydrogen Bonding in Solution and Solid State

M. Jantz, D. Klaverkamp, B. Bendel, T. Haj Hassani Sohi, M. Polko, L. Bunnemann, T. Böhmer, M. Putscher, C. Marian, C. Czekelius, V. Vasylyeva, M. Suta, P. Gilch

J. Mater. Chem. C, **2025**, *in revision.*

The study demonstrates that *N*-methyl-acridone (NMA) forms a hydrogen-bonded complex with Schreiner's catalyst (SCat). Solution-based experiments show a ninefold increase of the fluorescence quantum yield. In the solid state, the components form a 1:1 co-crystal, as confirmed by SCXRD. The photophysical measurements reveal a

threefold increase in fluorescence quantum yield, blue-shifted emission and sharper emission bands. Quantum-chemical calculations attribute the fluorescence enhancement to an energetic up-shift of $n\pi^*$ excited states.

Contributions of the author:

- Conceptualization of co-crystal part together with Vera Vasylyeva.
- Single-crystal preparation, SCXRD measurements and single-crystal structure data evaluation of NMA···SCat and SCat together with Martin Polko.
- PXRD and FTIR measurements and evaluation of the results.
- Writing paragraph about the effect of hydrogen bonding in NMA co-crystals together with Benedikt Bendel.
- Writing ESI paragraph about SCat crystal structure details.
- Preparation of figures 3, 4, S7, S9 and S10 and crystallographic table S3.
- Revision of the manuscript.

Co-crystals of zwitterionic GABA API's pregabalin and phenibut: properties and application

D. Komisarek, T. Haj Hassani Sohi and V. Vasylyeva

CrystEngComm, **2022**, *24*, 8390–8398.

Contributions of the author:

- Evaluation and validation of lattice energy calculations based on crystal structure data.
- Revision of the manuscript.

Polymorphism and Multi-Component Crystal Formation of GABA and Gabapentin

D. Komisarek, F. Demirbas, T. Haj Hassani Sohi, K. Merz, C. Schauerte and V. Vasylyeva

Pharmaceutics, **2023**, *15*.

Contributions of the author include the calculation, analysis and evaluation of QTAIM and NCI plots.

Indole Diketopiperazine Alkaloids from the Marine Sediment-Derived Fungus Aspergillus chevalieri against Pancreatic Ductal Adenocarcinoma

D. H. El-Kashef, D. D. Obidake, K. Schiedlauske, A. Deipenbrock, S. Scharf, H. Wang, D. Naumann, D. Friedrich, S. Miljanovic, T. Haj Hassani Sohi, C. Janiak, K. Pfeffer and N. Teusch

Marine drugs, **2023**, *22*.

Contributions of the author:

- Single-crystal preparation, SCXRD measurements, single-crystal structure data evaluation and crystal structure description of the rublumline derivative.
- Review and revision of the manuscript.

Experimental and computational studies on pseudotetrahedral nickel(ii)-(S or R)-dihalogen-salicylaldiminates with Δ- or Λ-chirality induction at-metal

A. Saadati, H. Amiri Rudbari, M. Aryaeifar, O. Blacque, I. Correia, M. K. Islam, D. Woschko, T. Haj Hassani Sohi, C. Janiak and M. Enamullah

CrystEngComm, **2023**, *25*, 365–377.

Contributions of the author:

- Calculation, evaluation and validation of NCI plot analyses for Ni*S*L[1], Δ-Ni*S*L[2] and Λ-Ni*R*L[3].
- Writing paragraph about the NCI plot analyses.
- Preparation of Figure 5.
- Review and revision of the manuscript.

Hydrogen-Bonded Ladder Motifs in Naphthalene Dicarboxamides: Influence of Linear vs. Angular Amide Orientation

A. Mohabbat, I. Boldog, T. Haj Hassani Sohi, N. Reistel, P. Seiffert and C. Janiak

Crystals, **2025**, *15*, 406.

Contributions of the author:

- Input preparation for *Gaussian* calculations for subsequent QTAIM analyses.
- NCI plot calculations and contributions to preparation of Figure 12.
- Validation of QTAIM and NCI plot analyses.

Syntheses and X-ray structures of enantiopure Schiff bases (R or S)-2-(((E)-1-(Ar)ethylimino)ethyl)phenol, copper(II) complex and (R or S)-(Ar)ethyl-ammonium sulphate/acetate

M. Enamullah, I. Haque, A. K. Resma, T. Aziz, T. Haj Hassani Sohi, D. Woschko and C. Janiak

Inorganica Chimica Acta, **2025**, *583*, 122657.

Contributions of the author:

- Single-crystal preparation, SCXRD measurements and single-crystal structure data evaluation of compound 1.
- Review of the manuscript.

Square planar vs. pyramidal copper(ii)-complexes with benzylal vs. naphthylal-based Schiff bases

M. Enamullah, I. Haque, A. K. Resma, G. Abdullah, M. N. Uddin, T. Haj Hassani Sohi, D. Woschko, P. Ferber and C. Janiak

RSC advances, **2025**, *15*, 18358–18371.

Contributions of the author:

- Single-crystal preparation, SCXRD measurements and single-crystal structure data evaluation of compounds HL2, HL3 and 3.
- Review and revision of the manuscript.

Ferromagnetically coupled tetranuclear Ni(ii)-2-oxy-aceto- or benzo-phenonate complexes

I. Haque, M. Enamullah, N. T. Jhumur, B. K. Sidhu, D. E. Herbert, T. Haj Hassani Sohi, L. Havlíček, I. Nemec and C. Janiak

RSC advances, **2025**, *15*, 4250–4261.

Contributions of the author:

- Single-crystal preparation, SCXRD measurements and single-crystal structure data evaluation of complex 1 and complex 2.
- Review and revision of the manuscript.

Dinuclear vs. mononuclear copper(ii) complexes with nitrophenylimino-benzylal- vs. -naphthylal-based Schiff base ligands

M. Enamullah, I. Haque, G. Abdullah, F. H. Sourav, N. T. Jhumur, M. K. Islam, T. Haj Hassani Sohi, P. Ferber and C. Janiak

New J. Chem., **2025**, *49*, 17106–17123.

Contributions of the author:

- Single-crystal preparation, SCXRD measurements and single-crystal structure data evaluation of compounds HL2, HL3 and 3.
- Review and revision of the manuscript.

---

7. References

1 J.-M. Lehn, Supramolecular Chemistry—Scope and Perspectives Molecules, Supermolecules, and Molecular Devices (Nobel Lecture), *Angewandte Chemie International Edition in English*, **1988**, *27*, 89–112.

2 E. Fischer, Einfluss der Configuration auf die Wirkung der Enzyme, *Berichte der deutschen chemischen Gesellschaft*, **1894**, *27*, 2985–2993.

3 J.-M. Lehn, *Supramolecular chemistry. Concepts and perspectives : a personal account built upon the George Fisher Baker lectures in chemistry at Cornell University [and] Lezioni Lincee, Accademia nazionale dei Lincei, Roma*, VCH, Weinheim, New York, **1995**.

4 D. J. Cram, The Design of Molecular Hosts, Guests, and Their Complexes, *Science (New York, N.Y.)*, **1988**, *240*, 760–767.

5 R. Pepinsky, Crystal Engineering - New Concept in Crystallography, *Physical Review*, **1955**, 971.

6 G. M. J. Schmidt, Photodimerization in the solid state, *Pure and Applied Chemistry*, **1971**, *27*, 647–678.

7 M. D. Cohen and G. M. J. Schmidt, 383. Topochemistry. Part I. A survey, *J. Chem. Soc.*, **1964**, 1996–2000.

8 J. M. Thomas, Topography and topology in solid-state chemistry, *Philosophical Transactions of the Royal Society of London. Series A, Mathematical and Physical Sciences*, **1974**, *277*, 251–286.

9 J. M. Adams, R. G. Pritchard and J. M. Thomas, Preparation and X-ray crystal structure of guanidinium oxalate dihydrate monoperhydrate: a novel example of crystal engineering, *J. Chem. Soc., Chem. Commun.*, **1976**, 358.

10 G. R. Desiraju, Crystal engineering: from molecule to crystal, *Journal of the American Chemical Society*, **2013**, *135*, 9952–9967.

11 G. R. Desiraju, Carrying out organic chemistry within crystalline solids, *Endeavour*, **1984**, *8*, 201–206.

12 G. R. Desiraju, The C-H.cntdot.cntdot.cntdot.O hydrogen bond in crystals: what is it?, *Accounts of Chemical Research*, **1991**, *24*, 290–296.

13 G. R. Desiraju, C-H••••O Hydrogen Bonding and the Deliberate Design of Organic Crystal Structures, *Molecular Crystals and Liquid Crystals Science and Technology. Section A. Molecular Crystals and Liquid Crystals*, **1992**, *211*, 63–74.

14 G. R. Desiraju, Organic solid state chemistry—Some perspectives, *Proceedings of the Indian Academy of Sciences - Chemical Sciences*, **1984**, *93*, 407–419.

15 G. R. Desiraju and G. W. Parshall, in *Materials science monographs*, **1989**.

16 G. R. Desiraju, Supramolecular Synthons in Crystal Engineering—A New Organic Synthesis, *Angewandte Chemie International Edition in English*, **1995**, *34*, 2311–2327.

17 G. R. Desiraju, The C-h···o hydrogen bond: structural implications and supramolecular design, *Accounts of Chemical Research*, **1996**, *29*, 441–449.

18 G. R. Desiraju, *Crystal engineering. The design of organic solids*, Elsevier, Amsterdam, **1989**.

19 T. Steiner and G. R. Desiraju, Distinction between the weak hydrogen bond and the van der Waals interaction, *Chemical Communications*, **1998**, 891–892.

20 G. R. Desiraju and J. A. R. P. Sarma, Crystal engineering via donor–acceptor interactions. X-Ray crystal structure and solid state reactivity of the 1 : 1 complex, 3,4-dimethoxycinnamic acid–2,4-dinitrocinnamic acid, *J. Chem. Soc., Chem. Commun.*, **1983**, 45–46.

21 M. C. Etter, J. C. MacDonald and J. Bernstein, Graph-set analysis of hydrogen-bond patterns in organic crystals, *Acta crystallographica. Section B, Structural science*, **1990**, *46*, 256–262.

22 C. Janiak, A critical account on π–π stacking in metal complexes with aromatic nitrogen-containing ligands, *Journal of the Chemical Society, Dalton Transactions*, **2000**, 3885–3896.

23 M. Nishio, CH/π hydrogen bonds in crystals, *CrystEngComm*, **2004**, *6*, 130.

24 M. Nishio, CH/π hydrogen bonds in organic reactions, *Tetrahedron*, **2005**, *61*, 6923–6950.

25 O. Takahashi, Y. Kohno, S. Iwasaki, K. Saito, M. Iwaoka, S. Tomoda, Y. Umezawa, S. Tsuboyama and M. Nishio, Hydrogen-Bond-Like Nature of the CH/π Interaction

as Evidenced by Crystallographic Database Analyses and Ab Initio Molecular Orbital Calculations, *Bulletin of the Chemical Society of Japan*, **2001**, *74*, 2421–2430.

26 M. Nishio, Y. Umezawa, K. Honda, S. Tsuboyama and H. Suezawa, CH/π hydrogen bonds in organic and organometallic chemistry, *CrystEngComm*, **2009**, *11*, 1757.

27 M. Nishio, M. Hirota and Y. Umezawa, *The CH/[pi] interaction. Evidence, nature, and consequences*, Wiley-VCH, New York, Chichester, **1998**.

28 P. Metrangolo, F. Meyer, T. Pilati, G. Resnati and G. Terraneo, Halogen bonding in supramolecular chemistry, *Angewandte Chemie (International ed. in English)*, **2008**, *47*, 6114–6127.

29 P. Metrangolo and G. Resnati, Halogen Bonding: A Paradigm in Supramolecular Chemistry, *Chemistry - A European Journal*, **2001**, *7*, 2511–2519.

30 P. Metrangolo, T. Pilati and G. Resnati, Halogen bonding and other noncovalent interactions involving halogens: a terminology issue, *CrystEngComm*, **2006**, *8*, 946.

31 P. Metrangolo, H. Neukirch, T. Pilati and G. Resnati, Halogen bonding based recognition processes: a world parallel to hydrogen bonding, *Accounts of Chemical Research*, **2005**, *38*, 386–395.

32 G. Cavallo, P. Metrangolo, R. Milani, T. Pilati, A. Priimagi, G. Resnati and G. Terraneo, The Halogen Bond, *Chemical Reviews*, **2016**, *116*, 2478–2601.

33 R. B. Walsh, C. W. Padgett, P. Metrangolo, G. Resnati, T. W. Hanks and W. T. Pennington, Crystal Engineering through Halogen Bonding: Complexes of Nitrogen Heterocycles with Organic Iodides, *Crystal Growth & Design*, **2001**, *1*, 165–175.

34 C. R. Groom, I. J. Bruno, M. P. Lightfoot and S. C. Ward, The Cambridge Structural Database, *Acta Crystallographica Section B, Structural Science, Crystal Engineering and Materials*, **2016**, *72*, 171–179.

35 J. P. M. Lommerse, W. D. S. Motherwell, H. L. Ammon, J. D. Dunitz, A. Gavezzotti, D. W. M. Hofmann, F. J. J. Leusen, W. T. M. Mooij, S. L. Price, B. Schweizer, M. U. Schmidt, B. P. van Eijck, P. Verwer and D. E. Williams, A test of crystal structure prediction of small organic molecules, *Acta crystallographica. Section B, Structural science*, **2000**, *56*, 697–714.

36 W. D. S. Motherwell, H. L. Ammon, J. D. Dunitz, A. Dzyabchenko, P. Erk, A. Gavezzotti, D. W. M. Hofmann, F. J. J. Leusen, J. P. M. Lommerse, W. T. M. Mooij, S. L. Price, H. A. Scheraga, B. Schweizer, M. U. Schmidt, B. P. van Eijck, P. Verwer and D. E. Williams, Crystal structure prediction of small organic molecules: a second blind test, *Acta crystallographica. Section B, Structural science*, **2002**, *58*, 647–661.

37 G. M. Day, W. D. S. Motherwell, H. L. Ammon, S. X. M. Boerrigter, R. G. Della Valle, E. Venuti, A. Dzyabchenko, J. D. Dunitz, B. Schweizer, B. P. van Eijck, P. Erk, J. C. Facelli, V. E. Bazterra, M. B. Ferraro, D. W. M. Hofmann, F. J. J. Leusen, C. Liang, C. C. Pantelides, P. G. Karamertzanis, S. L. Price, T. C. Lewis, H. Nowell, A. Torrisi, H. A. Scheraga, Y. A. Arnautova, M. U. Schmidt and P. Verwer, A third blind test of crystal structure prediction, *Acta crystallographica. Section B, Structural science*, **2005**, *61*, 511–527.

38 G. M. Day, T. G. Cooper, A. J. Cruz-Cabeza, K. E. Hejczyk, H. L. Ammon, S. X. M. Boerrigter, J. S. Tan, R. G. Della Valle, E. Venuti, K. V. J. Jose, S. R. Gadre, G. R. Desiraju, T. S. Thakur, B. P. van Eijck, J. C. Facelli, V. E. Bazterra, M. B. Ferraro, D. W. M. Hofmann, M. A. Neumann, F. J. J. Leusen, J. Kendrick, S. L. Price, A. J. Misquitta, P. G. Karamertzanis, G. W. A. Welch, H. A. Scheraga, Y. A. Arnautova, M. U. Schmidt, J. van de Streek, A. K. Wolf and B. Schweizer, Significant progress in predicting the crystal structures of small organic molecules--a report on the fourth blind test, *Acta crystallographica. Section B, Structural science*, **2009**, *65*, 107–125.

39 D. A. Bardwell, C. S. Adjiman, Y. A. Arnautova, E. Bartashevich, S. X. M. Boerrigter, D. E. Braun, A. J. Cruz-Cabeza, G. M. Day, R. G. Della Valle, G. R. Desiraju, B. P. van Eijck, J. C. Facelli, M. B. Ferraro, D. Grillo, M. Habgood, D. W. M. Hofmann, F. Hofmann, K. V. J. Jose, P. G. Karamertzanis, A. V. Kazantsev, J. Kendrick, L. N. Kuleshova, F. J. J. Leusen, A. V. Maleev, A. J. Misquitta, S. Mohamed, R. J. Needs, M. A. Neumann, D. Nikylov, A. M. Orendt, R. Pal, C. C. Pantelides, C. J. Pickard, L. S. Price, S. L. Price, H. A. Scheraga, J. van de Streek, T. S. Thakur, S. Tiwari, E. Venuti and I. K. Zhitkov, Towards crystal structure prediction of complex organic compounds--a report on the fifth blind test, *Acta crystallographica. Section B, Structural science*, **2011**, *67*, 535–551.

40 A. M. Reilly, R. I. Cooper, C. S. Adjiman, S. Bhattacharya, A. D. Boese, J. G. Brandenburg, P. J. Bygrave, R. Bylsma, J. E. Campbell, R. Car, D. H. Case, R. Chadha, J. C. Cole, K. Cosburn, H. M. Cuppen, F. Curtis, G. M. Day, R. A. DiStasio, A. Dzyabchenko, B. P. van Eijck, D. M. Elking, J. A. van den Ende, J. C. Facelli, M. B. Ferraro, L. Fusti-Molnar, C. A. Gatsiou, T. S. Gee, R. de Gelder, L. M. Ghiringhelli, H. Goto, S. Grimme, R. Guo, D. W. M. Hofmann, J. Hoja, R. K. Hylton, L. Iuzzolino, W. Jankiewicz, D. T. de Jong, J. Kendrick, N. J. J. de Klerk, H. Y. Ko, L. N. Kuleshova, X. Li, S. Lohani, F. J. J. Leusen, A. M. Lund, J. Lv, Y. Ma, N. Marom, A. E. Masunov, P. McCabe, D. P. McMahon, H. Meekes, M. P. Metz, A. J. Misquitta, S. Mohamed, B. Monserrat, R. J. Needs, M. A. Neumann, J. Nyman, S. Obata, H. Oberhofer, A. R. Oganov, A. M. Orendt, G. I. Pagola, C. C. Pantelides, C. J. Pickard, R. Podeszwa, L. S. Price, S. L. Price, A. Pulido, M. G. Read, K. Reuter, E. Schneider, C. Schober, G. P. Shields, P. Singh, I. J. Sugden, K. Szalewicz, C. R. Taylor, A. Tkatchenko, M. E. Tuckerman, F. Vacarro, M. Vasileiadis, A. Vazquez-Mayagoitia, L. Vogt, Y. Wang, R. E. Watson, G. A. de Wijs, J. Yang, Q. Zhu and C. R. Groom, Report on the sixth blind test of organic crystal structure prediction methods, *Acta Crystallographica Section B, Structural Science, Crystal Engineering and Materials*, **2016**, *72*, 439–459.

41 L. M. Hunnisett, J. Nyman, N. Francia, N. S. Abraham, C. S. Adjiman, S. Aitipamula, T. Alkhidir, M. Almehairbi, A. Anelli, D. M. Anstine, J. E. Anthony, J. E. Arnold, F. Bahrami, M. A. Bellucci, R. M. Bhardwaj, I. Bier, J. A. Bis, A. D. Boese, D. H. Bowskill, J. Bramley, J. G. Brandenburg, D. E. Braun, P. W. V. Butler, J. Cadden, S. Carino, E. J. Chan, C. Chang, B. Cheng, S. M. Clarke, S. J. Coles, R. I. Cooper, R. Couch, R. Cuadrado, T. Darden, G. M. Day, H. Dietrich, Y. Ding, A. DiPasquale, B. Dhokale, B. P. van Eijck, M. R. J. Elsegood, D. Firaha, W. Fu, K. Fukuzawa, J. Glover, H. Goto, C. Greenwell, R. Guo, J. Harter, J. Helfferich, D. W. M. Hofmann, J. Hoja, J. Hone, R. Hong, G. Hutchison, Y. Ikabata, O. Isayev, O. Ishaque, V. Jain, Y. Jin, A. Jing, E. R. Johnson, I. Jones, K. V. J. Jose, E. A. Kabova, A. Keates, P. F. Kelly, D. Khakimov, S. Konstantinopoulos, L. N. Kuleshova, H. Li, X. Lin, A. List, C. Liu, Y. M. Liu, Z. Liu, Z. P. Liu, J. W. Lubach, N. Marom, A. A. Maryewski, H. Matsui, A. Mattei, R. A. Mayo, J. W. Melkumov, S. Mohamed, Z. Momenzadeh Abardeh, H. S. Muddana, N. Nakayama, K. S. Nayal, M. A. Neumann, R. Nikhar, S. Obata, D. O'Connor, A. R. Oganov, K. Okuwaki, A. Otero-de-la-Roza, C. C.

Pantelides, S. Parkin, C. J. Pickard, L. Pilia, T. Pivina, R. Podeszwa, A. J. A. Price, L. S. Price, S. L. Price, M. R. Probert, A. Pulido, G. R. Ramteke, A. U. Rehman, S. M. Reutzel-Edens, J. Rogal, M. J. Ross, A. F. Rumson, G. Sadiq, Z. M. Saeed, A. Salimi, M. Salvalaglio, L. Sanders de Almada, K. Sasikumar, S. Sekharan, C. Shang, K. Shankland, K. Shinohara, B. Shi, X. Shi, A. G. Skillman, H. Song, N. Strasser, J. van de Streek, I. J. Sugden, G. Sun, K. Szalewicz, B. I. Tan, L. Tan, F. Tarczynski, C. R. Taylor, A. Tkatchenko, R. Tom, M. E. Tuckerman, Y. Utsumi, L. Vogt-Maranto, J. Weatherston, L. J. Wilkinson, R. D. Willacy, L. Wojtas, G. R. Woollam, Z. Yang, E. Yonemochi, X. Yue, Q. Zeng, Y. Zhang, T. Zhou, Y. Zhou, R. Zubatyuk and J. C. Cole, The seventh blind test of crystal structure prediction: structure generation methods, *Acta Crystallographica Section B, Structural Science, Crystal Engineering and Materials*, **2024**, *80*, 517–547.

42 T. Heng, D. Yang, R. Wang, L. Zhang, Y. Lu and G. Du, Progress in Research on Artificial Intelligence Applied to Polymorphism and Cocrystal Prediction, *ACS omega*, **2021**, *6*, 15543–15550.

43 D. H. Bowskill, I. J. Sugden, S. Konstantinopoulos, C. S. Adjiman and C. C. Pantelides, Crystal Structure Prediction Methods for Organic Molecules: State of the Art, *Annual review of chemical and biomolecular engineering*, **2021**, *12*, 593–623.

44 G. J. O. Beran, Frontiers of molecular crystal structure prediction for pharmaceuticals and functional organic materials, *Chemical science*, **2023**, *14*, 13290–13312.

45 Z. Chen, Z. Meng, T. He, H. Li, J. Cao, L. Xu, H. Xiao, Y. Zhang, X. He and G. Fang, Crystal Structure Prediction Meets Artificial Intelligence, *The journal of physical chemistry letters*, **2025**, *16*, 2581–2591.

46 X. Liang, A. S. Larsen, P. Hans, Di Xu, Y. Li, I. C. B. Martins, T. Rades and Y. Jiang, Recent developments on co-crystal polymorphs: from formation to prediction, *CrystEngComm*, **2025**, *27*, 6415–6432.

47 G. R. Desiraju, Crystal engineering: a holistic view, *Angewandte Chemie (International ed. in English)*, **2007**, *46*, 8342–8356.

48 A. J. Cruz-Cabeza, N. Feeder and R. J. Davey, Open questions in organic crystal polymorphism, *Communications chemistry*, **2020**, *3*, 142.

49 S. L. Price, From crystal structure prediction to polymorph prediction: interpreting the crystal energy landscape, *Physical chemistry chemical physics : PCCP*, **2008**, *10*, 1996–2009.

50 S. L. Price, Computational prediction of organic crystal structures and polymorphism, *International Reviews in Physical Chemistry*, **2008**, *27*, 541–568.

51 A. Gavezzotti, Are Crystal Structures Predictable?, *Accounts of Chemical Research*, **1994**, *27*, 309–314.

52 A. J. Cruz-Cabeza and J. Bernstein, Conformational polymorphism, *Chemical Reviews*, **2014**, *114*, 2170–2191.

53 A. Llinàs and J. M. Goodman, Polymorph control: past, present and future, *Drug Discovery Today*, **2008**, *13*, 198–210.

54 S. L. Price, D. E. Braun and S. M. Reutzel-Edens, Can computed crystal energy landscapes help understand pharmaceutical solids?, *Chemical Communications*, **2016**, *52*, 7065–7077.

55 D.-K. Bučar, Engineering Molecular Crystals: Backbreaking, yet Gratifying, *Crystal Growth & Design*, **2017**, *17*, 2913–2918.

56 M. Herbst, D. Komisarek, T. Strothmann and V. Vasylyeva, A Lection in Humbleness: Crystallization of Chiral and Zwitterionic APIs Baclofen and Phenibut, *Crystals*, **2022**, *12*, 1393.

57 D. Braga, F. Grepioni, L. Maini and S. d'Agostino, Making crystals with a purpose; a journey in crystal engineering at the University of Bologna, *IUCrJ*, **2017**, *4*, 369–379.

58 G. N. Lewis, the Atom and the Molecule, *Journal of the American Chemical Society*, **1916**, *38*, 762–785.

59 W. M. Latimer and W. H. Rodebush, Polarity and Ionization from the Standpoint of the Lewis Theory of Valence, *Journal of the American Chemical Society*, **1920**, *42*, 1419–1433.

60 L. Pauling, *The Nature of the Chemical Bond and the Structure of Molecules and Crystals. An introduction to modern structural chemistry*, Cornell Univ. Press, Ithaca, NY, **1939**.

61 G. C. Pimentel and A. L. McClellan, *The Hydrogen Bond*, W.H. Freeman and Company, **1960**.

62 R. M. Badger and S. H. Bauer, Spectroscopic Studies of the Hydrogen Bond. II. The Shift of the O–H Vibrational Frequency in the Formation of the Hydrogen Bond, *The Journal of Chemical Physics*, **1937**, *5*, 839–851.

63 D. Hadzi, Infrared spectra of strongly hydrogen-bonded systems, *Pure and Applied Chemistry*, **1965**, *11*, 435–454.

64 L. Pauling, R. B. Corey and H. R. Branson, The structure of proteins; two hydrogen-bonded helical configurations of the polypeptide chain, *Proceedings of the National Academy of Sciences of the United States of America*, **1951**, *37*, 205–211.

65 W. C. Hamilton and J. A. Ibers, *Hydrogen Bonding in Solids: Methods of Molecular Structure Determination*, W.A.Benjamin, **1968**.

66 J. Donohue, The Hydrogen Bond in Organic Crystals, *The Journal of Physical Chemistry*, **1952**, *56*, 502–510.

67 E. Arunan, G. R. Desiraju, R. A. Klein, J. Sadlej, S. Scheiner, I. Alkorta, D. C. Clary, R. H. Crabtree, J. J. Dannenberg, P. Hobza, H. G. Kjaergaard, A. C. Legon, B. Mennucci and D. J. Nesbitt, Definition of the hydrogen bond (IUPAC Recommendations 2011), *Pure and Applied Chemistry*, **2011**, *83*, 1637–1641.

68 S. J. Grabowski, What is the covalency of hydrogen bonding?, *Chemical reviews*, **2011**, *111*, 2597–2625.

69 G. Gilli and P. Gilli, *The nature of the hydrogen bond. Outline of a comprehensive hydrogen bond theory*, Oxford Univ. Press, Oxford, 1st edn., **2009**.

70 G. R. Desiraju, Hydrogen bridges in crystal engineering: interactions without borders, *Accounts of Chemical Research*, **2002**, *35*, 565–573.

71 J. W. Larson and T. B. McMahon, Gas-phase bihalide and pseudobihalide ions. An ion cyclotron resonance determination of hydrogen bond energies in XHY- species (X, Y = F, Cl, Br, CN), *Inorganic Chemistry*, **1984**, *23*, 2029–2033.

72 J. Emsley, Very strong hydrogen bonding, *Chemical Society Reviews*, **1980**, *9*, 91.

73 G. R. Desiraju, A bond by any other name, *Angewandte Chemie (International ed. in English)*, **2011**, *50*, 52–59.

74 J. D. Wuest, Engineering crystals by the strategy of molecular tectonics, *Chemical Communications*, **2005**, 5830–5837.

75 M. W. Hosseini, *Molecular networks*, Springer, Berlin, Heidelberg, **2009**.

76 R. F. W. Bader, A quantum theory of molecular structure and its applications, *Chemical Reviews*, **1991**, *91*, 893–928.

77 R. F. Bader, *Atoms in molecules. A quantum theory*, Clarendon Press, Oxford, **1990**.

78 S. Emamian, T. Lu, H. Kruse and H. Emamian, Exploring Nature and Predicting Strength of Hydrogen Bonds: A Correlation Analysis Between Atoms-in-Molecules Descriptors, Binding Energies, and Energy Components of Symmetry-Adapted Perturbation Theory, *Journal of computational chemistry*, **2019**, *40*, 2868–2881.

79 C. B. Aakeröy, A. M. Beatty and B. A. Helfrich, A high-yielding supramolecular reaction, *Journal of the American Chemical Society*, **2002**, *124*, 14425–14432.

80 F. Guthrie, XXVIII.—On the iodide of iodammonium, *J. Chem. Soc.*, **1863**, *16*, 239–244.

81 H. A. Bent, Structural chemistry of donor-acceptor interactions, *Chemical Reviews*, **1968**, *68*, 587–648.

82 O. Hassel, Structural aspects of interatomic charge-transfer bonding, *Science (New York, N.Y.)*, **1970**, *170*, 497–502.

83 P. Politzer, P. Lane, M. C. Concha, Y. Ma and J. S. Murray, An overview of halogen bonding, *Journal of Molecular Modeling*, **2007**, *13*, 305–311.

84 G. R. Desiraju, P. S. Ho, L. Kloo, A. C. Legon, R. Marquardt, P. Metrangolo, P. Politzer, G. Resnati and K. Rissanen, Definition of the halogen bond (IUPAC Recommendations 2013), *Pure and Applied Chemistry*, **2013**, *85*, 1711–1713.

85 T. Clark, M. Hennemann, J. S. Murray and P. Politzer, Halogen bonding: the sigma-hole. Proceedings of "Modeling interactions in biomolecules II", Prague, September 5th-9th, 2005, *Journal of Molecular Modeling*, **2007**, *13*, 291–296.

86 P. Politzer and J. S. Murray, σ-Hole Interactions: Perspectives and Misconceptions, *Crystals*, **2017**, *7*, 212.

87 T. Clark, Halogen bonds and σ-holes, *Faraday discussions*, **2017**, *203*, 9–27.

88 P. Politzer, J. S. Murray and T. Clark, Halogen bonding and other σ-hole interactions: a perspective, *Physical chemistry chemical physics : PCCP*, **2013**, *15*, 11178–11189.

89 J. G. Hill and A. C. Legon, On the directionality and non-linearity of halogen and hydrogen bonds, *Physical chemistry chemical physics : PCCP*, **2015**, *17*, 858–867.

90 K. E. Riley, Critical comparison of R X···Y and R H···Y directionality in halogen and hydrogen bonds using modern computational chemistry methods, *Chemical Physics Letters*, **2020**, *744*, 137221.

91 P. Politzer, J. S. Murray and T. Clark, Halogen bonding: an electrostatically-driven highly directional noncovalent interaction, *Physical chemistry chemical physics : PCCP*, **2010**, *12*, 7748–7757.

92 R. K. Rowe and P. S. Ho, Relationships between hydrogen bonds and halogen bonds in biological systems, *Acta Crystallographica Section B, Structural Science, Crystal Engineering and Materials*, **2017**, *73*, 255–264.

93 E. Corradi, S. V. Meille, M. T. Messina, P. Metrangolo and G. Resnati, Perfluorocarbon-hydrocarbon self-assembly. Part 6:1 α,ω-Diiodoperfluoroalkanes as pseudohalogens in supramolecular synthesis, *Tetrahedron Letters*, **1999**, *40*, 7519–7523.

94 R. Siddiqui, J. Rani, H. M. Titi and R. Patra, Unravelling the potential of sigma hole-assisted co-crystallization: Highlighting recent developments, *Coordination Chemistry Reviews*, **2024**, *517*, 215994.

95 M. H. Kolář, J. Hostaš and P. Hobza, The strength and directionality of a halogen bond are co-determined by the magnitude and size of the σ-hole, *Physical chemistry chemical physics : PCCP*, **2014**, *16*, 9987–9996.

96 J. Teyssandier, K. S. Mali and S. de Feyter, Halogen Bonding in Two-Dimensional Crystal Engineering, *ChemistryOpen*, **2020**, *9*, 225–241.

97 M. H. Kolář, P. Deepa, H. Ajani, A. Pecina and P. Hobza, Characteristics of a σ-Hole and the Nature of a Halogen Bond, *Topics in current chemistry*, **2015**, *359*, 1–25.

98 C. B. Aakeröy, S. Panikkattu, P. D. Chopade and J. Desper, Competing hydrogen-bond and halogen-bond donors in crystal engineering, *CrystEngComm*, **2013**, *15*, 3125–3136.

99 E. Corradi, S. V. Meille, M. T. Messina, P. Metrangolo and G. Resnati, Halogen Bonding versus Hydrogen Bonding in Driving Self-Assembly Processes, *Angewandte Chemie International Edition*, **2000**, *39*, 1782–1786.

100 J. C. Gamekkanda, A. S. Sinha, J. Desper, M. Đaković and C. B. Aakeröy, Competition between hydrogen bonds and halogen bonds: a structural study, *New Journal of Chemistry*, **2018**, *42*, 10539–10547.

101 C. B. Aakeröy, T. K. Wijethunga, M. A. Haj, J. Desper and C. Moore, The structural landscape of heteroaryl-2-imidazoles: competing halogen- and hydrogen-bond interactions, *CrystEngComm*, **2014**, *16*, 7218.

102 C. B. Aakeröy, M. Fasulo, N. Schultheiss, J. Desper and C. Moore, Structural competition between hydrogen bonds and halogen bonds, *Journal of the American Chemical Society*, **2007**, *129*, 13772–13773.

103 Q. Li, X. Xu, T. Liu, B. Jing, W. Li, J. Cheng, B. Gong and J. Sun, Competition between hydrogen bond and halogen bond in complexes of formaldehyde with hypohalous acids, *Physical chemistry chemical physics : PCCP*, **2010**, *12*, 6837–6843.

104 J. Lieffrig, O. Jeannin, T. Guizouarn, P. Auban-Senzier and M. Fourmigué, Competition between the C–H···N Hydrogen Bond and C–I···N Halogen Bond in TCNQF n (n = 0, 2, 4) Salts with Variable Charge Transfer, *Crystal Growth & Design*, **2012**, *12*, 4248–4257.

105 P. Politzer, J. S. Murray and P. Lane, σ-Hole bonding and hydrogen bonding: Competitive interactions, *International Journal of Quantum Chemistry*, **2007**, *107*, 3046–3052.

106 A. M. S. Riel, R. K. Rowe, E. N. Ho, A.-C. C. Carlsson, A. K. Rappé, O. B. Berryman and P. S. Ho, Hydrogen Bond Enhanced Halogen Bonds: A Synergistic

Interaction in Chemistry and Biochemistry, *Accounts of Chemical Research*, **2019**, *52*, 2870–2880.

107 Z. Han, J. Li, Q. Liao, R. Luo, L. Wu, Y. Shi, L. Zhou, Q. Zhang, M. Erdélyi, W. Zhu and Z. Xu, Hydrogen Bond-Induced Binding between Organofluorine and Protein via Fluorine Atoms: A Database Survey and Quantum Chemistry Calculation Study, *Journal of medicinal chemistry*, **2025**, *68*, 14882–14894.

108 D. A. Decato, J. Sun, M. R. Boller and O. B. Berryman, Pushing the limits of the hydrogen bond enhanced halogen bond-the case of the C-H hydrogen bond, *Chemical science*, **2022**, *13*, 11156–11162.

109 H. Torii, A. Kimura and T. Sakai, Nature of hydrogen-bond-enhanced halogen bonding viewed through electron density changes, *Physical chemistry chemical physics : PCCP*, **2022**, *24*, 17951–17955.

110 S. Scheiner, Enhancement of Halogen Bond Strength by Intramolecular H-Bonds, *The journal of physical chemistry. A*, **2023**, *127*, 4695–4703.

111 C. Präsang, H. L. Nguyen, P. N. Horton, A. C. Whitwood and D. W. Bruce, Trimeric liquid crystals assembled using both hydrogen and halogen bonding, *Chemical Communications*, **2008**, 6164–6166.

112 V. Vasylyeva, S. K. Nayak, G. Terraneo, G. Cavallo, P. Metrangolo and G. Resnati, Orthogonal halogen and hydrogen bonds involving a peptide bond model, *CrystEngComm*, **2014**, *16*, 8102–8105.

113 A. R. Voth, P. Khuu, K. Oishi and P. S. Ho, Halogen bonds as orthogonal molecular interactions to hydrogen bonds, *Nature Chemistry*, **2009**, *1*, 74–79.

114 A. R. Voth, F. A. Hays and P. S. Ho, Directing macromolecular conformation through halogen bonds, *Proceedings of the National Academy of Sciences of the United States of America*, **2007**, *104*, 6188–6193.

115 C. C. Robertson, J. S. Wright, E. J. Carrington, R. N. Perutz, C. A. Hunter and L. Brammer, Hydrogen bonding vs. halogen bonding: the solvent decides, *Chemical science*, **2017**, *8*, 5392–5398.

116 G. R. Desiraju, J. J. Vittal and A. Ramanan, *Crystal Engineering*, World Scientific Publishing Company, Singapore, **2011**.

117 J. D. Dunitz and A. Gavezzotti, Molecular recognition in organic crystals: directed intermolecular bonds or nonlocalized bonding?, *Angewandte Chemie International Edition*, **2005**, *44*, 1766–1787.

118 A. M. Reilly and A. Tkatchenko, van der Waals dispersion interactions in molecular materials: beyond pairwise additivity, *Chemical science*, **2015**, *6*, 3289–3301.

119 M. K. Corpinot and D.-K. Bučar, A Practical Guide to the Design of Molecular Crystals, *Crystal Growth & Design*, **2019**, *19*, 1426–1453.

120 J. Contreras-García, E. R. Johnson, S. Keinan, R. Chaudret, J.-P. Piquemal, D. N. Beratan and W. Yang, NCIPLOT: a program for plotting non-covalent interaction regions, *Journal of chemical theory and computation*, **2011**, *7*, 625–632.

121 C. A. Hunter and J. K. M. Sanders, The nature of pi.-.pi. interactions, *Journal of the American Chemical Society*, **1990**, *112*, 5525–5534.

122 C. R. Martinez and B. L. Iverson, Rethinking the term “pi-stacking”, *Chemical science*, **2012**, *3*, 2191.

123 J. H. Williams, The molecular electric quadrupole moment and solid-state architecture, *Accounts of Chemical Research*, **1993**, *26*, 593–598.

124 C. D. Sherrill, Energy component analysis of π interactions, *Accounts of Chemical Research*, **2013**, *46*, 1020–1028.

125 S. Grimme, Do special noncovalent pi-pi stacking interactions really exist?, *Angewandte Chemie International Edition*, **2008**, *47*, 3430–3434.

126 K. Carter-Fenk and J. M. Herbert, Reinterpreting π-stacking, *Physical chemistry chemical physics : PCCP*, **2020**, *22*, 24870–24886.

127 G. R. Desiraju and T. Steiner, *The weak hydrogen bond in structural chemistry and biology*, Oxford Univ. Press, Oxford, **1999**.

128 M. Nishio, Y. Umezawa, J. Fantini, M. S. Weiss and P. Chakrabarti, CH-π hydrogen bonds in biological macromolecules, *Physical chemistry chemical physics : PCCP*, **2014**, *16*, 12648–12683.

129 S. E. Wheeler, Revisiting the Hunter-Sanders Model for π-π Interactions, *Journal of the American Chemical Society*, **2025**, *147*, 19738–19750.

130 A. Mandal, C. E. Mohn, C. H. Görbitz, M. Rogowska and O. Nilsen, Elucidating the role of charge transfer on semiconductor properties in a new donor–acceptor cocrystal 1,5-dihydroxynaphthalene : TCNQ, *Molecular Systems Design & Engineering*, **2025**, *10*, 519–533.

131 X. Fan, H. Zhang, K. Li, Z. Dong, J. Huang, F. Teng, H. Fan, H. Jiang, X. He and P. Hu, Improved specific capacity and cycling stability of organic cocrystal lithium-ion batteries through charge transfer, *CrystEngComm*, **2025**, *27*, 2502–2509.

132 C. Wu, Z. Wang, X. Han, X. Yu, C. C. Sun and Z. Zhou, Simultaneously improving tabletability and solubility of diclofenac by cocrystallization with picolinamide, *International Journal of Pharmaceutics*, **2025**, *670*, 125172.

133 X. Ding, C. Wei, L. Wang, J. Yang, W. Huang, Y. Chang, C. Ou, J. Lin and W. Huang, Multicomponent flexible organic crystals, *SmartMat*, **2024**, *5*.

134 P. Naumov, S. Chizhik, M. K. Panda, N. K. Nath and E. Boldyreva, Mechanically Responsive Molecular Crystals, *Chemical Reviews*, **2015**, *115*, 12440–12490.

135 S. Saha, M. K. Mishra, C. M. Reddy and G. R. Desiraju, From Molecules to Interactions to Crystal Engineering: Mechanical Properties of Organic Solids, *Accounts of Chemical Research*, **2018**, *51*, 2957–2967.

136 P. Naumov, D. P. Karothu, E. Ahmed, L. Catalano, P. Commins, J. Mahmoud Halabi, M. B. Al-Handawi and L. Li, The Rise of the Dynamic Crystals, *Journal of the American Chemical Society*, **2020**, *142*, 13256–13272.

137 A. Ainurofiq, R. Mauludin, D. Mudhakir, D. Umeda, S. N. Soewandhi, O. D. Putra and E. Yonemochi, Improving mechanical properties of desloratadine via multicomponent crystal formation, *European journal of pharmaceutical sciences : official journal of the European Federation for Pharmaceutical Sciences*, **2018**, *111*, 65–72.

138 W. M. Awad, D. W. Davies, D. Kitagawa, J. Mahmoud Halabi, M. B. Al-Handawi, I. Tahir, F. Tong, G. Campillo-Alvarado, A. G. Shtukenberg, T. Alkhidir, Y. Hagiwara, M. Almehairbi, L. Lan, S. Hasebe, D. P. Karothu, S. Mohamed, H. Koshima, S. Kobatake, Y. Diao, R. Chandrasekar, H. Zhang, C. C. Sun, C. Bardeen, R. O. Al-Kaysi, B. Kahr and P. Naumov, Mechanical properties and

peculiarities of molecular crystals, *Chemical Society Reviews*, **2023**, *52*, 3098–3169.

139 P. Sanphui, M. K. Mishra, U. Ramamurty and G. R. Desiraju, Tuning mechanical properties of pharmaceutical crystals with multicomponent crystals: voriconazole as a case study, *Molecular pharmaceutics*, **2015**, *12*, 889–897.

140 K. V. Drozd, A. N. Manin, D. E. Boycov, A. V. Churakov and G. L. Perlovich, Pharmaceutical Multicomponent Crystals of Antifungal Drugs with Improved Dissolution Performance, *Crystal Growth & Design*, **2021**, *21*, 7285–7297.

141 O. D. Putra and H. Uekusa, in *Advances in Organic Crystal Chemistry*, ed. M. Sakamoto and H. Uekusa, Springer Singapore; Imprint Springer, Singapore, 1st edn., **2020**, pp. 153–184.

142 G. Bolla, B. Sarma and A. K. Nangia, Crystal Engineering of Pharmaceutical Cocrystals in the Discovery and Development of Improved Drugs, *Chemical Reviews*, **2022**, *122*, 11514–11603.

143 M. Karimi-Jafari, L. Padrela, G. M. Walker and D. M. Croker, Creating Cocrystals: A Review of Pharmaceutical Cocrystal Preparation Routes and Applications, *Crystal Growth & Design*, **2018**, *18*, 6370–6387.

144 F. J. Acebedo-Martínez, C. Alarcón-Payer, H. M. Barrales-Ruiz, J. Niclós-Gutiérrez, A. Domínguez-Martín and D. Choquesillo-Lazarte, Towards the Development of Novel Diclofenac Multicomponent Pharmaceutical Solids, *Crystals*, **2022**, *12*, 1038.

145 A. Chettri, A. Subba, G. P. Singh and P. P. Bag, Pharmaceutical co-crystals: A green way to enhance drug stability and solubility for improved therapeutic efficacy, *The Journal of pharmacy and pharmacology*, **2024**, *76*, 1–12.

146 J. W. Steed, The role of co-crystals in pharmaceutical design, *Trends in pharmacological sciences*, **2013**, *34*, 185–193.

147 M. Guo, X. Sun, J. Chen and T. Cai, Pharmaceutical cocrystals: A review of preparations, physicochemical properties and applications, *Acta pharmaceutica Sinica. B*, **2021**, *11*, 2537–2564.

148 B. Saikia, A. Seidel-Morgenstern and H. Lorenz, Multicomponent Materials to Improve Solubility: Eutectics of Drug Aminoglutethimide, *Crystals*, **2022**, *12*, 40.

149 Q. Zhou, Z. Tan, D. Yang, J. Tu, Y. Wang, Y. Zhang, Y. Liu and G. Gan, Improving the Solubility of Aripiprazole by Multicomponent Crystallization, *Crystals*, **2021**, *11*, 343.

150 C. Wu, Y. Xiao, Y. Jing, Q. Yin and Y. Bao, New Insights into the Solubilization of Multicomponent Crystals: A Case Study of Pipemidic Acid, *Crystal Growth & Design*, **2023**, *23*, 3367–3383.

151 Di Wu, J. Li, Y. Xiao, X. Ji, C. Li, B. Zhang, B. Hou, L. Zhou, C. Xie, J. Gong and W. Chen, New Salts and Cocrystals of Pymetrozine with Improvements on Solubility and Humidity Stability: Experimental and Theoretical Study, *Crystal Growth & Design*, **2021**, *21*, 2371–2388.

152 S. Qiu and M. Li, Effects of coformers on phase transformation and release profiles of carbamazepine cocrystals in hydroxypropyl methylcellulose based matrix tablets, *International Journal of Pharmaceutics*, **2015**, *479*, 118–128.

153 S. Kumar and A. Nanda, Pharmaceutical Cocrystals: An Overview, *Indian Journal of Pharmaceutical Sciences*, **2017**, *79*.

154 P. Yu, Y. Zhen, H. Dong and W. Hu, Crystal Engineering of Organic Optoelectronic Materials, *Chem*, **2019**, *5*, 2814–2853.

155 D. Yan and D. G. Evans, Molecular crystalline materials with tunable luminescent properties: from polymorphs to multi-component solids, *Mater. Horiz.*, **2014**, *1*, 46–57.

156 A. A. Dar and A. A. Malik, Photoluminescent organic crystals and co-crystals, *Journal of Materials Chemistry C*, **2024**, *12*, 9888–9913.

157 D. Barman, M. Annadhasan, A. P. Bidkar, P. Rajamalli, D. Barman, S. S. Ghosh, R. Chandrasekar and P. K. Iyer, Highly efficient color-tunable organic co-crystals unveiling polymorphism, isomerism, delayed fluorescence for optical waveguides and cell-imaging, *Nature Communications*, **2023**, *14*, 6648.

158 B. P. Mali, S. R. Dash, M. Annadhasan, A. Biswas, K. Manoj, K. Vanka and R. G. Gonnade, Cocrystal Approach to Modulate the Photoluminescent Properties of a GFP Chromophore Analogue: Role of Halogen/Hydrogen Bonding in Achieving a Wide Range of Solid-State Fluorescence Emissions, *Crystal Growth & Design*, **2023**, *23*, 5052–5065.

159 J. Zhao and X. Zheng, Progress on Exploring the Luminescent Properties of Organic Molecular Aggregates by Multiscale Modeling, *Frontiers in Chemistry*, **2021**, *9*, 808957.

160 G. R. Desiraju, Crystal and co-crystal, *CrystEngComm*, **2003**, *5*, 466.

161 A. D. Bond, What is a co-crystal?, *CrystEngComm*, **2007**, *9*, 833.

162 C. B. Aakeröy and D. J. Salmon, Building co-crystals with molecular sense and supramolecular sensibility, *CrystEngComm*, **2005**, *7*, 439.

163 J. D. Dunitz, Crystal and co-crystal: a second opinion, *CrystEngComm*, **2003**, *5*, 506.

164 A. Parkin, C. J. Gilmore and C. C. Wilson, What is a co-crystal – and does it matter?, *Zeitschrift für Kristallographie - Crystalline Materials*, **2008**, *223*, 430.

165 S. Aitipamula, R. Banerjee, A. K. Bansal, K. Biradha, M. L. Cheney, A. R. Choudhury, G. R. Desiraju, A. G. Dikundwar, R. Dubey, N. Duggirala, P. P. Ghogale, S. Ghosh, P. K. Goswami, N. R. Goud, R. R. K. R. Jetti, P. Karpinski, P. Kaushik, D. Kumar, V. Kumar, B. Moulton, A. Mukherjee, G. Mukherjee, A. S. Myerson, V. Puri, A. Ramanan, T. Rajamannar, C. M. Reddy, N. Rodriguez-Hornedo, R. D. Rogers, T. N. G. Row, P. Sanphui, N. Shan, G. Shete, A. Singh, C. C. Sun, J. A. Swift, R. Thaimattam, T. S. Thakur, R. Kumar Thaper, S. P. Thomas, S. Tothadi, V. R. Vangala, N. Variankaval, P. Vishweshwar, D. R. Weyna and M. J. Zaworotko, Polymorphs, Salts, and Cocrystals: What's in a Name?, *Crystal Growth & Design*, **2012**, *12*, 2147–2152.

166 C. B. Aakeröy and A. S. Sinha, *Co-crystals. Preparation, characterization and applications*, Royal Society of Chemistry, Cambridge, **2018**.

167 A. Mondal, B. Bhattacharya, H. Chen, S. Khazaei, S. Das, S. Bhunia, S. Dey, R. Chowdhury, M. Bhattacharya, A. Tkatchenko, L. L. Stevens, C. C. Sun and C. M. Reddy, Plasticization of a stiff pharmaceutical solid for better tabletability via cocrystallization: Shape synthons as supramolecular protecting groups, *Chemical Engineering Research and Design*, **2024**, *210*, 506–512.

168 A. M. Healy, Z. A. Worku, D. Kumar and A. M. Madi, Pharmaceutical solvates, hydrates and amorphous forms: A special emphasis on cocrystals, *Advanced Drug Delivery Reviews*, **2017**, *117*, 25–46.

169 S. Boothroyd, A. Kerridge, A. Broo, D. Buttar and J. Anwar, Why Do Some Molecules Form Hydrates or Solvates?, *Crystal Growth & Design*, **2018**, *18*, 1903–1908.

170 C. H. Gorbitz and H. P. Hersleth, On the inclusion of solvent molecules in the crystal structures of organic compounds, *Acta crystallographica. Section B, Structural science*, **2000**, *56 (Pt 3)*, 526–534.

171 I. Shruti, M. Almehairbi, Z. M. Saeed, T. Alkhidir, W. A. Ali, R. Vishwakarma, S. Mohamed and D. Chopra, Unravelling the Origin of Solvate Formation in the Anticancer Drug Trametinib: Insights from Crystal Structure Analysis and Computational Modeling, *Crystal Growth & Design*, **2022**, *22*, 5861–5871.

172 I. Ymén, in *Solid state characterization of pharmaceuticals*, ed. R. A. Storey and I. Ymén, Wiley, Chichester, 1st edn., **2011**, pp. 1–34.

173 S. L. Childs, G. P. Stahly and A. Park, The salt-cocrystal continuum: the influence of crystal structure on ionization state, *Molecular Pharmaceutics*, **2007**, *4*, 323–338.

174 A. J. Cruz-Cabeza, Acid–base crystalline complexes and the pKa rule, *CrystEngComm*, **2012**, *14*, 6362.

175 E. A. Losev and E. V. Boldyreva, A salt or a co-crystal – when crystallization protocol matters, *CrystEngComm*, **2018**, *20*, 2299–2305.

176 T. Wang, J. S. Stevens, T. Vetter, G. F. S. Whitehead, I. J. Vitorica-Yrezabal, H. Hao and A. J. Cruz-Cabeza, Salts, Cocrystals, and Ionic Cocrystals of a “Simple” Tautomeric Compound, *Crystal Growth & Design*, **2018**, *18*, 6973–6983.

177 B. R. Bhogala, S. Basavoju and A. Nangia, Tape and layer structures in cocrystals of some di- and tricarboxylic acids with 4,4′-bipyridines and isonicotinamide. From binary to ternary cocrystals, *CrystEngComm*, **2005**, *7*, 551.

178 J. M. Ha, S. H. Hur, A. Pathak, J.-E. Jeong and H. Y. Woo, Recent advances in organic luminescent materials with narrowband emission, *NPG Asia Materials*, **2021**, *13*, 53.

179 J. Song, H. Lee, E. G. Jeong, K. C. Choi and S. Yoo, Organic Light-Emitting Diodes: Pushing Toward the Limits and Beyond, *Advanced Materials*, **2020**, *32*, e1907539.

180 J.-H. Lee, C.-H. Chen, P.-H. Lee, H.-Y. Lin, M. Leung, T.-L. Chiu and C.-F. Lin, Blue organic light-emitting diodes: current status, challenges, and future outlook, *Journal of Materials Chemistry C*, **2019**, *7*, 5874–5888.

181 S. Sudheendran Swayamprabha, D. K. Dubey, Shahnawaz, R. A. K. Yadav, M. R. Nagar, A. Sharma, F.-C. Tung and J.-H. Jou, Approaches for Long Lifetime Organic Light Emitting Diodes, *Advanced science (Weinheim, Baden-Wurttemberg, Germany)*, **2020**, *8*, 2002254.

182 P. L. dos Santos, P. Stachelek, Y. Takeda and P. Pander, Recent advances in highly-efficient near infrared OLED emitters, *Materials Chemistry Frontiers*, **2024**, *8*, 1731–1766.

183 S. Grotjahn and B. König, Common ground and divergence: OLED emitters as photocatalysts, *Chemical Communications*, **2024**, *60*, 12951–12963.

184 Z. Xiong, S. Xiang, Y. Lv, B. Chen and Z. Zhang, Hydrogen-Bonded Organic Frameworks as an Appealing Platform for Luminescent Sensing, *Advanced Functional Materials*, **2024**, *34*.

185 A. Krishna Mitra and N. Chakraborty, Advancing luminescent Sensing: Harnessing Metal-Organic frameworks for enhanced detection and analysis, *Inorganica Chimica Acta*, **2025**, *578*, 122520.

186 J. Zhang, M. Zhou, X. Li, Y. Fan, J. Li, K. Lu, H. Wen and J. Ren, Recent advances of fluorescent sensors for bacteria detection-A review, *Talanta*, **2023**, *254*, 124133.

187 C. Guo, A. C. Sedgwick, T. Hirao and J. L. Sessler, Supramolecular Fluorescent Sensors: An Historical Overview and Update, *Coordination Chemistry Reviews*, **2021**, *427*.

188 M. Jiang, C. Zhen, S. Li, X. Zhang and W. Hu, Organic Cocrystals: Recent Advances and Perspectives for Electronic and Magnetic Applications, *Frontiers in Chemistry*, **2021**, *9*, 764628.

189 S. Ito, Recent Advances in Mechanochromic Luminescence of Organic Crystalline Compounds, *Chemistry Letters*, **2021**, *50*, 649–660.

190 S. Ito, Mechanochromic luminescence of soft crystals: Recent systematic studies in controlling the molecular packing and mechanoresponsive properties,

Journal of Photochemistry and Photobiology C: Photochemistry Reviews, **2022**, *51*, 100481.

191 B. Li, L. Liu, Y. Wang, K. Liu, Z. Zheng, S. Sun, Y. Hu, L. Li and C. Li, Structurally diverse macrocycle co-crystals for solid-state luminescence modulation, *Nature Communications*, **2024**, *15*, 2535.

192 M. Schwoerer and H. C. Wolf, *Organic molecular solids*, Wiley-VCH, Weinheim, **2007**.

193 M. Pope and C. E. Swenberg, *Electronic processes in organic crystals and polymers*, Oxford University Press, New York, 2nd edn., **1999**.

194 M. Shimizu and T. Hiyama, Organic fluorophores exhibiting highly efficient photoluminescence in the solid state, *Chemistry, an Asian journal*, **2010**, *5*, 1516–1531.

195 S. Varghese and S. Das, Role of Molecular Packing in Determining Solid-State Optical Properties of π-Conjugated Materials, *The journal of physical chemistry letters*, **2011**, *2*, 863–873.

196 A. S. Davydov, The Theory of Molecular Excitons, *Soviet Physics Uspekhi*, **1964**, *7*, 145–178.

197 J. R. Lakowicz, *Principles of fluorescence spectroscopy*, Springer, New York, NY, 3rd edn., **2006**.

198 A. Myers Kelley, *Condensed-phase molecular spectroscopy and photophysics*, Wiley, Hoboken, **2023**.

199 M. Kasha, Characterization of electronic transitions in complex molecules, *Discussions of the Faraday Society*, **1950**, *9*, 14.

200 J. Gierschner, S. Varghese and S. Y. Park, Organic Single Crystal Lasers: A Materials View, *Advanced Optical Materials*, **2016**, *4*, 348–364.

201 Q. Li and Z. Li, The Strong Light-Emission Materials in the Aggregated State: What Happens from a Single Molecule to the Collective Group, *Advanced science (Weinheim, Baden-Wurttemberg, Germany)*, **2017**, *4*, 1600484.

202 K. Araki and T. Mutai, in *Photochemistry*, ed. E. Fasani, Royal Society of Chemistry, Cambridge, 1st edn., **2015**, pp. 191–225.

203 J. Luo, Z. Xie, J. W. Lam, L. Cheng, H. Chen, C. Qiu, H. S. Kwok, X. Zhan, Y. Liu, D. Zhu and B. Z. Tang, Aggregation-induced emission of 1-methyl-1,2,3,4,5-pentaphenylsilole, *Chemical Communications*, **2001**, 1740–1741.

204 N. J. Hestand and F. C. Spano, Expanded Theory of H- and J-Molecular Aggregates: The Effects of Vibronic Coupling and Intermolecular Charge Transfer, *Chemical Reviews*, **2018**, *118*, 7069–7163.

205 H. Y. Zhang, Z. L. Zhang, K. Q. Ye, J. Y. Zhang and Y. Wang, Organic Crystals with Tunable Emission Colors Based on a Single Organic Molecule and Different Molecular Packing Structures, *Advanced Materials*, **2006**, *18*, 2369–2372.

206 B. A. Nogueira, C. Castiglioni and R. Fausto, Color polymorphism in organic crystals, *Communications chemistry*, **2020**, *3*, 34.

207 C. Liang, Organic Polymorphs Based on AIE-Active Molecules: Preparation, Characterization, and Application, *Crystal Growth & Design*, **2024**, *24*, 7322–7341.

208 N. Xue, H.-Y. Zhou, Y. Han, M. Li, H.-Y. Lu and C.-F. Chen, A general supramolecular strategy for fabricating full-color-tunable thermally activated delayed fluorescence materials, *Nature Communications*, **2024**, *15*, 1425.

209 A. Hori, S. Takatani, T. K. Miyamoto and M. Hasegawa, Luminescence from π–π stacked bipyridines through arene–perfluoroarene interactions, *CrystEngComm*, **2009**, *11*, 567.

210 S. P. Anthony, S. Varughese and S. M. Draper, Switching and tuning organic solid-state luminescence via a supramolecular approach, *Chemical Communications*, **2009**, 7500–7502.

211 D. Yan, A. Delori, G. O. Lloyd, T. Friščić, G. M. Day, W. Jones, J. Lu, M. Wei, D. G. Evans and X. Duan, A cocrystal strategy to tune the luminescent properties of stilbene-type organic solid-state materials, *Angewandte Chemie International Edition*, **2011**, *50*, 12483–12486.

212 J. D. Wuest, Molecular solids: Co-crystals give light a tune-up, *Nature Chemistry*, **2012**, *4*, 74–75.

213 M. Singh, K. Liu, S. Qu, H. Ma, H. Shi, Z. An and W. Huang, Recent Advances of Cocrystals with Room Temperature Phosphorescence, *Advanced Optical Materials*, **2021**, *9*.

214 X. Zhang, Z. Gao, X. He and P. Hu, Organic charge transfer cocrystals for photoluminescence, *CrystEngComm*, **2025**, *27*, 6572–6588.

215 L. Sun, F. Yang, X. Zhang and W. Hu, Stimuli-responsive behaviors of organic charge transfer cocrystals: recent advances and perspectives, *Materials Chemistry Frontiers*, **2020**, *4*, 715–728.

216 J. Gierschner, J. Shi, B. Milián-Medina, D. Roca-Sanjuán, S. Varghese and S. Park, Luminescence in Crystalline Organic Materials: From Molecules to Molecular Solids, *Advanced Optical Materials*, **2021**, *9*.

217 D. Yan, Micro-/nanostructured multicomponent molecular materials: design, assembly, and functionality, *Chemistry - A European Journal*, **2015**, *21*, 4880–4896.

218 B. Lu, S. Liu and D. Yan, Recent advances in photofunctional polymorphs of molecular materials, *Chinese Chemical Letters*, **2019**, *30*, 1908–1922.

219 B. Lu, X. Fang and D. Yan, Luminescent Polymorphic Co-crystals: A Promising Way to the Diversity of Molecular Assembly, Fluorescence Polarization, and Optical Waveguide, *ACS applied materials & interfaces*, **2020**, *12*, 31940–31951.

220 R. Gao, M. S. Kodaimati and D. Yan, Recent advances in persistent luminescence based on molecular hybrid materials, *Chemical Society Reviews*, **2021**, *50*, 5564–5589.

221 S. Wu, B. Zhou and D. Yan, Recent Advances on Molecular Crystalline Luminescent Materials for Optical Waveguides, *Advanced Optical Materials*, **2021**, *9*.

222 P. F. Heelis, The photophysical and photochemical properties of flavins (isoalloxazines), *Chemical Society Reviews*, **1982**, *11*, 15.

223 A. M. Edwards, in *Flavins*, ed. E. Silva and A. M. Edwards, Royal Society of Chemistry, Cambridge, **2007**, pp. 1–11.

224 T. Pavlovska and R. Cibulka, in *Flavin-based catalysis*, ed. R. Cibulka and M. W. Fraaije, Wiley-VCH, Weinheim, **2021**, pp. 1–27.

225 P. Mondal, K. Schwinn and M. Huix-Rotllant, Impact of the redox state of flavin chromophores on the UV–vis spectra, redox and acidity constants and electron

affinities, *Journal of Photochemistry and Photobiology A: Chemistry*, **2020**, *387*, 112164.

226 S. O. Mansoorabadi, C. J. Thibodeaux and H. Liu, The diverse roles of flavin coenzymes--nature's most versatile thespians, *The Journal of organic chemistry*, **2007**, *72*, 6329–6342.

227 V. Massey, The Chemical and Biological Versatility of Riboflavin, *Biochemical Society Transactions*, **2000**, *28*, 283–296.

228 I. Ahmad and F. H. Vaid, in *Flavins*, ed. E. Silva and A. M. Edwards, Royal Society of Chemistry, Cambridge, **2007**, pp. 13–40.

229 J. Drenth and M. W. Fraaije, in *Flavin-based catalysis*, ed. R. Cibulka and M. W. Fraaije, Wiley-VCH, Weinheim, **2021**, pp. 29–65.

230 M. Insińska-Rak, M. Sikorski and A. Wolnicka-Glubisz, Riboflavin and Its Derivates as Potential Photosensitizers in the Photodynamic Treatment of Skin Cancers, *Cells*, **2023**, *12*.

231 J. Ribes, P. Cossard, K. Al Yaman, I. Bestel and E. Badarau, Investigating the photosensitization activities of flavins irradiated by blue LEDs, *RSC Advances*, **2023**, *13*, 2355–2364.

232 M. Insińska-Rak and M. Sikorski, Riboflavin interactions with oxygen-a survey from the photochemical perspective, *Chemistry - A European Journal*, **2014**, *20*, 15280–15291.

233 M. V. Encinas and C. M. Previtali, in *Flavins*, ed. E. Silva and A. M. Edwards, Royal Society of Chemistry, Cambridge, **2007**, pp. 41–59.

234 M. Sikorski, I. Khmelinskii and E. Sikorska, in *Flavin-based catalysis*, ed. R. Cibulka and M. W. Fraaije, Wiley-VCH, Weinheim, **2021**, pp. 67–96.

235 A. S. Anderton, O. J. Knowles, J. A. Rossi-Ashton and D. J. Procter, Flavin-Mediated Photocatalysis Provides a General Platform for Sulfide C-H Functionalization, *ACS catalysis*, **2024**, *14*, 2395–2401.

236 V. Srivastava, P. K. Singh, A. Srivastava and P. P. Singh, Synthetic applications of flavin photocatalysis: a review, *RSC Advances*, **2021**, *11*, 14251–14259.

237 S. G. Schulman, pH dependence of fluorescence of riboflavin and related isoalloxazine derivatives, *Journal of Pharmaceutical Sciences*, **1971**, *60*, 628–631.

238 P. Drössler, W. Holzer, A. Penzkofer and P. Hegemann, pH dependence of the absorption and emission behaviour of riboflavin in aqueous solution, *Chemical Physics*, **2002**, *282*, 429–439.

239 A. Tyagi and A. Penzkofer, pH dependence of the absorption and emission behaviour of lumiflavin in aqueous solution, *Journal of Photochemistry and Photobiology A: Chemistry*, **2010**, *215*, 108–117.

240 S. Salzmann, J. Tatchen and C. M. Marian, The photophysics of flavins: What makes the difference between gas phase and aqueous solution?, *Journal of Photochemistry and Photobiology A: Chemistry*, **2008**, *198*, 221–231.

241 J. Wang and Y. Liu, Systematic Theoretical Study on the pH-Dependent Absorption and Fluorescence Spectra of Flavins, *Molecules (Basel, Switzerland)*, **2023**, *28*.

242 M. P. Kabir, Y. Orozco-Gonzalez and S. Gozem, Electronic spectra of flavin in different redox and protonation states: a computational perspective on the effect of the electrostatic environment, *Physical chemistry chemical physics : PCCP*, **2019**, *21*, 16526–16537.

243 S.-H. Song, B. Dick, A. Penzkofer, R. Pokorny, A. Batschauer and L.-O. Essen, Absorption and fluorescence spectroscopic characterization of cryptochrome 3 from Arabidopsis thaliana, *Journal of Photochemistry and Photobiology B: Biology*, **2006**, *85*, 1–16.

244 M. S. Islam, M. Honma, T. Nakabayashi, M. Kinjo and N. Ohta, pH dependence of the fluorescence lifetime of FAD in solution and in cells, *International Journal of Molecular Sciences*, **2013**, *14*, 1952–1963.

245 K. Sato, Y. Nishina and K. Shiga, Decomposition of the fluorescence spectra of two FAD molecules in electron-transferring flavoprotein from Megasphaera elsdenii, *Journal of Biochemistry*, **2013**, *154*, 61–66.

246 E. Sikorska, I. Khmelinskii, A. Komasa, J. Koput, L. F. Ferreira, J. R. Herance, J. L. Bourdelande, S. L. Williams, D. R. Worrall, M. Insińska-Rak and M. Sikorski,

Spectroscopy and photophysics of flavin related compounds: Riboflavin and iso-(6,7)-riboflavin, *Chemical Physics*, **2005**, *314*, 239–247.

247 E. Sikorska, I. V. Khmelinskii, W. Prukała, S. L. Williams, M. Patel, D. R. Worrall, J. L. Bourdelande, J. Koput and M. Sikorski, Spectroscopy and Photophysics of Lumiflavins and Lumichromes, *The Journal of Physical Chemistry A*, **2004**, *108*, 1501–1508.

248 M. Insińska-Rak, E. Sikorska, J. L. Bourdelande, I. V. Khmelinskii, W. Prukała, K. Dobek, J. Karolczak, I. F. Machado, L. F. Ferreira, A. Komasa, D. R. Worrall and M. Sikorski, Spectroscopy and photophysics of flavin-related compounds: 5-deaza-riboflavin, *Journal of Molecular Structure*, **2006**, *783*, 184–190.

249 M. Kowalczyk, E. Sikorska, I. V. Khmelinskii, J. Komasa, M. Insińska-Rak and M. Sikorski, Spectroscopy and photophysics of flavin-related compounds: Isoalloxazines, *Journal of Molecular Structure: THEOCHEM*, **2005**, *756*, 47–54.

250 J. Koziol, STUDIES ON FLAVINS IN ORGANIC SOLVENTS-I*. SPECTRAL CHARACTERISTICS OF RIBOFLAVIN, RIBOFLAVIN TETRABUTYRATE AND LUMICHROME, *Photochemistry and Photobiology*, **1966**, *5*, 41–54.

251 A. Kotaki and K. Yagi, Fluorescence properties of flavins in various solvents, *Journal of Biochemistry*, **1970**, *68*, 509–516.

252 E. V. Nemtseva, D. V. Gulnov, A. A. Deeva, N. S. Rodionova, M. V. Vavilov, R. I. Zagitova and V. N. Petushkov, Photoacidity and solvent-dependent fluorescence of 7,8-didemethyl-8-hydroxy-5-deazariboflavin, *Journal of Photochemistry and Photobiology B: Biology*, **2025**, *272*, 113280.

253 M. Insińska-Rak, E. Sikorska, J. L. Bourdelande, I. V. Khmelinskii, W. Prukała, K. Dobek, J. Karolczak, I. F. Machado, L. F. Ferreira, E. Dulewicz, A. Komasa, D. R. Worrall, M. Kubicki and M. Sikorski, New photochemically stable riboflavin analogue—3-Methyl-riboflavin tetraacetate, *Journal of Photochemistry and Photobiology A: Chemistry*, **2007**, *186*, 14–23.

254 M. Insińska-Rak, E. Sikorska, J. R. Herance, J. L. Bourdelande, I. V. Khmelinskii, M. Kubicki, W. Prukała, I. F. Machado, A. Komasa, L. F. V. Ferreira and M. Sikorski, Spectroscopy and photophysics of flavin-related compounds: 3-benzyl-lumiflavin, *Photochemical & photobiological sciences : Official journal of the*

European Photochemistry Association and the European Society for Photobiology, **2005**, *4*, 463–468.

255 Karl Decker, in *Chemistry and Biochemistry of Flavoenzymes*, CRC Press, **2018**, pp. 343–376.

256 K. Nishimoto, H. Fukunaga and K. Yagi, Studies in a model system on the effect of hydrogen bonding at hetero atoms of oxidized flavin on its electron acceptability, *Journal of Biochemistry*, **1986**, *100*, 1647–1653.

257 E. Breinlinger, A. Niemz and V. M. Rotello, Model Systems for Flavoenzyme Activity. Stabilization of the Flavin Radical Anion through Specific Hydrogen Bond Interactions, *Journal of the American Chemical Society*, **1995**, *117*, 5379–5380.

258 A. Niemz and V. M. Rotello, From Enzyme to Molecular Device. Exploring the Interdependence of Redox and Molecular Recognition, *Accounts of Chemical Research*, **1999**, *32*, 44–52.

259 J. L. Wells, B. L. Trus, R. M. Johnston, R. E. Marsh and C. J. Fritchie, Crystal structure of the yellow molecular complex lumiflavin–bis(naphthalene-2,3-diol), *Acta Crystallographica Section B Structural Crystallography and Crystal Chemistry*, **1974**, *30*, 1127–1134.

260 D. Voet and A. Rich, The crystal and molecular structure of an intermolecular complex between riboflavin and an adenosine derivative, *Proceedings of the National Academy of Sciences of the United States of America*, **1971**, *68*, 1151–1156.

261 M. C. Kuo, J. B. R. Dunn and C. J. Fritchie, The crystal structure of a flavin molecular complex: 10-propylisoalloxazine–bis(naphthalene-2,3-diol), *Acta Crystallographica Section B Structural Crystallography and Crystal Chemistry*, **1974**, *30*, 1766–1771.

262 F. E. Scarbrough, H.-S. Shieh and D. Voet, The X-ray crystal structure of the molecular complex bis(lumiflavin–2,6-diamino-9-ethylpurine)–ethanol–water, *Acta Crystallographica Section B Structural Crystallography and Crystal Chemistry*, **1977**, *33*, 2512–2523.

263 S. T. Caldwell, L. J. Farrugia, S. G. Hewage, N. Kryvokhyzha, V. M. Rotello and G. Cooke, Model systems for flavoenzyme activity: an investigation of the role

functionality attached to the C(7) position of the flavin unit has on redox and molecular recognition properties, *Chemical Communications*, **2009**, 1350–1352.

264 J. Wouters, G. Evrard and F. Durant, Lumiflavinium (7,8,10-Trimethylisoalloxazinium) Nitrate, *Acta Crystallographica Section C Crystal Structure Communications*, **1995**, *51*, 1223–1227.

265 J. H. Reibenspies, F. Guo and C. J. Rizzo, X-ray crystal structures of conformationally biased flavin models, *Organic letters*, **2000**, *2*, 903–906.

266 R. B. Bates, T. C. Sneath and D. N. Stephens, Crystal structure of 10-methylisoalloxazinium bromide dihydrate, *The Journal of organic chemistry*, **1970**, *35*, 1625–1627.

267 J.S. Sherfinski, A.J. deArmendi, C.J. Fritchie Junior, *American Crystallographic Association Abstracts, Papers (Summer)*, **1974**, *238*.

268 C. J. Fritchie Jr., G. D. Sproul, T. D. Wade, *Acta Crystallographica Section A: Cryst.Phys.,Diffr.,Theor.Crystallogr.*, **1972**, *28*, S48.

269 S. Otani, S. Kasai and K. Matsui, Isolation, chemical synthesis, and properties of roseoflavin, *Methods in enzymology*, **1980**, *66*, 235–241.

270 S. Kasai, R. Miura and K. Matsui, Chemical Structure and Some Properties of Roseoflavin, *Bulletin of the Chemical Society of Japan*, **1975**, *48*, 2877–2880.

271 B. Karasulu and W. Thiel, Photoinduced intramolecular charge transfer in an electronically modified flavin derivative: roseoflavin, *The journal of physical chemistry. B*, **2015**, *119*, 928–943.

272 P. Bombicz, Crystallization: from molecules to crystal structures, *Crystallography Reviews*, **2022**, *28*, 67–69.

273 K. Kurpiewska and T. Borowski, Seven quick tips for beginners in protein crystallography, *Acta biochimica Polonica*, **2021**, *68*, 535–546.

274 J. P. Metherall, R. C. Carroll, S. J. Coles, M. J. Hall and M. R. Probert, Advanced crystallisation methods for small organic molecules, *Chemical Society Reviews*, **2023**, *52*, 1995–2010.

275 N. Pawar, A. Saha, N. Nandan and J. Parambil, Solution Cocrystallization: A Scalable Approach for Cocrystal Production, *Crystals*, **2021**, *11*, 303.

276 T. Friščić and W. Jones, Recent Advances in Understanding the Mechanism of Cocrystal Formation via Grinding, *Crystal Growth & Design*, **2009**, *9*, 1621–1637.

277 F. Delogu and G. Cocco, Weakness of the “hot spots” approach to the kinetics of mechanically induced phase transformations, *Journal of Alloys and Compounds*, **2008**, *465*, 540–546.

278 J.-L. Do and T. Friščić, Mechanochemistry: A Force of Synthesis, *ACS central science*, **2017**, *3*, 13–19.

279 S. Hwang, S. Grätz and L. Borchardt, A guide to direct mechanocatalysis, *Chemical Communications*, **2022**, *58*, 1661–1671.

280 A. A. L. Michalchuk, On the physical processes of mechanochemically induced transformations in molecular solids, *Chemical Communications*, **2024**, *60*, 14750–14761.

281 W. Jones and M. D. Eddleston, Introductory lecture: Mechanochemistry, a versatile synthesis strategy for new materials, *Faraday discussions*, **2014**, *170*, 9–34.

282 M. Solares-Briones, G. Coyote-Dotor, J. C. Páez-Franco, M. R. Zermeño-Ortega, C. M. de La O Contreras, D. Canseco-González, A. Avila-Sorrosa, D. Morales-Morales and J. M. Germán-Acacio, Mechanochemistry: A Green Approach in the Preparation of Pharmaceutical Cocrystals, *Pharmaceutics*, **2021**, *13*.

283 S. Arfelis, A. I. Martín-Perales, R. Nguyen, A. Pérez, I. Cherubin, C. Len, I. Malpartida, A. Bala and P. Fullana-I-Palmer, Linking mechanochemistry with the green chemistry principles: Review article, *Heliyon*, **2024**, *10*, e34655.

284 P. F. M. de Oliveira, R. M. Torresi, F. Emmerling and P. H. C. Camargo, Challenges and opportunities in the bottom-up mechanochemical synthesis of noble metal nanoparticles, *Journal of Materials Chemistry A*, **2020**, *8*, 16114–16141.

285 T. Haj Hassani Sohi, F. Maass, C. Czekelius, M. Suta and V. Vasylyeva, Co-crystallization of organic chromophore roseolumiflavin and effect on its optical characteristics, *CrystEngComm*, **2022**, *24*, 7315–7325.

286 T. Haj Hassani Sohi, F. Maass, C. Czekelius and V. Vasylyeva, A Comparison Study of Roseolumiflavin Solvates: Structural and Energetic Perspective on Their Stability, *Crystals*, **2023**, *13*, 1512.

287 T. Haj Hassani Sohi, L. Pongratz, F. Maaß, S. Merzenich, L. Samperisi, C. Czekelius and V. Vasylyeva, Tuning Molecular Assembly and Optical Properties via Cocrystallization: A Case Study of Roseolumiflavin in Binary and Ternary Multicomponent Systems, *Crystal Growth & Design*, **2025**, *25*, 10482–10496.